

NAT'L INST. OF STAND & TECH



A11105 973541













REFERENCE

175167-Ref.

OCT 17 1975

A UNITED STATES  
DEPARTMENT OF  
COMMERCE  
PUBLICATION

NAT'L INST. OF STAND & TECH



A11106 040040

QC100

.U57



NBS SPECIAL PUBLICATION 372

# Laser Induced Damage In Optical Materials: 1972

U.S.  
DEPARTMENT  
OF  
COMMERCE

National  
Bureau

QC of  
100 rds

157

372

972

The National Bureau of Standards<sup>1</sup> was established by an act of Congress March 3, 1901. The Bureau's overall goal is to strengthen and advance the Nation's science and technology and facilitate their effective application for public benefit. To this end, the Bureau conducts research and provides: (1) a basis for the Nation's physical measurement system, (2) scientific and technological services for industry and government, (3) a technical basis for equity in trade, and (4) technical services to promote public safety. The Bureau consists of the Institute for Basic Standards, the Institute for Materials Research, the Institute for Applied Technology, the Center for Computer Sciences and Technology, and the Office for Information Programs.

**THE INSTITUTE FOR BASIC STANDARDS** provides the central basis within the United States of a complete and consistent system of physical measurement; coordinates that system with measurement systems of other nations; and furnishes essential services leading to accurate and uniform physical measurements throughout the Nation's scientific community, industry, and commerce. The Institute consists of a Center for Radiation Research, an Office of Measurement Services and the following divisions:

Applied Mathematics—Electricity—Heat—Mechanics—Optical Physics—Linac Radiation<sup>2</sup>—Nuclear Radiation<sup>2</sup>—Applied Radiation<sup>2</sup>—Quantum Electronics<sup>3</sup>—Electromagnetics<sup>3</sup>—Time and Frequency<sup>3</sup>—Laboratory Astrophysics<sup>3</sup>—Cryogenics<sup>3</sup>.

**THE INSTITUTE FOR MATERIALS RESEARCH** conducts materials research leading to improved methods of measurement, standards, and data on the properties of well-characterized materials needed by industry, commerce, educational institutions, and Government; provides advisory and research services to other Government agencies; and develops, produces, and distributes standard reference materials. The Institute consists of the Office of Standard Reference Materials and the following divisions:

Analytical Chemistry—Polymers—Metallurgy—Inorganic Materials—Reactor Radiation—Physical Chemistry.

**THE INSTITUTE FOR APPLIED TECHNOLOGY** provides technical services to promote the use of available technology and to facilitate technological innovation in industry and Government; cooperates with public and private organizations leading to the development of technological standards (including mandatory safety standards), codes and methods of test; and provides technical advice, and services to Government agencies upon request. The Institute also monitors NBS engineering standards activities and provides liaison between NBS and national and international engineering standards bodies. The Institute consists of a Center for Building Technology and the following divisions and offices:

Engineering Standards Services—Weights and Measures—Invention and Innovation—Product Evaluation Technology—Electronic Technology—Technical Analysis—Measurement Engineering—Fire Technology—Housing Technology<sup>4</sup>—Federal Building Technology<sup>4</sup>—Building Standards and Codes Services<sup>4</sup>—Building Environment<sup>4</sup>—Structures, Materials and Life Safety<sup>4</sup>—Technical Evaluation and Application<sup>4</sup>.

**THE CENTER FOR COMPUTER SCIENCES AND TECHNOLOGY** conducts research and provides technical services designed to aid Government agencies in improving cost effectiveness in the conduct of their programs through the selection, acquisition, and effective utilization of automatic data processing equipment; and serves as the principal focus within the executive branch for the development of Federal standards for automatic data processing equipment, techniques, and computer languages. The Center consists of the following offices and divisions:

Information Processing Standards—Computer Information—Computer Services—Systems Development—Information Processing Technology.

**THE OFFICE FOR INFORMATION PROGRAMS** promotes optimum dissemination and accessibility of scientific information generated within NBS and other agencies of the Federal Government; promotes the development of the National Standard Reference Data System and a system of information analysis centers dealing with the broader aspects of the National Measurement System; provides appropriate services to ensure that the NBS staff has optimum accessibility to the scientific information of the world, and directs the public information activities of the Bureau. The Office consists of the following organizational units:

Office of Standard Reference Data—Office of Technical Information and Publications—Library—Office of International Relations.

<sup>1</sup> Headquarters and Laboratories at Gaithersburg, Maryland, unless otherwise noted; mailing address Washington, D.C. 20234.

<sup>2</sup> Part of the Center for Radiation Research.

<sup>3</sup> Located at Boulder, Colorado 80302.

<sup>4</sup> Part of the Center for Building Technology.



# Laser Induced Damage In Optical Materials: 1972

---

Proceedings of a Symposium Sponsored by  
The American Society for Testing and Materials  
And by the National Bureau of Standards

June 14-15, 1972  
NBS, Boulder, Colorado 80302

Edited by

Alexander J. Glass  
Wayne State University  
Detroit, Michigan 48202

and

Arthur H. Guenther  
Air Force Weapons Laboratory  
Kirkland AFB, New Mexico 87117



---

U.S. DEPARTMENT OF COMMERCE, Peter G. Peterson, Secretary

U.S. NATIONAL BUREAU OF STANDARDS, Lawrence M. Kushner, Acting Director

Issued October 1972

Library of Congress Catalog Card Number: 72-600276

**National Bureau of Standards Special Publication 372**

Nat. Bur. Stand. (U.S.), Spec. Publ. 372, 215 pages (Oct. 1972)

CODEN: XNBSAV

## Foreword

*These proceedings report in detail the formal papers presented at the 4th Annual Symposium on Laser Damage in Optical Materials held at the National Bureau of Standards, Boulder, Colorado on June 14 and 15, 1972. This meeting was jointly sponsored by the National Bureau of Standards and the American Society of Testing and Materials. The major topics covered were bulk damage in transparent dielectrics, damage at dielectric surfaces, damage due to self-focusing, damage to dielectric coatings, as well as damage to mirrors and windows in the infrared.*

*The co-chairmen, Dr. Alexander J. Glass of Wayne State University, Detroit, Michigan, and Dr. A. H. Guenther of the Air Force Weapons Laboratory, Kirtland ARB, New Mexico, take full responsibility for the summary, conclusions, and recommendations contained in this report. Due to difficulties encountered in the recording process, it was not possible to include a summary of the discussions at the conclusion of each presentation as is our usual practice. It is suggested that individuals interested in the subject of this meeting obtain copies of those publications referenced in the bibliography contained in the summary and conclusions.*

*It is our intention to convene another symposium next year in Boulder during May to update and document the state-of-the-art of Laser Damage in Optical Materials at that time. This meeting will cover the subject historically presented at these symposia with additional emphasis on thin film damage, the problem of the damage of materials and components at 10.6  $\mu\text{m}$ , as well as address ourselves to the subject of optical reliability as influenced by laser applications. We wish to encourage the reader to contact us on matters pertinent to the intent of these conferences.*

A. H. Guenther

Library of Congress Catalog Card Number: 72-600276





	Page
Foreword .....	iii
A. H. Guenther	
Summary and Conclusions .....	vii
A. J. Glass and A. H. Guenther	
Opening Remarks.....	1
C. M. Stickley	
Laser Damage of HOYA Laser Glass, LCG-11.....	3
Tetsuro Izumitani, Kosaku Hosaka and Chiyoe Yamanaka	
Interaction Gradients, Concurrent Light Scattering Experiments and Bulk Damage in Solids.....	11
C. Y. She and David F. Edwards	
Optical Index Damage in Electrooptic Crystals .....	15
A. M. Glass, G. E. Peterson and T. J. Negran	
Comparison of Laser Induced Bulk Damage in Alkali-Halides at 10.6, 1.06, and 0.69 Microns.....	27
D. W. Fradin and Eli Yablonovitch	
Laser Induced Damage to Glass Surfaces.....	40
N. L. Boling and G. Dube'	
The Relation Between Surface Damage and Surface Plasma Formation.....	46
Concetto R. Giuliano	
Ion Beam Polishing as a Means of Increasing Surface Damage Thresholds in Sapphire.....	55
Concetto R. Giuliano	
Laser-Induced Damage Probability at 1.06 and 0.69 $\mu\text{m}$ .....	58
Michael Bass and Harrison H. Barrett	
Damage to GaAs Surfaces from Ruby- and Nd-Glass Laser Illumination.....	70
J. Lynn Smith	
Surface Science and Surface Damage.....	75
Jhan M. Khan	
Self-Focusing with Elliptical Beams .....	84
John Marburger	
Relative Contribution of Kerr Effect and Electrostriction to Self-Focusing.....	92
Albert Feldman, Deane Horowitz and Roy M. Waxler	
Damage Measurements with Subnanosecond Pulses.....	100
John M. McMahon	
Time Resolved Damage Studies of Thin Films and Substrate Surfaces.....	104
J. H. Parks and N. Alyassini	
Laser Induced Damage to Mirrors at Two Pulse Durations.....	108
E. S. Bliss and D. Milam	
Study of Laser-Irradiated Thin Films.....	123
Brian E. Newnam and L. G. DeShazer	
Influence of Structural Effects on Laser Damage Thresholds of Discrete and Inhomogeneous Thin Films and Multilayers.....	135
R. Russel Austin, Raymond C. Michaud, Arthur H. Guenther, Joseph M. Putman and Richard Harniman	
Fundamental Absorption Mechanisms in High-Power Laser Window Materials.....	165
Robert Hellwarth	

Contents-continued

	Page
Recent Developments in High-Power Infrared-Window Research..... M. Sparks	172
Low Emittance and Absorptance Measurements of Windows and Mirrors..... Geert Wijntjes, Norman J. E. Johnson and J. Morris Weinberg	176
Investigations of Pulsed CO <sub>2</sub> Laser Damage of Metal and Dielectric-Coated Mirrors..... V. Wang, A. I. Braunstein, M. Braunstein, and J. Y. Wada	183
Appendix	
Participants.....	194

*Laser Induced Damage in Optical Materials*  
4th ASTM Symposium  
June 14-15, 1972

Abstract

The fourth ASTM Symposium on Laser Induced Damage in Optical Materials was held at the National Bureau of Standards in Boulder, Colorado on June 14-15 of this year. This symposium is held as part of the activity of Subcommittee II on Lasers and Laser Materials, of the ASTM. Subcommittee II is charged with the responsibility of formulating standards for laser materials, components, and devices. The chairman of Subcommittee II is Haynes Lee, of Owen-Illinois, Inc. Co-chairmen for the damage symposia are Dr. Arthur H. Guenther, of the Air Force Weapons Laboratory, and Professor Alexander J. Glass, Chairman of the Department of Electrical Engineering at Wayne State University.

Approximately 125 attendees at the symposium heard 21 papers on topics relating to laser induced damage in glass, crystalline materials, nonlinear optical materials, thin film dielectric coatings, and infrared components. Particular attention was given to the processes of plasma formation at dielectric surfaces, the role played by self-focusing in bulk damage in solids, damage morphology of thin film coatings, and the role of absorption in IR component failure.

The proceedings of these Symposia represent the major source of information in the field of laser induced damage in optical materials. The Symposia themselves, along with the periodic meetings of Subcommittee II, provide a unique forum for the exchange of information regarding laser materials specifications among the manufacturers and users of laser devices, components, and systems. The Symposium also serves as a mechanism of information gathering, to enable the Subcommittee to write informed and realistic specifications.

Key Words: IR windows and mirrors; laser damage; laser materials; self-focusing; thin films.

1. Principal Conclusions

In his opening remarks to the 1972 Symposium on Damage in Laser Materials, C. Martin Stickley, of the Defense Advanced Research Projects Agency, summarized the progress which has been made to date in the identification, understanding, and remedy of damage mechanisms in laser materials, and the problems remaining to be solved. It is noteworthy that in the four-year span of these symposia, there has been substantive progress in the understanding and improvements of the damage resistance of laser materials, progress which is documented in the series of symposium proceedings. In the study of damage in solid laser hosts, there has been a healthy transition from Edisonian empiricism to carefully designed experimental investigation, coupled with refinements in theory. There have also been real advances in materials. Bulk damage due to microinhomogeneities is now reduced to a problem in quality control. Self-focusing damage can be avoided by design, once the material parameters are measured. Surface damage has been unequivocally associated with plasma formation within the dielectric at the surface, and has been shown to be sensitive to the local electric field strength and to the surface cleanliness and roughness, and insensitive to the mechanical strength of the surface, or the composition or absence of background gas. Both surface and bulk damage have been shown to be basically electron avalanche processes, with thresholds which depend on power density in the nanosecond region, and in energy density in the picosecond region. New and sophisticated diagnostic techniques have been developed for the detection and investigation of damage processes, and a data base of relevant material parameters has begun to be catalogued.

In other areas of concern, such as thin films, nonlinear optical materials, and infrared components, our understanding is more tentative and our theory more speculative. The reader of this year's proceedings will sense the somewhat empirical flavor of the investigations in these subject areas. It is our hope and our expectation that subsequent volumes of these proceedings will see the same transition from chance observation to careful experiment, and from conjecture to theory in these subjects. This transition has almost been reached in the area of thin films, but is more remote in the study of damage in nonlinear optical materials, and even further off regarding infrared components.



The specific conclusions arrived at as a result of the reports of this symposium are not startlingly different from those advanced in last year's proceedings. New results at a diversity of wavelengths, and at pulse durations in the picosecond region have substantiated the conclusion that damage in transparent dielectrics is essentially an electron avalanche process. Surface damage due to this process is the limiting factor in glass and crystalline lasers, and the present levels (30 to 40 J/cm<sup>2</sup> for 30 nanosecond pulses in laser glass) can be expected to be raised by a factor of 2 to 10 by surface treatment, such as careful cleaning, and ion-beam polishing, but probably not much more. As far as self-focusing is concerned, there seems to be little hope of changing the nonlinear index, especially the prompt component, by varying the composition of laser glass. The basic equations governing self-focusing are now well known, and, with the aid of a digital computer, detailed design calculations can be done for any time region or beam geometry, once the material parameters are known.

In materials other than glass and ruby, our conclusions are far less sweeping and certain. As stated last year, there is evidence that nonlinear absorption processes play an important role in damage in nonlinear optics materials. No new information regarding this effect was forthcoming this year.

Several important features of damage in thin films are beginning to emerge as a consequence of intensive investigation. Due, in general, to the poor homogeneity of thin films, both in single layer and multilayer form, it is difficult to evaluate the respective roles of absorption and electron avalanche. Whatever the operative mechanism, it is likely that it is sensitive to the local field strength which, in a multilayer dielectric, can exhibit profound spatial variation. The use of vapor phase mixtures enables films with a great variation in refractive index to be laid down with a minimum of residual stress. This should provide a valuable technique for the study of film damage. It seems clear that by reducing the stress in the film, the damage threshold can be raised. There is also evidence that damage in films is accompanied by an increase in light scattering, so that scattering measurements appear to provide a useful diagnostic tool.

With the tremendous increase in interest in powerful cw and pulsed IR lasers, problems of damage in the IR windows and mirrors are becoming increasingly important. It is generally assumed that for these systems, damage processes are essentially thermal in origin. Major importance is attached to increasing the mechanical strength and reducing the absorption constant in infrared window materials to its lowest possible value. This implies a theoretical ability to determine what that intrinsic value is, and an experimental ability to measure extremely weak absorptions. These capabilities are just beginning to emerge. The situation regarding IR window materials is comparable to the state of laser glass in the early Sixties; the limitations of these materials are defined more by impurity content than by intrinsic properties. This is particularly true for large samples, which may exhibit values of important parameters significantly different from small samples. These differences may have important consequences for system design.

We are in a very poor position to draw any conclusions regarding damage at metallic surfaces, other than to assume it is thermal in character. Very little information regarding the morphology of the damage, and its dependence on pulse duration and spot size has been obtained and made available to date.

## 2. Summary of Papers

The twenty-one papers presented at the 1972 Symposium can be logically divided into five categories. These are: Bulk Damage in Materials, Surface Damage, Self-Focusing Damage, Dielectric Coatings, and Infrared Component Damage. Four or five papers were presented in each category. The following summaries are intended to provide the reader with a brief but coherent review of the material presented at the Symposium, and to direct him to papers of specific interest.

### 2.1 Bulk Damage in Materials

The first group of presentations to be summarized are those concerned with damage occurring within the bulk material. It should be noted that research efforts are declining in the study of bulk damage in laser glass due to the generally high quality of present day laser glass and quantitative understanding of the subject. Reports were heard on the properties and characteristics of a new Japanese laser glass, the analysis of scattered radiation as a diagnostic tool for detecting the onset of damage, the possible causes of index damage in nonlinear optical crystals, and finally an excellent presentation on intrinsic damage levels of alkali halides from 0.69  $\mu\text{m}$  to 10.6  $\mu\text{m}$  lasers.

Tetsuro Izumatani, and Kosaku Hosaka, of the Hoya Glass Works, and Chiyo Yamaka, of Osaka University, reported on the development and testing of a new Japanese laser glass designated LCG-11. This material is a Barium Crown glass, which in finished form has a stimulated emission cross section of  $2 \times 10^{-20} \text{ cm}^2$ , and a loss coefficient of  $0.001 \text{ cm}^{-1}$ . Careful control of platinum inclusion leads to a glass similar in damage resistance to melts in  $\text{SiO}_2$  or ceramic crucibles. The ceramic-melted glass exhibited a higher lasing threshold, lower slope efficiency in the conventional mode, and lower saturation level in Q-switched operation than Pt-melted glass. From extensive testing it is concluded that the



surface damage is independent of glass strength, thermal expansion, or absorption of water on the glass surface. The damage threshold shown by this glass is comparable to other available laser glasses i.e. bulk  $\sim 400 \text{ J/cm}^2$  untreated surface  $\sim 28 \text{ J/cm}^2$  and HF-etched surface  $\sim 40 \text{ J/cm}^2$ , when employing a multimode laser of 30 nsec duration.

In a short communication, C. Y. She and E. Edwards, of Colorado State University, discussed their attempt at evaluating the damage sensitivity from an evaluation of the interaction gradients present in the focal volume, in fused and crystalline materials, using both multimode and TEM<sub>00</sub> ruby lasers. Based on their observation of the intensity and appearance of forward and back scattered radiation in relation to damage, they tentatively concluded that stimulated Brillouin scattering is responsible for laser-induced damage in both crystalline and fused quartz, while local heating is perhaps more important in the bulk damage of laser glass. Verification of these conclusions awaits detailed spectral measurements of the scattered signals.

Turning our attention more towards purely nonlinear crystalline materials, Alistair Glass, G. E. Peterson, and T. J. Megran of the Bell Laboratories reported on laser-induced optical index damage in  $\text{LiNbO}_3$  and  $\text{LiTaO}_3$ . A sensitivity in  $\Delta n$  of  $10^{-7}$  was claimed when evaluation was accomplished by measuring the diffraction efficiency of a holographic grating generated within the crystal. At large fields, or for multidomain crystals, where the above technique can not be used, they measured  $\Delta n$  directly from the birefringence. By comparison, this technique has a sensitivity of  $\sim 10^{-5}$  in  $\Delta n$ . They have definitely identified the  $\text{Fe}^{2+}$  ion as the source of nonlinear index. Damage probably proceeds by the reaction  $\text{Fe}^{2+} + h\nu = \text{Fe}^{3+} + e$  (cond). The electrons then drift or diffuse out of the interaction region and are trapped. At high spatial frequencies, diffusion becomes the more important process. They have not been able to ascertain why effects due to other impurities such as manganese are not observed.

In an attempt to elucidate the intrinsic bulk damage threshold without complications due to self-focusing, multiphoton absorption or cascade ionization of impurities, David Fraden, Eli Yablonovich of Harvard, and Michael Bass of Raytheon carefully performed extremely well-designed experiments to measure the absolute electric fields at breakdown in alkali halides, employing various laser sources ranging from  $0.69 \mu\text{m}$  to  $10.6 \mu\text{m}$ . The experimental arrangement insured that the incident power never approached the critical power  $P_c$  for self-focusing by employing strongly focusing optical systems. Sufficient attention was given to evaluation of the details of the incident laser pulses such that electric field strengths could be accurately computed. Corrections for reflection losses and changes in calculated beam diameter due to index nonlinearity were made. As usual, damage was always associated with visual plasma formation. Results indicated a definite correlation between observed thresholds for DC avalanche breakdown and the values of the optical field strength at the onset of laser-induced (AC) breakdown.

There was, in addition, excellent agreement in the ratios of damaging field strengths, for different series of alkali halides. Additional support for the avalanche breakdown mechanism was afforded by considering the variation of damage thresholds when employing a short pulse ( $< 5 \text{ ns}$ ) Nd:YAG laser, or varying the rise time of the ruby laser pulse. Further measurements employing very short optical pulses should conclusively demonstrate the applicability of the avalanche mechanism in the absence of nonlinear effects.

## 2.2 Surface Damage

With the improved control of absorbing impurities in bulk material, the dominant mechanism for damage of crystalline and glass materials is plasma formation at the dielectric surface. The investigations reported at the Symposium emphasized the role of plasma formation in the damage process, and the reasons why the observed threshold for damage at the entrance face is higher than that observed at the exit face. Following a proposal made at a previous damage symposium, improvements in surface damage threshold behavior were reported for the first time when sapphire elements were polished by ion beam techniques.

Norman Boling, of Owens-Illinois, described investigations carried out using amplified, Q-switched pulses from a Nd-glass system. The pulse duration was 30 nsec, and from 5 to 12 joules was obtained in the TEM<sub>00</sub> mode. The beam diameter at the sample surface was 2 mm. Samples of ED-2 laser glass were cleaned carefully, by washing in soap and water, rinsing in distilled water, and cleaning in a vapor of boiling isopropyl alcohol. With the beam normally incident on the sample face, entrance face damage was seen at 120 to 200  $\text{J/cm}^2$ , while exit face damage occurred at 80 to 120  $\text{J/cm}^2$ . The average ratio of entrance to exit threshold was 1.5. An explanation of this ratio was advanced, based on the work of M. Crisp. By considering the Fresnel ratios of incident, transmitted, and reflected waves at the dielectric surfaces, it was predicted that in order to obtain the same energy density in the sample at the entrance face as at the exit face, the energy density incident would have to be 1.48 times as great. Experiment and theory seem to be in agreement. Further substantiation was provided by experiments in which samples were irradiated with the beam incident at Brewster's angle. Since no reflection occurs at this angle, the same energy density occurs within the material at the entrance and exit surfaces. The damage thresholds observed at Brewster's angle incidence were essentially the same at entrance and exit surfaces.



As has been reported elsewhere, Boling observed that the most volatile element of the glass, in this case lithium, was deposited in a ring on the damaged surfaces, just outside the region of intense illumination. This was ascribed to the deposition of material from the damage plasma in contact with the cool surface surrounding the damage area.

Efforts to strengthen the surface by exchanging sodium for lithium ions, thereby creating a surface compression layer, led to no measurable increase in the surface damage threshold.

Concetto Giuliano of Hughes Research Laboratory investigated the role of plasma formation in surface damage. Using a ruby laser emitting 20 millijoules in a diffraction limited, single mode beam, in a 20 nsec pulse, entrance and exit surface plasmas formed on sapphire samples were investigated. By irradiating the surface at an angle to the normal, Giuliano was able to resolve the spatial components of the plasma. At the entrance surface only, a component of the plasma was observed to propagate back towards the laser during the time the laser pulse is present, vanishing thereafter. At both entrance and exit surfaces, another component of the plasma was observed to propagate away from the surface in a perpendicular direction, and to persist after the illuminating pulse was turned off. When samples were irradiated in vacuum, the laser-driven plasma at the entrance surface was not observed. Giuliano concluded that the laser-driven plasma was supported by the background gas, while the persistent plasma was emitted from the damaged material. Both Giuliano and Boling indicated that, although the plasma formed is sometimes very weak and difficult to detect, one can still say quite confidently, that surface damage is always accompanied by plasma formation.

Giuliano also examined the effect of ion-beam polishing on surface damage. Sapphire samples were polished with an argon ion beam at 7 KeV. From 2.5  $\mu\text{m}$  to 5  $\mu\text{m}$  of material were removed. X-ray topography indicated that at this depth, most of the surface scratches were removed, although some residual surface features were observed. At both entrance and exit faces, an improvement in damage threshold of a factor of 2 to 6 was observed. However, the spread in damage threshold values for ion-polished surfaces was much greater than for abrasively polished surfaces, and the damage, when it occurred on the ion-polished surface, was more extensive. Both these features were attributed to the fact that the ion-polishing removes regions of low threshold, which provide sites for failure in abrasively polished surfaces, leaving a surface of uniformly higher resistance to damage. The greater uniformity of the surface enhances the statistical nature of the damage process.

Michael Bass and Harrison Barrett of Raytheon studied surface damage in a variety of transparent dielectrics, using a Nd:YAG laser and Ruby laser of comparable output characteristics. In general, they found that a material is less likely to damage at a given power density level for electric field strength when illuminated at the shorter wavelength. In some materials, this may be due to the presence of resonance effects, but for most, they ascribe it to the fact that a nearly free electron gains less energy in a higher frequency field at the same field strength. Thus, a higher field strength is required at this higher frequency to create electrons energetic enough to initiate an avalanche ionization process.

Bass and Barrett studied the distribution of damage starting times near threshold for two different materials, at 1.06  $\mu\text{m}$ . They found a significant spread in damage onset times in relation to the laser pulse maximum, although the distributions tended to be narrower at higher power densities. A probabilistic explanation of the starting time distribution was advanced.

The laser-induced damage to GaAs semiconductive material was the subject of a study by J. Lynn Smith of U.S. Army Missile Command. Both conventional and Q-switched lasers, operating at wavelengths corresponding to photon energies below and above the band gap were employed. Modification of concentration uniformity was evident when samples were irradiated with long pulses, probably due primarily to thermal effects. Surface damage from Q-switched laser pulses (i.e. high power densities) was fairly sensitive to the surface condition and the presence of mechanical flaws. Damage thresholds were not observed to depend on the presence or type of doping (n-type, p-type) although doping changes affected the photocurrent signal amplitude. Observed thresholds were also insensitive to whether ruby or glass lasers were used, which was somewhat surprising. This may be the result of some breakdown plasma shielding of the surface. Damage which always occurred at the entrance face was undoubtedly due to surface imperfections, and not the intrinsic strength, or variations in composition of the GaAs samples tested. This observation was supported by photomicrographs of the damage areas.

Jhan Khan, of Lawrence Livermore Laboratories, made an impassioned plea for application of very fundamental and basic research methods to the surface damage question. A review of applicable techniques, including such recently developed methods as those employing electron analysis e.g., low energy electron diffraction (LEED), inelastic electron scattering (IES), Auger electron spectroscopy (AES) and electron spectroscopy for chemical analysis (ESCA). The use of these and other analytical tools should afford an improved characterization of the surface, such that the detailed structure, composition, and electro-optical properties can be evaluated as to their influence on laser-induced surface damage. By analogy, this careful attention to basic material properties has paid a handsome dividend to the semiconductor industry in terms of performance, reliability, reproducibility and economic advantage.



Once the manufacture of laser material is brought under sufficient control that absorbing inhomogeneities are absent, material failure due to the formation of intense filaments by self-focusing becomes the limiting process in long samples. Although the basic features of self-trapping are well understood, questions still remain regarding the actual values of nonlinear index coefficients for materials of interest, and the relative contributions of prompt nonlinearities (Kerr Effect) and delayed nonlinearities (electrostriction). In addition, the influence of variations in beam geometries on the measured threshold for trapping must be considered in interpreting experimental results.

John Marburger, of the University of Southern California, treated the case of self-focusing of a Gaussian beam of elliptical cross section. He used the self-similar, approximate solutions to the paraxial equation, under steady-state conditions. His analysis predicted that the critical power for self-focusing is a minimum for circular beams, and that it is increased for initially collimated, elliptical beams in the ratio,  $(x + 1/x)/2$ , where  $x$  is the ratio of the major and minor axes of the beam cross section. Similar increases over the critical power for circular beams were predicted for pre-focused elliptical beams, and for non-Gaussian beam profiles. Experimental data were cited to support these conclusions.

The respective contributions of electrostriction and Kerr effect to the nonlinear index,  $n_2$ , of BSC glass, fused silica, and flint glass were measured by Albert Feldman, Deane Horowitz, and Roy Waxler of the National Bureau of Standards in Gaithersburg. Their measurements were carried out at 1.06  $\mu\text{m}$ , using a laser pulse of 25 nsec duration using two different focal lengths (181 mm, 76 mm) for sample exposure. By comparing the focusing thresholds for circularly and linearly polarized light, they were able to deduce the electrostrictive and Kerr components of the nonlinear index. Once these respective contributions are known, one can compute the expected threshold for any pulse length and focal volume, as long as the material properties are known, and the Kerr effect can be treated as prompt.

John McMahon of the U.S. Naval Research Laboratory presented experimental measurements of  $n_2$  in four commercial laser glasses, measured by observing the self-focusing length at 1.06  $\mu\text{m}$  for pulse durations from 20 psec to 250 psec. Values obtained for  $n_2$ , in  $10^{-14}$  esu, were as follows: BK-7 (6), ED-2 (7 $\pm$ 3), Cast MG-915 (7 $\pm$ 3), and LG-56 (8 $\pm$ 3). Over the range of pulse duration from 20 to 250 psec, the value of  $n_2$  obtained was sensibly constant.

## 2.4 Damage to Optical Coatings

As expected, this year's symposium included many more papers on laser-induced damage to optical coatings. Some additional information on the damage threshold of specific coating materials was presented along with experimental evidence of the effect of film stress and specific multilayer design, and developments of improved diagnostic methods. There was an underlying thread of possible theoretical explanation for correlation of damage values and morphology of damage by recourse to considerations of the electric field strength distributions within the film system. Continuation along these lines will undoubtedly lead to a greater facility in the assessment of damage resistance of various film designs prior to fabrication. Specific papers dealt with the development of scattering measurements to assess the approach to damage prior to catastrophic failure, damage thresholds of various coatings at both picosecond and nanosecond pulse durations, morphology of film damage, the specific influence of film composition and design (including vapor phase mixtures and periodic inhomogeneous coatings), and measurements relating film stress to damage threshold. There was a definite improvement in film durability where stress compensation was utilized in vapor phase mixtures of opposite stress components.

J. H. Parks and W. Alyassini of the University of Southern California discussed the utility of employing a HeNe laser to measure variations in the scattering behavior of high power laser irradiated areas prior to, during, and after exposure to high power radiation. This time-resolved measurement allowed them to look at precursors, concurrent response, and long-term effects to the coated surfaces. They have demonstrated an ability to observe disturbances below as well as above the threshold for visually observed damage. They observed the effects of surface pitting and plasma formation; in addition, propagating surface disturbances were tentatively identified as Rayleigh waves. Monolayer films of ZnS,  $\text{CaF}_2$ , and NaCl on fused silica substrates as well as uncoated fused silica and LiF substrates were studied.

The laser-induced damage to overcoated mirrors at two pulse duration was the subject of a paper by E. S. Bliss and D. Milam of the Air Force Cambridge Research Laboratories. They employed both mode-locked (20 psec) and Q-switched (20 nsec) pulse durations from a ruby laser. Targets were 95% reflecting multilayer dielectric mirrors. Considerable effort was expended in ascertaining the specific spatial and temporal characteristics of the damage-producing lasers. Smooth layer removal over the whole irradiation area was observed when both psec and nsec pulses were employed, providing the intensity distribution was smoothly varying. However, if spatial inhomogeneities were evident (occasionally in the mode-locked case) nonuniform variation in damage sites was evidenced. A ragged pattern was normally produced at the edge of the damage area and was ascribed to coating inhomogeneities, since the laser output was determined to be highly homogeneous. Measured threshold values ranged from 0.6 to



2.9 J/cm<sup>2</sup> for the mode-locked case and from 16 to 58 J/cm<sup>2</sup> for the Q-switched experiments depending on film composition and number of layers. The specific materials used were 9 to 18 layer stacks of TiO<sub>2</sub>/SiO<sub>2</sub>, 13 to 25 layer stacks of ZrO<sub>2</sub>/SiO<sub>2</sub>; and a 21 layer stack of ZnS and ThF<sub>4</sub>. Based upon experimental observation and morphological examination, they conclude that plasma formation is the operative damage mechanism and that damage is best described in terms of energy densities at very short pulses and power density at Q-switched pulse lengths, consistent with an electron avalanche process.

In a series of experiments on the laser-induced damage of thin films Brian Newnam and Larry DeShazer of the University of Southern California investigated the damage of mono-, bi-, and multi-layered coatings of TiO<sub>2</sub>, SiO<sub>2</sub>, ZrO<sub>2</sub>, MgF<sub>2</sub>, and ZnS on substrates of glass, rock salt and spinel, under the action of a TEM<sub>00</sub> Q-switched ruby laser. In terms of decreasing damage resistance of quarter-wave films on BSC-2 glass, a hierarchy in order MgF<sub>2</sub> > SiO<sub>2</sub> > ZrO<sub>2</sub> > TiO<sub>2</sub> > ZnS was observed, which follows an approximately inverse relation to the refractive index. By computing the effective electric field strength at the boundary in different thickness films a correlation between damage and effective field was suggested. As films become simpler in design, it was suggested that an increase in scattering, when subsequently illuminated by a HeNe laser, was a more sensitive test for the onset of damage. In many single-layer films this operation preceded by a small amount the standard spark threshold. However, due to the inherently higher scattering manifest in more complex multilayer systems the spark threshold was more reliable and therefore recommended. One last interesting result of the work was a general tendency for the damage threshold to proceed in a manner inversely with the undamaged film scatter.

In an attempt to evaluate the influence of boundaries on the damage threshold of standard discrete multilayer film systems, Russ Austin and Ray Michaud of Perkin Elmer Corp. and Art Guenther, Joe Putnam, and Dick Harnniman of the Air Force Weapons Lab, constructed periodic inhomogeneous films in which the refractive index varied in an approximately sinusoidal manner without sharp optical or mechanical discontinuities. This was achieved through the simultaneous deposition of two materials employing independently controlled source rate generators. There was no significant difference in damage threshold when compared to their discrete film analogue. This was attributed to the overriding influence of the thin film, i.e. ThF<sub>4</sub> and ZnS, since these materials in pure form are grossly different in damage threshold. In a separate experiment, vapor mixtures of these films generally exhibited a damage threshold between the pure forms which was primarily dependent on the specific composition. Employing materials of opposite stress and similar damage threshold, MgF<sub>2</sub> and SiO<sub>2</sub>, a definite increase in damage threshold over the pure materials was evident due to this form of stress compensation. By choosing appropriate materials of opposite stress and different refractive indices, the film designer can have a great latitude in selecting films of intermediate refractive indices and low stress. Film systems can be designed which exhibit a higher damage threshold and thus increase utility as optical components. Variation in damage threshold due to different incident coating angles was attributed to stress variations as well. The presentation concluded with numerous scanning electron micrograph and Nomarski phase contrast micrographs depicting the morphology of damage. Correlations based upon film design, composition, and residual stress were made.

## 2.5 Damage to Infrared Windows and Mirrors

With the increasing emphasis on high power performance in the infrared, the attention of the laser materials community is being drawn to the problems of providing windows and mirrors capable of handling high power densities in the infrared, especially from 2 μm to 10 μm. Although at very short pulse durations plasma formation and gas breakdown can become important, for cw lasers in this wavelength region the limiting material property is the residual absorption of the material. At power densities exceeding one kW/cm<sup>2</sup>, absorptions which are almost unmeasurable at low intensity lead to system degradation and component failure. It is anticipated that the interest of the damage symposium will be concentrated on this problem for several years to come.

Robert Hellwarth, of the University of Southern California, presented a review of the possible absorption mechanisms which might contribute to the residual absorption in ostensibly transparent materials in the IR. He divided the processes into two categories, intrinsic and extrinsic. Intrinsic processes are these which occur in pure materials at thermal equilibrium, such as lattice vibrational bands, free-carrier absorption, and bound-electron excitation. Extrinsic processes arise due to impurities, dislocations, or deviations from stoichiometry. He provided a brief review of each process, and sketched the kind of wavelength dependence one would expect to observe. Even though there are significant gaps in the fundamental understanding of many of the processes involved, especially extrinsic processes, certain conclusions can be reached regarding the prognosis for material improvement. Since most materials exhibit fundamental lattice frequencies in the IR, these processes will play an important role in determining infrared absorption. Free-carrier absorption is also unavoidable, but its importance as a limiting mechanism can be strongly influenced by the presence of impurity levels and of interband transitions. It is expected that the same processes will be important in thin film materials as in bulk, once the films are produced with sufficient homogeneity.

Marshall Sparks, of Xonics Inc., presented a discussion of how weak absorption in window materials can limit system performance. Choosing a specific set of parameters for the window (10 cm diameter, 7.3 psi pressure differential) he defined a figure of merit on the basis of the maximum intensity which



could be transmitted through a given material without experiencing either thermal fracture or undue distortion. The latter can arise either through thermal distortion due to absorption heating or pressure-induced distortion (bowing). Of the materials reviewed, ZnSe is identified as the most promising at  $10.6\ \mu\text{m}$ . For the window dimensions assumed, a power density of  $3.76\ \text{kW}/\text{cm}^2$  could be transmitted, with a safety factor of 4, limited by the pressure-induced fracture of the window. Using a value for the absorption constant of KBr measured in large samples,  $(4 \times 10^{-3}\text{cm}^{-1}\text{ at } 10.6\ \mu\text{m})$ , that material is not very promising, but if one assumes the estimated intrinsic absorption coefficient value for KBr of  $5 \times 10^{-5}\text{cm}^{-1}$ , then it compares favorably with ZnSe. In order to measure these low absorption values, Sparks recommended use of emissivity measurements.

An instrument designed to provide the measurements of very low absorption values was described by Geert Wijntjes and J. Morris Weinberg of Block Engineering. They have developed a cryogenic interferometric spectrometer which can achieve a noise equivalent spectral radiance of  $\sim 1 \times 10^{-11}\ \text{W}/\text{cm}^2\text{-ster}-\text{cm}^{-1}$  at  $10.6\ \mu\text{m}$ , with a spectral resolution of  $\sim 1\ \text{cm}^{-1}$ . This performance requires about 10 secs of integration time. Absorption data is obtained from emittance measurements. The declared precision approaches one part in  $10^7$ . The high spectral resolution of this instrument permits examination of the effects of absorption band structure from substrate and coatings as well as identification of contaminant materials. Measurement of bulk scattering effects in transmissive materials is also possible. This technique should find wide application in selecting suitable new materials and in quality control.

A comparison of the performance of various types of high power mirrors at high heat loading was presented by Victor Wang, A. and M. Braunstein, and J. Y. Wada from the Hughes Research Laboratories. They examined the limiting damage mechanism in metal mirrors, gold-coated refractories, and multilayer dielectric coatings. Experimental data were presented showing that the failure mode of metal mirrors is generally by melting or oxidation; that metal-coated refractories tend to fail by melting, oxidation, bond separation, or cracking; and that multilayer dielectrics fail from melting, cracking, separation, or pitting. Observed damage levels in 8 to 10  $\mu\text{sec}$  pulses were  $140\ \text{J}/\text{cm}^2$  for simple metal mirrors, 70 to  $140\ \text{J}/\text{cm}^2$  for metal-coated metal mirrors, and as low as  $10\ \text{J}/\text{cm}^2$  for multilayer dielectrics. The last were admittedly of poor quality. Sputtered metal coatings on metal were identified as most promising for high pulse power applications.

### 3. Recommendations

It has been pointed out in the section on principal conclusions that not much remains to be done in the area of bulk damage in laser materials. The thresholds for damage due to bulk dielectric breakdown are so high that this phenomenon is clearly not a limiting factor in systems design. Similarly, in the case of self-focusing, this phenomenon is now so well understood that, given the prompt and electrostrictive components of the nonlinear refractive index, avoidance of self-focusing is a matter of straight forward, albeit tedious, numerical computation. One possible exception to this statement arises in the design of systems operating with pulse lengths less than 10 psec. For these very short pulses, the characteristic response time of the nonlinear index is still open to question. As reliable and reproducible systems operating in the time region of one to ten psec become available, it is recommended that further investigation of the transient response of optical nonlinearities be carried out.

There are some important recommendations to be made concerning laser-induced surface damage. This phenomenon is still the prime limitation in high power laser devices, especially if one is forced to short active elements or disk geometries to avoid self-focusing. We have heard in this symposium of possible damage improvement through the use of ion polishing, and as previously reported, by chemical etching with HF. Careful experiments on the characteristics of treated or polished surfaces is certainly warranted to evaluate the effect of the surface properties on damage threshold. The interrelation between surface roughness and damage threshold remains to be elucidated. Surface roughness obviously can be controlled by the appropriate choice of polishing technique.

The spectral dependence of surface damage has only been partially investigated. Bass's results show that the surface damage threshold at  $0.69\ \mu\text{m}$  is lower than at  $1.06\ \mu\text{m}$ . It would be of great interest to extend these experiments to  $0.53\ \mu\text{m}$ , for example, by using frequency doubled Nd:YAG. As a final step in verifying the electron avalanche nature of surface damage, threshold experiments in the subnanosecond regime, with good mode control, should be carried out. The efficacy of surface treatment for subnanosecond pulses remains to be verified. There is no reason to expect anomalies when ultra-short pulses are employed, but complete verification of the present model of surface damage is clearly in order.

In regard to nonlinear optical materials, emphasis should be placed on improved material fabrication, including purification of starting materials, to afford better reliability and reproducibility. Until this is accomplished, it will be difficult to evaluate properly the damage sensitivity of different candidate materials. Preliminary observations indicate a disastrous lowering of damage thresholds in nonlinear materials when multiple wavelengths are present, but no careful investigation of this effect has been carried out. Clearly, it should be investigated.

As predicted, considerable research was undertaken in the area of damage to thin films since the previous symposium. Based on the several excellent presentations at this year's symposium, several

positive recommendations can be made. The experimental determination of damage threshold in various thin film systems should be correlated with the microscopic electric field strengths throughout the structure. This obviously entails a detailed modeling of the electric field distribution, energy deposition, and material response of the film system. These computations should be carried out for both normal and off-normal incidence. The sudden awareness this year of the effect of the Fresnel relations at dielectric interfaces should provide a valuable lesson for those studying damage in multilayer dielectrics.

The effect of surface finish on thin film damage threshold has not been investigated. In this regard there could be valuable insight gained from the studies recommended of the surface damage of uncoated optical elements. While there now exist various tabulations of the relative damage threshold of commonly used coating materials, because of the lack of reproducibility in structure, method of preparation, impurity concentration, cleanliness and background coating pressure, no plausible hierarchy of damage resistance can be formulated which will be accepted with confidence by thin film manufacturers. We still have not pinned down those material properties which will allow a judicious selection of materials for any given high power application. Therefore, carefully controlled experiments with detailed statements of significant material properties are necessary. Not only should the damage resistance of specific materials be investigated, but attempts at elucidating the damage sensitivity in terms of scattering, reflectivity, and absorption should be made. Finally, it is suggested that to answer questions concerning mechanical failure due to separation at discontinuities in discrete films, that experiments on periodic inhomogeneous films be conducted using materials of similar damage threshold and compared to their discrete layer analogues.

Our knowledge of damage processes for infrared windows and mirrors is in its infancy. Clearly, this is an area to which the major research activity should be directed. Not much progress can be expected; however, until fabrication and polishing techniques, especially for crystalline materials, and purification methods for raw materials are improved. The characterization and measurement of weak absorption is of fundamental importance in reducing thermally induced damage. Both theoretical and experimental advances are needed in this area. Damage criteria for infrared components must reflect the degradation of system performance, which may result from the distortion of the optical element rather than from catastrophic damage, and must be so defined. Thus further study of system sensitivity to component degradation must accompany the investigation of material properties and damage phenomena. Improved diagnostic techniques will be required to detect and measure the thermomechanical response of optical elements, and correlate it with observations of reflectivity, scattering, absorption, depolarization, and other purely optical parameters. Although at present the assumption is made that thermal effects dominate, this conjecture remains to be substantiated.

Perhaps it is appropriate to conclude with some very general remarks concerning the future. Without question, an area of future endeavor will be in extending these damage studies into the ultra-violet and x-ray regions of the spectrum. Increasing interest in the high power Xe laser, for example, forewarns us of impending requirements for damage resistant uv windows and mirrors. In addition, numerous suggestions for realizing x-ray laser action have been published. Here in part specific crystalline materials may effectively act as wave guides or even amplifiers.

Because of the tremendous increase in our understanding of many aspects of laser-induced damage, it is probably appropriate to consider assembling this knowledge in a form suitable to the design engineer. This would be an entirely appropriate activity for the ASTM Subcommittee on Laser Materials to undertake. Such a compendium, including suggested approaches, material properties, and possible pitfalls to be avoided, could be generated either as an ASTM document or as a supplement to existing handbooks. This latter possibility is under consideration by the editors.

#### 4. Acknowledgment

We would like to acknowledge the invaluable assistance of Dr. Harold Boyne, Mrs. Pauline Smith, Mrs. Marjorie L. Wilson, and Mrs. Francis M. Stark of the National Bureau of Standards in Boulder, Colorado for their interest, support, and untiring efforts in the operation of this symposium and in the preparation and publication of the proceedings. The continued success of the damage symposium would not have been possible without their support.

#### 5. Bibliography

- [1] "Damage in Laser Glass", A. J. Glass and A. H. Guenther, Editors, ASTM Special Technical Publication 469, ASTM, Philadelphia, PA (1969).
- [2] "Damage in Laser Materials", A. J. Glass and A. H. Guenther, Editors, NBS Special Publication 341, U.S. Government Printing Office, Washington, D.C. (1970).
- [3] "Fundamentals of Damage in Laser Glass", N. Bloembergen, National Materials Advisory Board Publication NMAB-271, National Academy of Sciences, Washington, D.C. (1970).



- [4] "Damage in Laser Materials: 1971", A. J. Glass and A. H. Guenther, Editors, NBS Special Publication 356, U.S. Government Printing Office, Washington, D.C. (1971).
- [5] "High Power Infrared Laser Windows", N. Bloembergen, National Materials Advisory Board Publication NMAB-292, National Academy of Sciences, Washington, D.C. (1972).
- [6] Proceedings of the Conference on High Power Infrared Laser Window Materials, (October 1971). Ed. by C. S. Sahagian and C. A. Pitha (Air Force Cambridge Research Laboratories, Special Report No. 127, December 1971).

A. J. Glass  
A. H. Guenther



## "Opening Remarks"

C. Martin Stickley

Materials Sciences Office  
Defense Advanced Research Projects Agency  
Arlington, Virginia 22209

It is a pleasure to be here this afternoon attending this Fourth ASTM Conference on Laser Damage. This is also the fourth one I have attended since I have felt for a long time that materials damage places unnecessarily low limits on laser power output, and consequently have been pushing for financial support to study this area in order to see what could be done to increase our understanding of these nonlinear mechanisms and to raise the damage threshold.

Since work in this area has been underway for several years, it seems appropriate at this time to give a short assessment of the highlights of what we have learned, and then to point out some of what remains to be done. Unfortunately (or fortunately if you happen to be earning your keep working in this field) it appears that more needs to be done than we have accomplished, but I feel that future progress ought to come rapidly over the next two or three years since we are getting fairly high up on the learning curve, at least for transparent dielectrics.

To measure progress made, one must have a point of reference. At the start of most of the activity that has been reported here at these Conferences, ruby was thought to be free from iridium but that remained to be verified. Glass, on the other hand, still contained platinum which lead to low damage thresholds and ruination of the laser rod. Some reports of damage thresholds for glass were in the literature but their values spread over three orders of magnitude at 30 ns. The problem of damage to nonlinear optical materials was only beginning to be recognized, and mirror damage was known to all but understood by no one.

What have we accomplished? First, we learned iridium played no part in ruby damage, and we have succeeded in removing platinum from glass. Second, our measuring techniques have improved vastly. We all now recognize the necessity of working with TEM<sub>00</sub> mode beams in order to obtain reproducibility and understanding of what goes on. Our refined measuring techniques have also led us to distinguish between the different kinds of damage - exit surface, self-focusing, inclusion, and entrance surface. Third, we have determined that self-focusing is the most important mechanism leading to damage in the material. Although we still may not be absolutely certain what drives the self-focusing, we can, in principle, design laser systems around it which can operate at hundreds of Joules/cm<sup>2</sup>. Fourth, and this is perhaps still somewhat subject to argument, it appears that the final breakdown, at least in the picosecond regime and perhaps for longer pulse lengths, is avalanche and that the track diameter is consistent with the size necessary to trap sufficient power to breakdown the material by this mechanism. It turns out that the breakdown field strength in alkali halides are equal to the dc values observed by von Hippel some 35 years ago. Fifth, surface breakdown also appears to be initiated by avalanche and by treating the surface so as to minimize the chances of an encounter of the laser beam with the right type of electrons, whatever they are, one can raise the surface damage threshold significantly. This total process, however, is very poorly understood. With respect to nonlinear optical materials, damage thresholds have been obtained but it is not clear why the large spread exists over the range of materials examined nor if any of the thresholds represent a fundamental limit. That is, surface treatments and inclusion removal might be quite important in increasing the power levels at which they can be used successfully. With respect to mirror and coating damage, the values are certainly higher than they were several years ago, but this came about more through fine tuning of the art of making these than by any great depth of understanding of what goes on during the breakdown process.

Now what remains to be done? It seems to me that there are a number of areas, with varying degrees of importance, which it is necessary to pursue. First, in bulk damage, what mechanism leads to self-focusing in the different time regimes of interest? In the 30 ns or longer regime, it seems that electrostriction is responsible, but for shorter pulses it is more debatable. Next knowing the mechanism, is it possible to design materials which have minimum susceptibility to damage? Second, now that we have a rough feel for what goes on in the bulk, one of the most fruitful areas to pursue is surface damage. We need to increase our understanding of it and devise surface treatments to raise the threshold. Knowing this we need to translate these treatments into recipes which can be used by the optical material firms which make these materials. This fits perfectly into the role of ASTM, our sponsoring organization for this meeting. Regarding nonlinear optical materials, the success of surface treatments needs to be demonstrated on them. Further, I feel that more work needs to be done to determine the



damage thresholds in a way which is more simply translatable to the device designer. Regarding material inhomogeneity, that is a major problem; it will probably require a very important application to arise before significant resources will be expended in that direction. With respect to mirror and coating damage, this has almost no base of understanding. As laser powers grow larger, this area will increase in importance since the cost of replacing the optics, as we have become used to doing in low average power systems, will become prohibitive. In fact, our scientific knowledge bank of optical coatings and surfaces is rather empty relative to that possessed by the electronics community, and thus, I see this as a major area of interest and an opportunity for dramatic gains over the next several years.

One other topic which has not been addressed before until this meeting is that of high power infrared laser windows. Much needs to be done here in areas of interest to ASTM: techniques for measuring bulk and surface scatter and absorption, techniques for specifying bulk and surface homogeneity, test procedures for specifying surface and coating damage thresholds, and others. Although there is a large amount of activity going on that is not being reported here I urge you to move in this direction since, in the long run, ASTM can be of great benefit to the users of these components as well as the producers.

In summary, we have learned a lot but there is a lot more to be done on laser damage to optical components. I think that our understanding of the processes that go on has increased tremendously, and that it is now time to turn our attention more towards making this knowledge pay off where it can. I also feel that it would be appropriate to consider changing the name of this conference to the ASTM Conference on Optical Reliability. The title of "The Laser Damage Conference" to me described a group concerned with how things damage. That is certainly important, but I feel it is but one aspect of the overall problem of Optical Reliability, the other aspect being how do we increase the reliability of these components once we know how and why they fail. Thus, this title change would tend to put our work in a more positive, useful light. It further recognized the fact that with the advent of high power lasers, optical systems now have reliability problems - a situation which did not really exist before.

In closing, I wish to thank the National Bureau of Standards for the excellent job they do both as our host and in publishing the Proceedings of this meeting. We are indebted to them all, again, for their help in these ways.

Tetsuro Izumitani & Kosaku Hosaka

HOYA Glass Works  
Akishima, Tokyo, Japan  
and

Chiyoë Yamanaka

Osaka University  
Yamada-Kami, Suita  
Osaka, Japan

In HOYA Glass Works we have developed a Barium Crown Laser Glass, LCG-11. It has a stimulated emission cross section ( $\sigma$ ) of  $2.0 \times 10^{-20} \text{ cm}^2$  and a loss coefficient ( $\gamma$ ) of  $0.001 \text{ cm}^{-1}$ .

In this report we show that, while platinum lowers the damage threshold of laser glass, by controlling the number and size of the platinum inclusion, the damage threshold of platinum crucible melts of LCG-11 laser glass does not go below  $400 \text{ J/cm}^2$  in the passive test, nor below  $28 \text{ J/cm}^2$  in the active test. This compares favorably with the damage threshold of melts in  $\text{SiO}_2$  and ceramic crucibles. The ceramic melted glass showed a higher lasing threshold, a lower slope efficiency in normal oscillation and an output saturation tendency in Q-switched oscillation.

We find that surface damage is independent of glass strength, glass thermal expansion, and adsorption of water in glass surface. We find that LCG-11 glass, upon treatment with hydrofluoric acid, was improved from  $28 \text{ J/cm}^2$  to  $40 \text{ J/cm}^2$ , a higher damage threshold in passive test, yet we were unable to find a change in glass surface composition due to hydrofluoric acid treatment by using electron microprobe. We assume that surface damage is dependent upon the multi-photon ionization tendency of a glass surface. This assumption is based upon our observation of silica glass which has no single-bond oxygen and a high damage threshold.

Key Words: HF treatment, inclusion damage, passive and active testing, platinum inclusion, surface damage, thin film coating

## 1. Introduction

New optical glass materials have been developed, in Hoya Glass Works, for example, laser glass, LCG-11, acoustic-optical glass, AOT-5, and a photochromic glass with rapid fading rate. In this paper the properties and damage of laser glass LCG-11 will be reported.

LCG-11 is a Barium Crown Glass. It has properties as shown in table 1. Its cross section for stimulated emission  $\sigma$  is  $2.0 \times 10^{-20} \text{ cm}^2$  and its loss coefficient is  $0.001 \text{ cm}^{-1}$ . It has an internal damage threshold of  $400 \text{ J/cm}^2$  and a surface damage threshold of  $40 \text{ J/cm}^2$  for a multimode laser pulse of 30 ns. in the passive test. In the active test it showed a surface damage threshold of over  $28 \text{ J/cm}^2$  for the same pulse. These damage thresholds were measured in Osaka University, using samples we made.

The compositions of LCG-11 was determined on the bases of the relationships between the life time and intensity of fluorescence versus glass composition of the  $\text{R}_2\text{O}-\text{RO}-\text{SiO}_2-\text{Nd}_2\text{O}_3$  system. The  $\text{Nd}_2\text{O}_3$  concentration was limited to 3.5 wt.% by

concentration quenching.

LCG-11 is melted in platinum vessel using a special furnace to avoid platinum contamination.

Table 1. Properties of LCG-11 laser glass

Glass type	Barium Crown Glass
Neodium doping	3.5 wt.%
Neodium Concentration	$3.80 \times 10^{20}$ ions/cc glass
Fluorescent life time	575 $\mu$ sec.
Fluorescent wave length	1.0624 $\mu$
Fluorescent line width	290 Å
Cross section for stimulated emission	$2.0 \times 10^{-20}$ cm <sup>2</sup>
Specific gain	0.101/cm/joule
Loss Coefficient (at 1060 m $\mu$ )	0.001 cm
Lasing threshold	180 J (10 $\phi$ x 160 mm rod, reflecting mirror 60 %, normal oscillation)
Max slope efficiency	1.52 %
Damage threshold (multimode, 30 nsec.)	
Internal damage threshold	400 J/cm <sup>2</sup> (passive test)
Surface damage threshold	{ 40 J/cm <sup>2</sup> (HF-treatment, passive test) 28 J/cm <sup>2</sup> (no HF-treatment, active test)

## 2. Damage testing method

In damage testing laser glass, both passive and active tests were performed. In the passive test a Q-switched laser beam was irradiated through a lens to the test samples. A schematic diagram of the apparatus is shown in fig. 1A.

In the active test a Q-switched and amplified laser beam was irradiated to a pumped test sample. A schematic diagram of the apparatus is shown in fig. 1B.

In the passive test, an oscillation glass rod with a diameter of 10 mm and a length of 160 mm was pumped by a 1 kJ linear flash tube. The output mirror reflectivity was 60 %. A rotating prism was used for Q-switching and a beam splitter-photo diode-tektronix-519 combination was used to measure the beam energy and pulse duration. Calibration was performed using TRG 107 calorimeter. The half pulse width was 30 nsec. The focal length of the lens used for focussing the laser beam was 10 cm. The size of the focal spot was determined from the diameter of the damage spot in Al-foil.

In the active test, the amplification was accomplished in 4 stages. The 4th amplifier laser rod used was the test sample. In 1st and 2nd stage of amplification amplifier glass rods with a diameter of 20 mm and length of 300 mm were pumped by 4 linear flash tubes with a total pumping power of 4 kJoules. In the 3rd amplification stage, an amplifier glass rod with a diameter of 30 mm and a length of 300 mm was pumped by a pumping power of 6 kJoules. In the 4th amplification stage, the glass rod was 20 mm in diameter and 300 mm in length and the pumping power was 7 to 10 kJoules. Two-element lens were placed between the 3rd amplifier and the 4th amplifier to maintain a beam diameter of 15 mm and to increase the beam flux density. Q-switched oscillation and the measurements of beam energy and pulse width were accomplished in the same manner as in the passive test.

## 3. Inclusion damage

It is well known (1)<sup>1</sup>(2) that colloidal state platinum inclusions deposited in a melt lower the damage threshold. But there is a question as to whether platinum dissolved in the form of platinate ions PtO<sub>2</sub><sup>2-</sup> lowers the damage threshold, or whether laser glass melted in a platinum crucible can be used as a high power laser glass.

<sup>1</sup>Figures in parenthesis indicate literature references at the end of this paper.



### 3.1. Effect of Platinum Inclusion on Damage Threshold

The damage threshold was measured in passive test. The glass samples (15 x 15 x 50 mm), which were melted in SiO<sub>2</sub> crucible using platinum added glass batches. The results are shown in Table 2.

As may be seen, the glass samples with platinum added showed a very low damage threshold of 15 J/cm<sup>2</sup>, while the glass sample without platinum added showed a very high damage threshold. The glass samples with Pt added included metallic colloidal platinum particles.

Table 2. Effect of Pt inclusions on the threshold damage in passive test using multi-mode pulse of 30 ns.

Sample	Damage Threshold (J/cm <sup>2</sup> )
Barium Crown Glass (100 ppm of Pt added)	15
Barium Crown Glass (10 ppm of Pt added)	15
Barium Crown Glass (no Pt added)	465
Barium Crown Glass (3.5 % of Nd <sub>2</sub> O <sub>3</sub> doped) (no Pt added)	351

### 3.2. Effect of crucible materials on damage threshold of LCG-11

Next, LCG-11 glass was melted in a platinum crucible, in a ceramic (electrically fused zirconia) pot and in a clay pot as shown in Table 3. The LCG-11 internal damage threshold showed to be over 400 J/cm<sup>2</sup>, regardless of crucible materials. In the platinum crucible melting, a special melting apparatus was used to void colloidal platinum particles. In this glass sample, ionized platinum might be dissolved or particles that are less than 0.1 μ might be included. The damage threshold, however, was not affected by either the ionized platinum or the very small sizes of colloidal platinum. It can therefore be concluded that laser glass melted in a platinum crucible can be used as high power laser material if we can avoid the colloidal platinum particles (3). It is interesting to note that glass samples containing ceramic inclusions melted in ceramic or clay pots have a damage threshold of only 120 J/cm<sup>2</sup>.

Table 3. Damage threshold of LCG-11 melted in various crucibles.  
(in passive test using multi-mode pulse of 30 ns.)

Sample	Damage Threshold (J/cm <sup>2</sup> )
LCG-11 (3.5 wt.% of Nd <sup>3+</sup> ) melted in Pt	400 ~ 560
LCG-11 glass (no dope) melted in ceramic pot	480 ~ 540
	120 (glass samples with ceramic inclusions)
LCG-11 glass (no dope) melted in clay pot	480 ~ 540
	120 (glass samples with ceramic inclusions)

### 3.3 Normal and Q-switched oscillation

Characteristics of LCG-11 glasses melted in platinum, ceramic and clay pots, respectively.

#### a) Normal oscillation characteristics

Normal oscillation was performed. The glass rod  $10 \times 160$  mm was used. Mirror reflectivity was 60 %. As shown in fig. 2A the glasses melted in the ceramic and clay pots showed higher lasing threshold energies, which are attributed to the high loss coefficient. They also showed lower slope efficiencies, which are probably attributed to the shorter fluorescent life time.

#### b) Q-switched oscillation characteristics

Q-switch oscillation was performed using a rotating prism. The pulse duration was 30 nsec. As shown in fig. 2B, glasses melted in both ceramic and clay pots showed a saturation tendency in output. This is perhaps attributable to the increase of lasing threshold energy due to the increased loss coefficient.

### 4. Surface damage of LCG-11

The surface damage threshold ( $20 \sim 40 \text{ J/cm}^2$ ) is always very low compared to the internal damage threshold  $400 \text{ J/cm}^2$  when platinum free. The reason is not sufficiently clear. The surface damage mechanism of transparent dielectrics is considered as follows (4)(5).

The initial electrons produced by multi-photon ionization absorb laser photon energy by Inverse Bremsstrahlung and then multiply. Once the plasma is produced, the lattice is heated suddenly and a shock wave will be driven to the glass surface (6) and thus both thermal and mechanical fracture is induced.

If the above is true, then the surface damage threshold relates to glass properties, such as mechanical strength and thermal expansion, and it also depends upon adsorbed impurities such as water vapor, and glass composition, because initial electrons will perhaps come from non-bridging oxygen.

We therefore measured the surface damage thresholds of chemically strengthened glass, of zero-expansion glass and of coated glass, of HF-treated glass, and of fused silica glass.

#### 4.1. Effect of mechanical strength on damage threshold

A plasma formation is found whenever surface damage is induced. We therefore measured the threshold for plasma formation.

As shown in table 4, contrary to our expectation the plasma formation threshold becomes lower after the ion exchange between  $\text{Na}^+$  and  $\text{K}^+$  ions while the surface damage threshold increased a little. Thus, a higher mechanical strength does not always give a high surface damage threshold.

#### 4.2. Effect of thermal expansion on the plasma formation threshold

The plasma formation threshold was measured on Hoya Crystron-0 glass ceramics which has a thermal expansion coefficient of  $0 \pm 1.5 \times 10^{-7}$  ( $-50 \sim 200^\circ \text{C}$ ). As shown in table 4, the plasma formation threshold ( $15 \sim 19 \pm 2 \text{ J/cm}^2$ ) was low. Thus, low thermal expansion does not always give a high surface damage threshold.



Table 4. Effect of mechanical strength and thermal expansion on surface damage

Glass Sample	Chemical treatment	Threshold for plasma generation (J/cm <sup>2</sup> )	Surface damage threshold (J/cm <sup>2</sup> )	Reference
Chemical Strengthened Glass	before	16 ~ 20 ± 2	24 ± 2	mechanical strength 1,000 kg/cm <sup>2</sup>
	after	8 ~ 14 ± 2	25 ± 2	6,300 kg/cm <sup>2</sup>
Crystron-0		15 ~ 19 ± 2		Thermal expansion 0 ± 1.5 x 10 <sup>-7</sup> /°C

#### 4.3. Effect of thin film coating on surface damage threshold

On a glass surface, organic material such as oil, inorganic material such as polishing powder, and adsorbed gas such as water vapor will remain. After cleaning, this film such as MgF<sub>2</sub> and SiO<sub>2</sub> was coated and then the plasma formation was observed. The result is as shown in table 5. Note that the MgF<sub>2</sub> film coating does not improve the plasma formation threshold. The SiO<sub>2</sub> film coating improves the threshold a little, but result needs further investigation. As a comparison, the silica glass plasma formation threshold is given on the same table. It is very high.

The high surface damage threshold of fused silica seems to suggest that impurities on glass surface does not always determine surface damage threshold.

Table 5. Effect of thin film coating on plasma formation

Glass Sample	Coating	Plasma formation threshold (J/cm <sup>2</sup> )
LCG-11	no	23 ~ 28 ± 5
LCG-11	MgF <sub>2</sub> coating	9 ~ 10 ± 5
LCG-11	SiO <sub>2</sub> coating	26 ~ 30 ± 5
Fused Quartz	-	130 ± 10

#### 4.4. Effect of alkali or alkali earth oxide on plasma generation

Alkali ions may have an effect on the initial electron generation in plasma. Then, alkali ions were replaced by alkali earth ions. The result is shown in table 6. In this case, however a single mode pulse was used.

As shown in table 6, no difference between alkali ions and alkali earth ions can be seen on the plasma formation threshold. However, as mentioned above, the threshold for fused SiO<sub>2</sub> is very high. These results seem to suggest that the damage threshold is affected by the multi photon ionization tendency. Fused silica glass has no non-bridging oxygen. To the contrary, alkali ions as well as alkali earth ions gives non-bridging oxygen. Therefore initial electrons are easily produced in alkali or alkali earth containing glasses by multi photon ionization.

Table 6. Effect of glass composition on plasma formation threshold using single mode pulse of 30 nsec.

Glass Sample	Alkali or alkali earth	Plasma formation threshold (J/cm <sup>2</sup> )
BaCD 11 (SK 11)	Alkali (R <sub>2</sub> O 6.3 mol %) (RO 16.8 mol %)	53 ~ 63 ± 5
BaCD 5 (SK 5)	Alkali earth (RO 23.0 mol %)	54 ~ 66 ± 5
BaF 8	Alkali (R <sub>2</sub> O 4.5 mol %) (RO 31.3 mol %)	62 ~ 94 ± 8
BaF 9	Alkali earth (RO 34.4 mol %)	67 ~ 90 ± 5

#### 4.5. Effect of Hydrofluoric acid treatment on surface plasma formation threshold

Swain (7) showed that HF treatment improves surface damage. We treated LCG-11 glass with a 10 % hydrofluoric acid solution. The results are shown in table 7.

Note that the HF treatment substantially improves the plasma formation threshold. The threshold in single mode pulse was over 140 J/cm<sup>2</sup>. There is no doubt of the effect HF-treatment has on surface damage. However, the reason is not clear. We measured the change of glass composition on the glass surface, using an electron micro probe x-ray analyzer (Shimadzu EMX-SM), because we expected the formation of a SiO<sub>2</sub> rich layer or fluoride layer by HF-treatment. But we could not detect a composition difference, as shown in Fig. 3A,B,C.

Table 7. Effect of HF-treatment on surface plasma formation in multi-mode and single-mode pulse

Glass Sample	HF-treatment	Plasma formation thresholds	
		multi-mode (J/cm <sup>2</sup> )	single-mode (J/cm <sup>2</sup> )
LCG-11	no	28 ± 5	88 ± 5
LCG-11	10 % HF-treatment	40 ± 5	> 140 ± 5

#### 5. Damage threshold of LCG-11 in active test

The damage threshold of LCG-11 was measured in an active test. The result is shown in Table 8.

Table 8. Damage threshold in active test

Sample	Damage threshold (J/cm <sup>2</sup> )	Reference
LCG-11 (20 x 300 mm)	over 28 J/cm <sup>2</sup>	multi-mode pulse of 30 ns.

LCG-11, which was not treated by hydrofluoric acid solution, showed surface damage threshold of over 28 J/cm<sup>2</sup> without any internal damage. This surface damage threshold is almost the same as in the passive test.

## 6. Discussion and Conclusion

Fused silica glass has only bridging oxygens, therefore its ionization potential is expected to be very high. The high surface damage threshold of fused silica glass seems to have a relationship with its multi-photon ionization tendency. But at present, we don't know why the surface damage threshold is lower than the internal damage threshold. Perhaps the ionization potential on the surface is lower than that in the interior. Neither do we know the reason why hydrofluoric acid treatment improves the surface damage threshold.

The following conclusions are derived.

- 1) By controlling the number and size of the platinum inclusion, the internal damage threshold of platinum crucible melts of LCG-11 laser glass does not go below 400 joules/cm<sup>2</sup> for a multi-mode pulse of 30 ns. in the passive test.
- 2) By hydrofluoric acid treatment, the surface damage threshold of LCG-11 does not go below 40 joules/cm<sup>2</sup> for the same pulse of in the passive test.
- 3) In the active test, LCG-11 showed the threshold of surface damage over 28 J/cm<sup>2</sup>.
- 4) Surface damage threshold is independent of glass strength, glass thermal expansion. It is not always determined by adsorbed impurities. It seems to be dependent upon multi-photon ionization tendency.

## 7. References

- |   |  |
|---|--|
| <p>(1) Young, C.G. &amp; Woodcock, R.F., Damage in Laser Glass, ASTM STP 469 84 (1969)</p> <p>(2) Bliss, E.S., Damage in Laser Glass, ASTM STP 469 9 (1969), Damage in Laser Materials, NBS Special Publ. 341 105 (1970)</p> <p>(3) Hopper, R.W., Lee, C. and Uhlmann, D.R., Damage in Laser Materials, NBS Special Publ. 341 55 (1970)</p> <p>(4) Sherma, B.S. &amp; Rieckhoff, K.E., Can. J. Phys. 45 9781 (1967)</p> | <p>(5) Sherma, B.S., Can. J. Phys. 48 1178 (1970)</p> <p>(6) Boling, N.L. &amp; Beck, R.W., Damage in Laser Materials, NBS Special Publ. 356 15 (1971)</p> <p>(7) Swain, J.E., Damage in Laser Glass, ASTM STP 469 69 (1969)</p> |
|---|--|

## 8. Figures

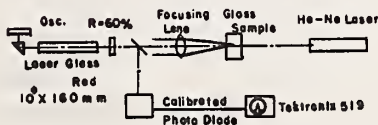


Figure 1A. Schematic diagram of the apparatus for laser damage testing.  
Passive Test

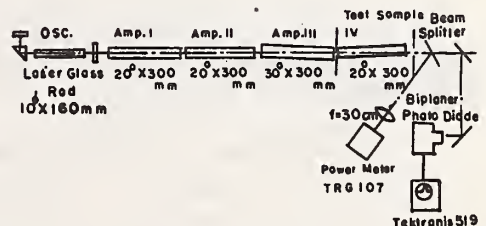


Figure 1B. Schematic diagram of the apparatus for laser damage testing.  
Active Test



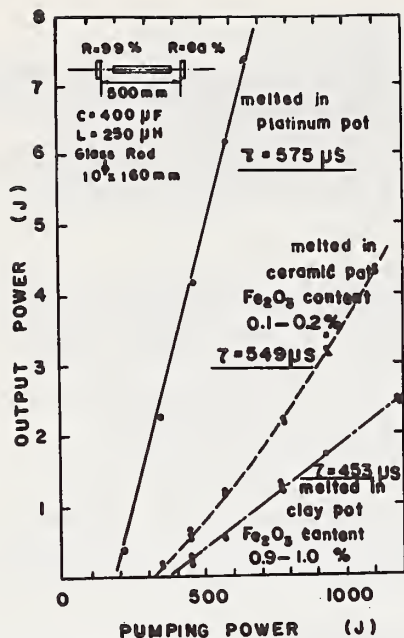


Figure 2A. Normal oscillation characteristics of LCG-11 glasses melted in platinum, ceramic and clay pots.

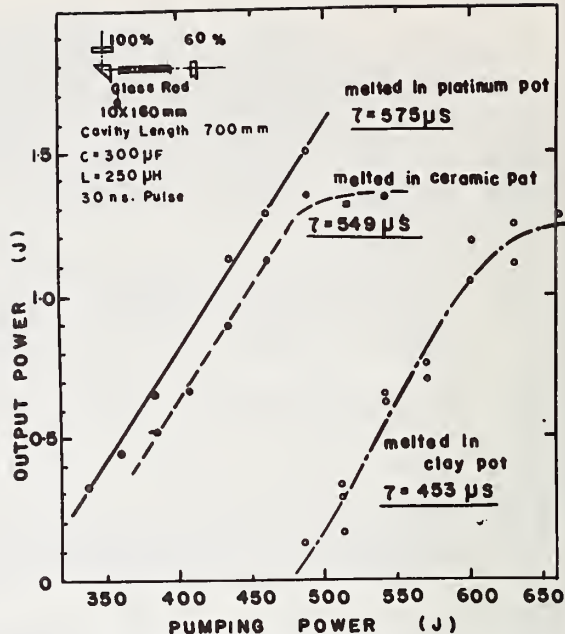


Figure 2B. Q-switched oscillation characteristics of LCG-11 glasses melted in platinum, ceramic and clay pots.

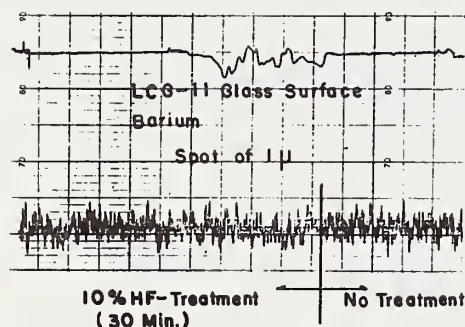


Figure 3A. Line analysis of K in HF-treated LCG-11 glass by electron micro probe x-ray analyzer.

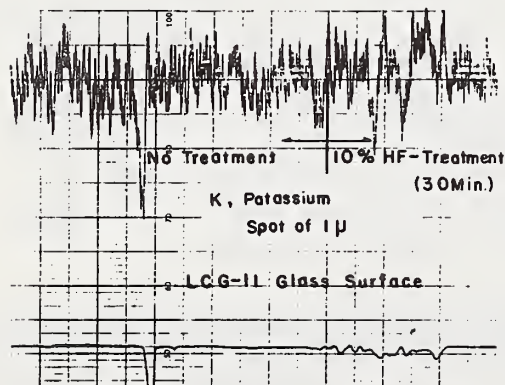


Figure 3B. Line analysis of Ba in HF-treated LCG-11 glass by E.M.X.

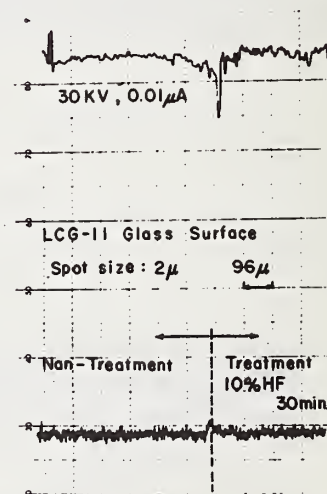


Figure 3C. Line analysis of Si in HF-treated LCG-11 glass by E.M.X.

Interaction Gradients, Concurrent Light Scattering  
Experiments and Bulk Laser Damage in Solids

C. Y. She<sup>1</sup> and David F. Edwards<sup>2</sup>

Quantum Electronics Laboratory  
Colorado State University  
Fort Collins, Colorado 80521

The concept of interaction gradient and its role on bulk laser damage is discussed. Results of light scattering experiments concurrent with damaging laser pulses on crystalline quartz, fused quartz and laser glass samples are compared to substantiate the role of interaction gradient and stimulated Brillouin scattering on bulk laser damage in solids.

Key Words: Bulk, crystalline quartz, fused quartz, interaction gradient, laser glass, laser induced damage, light scattering, stimulated Brillouin scattering.

## 1. Introduction

Our previous observations of the differences in damage properties of crystalline quartz for ruby laser pulses having different mode structures [1,2]<sup>3</sup> suggested that the onset of laser-produced damage in solids depends, in a critical way, on the spatial and/or temporal gradient of the interaction strength across the focal volume. The crystalline quartz in the scale of laser radiation and acoustic phonon wavelengths appears uniform to the light beam and the interaction gradient could exist only when a multi-mode laser is used. The existence and non-existence of interaction gradients when a multi-mode laser and a TEM<sub>00</sub> laser is used, respectively, are also evident in the forward scattering data presented. [2,3] The highly irregular data in figure 5 of reference 2 when a multimode laser was used as opposed to the relatively smooth data in figure 8 of reference 3 when a TEM<sub>00</sub> laser was used, is indicative of the presence of strong interaction gradient in one case (former), but not in the other. A piece of amorphous material, such as fused quartz and laser glass, however, is non-uniform in the same scale, and the interaction gradients (either spatial and/or temporal) may exist in the focal volume even when a uniform light beam from a TEM<sub>00</sub> laser is incident upon it. One purpose of this paper is to test the role of interaction gradient on laser damage by comparing the experimental results on crystalline quartz, fused quartz and laser glass samples.

By monitoring the light scattered, both backward and at 90°, concurrently with the damaging laser pulses, information about interaction gradients on laser damage was obtained. In addition, the role of stimulated Brillouin scattering as viewed from backward scattering, on laser damage of crystalline quartz, fused quartz and laser glass are compared experimentally. A second purpose of this paper is thus to describe the concurrent light scattering experiments and to discuss the significance of the findings to bulk laser damage in solids.

---

<sup>1</sup>Department of Physics .

<sup>2</sup>Department of Electrical Engineering and Department of Physics .

<sup>3</sup>Figures in brackets indicate the literature references at the end of this paper.



## 2. Experimental

The experimental set-up is shown in figure 1. Using the proper optical delays, the incident, transmitted, and backscattered laser pulses may all be recorded with a FW-114 photodiode on a Tektronix 519 oscilloscope. To minimize the confusion, the transmitted beam was monitored only in the forward scattering experiments as were reported in references 2 and 3. Otherwise, the transmitted beam was blocked by a stopper, and only the incident and backscattered pulses were detected by the FW-114 photodiode. In  $90^\circ$  scattering experiments, we monitored simultaneously both the incident and  $90^\circ$  scattered pulses. The weak  $90^\circ$  scattered light pulse was detected by a 1P22 photo-multiplier and a 6943 Å spike filter on a Tektronix 547 oscilloscope. In order to obtain desirable power (near the damage threshold) for the experiments,  $\text{CuS}_2$  attenuators and cut-and-try method were used.

The ruby rod of the  $\text{TEM}_{00}$  laser was cooled to  $21^\circ\text{C}$  before firing, and this way a sequence of consecutive shots in an interval of about 2.5 min. were fired into the same spot in the crystal until bulk damage was induced. The experiment was then repeated on a new spot in the solid.

## 3. Results and Discussions

Using the setup described above, the forward scattering intensity ratio on crystalline quartz and the  $90^\circ$  scattering intensity ratio on crystalline quartz and fused quartz were recorded. These results and their significances with respect to laser damage have been reported elsewhere [3] and will not be repeated here.

In the process of carrying out these experiments, a significant amount of backward scattering was observed when the incident laser pulse was near the damage threshold. Also, the ratio of the incident power of the damaging shot  $P_2$  to that of the preceding shot  $P_1$  for crystalline quartz, fused quartz and laser glass (Nd doped) samples have been evaluated. These new results and their significances in relation to bulk laser damage in solids will be reported here.

Shown in figure 2 are a sequence of oscilloscope pictures of laser pulses scattered from a piece of crystalline quartz. From the bottom up, the first four similar traces show the superposition of the incident laser pulse and the amplified backscattered pulses. The time intervals between peaks of the trace correlate well with the distances in the experimental set-up and they can be changed as the distance between the sample and the laser changes. In this instance, the bulk damage occurred in the fourth shot; no observable back-scattering was noted after the bulk damage was induced as seen in the fifth trace. The top trace in the figure is a typical  $90^\circ$  scattered pulse as recorded from the 1P22 photo-multiplier.

As far as back-scattering is concerned, the situation is nearly the same with fused quartz. This is evident as one compares figure 2 with figure 3. However, when the ratio of the incident power of the damaging shot  $P_2$  to that of the preceding shot  $P_1$  is calculated, the crystalline quartz and fused quartz appear to behave quite differently as can be seen in figure 4, in which the ratio  $P_2/P_1$  was plotted for all experiments leading to bulk damage. This ratio  $P_2/P_1$  for some experiments is less than unity in fused quartz. In fact, one can set the laser power so that a fused quartz sample could be damaged in a few shots. This has been difficult for crystalline quartz, i.e. under normal conditions, we either produced macroscopic damage in crystalline quartz in the first shot or produced no damage at all. The  $P_2/P_1$  ratio for the laser glass sample behaved similar to that of the fused quartz. This result is in agreement with the concept of interaction gradient which exists in the interaction between amorphous material and a uniform light beam.

Due to the absorption centers existing in laser glass, this behavior mentioned above appears more pronounced. Under the experimental conditions, we were able to control the laser power (by adjusting the  $\text{CuS}_2$  attenuators) to produce bulk damage in laser glass in the second shot every time. Furthermore, no backward scattering was noticed before the bulk damage was produced in the laser glass. Instead, a considerable amount of backward scattering was observed after bulk damage was induced. This is shown in figure 5 in which a sequence scope traces representing the laser pulses (from the bottom up) shot into the same spot in the laser glass sample are compared. The bulk damage occurred in the second shot in this figure, and the back-scattering was observed in the third and fourth shot after the bulk damage was produced. The backward scattered pulses in figure 2 and figure 3 were due to stimulated Brillouin scattering. Comparing the differences between figures 2 and 3, and figure 5, we would tentatively conclude that stimulated Brillouin scattering (catastrophic acoustic waves [1]) is responsible for laser induced damage in both crystalline and fused quartz, but local heating is perhaps more important in the bulk damage of laser glass samples.

#### 4. Acknowledgements

We thank Dr. T. W. Broberg of Systems Research Laboratories, Inc. for technical assistance and helpful discussions. The initial phase of this work was sponsored in part by a contract with the Air Force Cambridge Research Laboratories, Office of Aerospace Research, USAF.

#### 5. References

- [1] Draggoo, V. G., She, C. Y., McAllister, G. L. and Edwards, D. F., "Effects of Laser Mode Structure on Damage in Quartz", IEEE Jour. of Quantum Electronics QE-8, 54 (1972).
- [2] Edwards, D. F., She, C. Y., Draggoo, V. G., Broberg, T. W. and McAllister, G. L., "Investigation of Cumulative Effects in Microscopically Damaged Quartz", in Damage in Laser Materials: 1971, Edited by Glass, A. J. and Guenther, A. H., NBS Special Publication 356, p. 24 (1971).
- [3] Edwards, D. F. and She, C. Y., "Laser Produced Damage in Transparent Solids", Technical Report AFCRL-72-0143, Air Force Cambridge Research Laboratories, USAF (1972).

#### 6. Figures

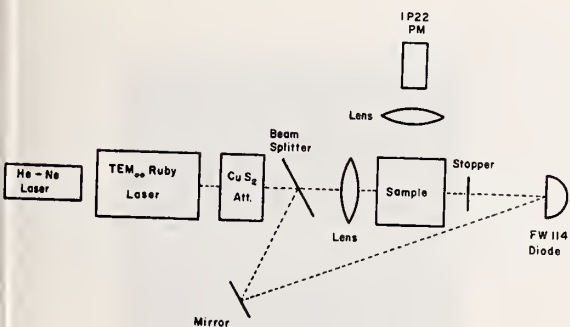


Figure 1. Schematic of the concurrent light scattering experimental set-up.



Figure 2. Scope traces of the incident and backward and 90° scattered laser pulses and crystal-line quartz. The time scale for the five bottom traces is 10 ns/cm and for the top trace is 50 ns/cm.

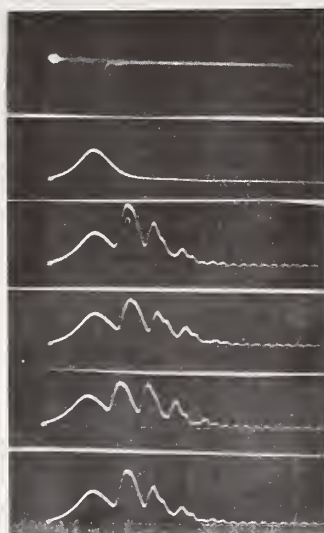


Figure 3. Scope traces of the incident and backward and  $90^\circ$  scattered laser pulses from fused quartz. The time scale for the five bottom traces is 10 ns/cm and for the top traces is 50 ns/cm.

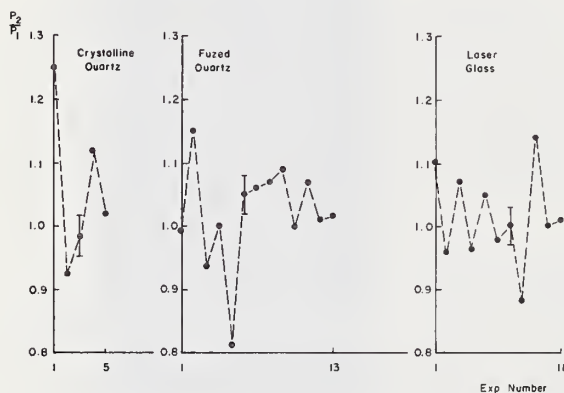


Figure 4. The ratio of the incident power of the damaging shot to that of the preceding shot  $P_2/P_1$  for crystalline quartz, fused quartz and laser glass samples.

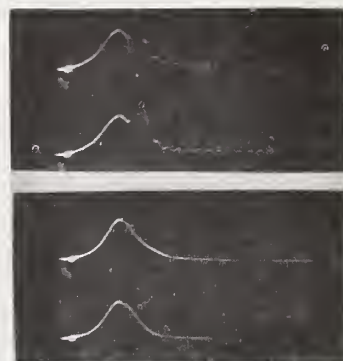


Figure 5. Scope traces of the incident and backward scattered laser pulses from a laser glass sample. The time scale is 10 ns/cm.



# Optical Index Damage in Electrooptic Crystals

A. M. Glass, G. E. Peterson and T. J. Negran

Bell Laboratories  
Murray Hill, New Jersey 07974

Optically induced refractive index changes which occur at low incident power densities ( $<1 \text{ KW/cm}^2$ ) in many electrooptic crystals have severely limited the application of these materials in the visible spectrum. Following a brief historical review of the subject, we discuss the recent advances in the understanding of the physical mechanisms involved, progress in reducing the damage susceptibility, and in enhancing the effect for holographic applications.

Particular attention is paid to  $\text{LiNbO}_3$  and  $\text{LiTaO}_3$  crystals. Optical and EPR studies of these materials have demonstrated that  $\text{Fe}^{2+}$  impurity ions present in nominally pure material are responsible for the index damage. The effects of stoichiometry variation, heat treatment, impurity and color center content, X-irradiation of crystals and the kinetics of the index damage process are accounted for by  $\text{Fe}^{2+}$ - $\text{Fe}^{3+}$  reactions.

By careful control of crystal growth and stabilization of the  $\text{Fe}^{3+}$  impurity ion state,  $\text{LiNbO}_3$  and  $\text{LiTaO}_3$  crystals with greatly improved damage resistance have been prepared.

Key Words: Holographic measurements, laser induced index change, optical memories, reversible low power damage.

## 1. Introduction

Laser induced refractive index changes occur in many electrooptic crystals. The index change distorts the wavefront of a transmitted optical beam and provides a serious limitation of the use of these potentially useful materials for nonlinear optical applications. For this reason it is usually referred to as laser damage, but it differs from the catastrophic damage which generally occurs at much higher power densities in that the index change is reversible. Following a brief historical review of the subject, recent progress in understanding the origin and mechanism of the index change is described. While index damage has been observed in several important materials including  $\text{LiNbO}_3$  [1,2]<sup>1</sup>,  $\text{LiTaO}_3$  [2], KTN [3],  $\text{BaTiO}_3$  [4],  $\text{Sr}_{1-x}\text{Ba}_x\text{Nb}_2\text{O}_6$  [5] and CdS [6] primary attention will be focused on  $\text{LiNbO}_3$  and  $\text{LiTaO}_3$  since we have studied these more extensively than the others. Methods of controlling the susceptibility of crystals to the index damage, both from the point of view of minimizing the effect for nonlinear optical applications and maximizing the effect for optical memory applications are described.

## 2. Historical Review

In his early studies of laser induced index changes, Chen [7] accounted for his results by the drift of photoexcited electrons outside the illuminated region of the crystal where they are subsequently trapped. Chen proposed that the resulting space charge field gave rise to the index change via the electrooptic effect. Bleaching of the index change is possible either by illuminating the entire crystal with the same light that created the index change or by heating the crystal, both of which result in reactivation of the trapped electrons which return to their original sites. In the case of cubic materials such as KTN an external applied field is required to observe index damage, but in the pyroelectric crystals no external field is necessary.

---

<sup>1</sup>Figures in brackets indicate the literature references at the end of this paper.

Chen's model had the following requirements:

1. A source of photoexcited carriers of concentration  $> 10^{15} \text{ cm}^{-3}$ .
2. Suitable trapping sites.
3. A permanent internal field of  $\sim 10^5 \text{ V/cm}$ .
4. A crystal resistivity sufficiently high that the space charge fields remained for extended periods (weeks).

A considerable amount of work followed on the identification of the defects responsible for the damage. Reduction of  $\text{LiNbO}_3$  and  $\text{LiTaO}_3$  was found to increase the effect, [7] while field annealing of these crystals at  $\sim 600^\circ\text{C}$  reduced the effect [8]. The latter effect was subsequently associated with  $\text{OH}^-$  impurity ions (or protons) drifting into the crystals from the atmosphere [9]. Defects associated with off-stoichiometry [10] of  $\text{LiNbO}_3$  and  $\text{LiTaO}_3$ , such as oxygen vacancies [7,11] and stacking faults [12] were also suggested as possible trapping sites.

The large spontaneous internal field required by Chen's model was difficult to account for, since it was of the wrong sign to be due to the pyroelectric effect and was too large to be due to surface effects. However, Johnston [12] pointed out that no initial internal field is required for the damage process. Optical excitation of a pyroelectric crystal gives rise to a macroscopic polarization change in the illuminated region and the divergence of this polarization acts as a source for an electric field. Furthermore, the equilibrium requirement that the total electric field  $E_{\text{tot}} = 0$  means only that  $V.P = (\epsilon-1)\rho$  where  $\rho$  is the space charge density and  $\epsilon$  is the dielectric constant, so it is possible, in a pyroelectric crystal to have a spatial variation of polarization without a corresponding variation of field. This polarization gives an index change via the electrooptic effect. In this way Johnston showed that the distribution of trapped carriers resulting from the diffusion of conduction electrons, skewed by electric field due to V.P was able to account for all the details of Chen's observations (which Chen's model could not) without the introduction of any fields before or after illumination of the crystal. This also removed requirement #4 of Chen's model.

The purpose of our work was to identify the defects involved so that some control over the optical damage process may be possible. Early experiments on the effects of heat treatment, oxidation and reduction, stoichiometry and field annealing were not reproducible and it was not until our discovery [13] of the importance of iron contamination of nominally undoped material in the damage process that the confusion was removed.

### 3. Quantitative Measurement of Index Damage

There are two basic techniques for the measurement of index damage. One is to write in the index change with a focused green or blue laser and to measure the birefringence change with a red probe beam which does not affect the damage. One such arrangement is shown in figure 1. The crystal polar axis is normal to the incident beams and  $45^\circ$  to the polariser axis. If the transmission of the Pockel's cell arrangement is initially set at zero with the compensator then the birefringence  $\Delta n$  induced by the 5145 Å

$$T = \sin^2 (\pi/\lambda) \int_0^d \Delta n_x dx \quad (1)$$

where  $d$  is the crystal thickness. Since most of the birefringence is induced over the near field distance of the focal spot an approximate measure of  $\Delta n$  is obtained. The sensitivity of this technique is limited by the crystals extinction ratio and typically  $\Delta n > 10^{-5}$  can be measured. This technique gives a direct measure of the usefulness of a crystal for nonlinear applications and enables the use of high power densities in the write beam. It suffers from the disadvantage that thermally induced birefringence changes may be larger than the laser damage and confuses some measurements. The holographic technique [4,14] provides a more accurate method for quantitative measurement of the index (not birefringence as before) change and the kinetics of the process. Two plane waves intersect in the crystal at an angle  $\theta$  as shown in figure 2 and the interference pattern forms an elementary hologram because of the induced index change. The diffraction efficiency of the grating [15]

$$\eta = \sin^2 \pi \Delta n d / \lambda \cos \theta \quad (2)$$

where here  $\Delta n$  is the modulation amplitude of the index change and  $d$  is the interaction length which in our case is the crystal thickness. The minimum index change which can be measured is limited by scattering from defects and typically  $\Delta n > 10^{-7}$  can be measured. This greater apparent sensitivity is offset by the fact that much lower power densities must be used. Thermal effects are unimportant, but vibration effects become important. Thus the holographic technique was used for its greater flexibility and accuracy throughout most of this work, while the focused beam technique was used when higher power densities were necessary, or unpoled (multidomain) crystals were examined. For measurement of damage susceptibility the 5145 Å writing beams were  $\sigma$  polarized with a power density  $\sim 1 \text{ W/cm}^2$  while the 6328 Å read beam was  $\pi$  polarized, the  $c$  axis of the crystal being normal to the grating planes. This measures  $\Delta n_3$ . Other polarizations and crystal orientations were used to study the damage mechanism as discussed later.



#### 4. Early Experiments

Crystals obtained from different sources grown from melts of the same stoichiometry varied widely in their damage susceptibility. Even crystals from the same source, same stoichiometry and same heat treatment varied greatly from one to another. Variation of crystal stoichiometry from a Li/Nb ratio in the melt of 44% to 54% had no observable effect on index damage, which seemed to remove the possibility of stoichiometric defects as the origin of damage. Studies of the thermal bleaching kinetics showed that at each temperature the index decays were exponential (monomolecular) with a single activation energy of  $1.2 \pm 0.1$  eV for all crystals regardless of damage susceptibility, although the entropy of activation was found to vary somewhat from one crystal to another and depended on heat treatment. The results are summarized in figure 3. Both the thermal and optical bleaching kinetics were independent of the spatial frequency of the index variation.

All crystals annealed in oxygen at  $1000^\circ\text{C}$  damaged less than crystals annealed in oxygen partial pressures of 100 mm Hg, but at lower oxygen partial pressures there was no further increase in damage susceptibility. A typical result is shown in figure 4. This seemed to eliminate oxygen vacancies as the origin of damage and point to impurities, or other charge compensating defects.  $\text{OH}^-$  ion impurities were observed to enter crystals during field annealing in air, with a general reduction in damage [8], but these  $\text{OH}^-$  ions could be subsequently removed by annealing crystals in oxygen without any corresponding increase in damage.  $\text{OH}^-$  ion content was in all cases measured by the absorption at  $\sim 3470\text{ cm}^{-1}$ . Crystals were analyzed and found to contain several impurities, but doping with these impurities gave no measurable increase in damage. Long term field annealing and heat treatments often gave erratic and irreproducible results. No optical luminescence associated with damage and no laser induced epr signals (10 KMc) were found. Any photoconductivity was masked by the pyroelectric effect [16].

While all this data to some extent characterized the index damage process, and eliminated a few possible defects as the origin of the damage, little progress toward identification of the active centers was achieved.

#### 5. Iron Contamination

510 MHz epr equipment was set up to study impurities in  $\text{LiNbO}_3$ . This equipment was well suited for the study of ferroelectrics both because of the large volume of crystal which could be contained in the cavity and because large fractional modulation of the magnetic field is possible. This is useful for studying the broad paramagnetic resonances in these materials when g broadening is suspected.

In all nominally undoped crystals it was found that the  $\text{Fe}^{3+}$  resonance line at  $g = 6$  when H1/c and  $g = 2$  when H1/c dominated the spectrum [17], the impurity concentration varying from 10 to 100 parts per million in different crystals. A typical epr spectrum is shown in figure 5. Earlier spectroscopic analysis had not revealed the presence of these impurities due to interference from niobium lines but these impurities have now been identified by more careful analysis [18] and results are consistent with the epr data.

The damageability of crystals was found to correlate well with the iron impurity concentration, in fact, crystals doped with 0.05 wt%  $\text{Fe}_2\text{O}_3$  were found to be far more susceptible to index damage than any other crystals examined. By analysis of  $\text{LiNbO}_3$  at each stage of the powder preparation and crystal growth process it was found that most of the contamination of undoped crystals came from the ceramics used as furnace tubes or crucible insulation [17]. By taking care to avoid any contact or proximity of heavily contaminated materials with the  $\text{LiNbO}_3$  at high temperatures crystals as pure as the starting materials (1 to 2 parts per million) were prepared. These crystals showed lower damage than any of the crystals we had studied. Comparison of the holographic diffraction efficiencies of newly poled crystals with different iron content, rapidly cooled from  $1100^\circ\text{C}$  is shown in the first row of table 1. Valence Change of iron in  $\text{LiNbO}_3$  occurs readily with suitable heat treatment. Almost complete conversion of  $\text{Fe}^{2+}$  to  $\text{Fe}^{3+}$  is possible by heating crystals in oxygen at  $600^\circ\text{C}$  for two days. Even crystals doped with 0.05 wt% iron were perfectly clear after this treatment and the absorption spectrum is shown in figure 6. Rapid cooling of crystals following an anneal in oxygen for a few minutes at  $1000^\circ\text{C}$  always gave a high  $\text{Fe}^{2+}$  concentration owing to the very small energy difference between the  $\text{Fe}^{2+}$  and  $\text{Fe}^{3+}$  states in the crystal. The crystal spectrum following this treatment is shown in figure 6, - crystals appeared quite brown. Heating crystals in lower oxygen partial pressures gave increased  $\text{Fe}^{2+}$  and almost complete conversion to the  $\text{Fe}^{2+}$  state was obtained by heating crystals in nitrogen - after which the crystals appeared black.

While measurement of the  $\text{Fe}^{3+}$  content was possible with epr, identification of the  $\text{Fe}^{2+}$  state was made on the basis of the optical spectra. The absorption band at 1.1 microns seen in the brown crystals is characteristic of  $\text{Fe}^{2+}$  ions in octahedral coordination [19]. Since there are no allowed crystal field transitions of the  $\text{Fe}^{3+}$  ion this spectrum is clear until the charge transfer band  $0.4\text{ }\mu\text{m}$ .



The susceptibility of crystals to index damage was found to depend only on the  $\text{Fe}^{2+}$  concentration of crystals. (The holographic diffraction efficiency depends on approximately the square of the  $\text{Fe}^{2+}$  concentration.) Diffraction efficiencies of oxidized crystals are shown in the second row of table 1 where it is seen that the damage is considerably lower than the quenched crystals in the first row. In order to increase the damage resistance of crystals still further attempts were made to completely stabilize the  $\text{Fe}^{3+}$  by the addition of colorless impurities of different valence such as  $\text{Ti}^{4+}$ ,  $\text{W}^{6+}$ ,  $\text{Mg}^{2+}$ , and  $\text{Al}^{3+}$  ions. None of these attempts were successful however. Since it is not known which sites the Fe ions occupy, nor what the charge compensating mechanisms are, the failure of these attempts has no special meaning.

Table 1. Diffraction efficiencies (%) of  $\text{LiNbO}_3$  crystals, 0.2 cm thick, after various heat treatments. The low Fe crystals are the highest purity crystals obtained by careful crystal growth.

Treatment	Undoped	0.05% $\text{Fe}_2\text{O}_3$	low Fe #1	low Fe #2
Poled from 1150°C and quenched	0.20	95 <sup>a</sup>	0.019	0.010
Annealed for 75 hr at 600°C	0.021	1.0	0.0039	not detected
Field annealed at 600°C for 15 min with 5 mA/cm <sup>2</sup>	0.007	b	0.0004	"

a. This was the maximum diffraction efficiency observed. An efficiency of 50% was still obtained with this crystal thinned down to 0.02 cm.

b. This crystal had very uneven  $\text{Fe}^{2+}$  distribution.

Crystals heated in oxygen pressures below 100 mTorr appear black. Thin wafers of these crystals actually have a deep blue color. These reduced crystals have a much higher electrical conductivity than clear crystals. A spectrum of a thin wafer is shown in figure 7. The absorption band centered at about 0.5  $\mu\text{m}$  ( $20,000\text{ cm}^{-1}$ ) is characteristic of  $\text{Nb}^{4+}$  ions [19] and is not associated with the Fe content of crystals. These ions act as donors (the conduction band of  $\text{LiNbO}_3$  being  $\text{Nb}^{5+} d_c$  orbitals [20]) thereby increasing the crystal conductivity. Field Annealing of iron-doped crystals results in a visible concentration gradient of  $\text{Fe}^{2+}$  ions in the crystals, the higher concentration being near the negative electrode. EPR measurements show a slightly higher  $\text{Fe}^{3+}$  concentration near this electrode also. The results indicate that these impurities carry an effective positive charge (possibly substituting for  $\text{Li}^+$  ions) and drift toward the negative electrode.  $\text{OH}^-$  ions (or  $\text{H}^+$  ions) enter the crystal from the positive electrode to compensate for the Fe ion current. The corresponding decrease in damageability of crystals is due to the decrease in  $\text{Fe}^{2+}$  content (Fe ions being pulled right out of the crystal) and not due to the increased  $\text{OH}^-$  ion content. If field annealing is performed in an atmosphere free of water vapor the Fe ion drift is not as effective since there is no compensation mechanism. The effect of field annealing crystals of various iron concentrations on the holographic diffraction efficiency is shown in the third row of table 1. A further decrease of damageability is seen. Extended field annealing gave no further decrease in damage, possibly because of Fe impurities entering the crystal from the positive electrode (evaporated platinum) or because of iron impurities becoming immobile at crystal defects. Although no diffraction was observed from one of the low iron crystals after the field annealing, index damage was still evident at higher power densities using the focused beam technique.

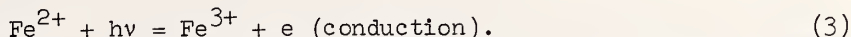
All these experiments show the correlation of index damage with  $\text{Fe}^{2+}$  content of crystals and account for all the previously observed effects. The importance of the cooling rate and the contamination of crystals from furnace ceramics during poling and heat treatments account for the erratic behavior of our own early experiments. It is of prime importance to monitor the Fe concentration of crystals to understand their damage characteristics. All heat treatments and poling of crystals for these results were performed in furnaces sheathed with silica and high purity platinum electrodes and containers.

## 6. X-irradiation

X-irradiation of crystals also makes them more susceptible to index damage. This is again due to valence changes of iron impurities due to the ionizing radiation, as demonstrated by optical and epr experiments. Crystals turn brown after irradiation, the absorption depth depending on the iron concentration and the spectrum is the same as the  $\text{Fe}^{2+}$  spectrum. (There is also some evidence of Nb reduction.) Annealing of crystals at about 150°C restores the crystal to its initial state. The activation energy for the thermal bleaching of the X-ray induced absorption is  $1.3 \pm 0.2$  eV, much the same as that for the decay of the index damage, but the entropy of activation is smaller (decays occur nearer room temperature) and the decay appears to be bimolecular (retrapping of thermally activated carriers is important). The effects of  $\gamma$  irradiation on the damageability of crystals [21] also seem to be due to valence change of Fe ions from the induced absorption spectrum.

## 7. Mechanism of Index Change

We now have strong evidence that Fe ions are the basis for the index damage. The  $\text{Fe}^{2+}$  ions are the source of photoelectrons via the reaction



These electrons (e) drift or diffuse out of the illuminated region where they can be trapped, possibly by  $\text{Fe}^{3+}$  ions via the reverse of reaction (3). This is indeed suggested by the similar wavelength dependence of the optical bleaching and writing processes. The index damage is then due to a spatial modulation of  $\text{Fe}^{2+}$  and  $\text{Fe}^{3+}$  ions. There is some assurance that the charge compensating defects of the iron impurities do not play a primary role in the damage process since other divalent and trivalent impurities have no noticeable effect in index damage and one might expect the charge compensating mechanism to be the same for some of these ions.

The broad absorption band observed around 0.5  $\mu\text{m}$  in the  $\text{Fe}^{2+}$  ion spectrum must be due to charge transfer from  $\text{Fe}^{2+}$  ions to the conduction band [22]. Since comparison of figures 6 and 7 confirm that it is not due to reduced niobium. The shape of this band accounts for the wavelength dependence of optical damage.

There is no reason why other multivalent impurities such as  $\text{Mn}^{2+} - \text{Mn}^{3+}$  should not give rise to index damage by the same process. The apparent absence of any effect of these ions [23] in our experiments must either be due to the absence of a suitable charge transfer process at 5145 Å or masking by other optical absorption processes which do not give rise to conductivity. It appears that the set of conditions required for index damage is energetically favorable for Fe ions and other impurities have smaller effects which are not observable above the effects of residual iron impurities.

Once photoactivated electrons are in the conduction band they can move by drift or diffusion. Johnston [12] pointed out that both effects are important to account for the index changes observed by Chen [7], with diffusion being the more important for short exposures. In fact, one might expect that with increasing spatial frequency diffusion becomes more important since the concentration gradient of conduction electrons increases for a given optical intensity. In figure 8 we show a photograph of the birefringence induced by a focused beam of 5145 Å radiation in a  $\text{LiTaO}_3$  crystal doped with iron. Similar results were obtained with  $\text{LiNbO}_3$  crystals. The birefringence pattern is symmetrical about the focal point which indicates that drift effects are small and the redistribution of carriers is by diffusion. The results of figure 8 are qualitatively the same as Chen's results on undoped  $\text{LiNbO}_3$  for short exposures. Recent work [24] suggests that diffusion is dominant for the higher spatial frequencies encountered in holographic storage, using  $\gamma$  irradiated  $\text{LiNbO}_3$ . The birefringence pattern of figure 8 also shows that the index change does not result from a space charge field (this would give the birefringence change shown by the broken line in figure 8) but from the polarization change associated with the redistribution of electrons. This result is expected since the conductivity of these  $\text{LiNbO}_3$  crystals ( $<10^{14}$  ohm cm) would relax the space charge fields in a few minutes or less. If higher resistivity crystals are available then space charge fields could play an important role for extended periods [25].

Johnston's model for the spatial variation of polarization requires that there be a significant difference between the dipole moment of unit cells containing  $\text{Fe}^{2+}$  ions and  $\text{Fe}^{3+}$  ions. The change in dipole moment of each impurity is additive, owing to the polar nature of the host, giving a macroscopic polarization change. Such changes of dipole moment  $\Delta\mu$  upon optical excitation have been measured experimentally for the  $\text{Cr}^{3+}$  ion to be about 0.6 Debye in  $\text{LiNbO}_3$  [26] and preliminary results for  $\text{Fe}^{2+}$  ions suggest a change  $\Delta\mu$  of about 1 Debye. Using this value we can obtain a rough estimate of the quantum efficiency of the holographic writing process if other contributions to the macroscopic polarization change are neglected.



## 8. Quantum Efficiency

The quantum efficiency  $q$  of the writing process in the case of laser induced index damage is the probability of the electron from an excited  $\text{Fe}^{2+}$  ion being trapped outside the laser beam and contributing to the index change. This will be a function of the spatial frequency written into the crystal since for the lower spatial frequencies the electrons have to travel further and the probability of being trapped within the illuminated region without contributing to the index change increases. Of course, in the limit of dc (uniform crystal illumination) no index change is recorded. This effect could account for the decreasing diffraction efficiency with increasing grating spacing observed in  $\text{BaTiO}_3$  [4]. To estimate the quantum efficiency for a grating spacing of  $1 \mu\text{m}$  we use the data of figure 9 where the diffraction efficiency  $\eta$  of 0.018 cm and 0.14 cm thick crystals of iron doped  $\text{LiNbO}_3$  have been plotted as a function of time for various incident power densities. These crystals had an extinction coefficient of  $\alpha = 1.4 \text{ cm}^{-1}$  at  $5145 \text{ \AA}$ . The initial slope of the curve at short times for an incident power  $W$  of  $0.9 \text{ W/cm}^2$  is for the thinner crystal

$$\left(\frac{d\eta}{dt}\right) = 0.0011 \text{ sec}^{-1} \quad \text{or} \quad \left(\frac{d\eta}{dW}\right) = 1.2 \times 10^{-7} \text{ m}^2 \text{J}^{-1}.$$

From eq. 2 we calculate for  $\eta \ll 1$

$$\left(\frac{d\eta}{dW}\right)_{t \rightarrow 0} = \frac{\pi t}{\lambda c \cos \theta} \left(\frac{dn_3}{dW}\right)_{t \rightarrow 0} \sim 10^3 \left(\frac{dn_3}{dW}\right)_{t \rightarrow 0}.$$

Since  $1 \text{ Joule} \sim 4.5 \times 10^{18}$  photons at  $5145 \text{ \AA}$  we have the index change per absorbed photon density  $N$

$$\frac{dn_3}{dN} = \frac{1}{\alpha} \frac{dn_3}{dW} = 1.3 \times 10^{-31} \text{ m}^3/\text{photon}. \quad (4)$$

The same result is obtained for the thicker crystal in figure 9. Since the index change has electrooptic origin, for the configuration used

$$\Delta n_3 = \frac{n_3^3 r_{33} \Delta P_3}{2(\epsilon_{33} - 1)} = \frac{n_3^3 r_{33} q N \Delta \mu}{2(\epsilon_{33} - 1)} \quad (5)$$

where  $\Delta \mu$  is the change in dipole moment associated with the  $\text{Fe}^{2+}$  to  $\text{Fe}^{3+}$  change. Using published values for  $n_3$ ,  $\epsilon_{33}$ , and  $r_{33}$  [28] and the preliminary value for  $\Delta \mu \sim 1$  Debye we calculate from eqs. 4 and 5 a quantum efficiency of 1.3%. It has been demonstrated that larger values of  $q$  may be obtained with an external applied field to increase the drift velocity of the excited carriers [27].

It must be emphasized that this calculation assumes that space charge fields, and contributions to  $\Delta P_3$  from sources other than the excited state dipole, were unimportant. This assumption is almost certainly invalid - especially for short exposures, but the estimate does point out that this model provides a reasonable interpretation of the data.

Within these approximations it is also possible to estimate the  $\text{Fe}^{2+}$  ion concentration necessary to obtain the maximum observed diffraction efficiency in figure 9. From this data and eq. 2 we calculate a maximum index change  $\Delta n_{\text{max}} \sim 7 \times 10^{-4}$ . Thus from eq. 5 we estimate the maximum number of trapped electrons (using  $\Delta \mu \sim 1$  Debye) to be about  $7 \times 10^{25} \text{ m}^{-3}$ . This is some three times greater than the total Fe concentration of the crystal. It is doubtful that  $\Delta \mu$  can be increased to account for this discrepancy since the dipole moment of a  $\text{LiNbO}_3$  unit is only 2.5 Debye, thus other contributions to the polarization - dipole induced polarization - are important. In view of the above assumptions this mechanism gives reasonable interpretation of the observations.

## 9. Photochromic Effects

Evidence that the laser induced index change has electrooptic origin is afforded by the polarization dependence of the diffraction efficiency of an elementary hologram [14]. If the hologram is written with the  $c$  axis normal to the grating planes, then the diffraction efficiencies of  $\pi$  and  $\sigma$  polarized read beams at  $6328 \text{ \AA}$  are in the ratio 8.6:1 for  $\eta \ll 1$ . This is precisely what one expects from the ratio of electrooptic coefficients [28]:

$$\frac{\eta_\pi}{\eta_\sigma} \approx \left(\frac{\Delta n_3}{\Delta n_1}\right)^2 = \left(\frac{n_3^3 r_{33}}{n_1^3 r_{13}}\right)^2 = 8.4.$$

This result does not depend on the origin of the variation of  $P_3$  since both space charge fields and excited state dipoles will both contribute to  $\Delta P_3$  such that  $\nabla \cdot P_3 \neq 0$ .

If, however, a hologram is written with the  $c$  axis parallel to the grating planes, then some information concerning the microscopic origin of  $\nabla \cdot P_3$  can be obtained. The excited state dipole moment can only, by symmetry, give a variation in  $P_3$ , while space charge fields will give a variation in  $P_1$  or  $P_2$  only for this configuration. Thus in equilibrium  $\nabla \cdot P = 0$  and no diffraction would be observed due to



the electrooptic effect. If the crystal is not in equilibrium and there are net space charge fields due to trapped carriers (at times shorter than the relaxation time), then diffraction will be observed. When the crystal b axis is normal to the grating planes

$$\eta\pi = 0 \quad \text{and} \quad \eta\sigma = \frac{n_2^3 r_{22} \Delta P_2}{(\epsilon_2 - 1)}.$$

For the same space charge fields  $\eta\sigma$  for this configuration should be about half of  $\eta\sigma$  for the previous configuration. No diffraction is measured with this configuration at 6328 Å in our experiments suggesting that no space charge fields are present. However, when the 5145 Å laser is used as the read beam, then a diffraction efficiency of about 1% of  $\eta\sigma$  for the previous configuration with the same exposure was observed in an iron-doped LiNbO<sub>3</sub> crystal 1.5 mm thick. This difference for the two wavelengths was too great to be due to dispersion of  $r_{22}$ . A possible explanation of the result is photochromism. Since the basis for the index variation is the photochromic Fe<sup>2+</sup> - Fe<sup>3+</sup> reaction, an amplitude hologram is expected. The diffraction efficiency of such an elementary hologram is [15]

$$\eta = \exp - \left( \frac{2 \alpha d}{\cos \theta} \operatorname{sh}^2 \frac{\alpha d}{2 \cos \theta} \right) \quad (6)$$

where  $\alpha$  is the modulation amplitude of the absorption depth. To estimate the importance of this effect, we will assume that all Fe<sup>2+</sup> ions possible contribute to the hologram, then for the 0.15 cm thick crystal, using  $\alpha \sim 1.4$  from figure 6 we find  $\eta = 0.009$  with little dependence of the efficiency on the polarization of the read beam, due to the small dichroism. This estimate is considerably greater than the measured diffraction efficiency of 0.1% so the observed effect could indeed be due to photochromism.

#### 10. LiTaO<sub>3</sub>

Qualitatively the behavior of LiNbO<sub>3</sub> and LiTaO<sub>3</sub> is similar. There are, however, important quantitative differences. The index damage susceptibility of LiTaO<sub>3</sub> is much lower than LiNbO<sub>3</sub> for both undoped and iron-doped crystals by a factor of about 30. A comparison of the two materials is shown in table 2. The data in this table was obtained using the focused beam technique of figure 1 with a 7 cm focal length lens. The incident power listed is the minimum power density necessary to just see transmission through the pockels cell due to the laser induced index change for the exposure times given. At these powers defocusing of the beam was also just observed. It was necessary to use this technique since high temperature heat treatments depole LiTaO<sub>3</sub> (Curie temperature  $\sim 620^\circ\text{C}$ ) and repoling of course changes the crystal characteristics. The results of table 2 give some semiquantitative idea of the damage susceptibility for comparing different crystals, but the absolute magnitudes depend on the spatial frequencies (focal length of the lens) and the exposure time. The LiTaO<sub>3</sub> crystals obtained from Crystal Technology Inc. had the highest damage resistance of all those studied after suitable heat treatments and field annealing, even though the Fe<sup>3+</sup> content of these crystals was greater than 10 parts per million. The iron is almost entirely stabilized in the Fe<sup>3+</sup> state.

Table 2. Peak intensity in watts/cm<sup>2</sup> at the focus of a 5145 Å argon laser beam, necessary to just observe index damage during a 10 second exposure.

Crystal	Quenched from 1000°C	Slow cooled and field annealed <sup>a</sup>
LiTaO <sub>3</sub> annealed at 1200°C for 25 hrs after growth	200	900
LiTaO <sub>3</sub> annealed at 1400°C for 25 hrs after growth	600	3000
LiTaO <sub>3</sub> : Crystal Technology	1500	8000
LiTaO <sub>3</sub> + 0.05% Fe <sub>2</sub> O <sub>3</sub>	10	30
LiTaO <sub>3</sub> + 0.05% Fe <sub>2</sub> O <sub>3</sub> (reduced in H <sub>2</sub> and annealed 15 minutes in N <sub>2</sub> at 1000°C)	25	--
LiNbO <sub>3</sub> low iron	40	300
LiNbO <sub>3</sub> + 0.05% Fe <sub>2</sub> O <sub>3</sub>	0.5	6

a. Field annealed at 600°C for about 10 minutes with 5 mA/cm<sup>2</sup>. This procedure poled LiTaO<sub>3</sub>.

A clue to the reason for the difference in damageability of  $\text{LiNbO}_3$  and  $\text{LiTaO}_3$  may be given by the absorption spectrum of figure 10.  $\text{LiTaO}_3\text{:Fe}^{2+}$  does not have the pronounced absorption band at about  $0.5 \mu\text{m}$  which is present in  $\text{LiNbO}_3$ . The excitation of an electron from an  $\text{Fe}^{2+}$  ion to the conduction band may be less probable than excitation to a nonconducting state with  $5145 \text{ \AA}$  radiation. This may be related to the fact that the  $\text{Ta}^{5+}$  ion is a great deal more difficult to reduce to  $\text{Ta}^{4+}$  than the equivalent  $\text{Nb}^{5+}$ - $\text{Nb}^{4+}$  reaction.  $\text{Ta}^{4+}$  can only be obtained in sufficient concentration to color the crystal if crystals are heated in hydrogen at  $1000^\circ\text{C}$ , while  $\text{Nb}^{5+}$  reduces with much less severe treatment. Because of this property it is possible to obtain almost complete conversion of  $\text{Fe}^{3+}$  to  $\text{Fe}^{2+}$  in  $\text{LiTaO}_3$  before the crystals turn black. It is interesting to see from table 2 that the heavily reduced crystal seemed to damage less than the quenched crystal. This implies that the presence of  $\text{Fe}^{3+}$  ions as traps are essential to maximize the damage. It is also interesting to see that annealing  $\text{LiTaO}_3$  crystals in air at  $1400^\circ\text{C}$  for several hours results in lower damage than crystals annealed at  $1200^\circ\text{C}$  for the same time. This treatment increases the oxidation state of the  $\text{LiTaO}_3$  thereby increasing the  $\text{Fe}^{3+}/\text{Fe}^{2+}$  ratio. The improvement of the Crystal Technology crystal is presumably due to a variation of the crystal growth procedure.

## 11. Applications of Laser Induced Index Damage

Laser induced index changes have been used as the basis of an erasable pure phase holographic memory [14] and may find future application in distributed feedback systems [29] and integrated optics. For these applications maximum writing sensitivity is required so that iron doped  $\text{LiNbO}_3$  is particularly useful. By suitable doping, choice of crystal thickness and heat treatment, a compromise between optical absorption loss and writing sensitivity may be achieved for any application. We have been able to achieve holographic diffraction efficiencies of 50% using  $\sim 1 \text{ J/cm}^2$  of incident energy with  $\text{LiNbO}_3 + 0.05\% \text{ Fe}$  crystals  $0.2 \text{ cm}$  thick with  $\sim 30\%$  absorption loss at  $5145 \text{ \AA}$ . The angular selectivity

$$\Delta\theta = \frac{n\lambda}{2t \sin \theta} \quad (7)$$

of this crystal was about  $1 \text{ mR}$  for a grating spacing of  $1 \mu\text{m}$ . With thicker crystals higher angular selectivity can be obtained, but without improvement in writing sensitivity since these crystals have to be oxidized somewhat to prevent excessive absorption loss. An advantage, in principle, of higher angular selectivity is that many holograms can be superimposed in the same volume of crystal and independently read out. However, it is not possible to erase one hologram without erasing all the others in the same volume. Furthermore, partial erasure occurs during readout, by optical bleaching since read and write wavelengths must be the same to avoid distortion in the thick crystals. Fixing holograms eliminates the problem of optical bleaching during reading but it also removes the versatile feature of optical erasability. Fixing holograms may be accomplished by any polarization relaxation process which compensates wholly or partially for the polarization variation in the crystal, then subsequent optical bleaching of the trapped electrons will leave a fixed hologram. Such procedures have been demonstrated for undoped  $\text{LiNbO}_3$  [21,25] and  $\text{BaTiO}_3$  [30]. The polarization relaxation process could be local polarization reversal [30], or other ionic rearrangement. For crystals not in equilibrium when there are space charge fields present, fixing could be accomplished by ionic conductivity to relax these fields [25]. Polarization relaxation requires only local changes while field relaxation requires ionic drift over macroscopic distance. Since there is no dependence of the thermal bleaching associated with the fixing on the spatial frequency of the index pattern in  $\text{LiNbO}_3$ , the former mechanism seems to be operative, consistent with earlier observations that space charge fields do not persist.

For some memory applications it may be advantageous to use thin crystals, heavily doped with iron to maximize the writing sensitivity, so that the angular selectivity is poor. Then readout may be performed with a longer wavelength radiation such that optical bleaching is not a problem. Second order distortion effects may be tolerable. We can see from eqs. 2 and 7 that for writing with  $5145 \text{ \AA}$  radiation and reading with  $6328 \text{ \AA}$  we need  $\Delta\theta > 50 \text{ mR}$  or crystal thicknesses  $< 4 \times 10^{-2} \text{ cm}$ . With this kind of system the holograms would not be superimposed but arranged in an array so that each can be spatially addressed. In this way single holograms can be erased.

## 12. Diffusion Doping

To achieve such thin holograms of high sensitivity is relatively simple by diffusion doping of crystals. Heavily iron-doped layers about  $25 \mu\text{m}$  (measured by the angular selectivity of an elementary hologram) can be diffused into  $\text{LiNbO}_3$  in a few hours at  $1100^\circ\text{C}$ , while leaving the crystal in a single domain state.  $1\%$  diffraction efficiency could be obtained with  $10 \text{ J/cm}^2$  incident energy or  $3\%$  with  $60 \text{ J/cm}^2$  and less than  $10\%$  absorption loss at  $5145 \text{ \AA}$ . This corresponds to a peak to peak index change of about  $0.0025$  without even focusing. The measured angular selectivity  $\Delta\theta \sim 100 \text{ mR}$  was sufficiently great that both diffracted beams, each side of the normal to the crystal surface, could be observed with normal incidence of the read beam.



### 13. Conclusions

The optically induced refractive changes in  $\text{LiNbO}_3$  and  $\text{LiTaO}_3$  have been reasonably well characterized and the basic mechanisms understood. Our measurements are consistent with the interpretation that only iron impurities contribute to the laser damage in these two materials, even though there is no fundamental reason why other impurities might not result in similar effects. The set of conditions necessary for index damage appears particularly favorable for iron impurities in  $\text{LiNbO}_3$ . It is known that the addition of iron increases the damageability of  $\text{Ba}_2\text{Na Nb}_5\text{O}_{15}$  [21] and  $\text{BaTiO}_3$  [30] but at the present time it is not known whether this impurity is the only cause of damage in these materials. In the case of  $\text{BaTiO}_3$  the situation is a little more complicated in that the addition of some impurities is accompanied by an increase in the electrooptic coefficients at room temperature so that increased damage susceptibility could be due to this effect rather than the direct effect of charge transfer from the impurities.

Solely by varying the  $\text{Fe}^{2+}$  concentration of  $\text{LiNbO}_3$  and  $\text{LiTaO}_3$  it has been possible to vary the laser induced index changes over about four orders of magnitude for the same exposure. It has only been possible to prepare  $\text{LiNbO}_3$  and  $\text{LiTaO}_3$  with resistance to index damage for incident powers less than 100 W/cm<sup>2</sup> and 10 KW/cm<sup>2</sup> respectively by careful control of crystal growth. Since the distribution coefficient of iron in  $\text{LiNbO}_3$  is less than, but close to unity [16] zone refining is not expected to give great improvement. However, any improvement at all increases the usefulness of crystals both as electrooptic modulators, since increased powers can be used, and as parametric oscillators, since the temperature of operation can be decreased, thereby increasing the useful tuning range. Each order of magnitude decrease in damage susceptibility decreases the lowest possible operating temperature by 20°C.

The study of iron in  $\text{LiNbO}_3$  and  $\text{Ba}_2\text{Na Nb}_5\text{O}_{15}$  has also led to progress in the understanding of self-focusing by two step absorption in these materials at high power densities [31]. In this context it is worth pointing out that the excited state dipole effect provides a direct index change in addition to thermal effects which may contribute to self-focusing.

### 14. Acknowledgments

Throughout this work we have had the assistance and interest of many of our colleagues. In particular we would like to thank P. M. Bridenbaugh and A. A. Ballman for growing the crystals used in this work, Miss B. E. Prescott and Mrs. G. A. Pasteur for measuring the optical absorption spectra of our crystals and A. Carnevale for assistance with the epr measurements. Helpful discussions of unpublished work with D. L. Nash and F. Micheron, M. Clark and L. K. Anderson are gratefully acknowledged.

### 15. References

- [1] Peterson, G. E., Ballman, A. A. Lenzo, P. V. and Bridenbaugh, P. M., Appl. Phys. Letters, 5, 62 (1964).
- [2] Ashkin, A., Boyd, G. D., Dziedzic, J. M., Smith, R. G., Ballman, A. A., Levinstein, H. J. and Nassau, K., Appl. Phys. Letters 9, 72 (1966).
- [3] Chen, F. S., J. Appl. Phys. 38, 3418 (1967).
- [4] Townsend, R. L. and LaMacchia, J. T., J. Appl. Phys. 41, 5188 (1970).
- [5] Thaxter, J. B., Appl. Phys. Letters 15, 210 (1969).
- [6] Ashkin, A., Tell, B. and Dziedzic, J. M., IEEE J. Quantum Electron. 3, 400 (1967).
- [7] Chen, F. S., J. Appl. Phys. 40, 3389 (1969).
- [8] Levinstein, H. J., Ballman, A. A., Denton, R. T., Ashkin, A. and Dziedzic, J. M., J. Appl. Phys. 38, 3103 (1967).
- [9] Smith, R. G., Fraser, D. B., Denton, R. T. and Rich, T. C., J. Appl. Phys. 39, 4600 (1968).
- [10] Peterson, G. E. and Carruthers, J. R., Solid State Chemistry 1, 98 (1969).
- [11] Jorgensen, P. J. and Bartlett, R. W., Tech. Rep. No. ONRAD686721, Stanford Research Institute (1969). Unpublished.
- [12] Johnston, Jr., W. D., J. Appl. Phys. 41, 3279 (1970).
- [13] Peterson, G. E., Glass, A. M. and Negran, T. J., Appl. Phys. Letters 19, 130 (1971).
- [14] Chen, F. S., LaMacchia, J. T. and Fraser, D. B., Appl. Phys. Letters 13, 223 (1968).
- [15] Kogelnik, H., Bell System Tech. Journal 48, 2909 (1969).
- [16] Phys. Stat. Sol. (a) 9 301 (1972). The optically excited current observed in this work appears to have pyroelectric origin - not photoconductivity as reported.
- [17] Peterson, G. E., Glass, A. M. and Carnevale, A., (to be published).
- [18] Nash, D. L., submitted to Applied Optics.



- [19] See for instance C. J. Ballhausen "Introduction to Ligand Field Theory" McGraw Hill Book Co., Inc., NY (1962).
- [20] DiDomenico, M., private communication.
- [21] Amodei, J. J., Phillips, W. and Staebler, D. L., Appl. Optics 11, 390 (1972).
- [22] Clark, M. and Glass, A. M., to be published.
- [23] Ref. 21 reports small effects due to Mn and Cu impurities, but the Fe content of these crystals is not reported.
- [24] Staebler, D. L. and Amodei, J. J., J. Appl. Phys. 43, 1042 (1972).
- [25] Resistivities of  $10^{18}$  ohm cm have been reported for  $\text{LiNbO}_3$  by Staebler, D. L. and Amodei, J. J., Ferroelectrics 3, 107 (1972).
- [26] Glass, A. M. and Auston, D. H., Optics Communication 5, 45 (1972).
- [27] Staebler, D. L. and Amodei, J. J., 1972 Int. Quantum El. Conference, Montreal.
- [28] Kaminow, I. P. and Turner, E. H., "Tables of Electrooptic Coefficients," Handbook of Lasers Chemical Rubber Co. Press (1971).
- [29] Kogelnik, H. and Shank, C. V., J. Appl. Phys. 43, 2327 (1972).
- [30] Micheron, F. and Bismuth, G., Int. Electro-optics Conference (1972) Brighton, England.
- [31] Shenke, D. P. and Smith, R. G., to be published.

## 16. Figures

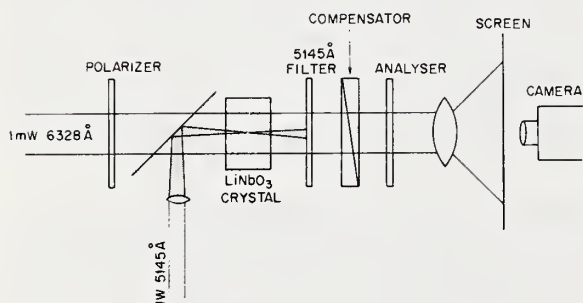


Figure 1. Apparatus for measuring and photographing the birefringence change induced at the focus of a 5145 Å argon laser beam.

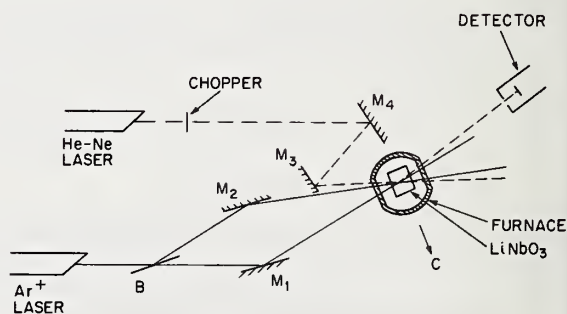


Figure 2. Holographic technique for measuring laser induced index changes. B is a beam splitter and the  $M_i$  are mirrors.

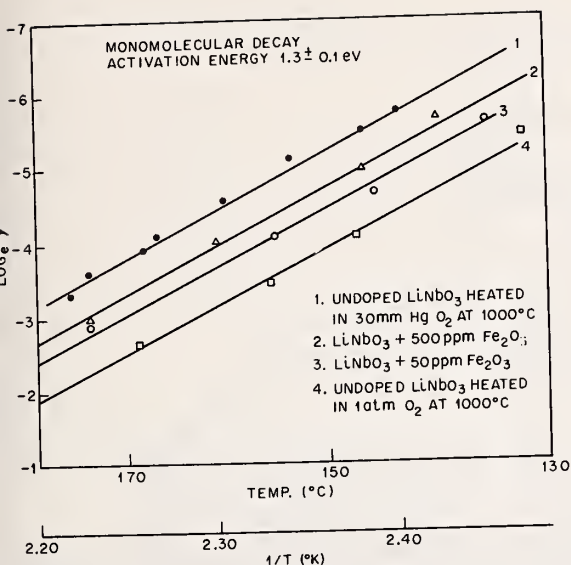


Figure 3. A plot of the thermal decay constant  $\gamma$  defined by  $\Delta n = \Delta n_0 \exp(-\gamma t)$ , against the reciprocal absolute temperature for 1) undoped  $\text{LiNbO}_3$  heated in 0.04 atm.  $\text{O}_2$  at  $1000^\circ\text{C}$  2) as grown  $\text{LiNbO}_3$  + 0.05%  $\text{Fe}_2\text{O}_3$  3) as grown  $\text{LiNbO}_3$  + 0.005%  $\text{Fe}_2\text{O}_3$  4) undoped  $\text{LiNbO}_3$  heated at 1 atm  $\text{O}_2$  at  $1000^\circ\text{C}$ .

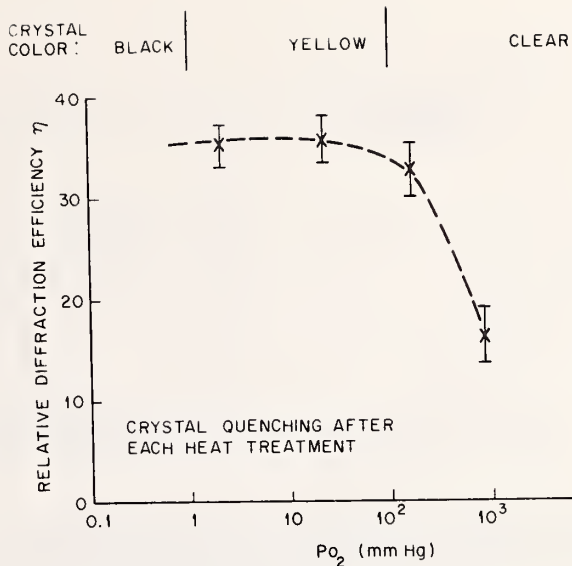


Figure 4. Relative diffraction efficiency of a typical  $\text{LiNbO}_3$  crystal after heat treatments in various oxygen partial pressures. Crystals were quenched from  $1000^\circ\text{C}$ .

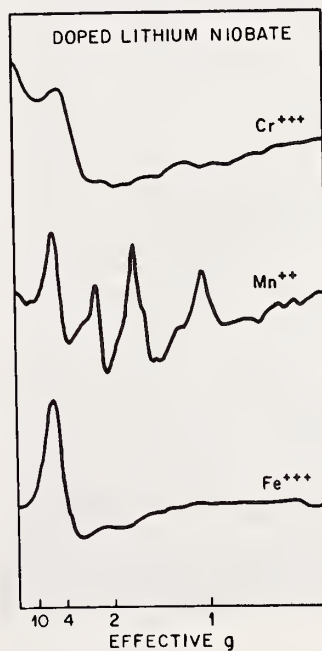
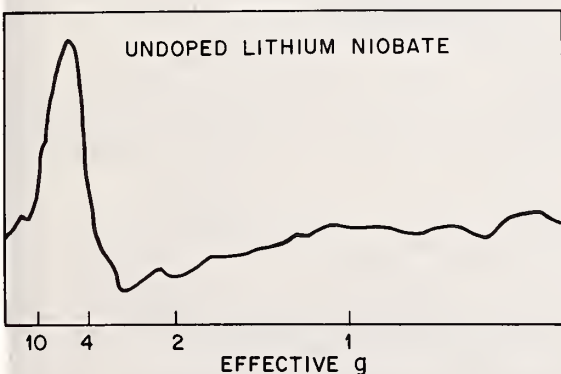


Figure 5. E.P.R. spectrum of an undoped  $\text{LiNbO}_3$  crystal (ground to a powder) compared with  $\text{LiNbO}_3$  powder doped with  $\text{Cr}^{3+}$ ,  $\text{Mn}^{2+}$ , and  $\text{Fe}^{3+}$  impurities.

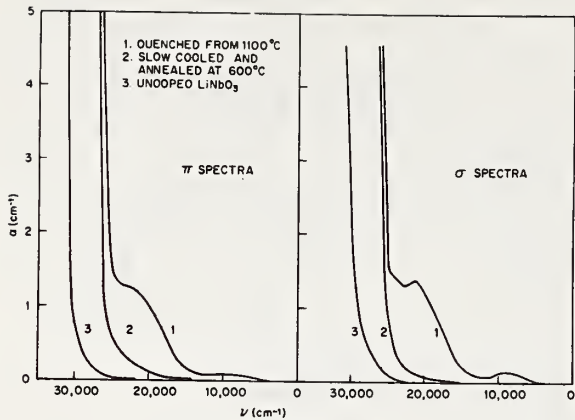


Figure 6. Optical absorption spectra of iron doped  $\text{LiNbO}_3$  (0.05%  $\text{Fe}_2\text{O}_3$ ), 1) after quenching from  $1100^\circ\text{C}$  2) after slow cooling and annealing at  $600^\circ\text{C}$  compared with 3) undoped  $\text{LiNbO}_3$  for both  $\pi$  and  $\sigma$  polarizations.

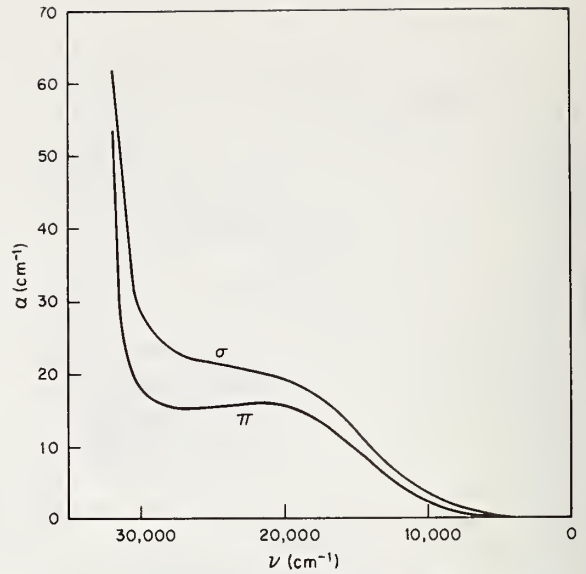


Figure 7. Optical absorption spectra of  $\text{LiNbO}_3$  after reduction in a nitrogen atmosphere at  $1000^\circ\text{C}$  for 10 minutes. The crystal appeared deep blue.



Figure 8. Typical laser induced birefringence patterns in  $\text{LiTaO}_3:\text{Fe}$  (0.05%). The line drawing is a plot of the birefringence change along the  $c$  axis. The broken line is the birefringence change which would occur due to space charge fields due to diffused carriers.

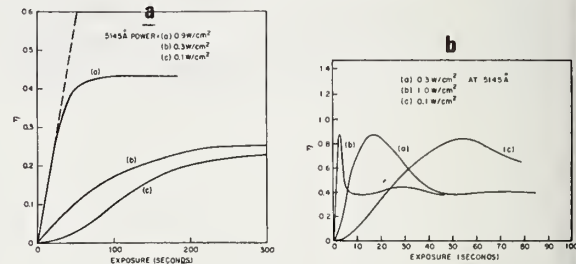


Figure 9. Formation of elementary holograms as a function of exposure to  $5145\text{\AA}$  radiation; a) is from a  $0.018\text{ cm}$  thick crystal and b) is from a  $0.14\text{ cm}$  thick crystal.

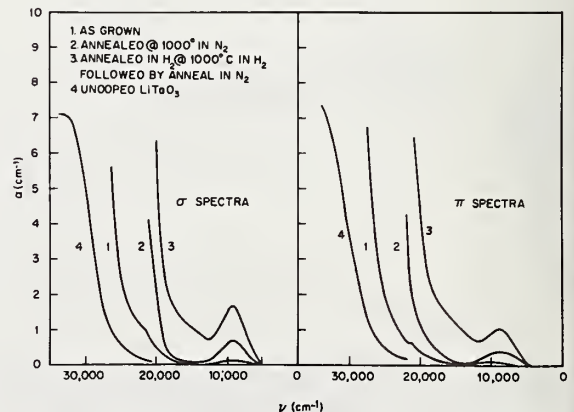


Figure 10. Optical absorption spectra of iron doped  $\text{LiTaO}_3$  (0.05%  $\text{Fe}_2\text{O}_3$ ) 1) as grown 2) after annealing at  $1000^\circ\text{C}$   $\text{N}_2$ , 3) after annealing in  $\text{H}_2$  at  $1000^\circ\text{C}$ , compared with 4) undoped  $\text{LiTaO}_3$ , for  $\pi$  and  $\sigma$  polarizations.



Comparison of Laser Induced Bulk Damage in Alkali-Halides  
at 10.6, 1.06, and 0.69 Microns

D. W. Fradin and Eli Yablonovitch\*

Gordon McKay Laboratory, Harvard University  
Cambridge, Mass. 02138

and

Michael Bass†

Raytheon Research Division  
Waltham, Mass. 02154

It has long been recognized that catastrophic self-focusing cannot occur below a critical power  $P_c$  and that perturbations from self-focusing become progressively less important as the power of a probe optical beam is lowered below  $P_c$ . Using this fact, we have designed and conducted a number of experiments to study bulk damage in alkali-halides in which self-focusing was eliminated and unequivocal measurements of damaging fields obtained. Strongly focusing optical systems were used so that damage could be achieved while probe powers could be restricted to between one and two orders-of-magnitude below theoretical critical powers for electrostrictive self-focusing. Experimental evidence confirms the absence of self-focusing.

By observing the absolute magnitude of breakdown strengths and relative values among the alkali-halides, striking similarities between 10.6, 1.06 and 0.69  $\mu\text{m}$  and d.c. avalanche breakdown were found. The results also showed no frequency dispersion over the wavelength range of 10.6 to 0.69 microns. The implications of this work for surface damage studies are explored, and, in addition, the effects of inclusions on bulk optical strength are considered.

Key Words: Alkali halides, avalanche breakdown, bulk damage, self-focusing, surface damage.

## 1. Introduction

Laser induced breakdown [1]<sup>1</sup> in transparent dielectrics has been studied since high intensity optical fields have been available. Nevertheless, it has been difficult to ascertain the intrinsic bulk damage mechanism for these materials because of complications arising from self-focusing [2], multiphoton absorption and cascade ionization of impurities [3].

Recent work at 10.6  $\mu\text{m}$  [4], however, indicates that intrinsic damage can be isolated. By choosing pure wide bandgap insulators, multiphoton ionization or its low frequency limit [5], tunnel ionization, can be eliminated. In addition, by confining laser powers to well below critical powers for self-focusing [6] catastrophic beam collapse becomes impossible and corrections from the index nonlinearity become quite small.

---

\*Supported by the Joint Services Electronics Program at Harvard University under Contract No. N00014-67-A-0298-0006.

†Supported by the Advanced Research Projects Agency of the Department of Defense and was monitored by the Air Force Cambridge Research Laboratories under Contract No. F19628-70-0223.

<sup>1</sup>Figures in brackets indicate the literature references at the end of this paper.

The alkali-halide family is a natural choice for breakdown studies. Besides being of practical importance for their application as optical materials in CO<sub>2</sub> lasers, they have large bandgap (about 7 eV or more) and have been studied extensively for both their d.c. dielectric strength [7] and their 10.6  $\mu$ m characteristics [4].

The experimental studies reported here were conducted at 1.06 and 0.69  $\mu$ m using Q-switched lasers. Since self-focusing may reach threshold before breakdown at these frequencies [8], it is important to understand both the conditions under which catastrophic self-focusing occurs and the corrections from the index nonlinearity when a catastrophic focus is prevented. For this reason an analysis of self-focusing is outlined in the appendices, and the general results relevant to our measurements are discussed in Section 3. Confirming theoretical predictions that catastrophic self-focusing is absent, two important experimental checks are then reported. We present in Section 4 the results of a series of carefully controlled experiments in which intrinsic bulk damage in alkali halides was measured. A well-characterized TEM<sub>00</sub> mode laser beam with total power more than one order of magnitude below calculated critical powers for self-focusing was tightly focused within the samples in order to obtain the high intensities needed for damage. Then, in Section 5 we show how the experimental results can be fully explained in terms of avalanche breakdown.

## 2. The Lasers and Beam-Handling Optics

Figure 1 shows schematically the principal features of the laser damage source. The experiments were performed using a pulse pumped, electro-optically Q switched, Nd:YAG, or ruby laser. Some important properties of these devices are summarized in table 1. Figure 2 shows that the Nd:YAG laser output was in the lowest order Gaussian or TEM<sub>00</sub> mode.

The time structure of the pulses from both lasers appears reasonably smooth when viewed with a fast photodiode oscilloscope combination having a measured risetime of 0.5 nsec. We have conducted Fabry-Perot studies on the ruby output and have found that normally fewer than four adjacent modes are oscillating simultaneously, so that at least with the ruby, the time structure is effectively fully resolved. Longitudinal mode selection is accomplished by aligning the faces of plane parallel laser rods parallel to the resonator mirror. Despite the low reflectivity of the anti-reflection coated rod surfaces, the high gain of the rod and the high reflectivity of the rear mirror create an effective resonant reflector.

To verify that the transverse mode structure on axis is constant with time, the centers of the beams were sampled with a 25-micron pinhole and found to have the same time structure as the entire beam. The stability on axis was found to be superior to stability of the spatially integrated power.

The breakdown data was taken by focusing through a  $\frac{1}{2}$ -inch focal length lens to approximately 2 mm inside the samples. Care was taken to insure that spherical aberrations from both the lens and the plane entrance surface of the sample being tested were unimportant. A fast photodiode was used to monitor the transmitted light, and an energy monitor recorded the energy in each laser pulse.

Table 1. Laser parameters

Wavelength	Nd:YAG 1.06 $\mu$ m	Ruby 0.694 $\mu$ m
Energy TEM <sub>00</sub> Mode	1.5 mJ	2.0 mJ
Beam Diameter at Output Mirror TEM <sub>00</sub> Mode	0.8 mm	0.7 mm
Polarization	Linear	Linear
Pulse Repetition Rate	1 pps	1 pulse/5 sec
Pulse Duration in TEM <sub>00</sub> Mode	4.7 nsec (FWHP)	14 nsec (FWHP)
Pulse to Pulse Energy Reproducibility	$\pm 7\%$	$\pm 10\%$

The combination of one rotatable and one fixed polarizer resulted in a variable light attenuator which was highly sensitive, quite reproducible, and which did not affect the laser pulse's polarization, spatial distribution, or duration. If the fixed polarizer is oriented to transmit the laser polarization and if  $\theta = 0^\circ$  is the angle of the rotating polarizer which gives maximum transmission through this attenuator, then the transmitted intensity at any other angle of rotation about the beam axis is

$$I(\theta) = bI_0 \cos^4 \theta .$$

$I_0$  is the incident light intensity and  $b$  is the fraction transmitted when  $\theta = 0^\circ$ . Calibrated neutral density filters were often used in conjunction with the variable Glan attenuator.

### 3. Self-Focusing

A laser beam propagating in a transparent medium induces an increase in the index of refraction by an amount proportional to the laser intensity. At powers in excess of some critical power this non-linearity causes the intensity distribution to become unstable, and a catastrophic beam collapse results.

Self-focusing may occur as the result of a number of nonlinearities. In solids for Q-switched laser pulses the process which normally leads to the smallest value of critical power and hence dominates self-focusing is electrostriction [10]. This is the case for the alkali halides where thermal and electronic contributions to self-focusing are much smaller than the electrostrictive effect [11] and can be neglected.

An intense light wave whose power lies below a critical power  $P_c$  will not experience a catastrophic collapse in a nonlinear medium, because although focusing by self-action will always be present, diffraction acts in the opposite sense to cause divergence and dominates at such powers [10]. At powers sufficiently far below  $P_c$ , therefore, the intensity distortion due to the index nonlinearity can be treated as a constant perturbation on diffraction effects and usually neglected. These observations allow us to effectively eliminate self-focusing by restricting probe powers to well below calculated critical powers while focusing strongly by external optics to reach the field intensities necessary to cause optical damage.

Theoretical self-focusing parameters are defined and derived in the appendices where quantitative corrections from the index nonlinearity at powers below  $P_c$  are discussed. Table 2 summarizes the numerical results. The probe power is the experimental peak power on axis and is more than one order of magnitude below  $P_c$ . From a purely theoretical viewpoint, therefore catastrophic self-focusing is impossible, and it can be shown that beam distortion from the index nonlinearity introduces at most a few percent correction in the measured electric field strengths. If catastrophic self-focusing does occur, then the breakdown damage data is a measure of the critical powers rather than intrinsic breakdown field. The measured threshold intensity will then scale with the square of the calculated focal diameter if the process is steady-state and will depend on the pulse-width if the process is transient. (The diameter dependence in the steady-state results from the existence of a constant critical power  $P_c$  which does not vary with beam diameter.)

Table 2. Calculated steady-state, self-focusing parameters and experimental values of pulse-width and peak power

	Wavelength (microns)	$\tau$ ( $10^{-9}$ sec)	$t_p$ ( $10^{-9}$ sec)	$n_2 \times 10^{22}$ (mks)	$P_{cr}$ ( $10^3$ watts)	$P_c$ ( $10^3$ watts)	$P_{probe}$ ( $10^3$ watts)
	10.6*	11.0	200		48,000	175,000	120
NaCl	1.06	5.3	4.7	2.3	480	1,750	37.8
	0.69	3.94	14		204	746	20
	10.6*	22.3	200		13,200	50,000	20
RbI	1.06	10.7	4.7	8.4	132	500	6.1
	0.69	8.0	14		56	203	--

For  $P_{probe} < P_c$  catastrophic self-focusing will not occur.

\* The 10.6  $\mu$ m data is taken from E. Yablonovitch, Appl. Phys. Letters 19, 495 (1971).



To test our belief that self-focusing was absent we conducted two experiments. In the first the relative field strength threshold for damage in NaCl was measured with three different focusing lenses, corrected for spherical aberrations, and having focal lengths of 0.5, 1.0, and 1.5 inches. The experiment was conducted at  $1.06\ \mu\text{m}$ . If steady-state self-focusing were present, the observed damage threshold would have scaled with the inverse of the focal length. It did not, and, in fact, to within 5 percent the field strength was independent of focal length. This effectively eliminated the possibility of steady-state self-focusing. Since  $t_c/\tau$  was just under unity, however, self-focusing could be transient, and equation (A15) predicts the results observed. For this reason it was necessary to measure the damage threshold as a function of pulse width with the beam diameter held essentially constant.

By changing the pumping level for the YAG laser, we were able to extend the pulse width by a factor of 2.3 to 10.8 nsec. In addition, the breakdown strength at  $0.69\ \mu\text{m}$  was measured with ruby laser pulses of 14-nanosecond duration and a focused diameter 25 percent smaller than that obtained with the YAG laser. The same  $\frac{1}{2}$ -inch focal length lens was used in all three measurements, and to compute the ruby value, we assumed the same transverse intensity variation as that present at  $1.06\ \mu\text{m}$ . To within 15 percent no change was noted in the threshold field despite the pulse-width dependence in eq (16). The agreement for the ruby pulses was especially reassuring, because the critical power varies with wavelength squared. If transient self-focusing were present, we would have seen a change by a factor of 4.2 in the field strength or a factor of 18 in the measured intensity--an effect which would have been quite dramatic. A factor of 9 comes from the pulse-width dependence of the transient critical power and a factor of 2 from the wavelength dependence.

Perhaps the best experimental check for self-focusing is the actual measurement of breakdown strengths. Self-focusing theory appears to be totally unable to account for the experimental results given below in which both relative and absolute values of breakdown strengths show striking similarities to  $10.6\ \mu\text{m}$  values. We thus conclude that prior to the onset of material damage, self-focusing has been effectively eliminated as a competing nonlinearity.

The possibility may exist that self-focusing by a mechanism other than electrostriction will be effective after a sufficient number of electrons have been generated to cause intense local heating of the sample. Evidence for such an effect has been observed with gas breakdown [12], but the results are not entirely unambiguous. While theoretical arguments can be given against such an effect, it is sufficient to note that our experimental findings indicate that any late developing nonlinearity is unimportant in our measurements.

#### 4. Experimental Measurements of Breakdown

##### 4.1 Damage Measurements at 1.06 Microns

To measure the breakdown strengths of the alkali halides, we focused the laser beam approximately 2mm into each sample and recorded the number of laser pulses necessary to produce internal damage at various power levels. In every case where damage occurred, a white spark was produced, and the damage was later carefully inspected with a microscope. Because of the small volume damaged by our highly focused  $1.06\ \mu\text{m}$  pulses (less than  $2 \times 10^{-3}\text{mm}^3$ ), a large number of data points could be taken with each sample (40 to 100).

Defining threshold as that value of incident power necessary to produce intrinsic damage in a single shot for 50 percent of the positions probed [4], we calculated the r.m.s., on-axis electric field at the measured threshold in NaCl. Corrections were made for reflections from various surfaces and the changes in the beam diameter due to the effect of the index nonlinearity. This was the basic calibration, and all other values of threshold were measured relative to  $E_{\text{NaCl}}$ . In order to avoid errors from daily power fluctuations and possible alignment changes, a single sample of NaCl was tested with each alkali halide. It was readily determined that a slight misalignment of the focusing lens ( $\frac{1}{2}$ -inch focal length) had no measurable effect on the relative breakdown strengths.

Visual inspection and the breakdown statistics suggested that spatial inhomogeneities from inclusions were not affecting the results except in the single case of RbCl. Damage which we regarded as intrinsic consisted at each damage position of a single pointed region which began at the geometrical focus and extended a very short distance back toward the laser, increasing in cross-section to give a tear-drop appearance. A typical example is indicated in figure 3. In RbCl, on the other hand, regions with low breakdown thresholds consisted typically of one or more spherical voids randomly distributed about the focus (figure 4). A number of points, however, did appear visually to have intrinsic damage and were consistently more difficult to breakdown. These data points were used for the RbCl results.

Finally, a fast photodiode detector system with a 0.5 nsec risetime monitored the transmitted light as shown in figure 5 and was used to confirm threshold levels in NaCl and KCl as well as to establish the approximate time structure and stability of the laser output.

Values for the breakdown field obtained at 1.06  $\mu\text{m}$  are summarized in figure 6 and in table 3 along with both the 10.6  $\mu\text{m}$  data collected by Yablonovitch [4] and accepted d.c. results [9]. These results are normalized to the respective values of field necessary to damage NaCl. The breakdown fields for NaCl are listed in table 4. This allows the striking similarity in trend of breakdown field to be easily observed and the possible systematic deviations at 1.06  $\mu\text{m}$  to be easily recognized. The quoted errors at 10.6  $\mu\text{m}$  are  $\pm 10$  percent, and our random experimental errors in relative fields are estimated to be no more than  $\pm 10$  percent with possible errors due to microscopic strains adding another  $\pm 5$  percent. For NaCl and KBr two different samples from two different manufacturers gave nearly identical results.

Table 3. Relative breakdown fields - normalized to  
 $E_{\text{NaCl}} \approx 2 \times 10^6 \text{ V/cm}$

	NaI	NaBr	NaCl	NaF
DC	0.460	0.553	1	1.60
10.6 $\mu\text{m}$	0.405	0.476	1	----
1.06 $\mu\text{m}$	(0.293)*	0.675	1	1.78
	KI	KBr	KCl	KF
DC	0.380	0.460	0.667	1.27
10.6 $\mu\text{m}$	0.369	0.482	0.713	1.23
1.06 $\mu\text{m}$	0.272	0.375	0.568	----
	RbI	RbBr	RbCl	
DC	0.327	0.387	0.553	
10.6 $\mu\text{m}$	0.323	0.400	0.472	
1.06 $\mu\text{m}$	0.400	0.550	0.670	

\* Crystal was extremely hygroscopic and no final check was made with the microscope to determine if inclusions were responsible for the damage observed.

Table 4. Absolute breakdown strength of NaCl

$E_{\text{peak}}(\text{dc})$	$1.50 \times 10^6 \text{ V/cm}$	
$E_{\text{rms}}(10.6 \text{ microns})$	$1.95 \times 10^6 \text{ V/cm}$	$\pm 10 \text{ Percent}$
$E_{\text{rms}}(1.06 \text{ microns})$	$2.3 \times 10^6 \text{ V/cm}$	$\pm 20 \text{ Percent}$
$E_{\text{rms}}(0.69 \text{ microns})^*$	$2.2 \times 10^6 \text{ V/cm}$	$\pm 20 \text{ Percent}$

\* Gaussian profile assumed.

A 4 percent correction is incorporated into the 0.69 micron value because of equation (A12) in the text. The data at 1.06 microns, however, is transient as seen from table 2. Equation (A15) is therefore used to evaluate  $P_{\text{cr}}$  and a 1.8 percent correction determined from (A12).

Careful statistics for variations in the breakdown strength were collected on NaCl because of the high quality of the two samples we obtained. It was found that, accounting approximately for experimental uncertainties, the process appeared threshold-like. For the other samples larger fluctuations were noticed, but the sample qualities were somewhat inferior to that of NaCl. Experimental uncertainties are considered to result from surface imperfections, internal strains, and laser fluctuations. No measurement of any probabilistic nature to breakdown was made.

Some evidence for intrinsic fluctuations, however, was found by monitoring the light transmitted through the samples. On several occasions a laser pulse produced damage in the same position where a more intense pulse one second before had been focused without damaging the sample. While these observations may have resulted from unresolved time-structure in the second laser pulses, the same observations

were made at ruby wavelength where Fabry-Perot studies indicated that the pulses were normally free of such fluctuations.

#### 4.2 Damage Measurements at 0.69 $\mu\text{m}$

The breakdown strength of NaCl was also measured with a ruby laser. Table 4 records the average of about 50 damage measurements. Although the laser was normally operating in a single longitudinal mode as indicated by Fabry-Perot and photodiode studies, each laser shot during the measurement was monitored with a fast photodiode and recorded.

In figure 7 time-resolved photographs of transmitted light indicate the sudden attenuation normally seen for laser pulses which caused damage. Because of the smooth time-structure of most of the pulses, we are able to record a few cases in which the instant of first attenuation, considered to be the onset of material damage, occurred after the peak of the laser pulse had passed. An example is given in figure 7c. The same effect was observed at 1.06  $\mu\text{m}$ . This may be explained both by invoking a statistical model for breakdown [13] or by the considerations of a time-dependent avalanche discussed in the next section.

### 5. Discussion of Results

#### 5.1 Bulk Damage

The experiments reported here were performed under carefully controlled conditions using stable, well-characterized lasers and optical systems for which aberrations were unimportant. Because we were able to probe each sample in many different positions, random fluctuations in breakdown strength were averaged out. It was possible to distinguish between inclusion and intrinsic damage by inspection of the residual damage and to correct for the effects of inclusions in the one material for which they were important. In addition, experimental tests showed that catastrophic self-focusing was absent and, consistent with theory, that the index nonlinearity did not affect the results to within experimental error. It is therefore concluded that the results of the 1.06 and 0.69  $\mu\text{m}$  study as summarized in figure 6 and table 4 represent accurate measurements of intrinsic bulk damage.

Because the techniques of this study are virtually identical to those of reference 4, direct comparison can be made to breakdown strengths at 10.6  $\mu\text{m}$ . It has already been observed that the damage thresholds for the alkali-halides at 1.06  $\mu\text{m}$  follow a trend nearly identical to that observed with the  $\text{CO}_2$  laser and, in fact, to the d.c. measurements of reference 9. It thus appears that the intrinsic process of laser-induced damage for the alkali-halides has the same fundamental character as both a.c. damage in the infrared and d.c. avalanche breakdown. Moreover, the consistency of the absolute breakdown strengths at 0.69  $\mu\text{m}$  suggests that this same process dominates at frequencies as high as  $4.3 \times 10^{14}$  hertz.

Additional support for an avalanche mechanism comes from three experimental observations concerning the time-structure of the laser probe pulses. The first is that increasing the pulse-width of the YAG laser output by a factor of 2.3 resulted in a 14 percent average drop in threshold intensity for NaCl. Averages were taken at about 20 shots at each pulse width. This change, though small, is probably real, because the test was made on a single sample of high-quality NaCl and thereby avoided a major source of experimental uncertainties arising from material variations. The second observation, noted at both 1.06 and 0.69  $\mu\text{m}$ , is that high-frequency time-structure on the pulse has little measurable effect on the breakdown strength. And finally, after adjusting the power level so that damage occurred regularly near the top of the laser pulses, the probe intensities were increased by a factor of about three by changing the beam attenuation. When this was done, the intensity at which the transmitted light dropped (cf. figure 7) was higher by 15 percent or more than it had been with the lower intensity pulses. This was determined to mean that increasing the effective risetime of the optical field raises the measured breakdown strength. To understand both this set of observations and the results from table 4, some discussion of existing electron avalanche theories [7, 14] is given.

An electron avalanche in solids is a rapid multiplication of conduction-band electrons in which an initially low density  $N_0$  of free carriers interacts with an intense electric field in the presence of phonons. When the electric field reaches a critical value, the number of electrons increases with time approximately as

$$N(t) = N_0 \exp \left[ \int_0^t \alpha(E) dt \right].$$

The gain coefficient  $\alpha(E)$  is a strongly varying function whose value can be inferred from d.c. measurements of breakdown strength as a function of sample thickness for extremely thin specimens [15]. Lattice disruption then results from joule heating.



Two important conclusions develop from such an analysis. The first is that the entire process of avalanche and damage involves energy exchange between the field and the material which is approximately described by the well-known formula for a.c. conductivity

$$\frac{dW}{dt} = \frac{Ne^2\tau}{m(1 + \omega^2\tau^2)} E^2 \quad (1)$$

where  $N$  is the time-dependent electron density,  $\omega$  the angular frequency, and  $\tau$  the characteristic relaxation-time determined principally from phonon collisions. While this precise form of the conductivity may not be correct for polar materials such as the alkali-halides, we will use it to qualitatively describe breakdown for high frequencies.

Because of eq (1), energy input to the material scales with frequency and field as  $E^2/(1 + \omega^2\tau^2)$ , and because the details of energy input determine the electron distribution function and hence  $N(t)$ , the threshold for damage will scale in the same manner. This justifies the use of root-mean-square fields in table 4. It also indicates that the a.c. breakdown strength will increase for frequencies near  $1/\tau$ . Calculation of  $\tau$  for NaCl [15] indicates that frequency dispersion should begin to occur somewhere near that of the ruby laser.

The second relevant conclusion from an analysis of avalanche breakdown is that if insufficient time exists for the electron density to reach values necessary to damage, then damage will not occur even though electron recombination losses have been exceeded and an electron avalanche is underway. Damage will only be produced when the field is subsequently raised above the steady-state breakdown strength and the gain coefficient  $\alpha$  is correspondingly increased. Such an effect has been observed in d.c. experiments by varying the duration of constant applied fields [16] and by measuring threshold fields for samples of thickness less than about 100  $\mu\text{m}$  [17], where transit effects limit the build-up time. When the time available for the build-up of the avalanche is reduced below about 50 ns, larger fields are needed to damage.

The experiments of reference 16 give a useful comparison to our work. It was found that when the applied d.c. field duration was reduced to 10 ns, the breakdown strength of NaCl increased to  $2.1 \times 10^6$  volts/cm. Because our laser pulses had durations of about 10 ns, the discrepancy in absolute field strengths between optical and d.c. measurements may be fully explained. In addition, the field dependence of  $\alpha(E)$  in NaCl is qualitatively correct to explain our observations of the pulse-width dependence to breakdown, the insensitivity of threshold to fast-time structure, and the increase in breakdown strength for rapidly rising pulses. It also indicates that when approximate corrections from pulse-width considerations are made and experimental uncertainties ignored, the ruby laser threshold is a few percent greater than the threshold at 1.06  $\mu\text{m}$ .

The essential details of the breakdown studies reported here are thus fully explained by the process of avalanche breakdown.

## 5.2 Implications For Surface Damage Studies

Surface damage is often a practical problem in the operation of high-power lasers. For this reason a number of investigations of surface breakdown [13, 18], have been made with the aim of elucidating the conditions and mechanisms of surface damage. The techniques of the studies reported here may provide a valuable tool for understanding surface damage by allowing direct comparison to bulk damage thresholds. This comparison can be made by focusing a low-power laser beam first on a surface and then about 2 mm into the bulk. Because focusing problems are much less severe in the bulk and damage from inclusions can apparently be distinguished by visual observation, a stable and repeatable reference exists for surface studies. Careful investigation should help elucidate, in particular, the mechanisms responsible for surface damage under various conditions of surface preparation.

## 6. Conclusions

Careful measurements of laser-induced bulk damage have been made in ten alkali-halides without the confusing effects of self-focusing. Comparison of the results to studies at d.c. and 10.6  $\mu\text{m}$  indicated that the process of a.c. avalanche breakdown, similar in fundamental character to d.c. avalanche breakdown, is responsible for the damage observed. Analysis of time-related observations confirm this conclusion.

## 7. Acknowledgments

The skillful assistance and advice of D. Bua and S. Maurici are gratefully acknowledged. We are also indebted to Prof. N. Bloembergen for valuable discussions of breakdown theory.

To demonstrate the claim that the relative balance between diffraction and self-focusing effects is set at the entrance plane for a general steady state nonlinearity, we calculate the curvature of the ray path from a modified, eikonal equation formalism that incorporates both diffraction effects and the steady-state nonlinearity [19]. Its applicability is restricted to beams with diameters  $2a$  much less than a wavelength -- a condition fulfilled in our experiments.

Writing the electric field vector  $\vec{E}(\vec{r})$  as  $\vec{A}(\vec{r}) \exp i [k_0 \phi(\vec{r}) - \omega t]$  where  $k_0 = \omega/c$  and the index nonlinearity is  $n_2 A^2$  and ignoring terms of order  $n_2 A^2 / n_0$ , we can write Maxwell's equations in the simplified form

$$[(n_0 + n_2 A^2)^2 - (\text{grad } \phi)^2] \vec{A} + \frac{1}{k_0^2} \nabla^2 A = 0.$$

If the scalar product of this equation is taken with  $\vec{A}$ , a term containing the factor  $1/k_0^4$  dropped and a cross term with  $n_2 A^2$  neglected, this leads directly to an effective eikonal equation

$$n_1^2 - (\text{grad } \phi)^2 = 0 \quad (\text{A1})$$

where

$$n_1 = n_0 + n_2 A^2 + \frac{1}{2k_0^2 n_0} \frac{\nabla^2 A}{A}. \quad (\text{A2})$$

In the limits of zero nonlinearity, and infinitesimal wavelength, this is just the basic equation of geometrical optics. Results derived from the usual eikonal equation [20] can now be used with the index of refraction replaced by eq (A2). In particular, the curvature  $d^2 \vec{r} / d\rho^2$  for a pencil of rays with position vector  $\vec{r}$  and with  $\rho$  the coordinate along the ray path is given by

$$d^2 \vec{r} = \frac{1}{n_1} \left[ \text{grad } n_1 - \frac{dn_1}{d\rho} \frac{d\vec{r}}{d\rho} \right] \quad (\text{A3})$$

Equation (A3) can be simplified by restricting the treatment to cylindrically symmetric beams and by assuming that the maximum ray slope is small compared to unity. (In our experiments the maximum slope inside the sample and before the focus is less than 0.05.) Both the second term on the right in eq (A3) and the longitudinal component of the Laplacian in eq (A2) are negligible. The curvature is now expressed in a form first derived by Talanov [21].

$$\frac{d^2 \vec{r}}{d\rho^2} \approx \frac{d^2 \vec{r}}{dz^2} = \frac{1}{n_1} \text{grad}_\perp n_1.$$

This result is important to the study of self-focusing effects because the sign of  $d^2 \vec{r} / dz^2$  indicates whether or not the beam is converging and its magnitude is a quantitative measure of that convergence or divergence. A positive curvature results in an increase in the slope of the ray path with respect to the propagation direction and thus represents a divergence from the axis. Diffraction alone will produce a positive curvature in an isotropic medium. A negative curvature, on the other hand, will cause convergence of the beam towards the axis and indicates the dominance of the self-focusing nonlinearity.

$A^2(\vec{r})$  is proportional to the light intensity, and where the beam propagates with little or no change in shape, the intensity is equal to the power in the beam divided by the beam area  $\pi a^2(z)$ . Let  $p$  be an effective power which absorbs these proportionality constants including the factor  $\pi$  in the beam area. This effective power has, in fact, a functional form -- it may be Gaussian ( $\exp[-2r^2/a^2]$ ) for example -- and it is this functional form which describes the beam shape. We can therefore consider  $p$  to be a function of a radial variable which is independent of beam size. Defining the coordinate  $x$  as  $x = r/a(z)$ , we can write

$$A^2(\vec{r}) = \frac{p(x)}{a^2(z)} = \frac{\text{effective power}}{\text{beam area}} \quad (\text{A5})$$

Equation (A5) is normally assumed in numerical calculations and has been referred to as the "constant shape approximation" [22]. Along with eq (A4) it provides the basic relationships to calculate the critical power, the self-focusing length, and the quantitative influence of the index nonlinearity when diffraction dominates.

By expanding  $\nabla_{\perp}^2$  in cylindrical coordinates  $r$  and  $z$  it is easily seen that  $\nabla_{\perp}^2 A/A$  is also proportional to  $a^2$ . We can then write eq (A2) as

$$n_1 = n_0 + \frac{1}{a^2(z)} f(x)$$

where  $f(x)$  is the sum of contributions from both diffraction and the index nonlinearity. Since  $\text{grad}_{\perp}$  is just  $a(z)^{-1}[\partial/\partial x]$ , and since  $n_1$  in the denominator of eq (4) can be replaced by  $n_0$ , the derivative of  $f(x)$ , which contains no dependence on  $z$ , determines the relative importance of diffraction and self-focusing. Once this relative importance is determined for one value of  $z$ , such as  $z = 0$  at the entrance plane, it is determined for all  $z$ .

For completeness we write eq (A4) in the final form

$$\frac{d^2 r}{dz^2} = \frac{1}{n_0} \frac{1}{a^3(z)} \frac{d}{dx} [f(x)] \quad (\text{A7})$$

where, using (A5),

$$f(x) = n_2 (aA)^2 + \frac{1}{(2A)} \left[ \frac{d^2 (aA)}{dx^2} + \frac{1}{x} \frac{d(aA)}{dx} \right] \quad (\text{A8})$$

The importance of neglected terms can be determined for a particular beam shape and has been shown to be negligible [19] except near a catastrophic self-focus or under experimental condition where extreme external focusing is used.

The critical power  $P_c$  is in principle calculated from the requirement that the derivative  $f(x)$  vanish for all  $x$ , leading to a detailed balance of self-focusing and diffraction. Since  $f(x)$  contains no dependence on beam diameter, the critical power will not be dependent on beam diameter for a steady-state nonlinearity.

## Appendix B

The index nonlinearity leads to intensity distortions even below the critical power for catastrophic self-focusing. Using the results of Appendix A quantitative corrections from the nonlinearity can be derived.

In eq (A7)  $r$  is replaced by  $x a(z)$  and a new function  $g(x)$  defined. This gives

$$\frac{d^2 a}{dz^2} = \frac{1}{a^2(z)} g(x) \quad (\text{A9})$$

where

$$g(x) = \frac{1}{n_0 x} \frac{d}{dx} f(x). \quad (\text{A10})$$

If eq (A9) is multiplied by  $dz(da/dz)$  and integrated, we find

$$\left(\frac{da}{dz}\right)^2 = - \frac{g(x)}{a^2} + c. \quad (\text{A11})$$

Considerable simplifications results from expanding  $A^2$  and therefore  $g(x)$  about small  $x$  and retaining terms to order  $x^2$ . In reference 2 this expansion is carried out for a Gaussian beam. We can investigate the geometrical focus at low powers by setting the derivative in eq (A11) equal to zero [6]. After some manipulation the focal diameter  $d$  is evaluated in terms of  $d_0$ , the diameter in absence of a nonlinearity. In particular,

$$d = d_0 (1 - P/P_{cr})^{\frac{1}{2}} \quad (\text{A12})$$



where  $P$  is the full power in the beam and  $P_{cr}$  is given in cgs units by

$$P_{cr} = \frac{c\lambda^2}{32\pi n^2} \quad (A13)$$

The result (A12) is useful for  $P/P_{cr}$  less than about 0.5. The calculated on-axis intensity at breakdown must be multiplied by a factor  $(d_0/d)^2$  to approximately correct for the effects of the nonlinearity.

More extensive analysis shows that  $P_{cr}$  is the critical power for self-focusing near the center of a Gaussian beam [22]. For input powers greater than  $P_{cr}$  but less than  $P_c$ , diffraction dominates everywhere except near the beam center. A collimated beam will initially intensify at such powers until the diffraction of the wings causes the on-axis intensity to drop.  $P_{cr}$  differs from  $P_c$  because the latter is a quantity averaged over the entire beam while  $P_{cr}$  is determined by the behavior near the center. In fact,  $P_c$  is not a precisely defined quantity because it is not possible to exactly balance diffraction and self-focusing over the entire beam cross-section. At an input power of  $P_c$ , therefore, a propagating beam will not change its size measurably and so not experience a catastrophic self-focus, but its intensity distribution will be distorted.  $P_c$  has the same functional form as  $P_{cr}$  and differs by just a numerical factor as  $P_{cr} = 0.273 P_c$  for Gaussian beams.

### Appendix C

The analysis of Appendix A and the results derived from it are correct only in the steady state. In solids the dominant nonlinearity is normally electrostriction, and if the process is transient, it is no longer true that the relative balance between diffraction and self-focusing is independent of propagation distance and that the critical powers are independent of beam diameter. The changes occur because electrostriction becomes non-local in both a temporal and a spatial sense. Although a susceptibility approach such as we have used is no longer strictly correct, it is nonetheless useful for establishing functional dependences for self-focusing parameters and approximate quantitative values.

For our experiments two results from a transient analysis are important [23]. The first is that transient effects decrease the effective nonlinear index  $n_2$  and thus make self-focusing more difficult. If we wish to avoid self-focusing by restricting our powers to well below the critical power, the steady-state analysis gives us a lower bound on  $P_c$ . Being in a transient regime can, therefore, only increase our margin of safety and improve the accuracy of our experiment by making the corrections indicated by eq (A12) less important.

The second important result involves the dependence of the critical power on laser pulse-width and on beam diameters. In the steady state the nonlinear index  $n_2$  is given by [10]

$$n_2 = \frac{n_o(\rho) \frac{\partial n_o}{\partial \rho}}{4\pi\rho v^2}$$

where  $n$  is the index of refraction in the absence of the nonlinearity,  $\rho$  is the material density, and  $v$  is the acoustical sound velocity. The quantity  $(\rho \frac{\partial n_o}{\partial \rho})$  for cubic materials such as the alkali-halides may be found approximately by differentiating the Clausius-Mosotti equation. The remaining constants are tabulated in handbooks.

When the laser pulse width  $t_p$  is shorter than the electrostrictive response time  $\tau = a/v$ ,  $n_2$  is decreased in value, thereby increasing the critical power. For a triangular pulse, Kerr [13] has shown that

$$(n_2)_{transient} = (n_2)_{steady-state} [1 - \frac{a}{v\rho} D(\frac{v\rho}{a})] \quad (A14)$$

where  $D(\frac{v\rho}{a})$  is Dawson's integral with

$$D(\xi) = \exp(-\xi) \int_0^\xi \exp \eta^2 d\eta.$$

When  $t_p \lesssim \tau/2$ ,

$$(n_2)_{\text{transient}} \approx k(n_2)_{\text{steady state}} \frac{v^2 t_p^2}{a^2}.$$

This result is valid for more general and realistic pulse-shapes with the numerical constant  $k$  being of order unity and having a value dependent on the precise time-structure of the pulse. When this result is inserted into eq (A13), the critical power becomes

$$P_c \frac{t_p}{\tau} \lesssim \frac{1}{2} = (P_c)_{\text{steady state}} \frac{a^2}{k v^2 t_p^2}. \quad (\text{A15})$$

For short laser pulses, therefore, there exists more properly a critical intensity rather than a critical power, and in this transient regime fairly small changes in pulse-width will have a significant effect on the critical power.

## 9. References

- [1] Zverev, G. M. et al., Zh. Eksp. Teor. Fiz. 53, 1849 (1967) [Sov. Phys. JETP 26, 1053 (1968)].
- [2] Akhmanov, S. A. et al., Usp Fiz Nauk. 93, 19 (1967) [Sov. Phys. Uspekhi 10, 609 (1968)].
- [3] Hellwarth, R. W., in Damage in Laser Materials, edited by A. J. Glass and A. H. Guenther, NBS Spec. Publ. 341 (U. S. Dept. of Commerce, Wash., D. C., 1970), p. 67.
- [4] Yablonovitch, E. Appl. Phys. Lett. 19, 495 (1971).
- [5] Keldysh, L. V., Zh. Eksp. Teor. Fiz. 47, 1945 (1964) [Sov. Phys. JETP 20, 1307 (1965)].
- [6] Zverev, R. M. and Pashkov, V. A., Zh. Eksp. Teor. Fiz 57, 1128 (1969) [Sov. Phys. JETP 30, 616 (1970)].
- [7] For a review, see J. J. O'Dwyer, The Theory of the Dielectric Breakdown of Solids (Oxford University Press, London, 1964).
- [8] Giuliano, C. R. and Marburger, J. H., Phys. Rev. Lett. 27, 905 (1971).
- [9] Von Hippel, A., J. Appl. Phys. 8, 815 (1937).
- [10] Akhmanov, S. A., Sukhorukov, A. P., and Khokhlov, R. V., Sov. Phys. Usp. 10, 609 (1968).
- [11] Bloembergen, N., private communication.
- [12] Alcock, A. J., DeMichelis, Claudio, and Richardson, M. C., IEEE J. Quantum Elec. QE-6, 622 (1970).
- [13] Bass, M. and Barrett, H. H., IEEE J. of Quantum Elec. QE-8, 338 (1972).
- [14] Zverev, G. M., Mikhailova, T. N., Pashkov, V. A., and Solov'na, N. M., Zh. Eksp. Teor. Fiz. 53, 1849 (1967). [Sov. Phys. JETP 26, 1053 (1968).]
- [15] Yablonovitch, E., Thesis, Harvard University (1972).
- [16] Kuchin, V. D., Rep. Akad. Sci. USSR, 114, 301 (1957); Sov. Phys. Solid State, 1, 405 (1959).
- [17] Watson, D. W., Heyes, W., Kao, K. C., and Calderwood, J. H., IEEE Trans Elec. lus. E1-1, 30 (1965). Also, Vorob'ev, G. A. Lebedeva, N. I., and Naderova, G. S., Fizika Tverdogo Tela, 13, 890 (1971), [Sov. Phys. Solid State, 13, 736 (1971)].
- [18] Giuliano, C. R., to be published.
- [19] Wang, Chen-Show, Phys. Rev. 173, 908 (1968).
- [20] Born, M. and Wolf, E., Principles of Optics, (Pergamon Press, Inc., New York, 1959).
- [21] Talanov, V. I., Zh. Eksperim. i. Teor. Fiz. Pis'ma Redaktsiyu 2, 218 (1965) [Sov. Phys. JETP Letters 2, 138 (1965)].
- [22] Dawes, E. L., and Marburger, J. H., Phys. Rev. 179, 862 (1969).
- [23] Kerr, E. K., IEEE J. Quantum Elec. QE-6 616 (1970).

## 10. Figures

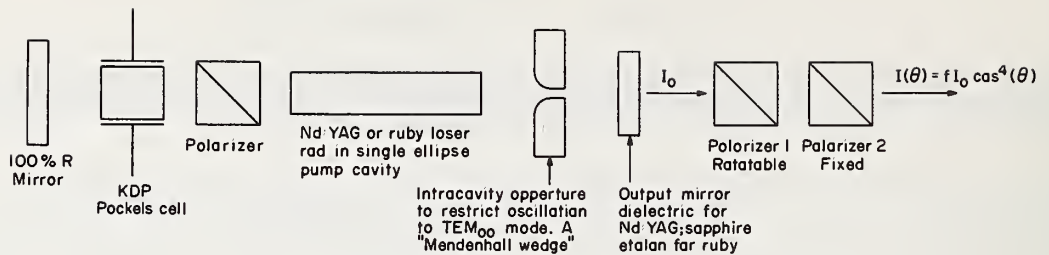


Figure 1. Laser and variable attenuator configuration for damage studies.

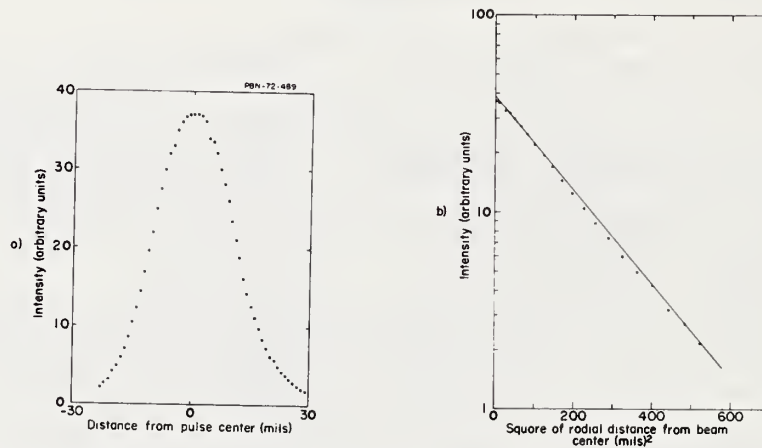


Figure 2. Intensity distribution of the YAG laser as a function of radial distance from the beam center at the position of the focusing lens. (a) The data was taken by sweeping a 1-mil aperture through the beam with each data point corresponding to a different laser shot. A small dip near the center could not be reproduced and indicates the experimental errors in the measurement. (b) By plotting the log of the intensity as a function of the radial distance squared, it was found that the output beam has a Gaussian profile  $[-2r^2/\sigma^2]$  where  $\sigma$  is measured to be  $0.485 \pm 0.005$  millimeters.

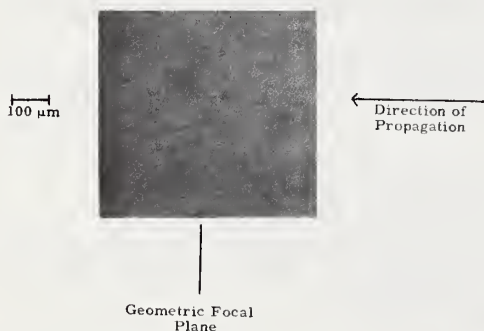


Figure 3. Intrinsic damage in RbCl. Damage which we have considered to be intrinsic had this basic shape in all the materials tested.

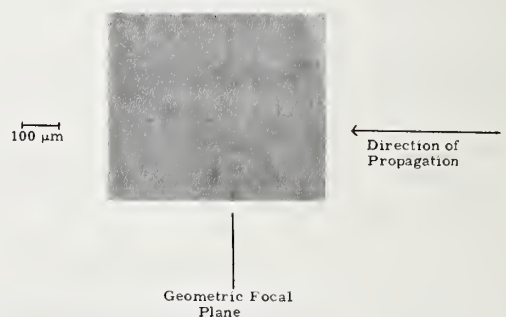
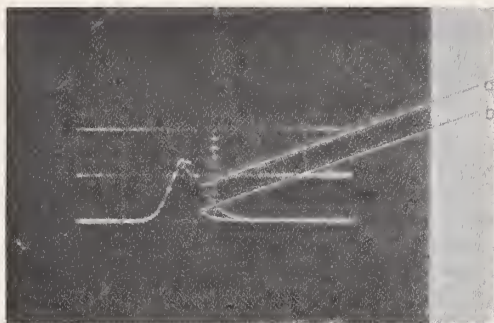


Figure 4. Inclusion damage in RbCl.





5 ns

Figure 5. Nd:YAG laser pulse transmitted through the sample. (a) No damage produced. (b) Damage produced at or just before the pulse reached its maximum intensity. These were two successive pulses in the same volume. Note that there is no evidence that the second pulse, the one which produced damage, is any different from the rest.

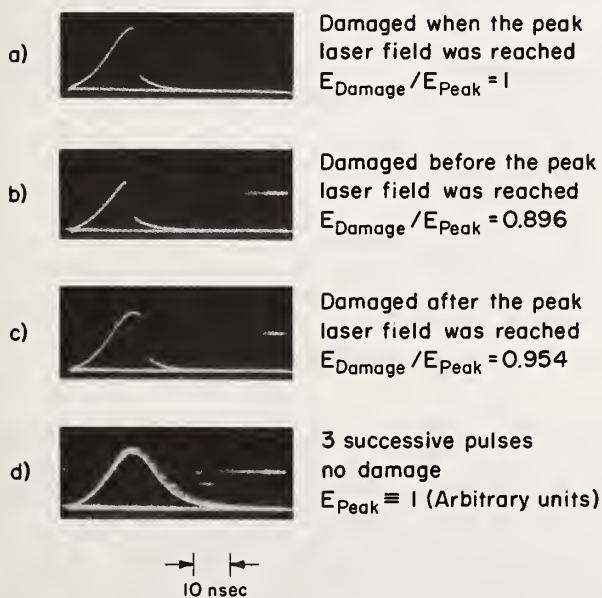


Figure 7. Ruby laser pulses transmitted through NaCl sample.

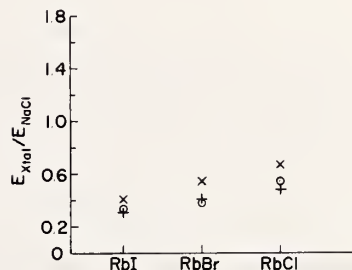
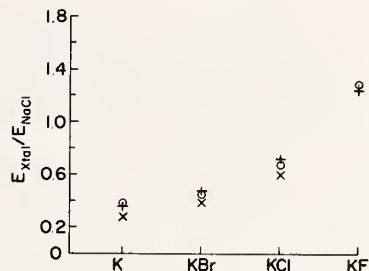
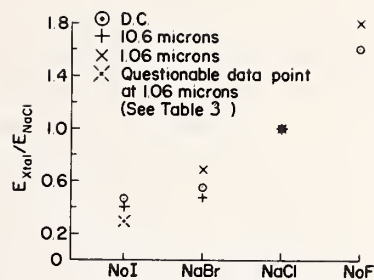


Figure 6. Comparison of breakdown strengths for various alkali halides studied at dc, 10.6 microns, and 1.06 microns. Values for 10.6 and 1.06 microns are root-mean-square field strengths and not peak fields. The data at dc is taken from reference 9 and the 10.6 micron data is taken from reference 4. (a) Relative breakdown fields for Na salts normalized to  $E_{\text{NaCl}}$ . (b) Relative breakdown fields for K salts normalized to  $E_{\text{NaCl}}$ . (c) Relative breakdown fields for Rb salts normalized to  $E_{\text{NaCl}}$ .

## Laser Induced Damage to Glass Surfaces

N. L. Boling and G. Dube<sup>1</sup>

Owens-Illinois, Inc.  
Toledo, Ohio 43651

Entrance and exit surface damage thresholds for Owens-Illinois ED-2 laser glass are measured at Brewster's angle and near normal incidence. A theory that accounts for the observed asymmetry in exit/entrance face damage thresholds is presented. The nature of the damage at both surfaces is described for both untreated and chemically strengthened ED-2 laser glass.

Key Words: Chemically strengthened glass, glass damage, glass lasers, laser damage, Q-switched, surface damage.

### 1. Introduction

This paper describes investigations of damage to glass surfaces by high power laser beams. A glass oscillator-amplifier system operating in the TEM<sub>00</sub> mode and emitting several joules in a 30 nanosecond pulse is used to damage Owens-Illinois ED-2 laser glass. Exit and entrance damage thresholds of untreated glass and of glass subjected to a surface strengthening process are reported. The reason for the difference between the entrance and exit thresholds is briefly explained.

### 2. Experimental Arrangement

The single transverse mode laser used in this study consists of an oscillator and four amplifiers. For the purposes of this paper the essential characteristics of the laser are listed in table 1:

Table 1. Laser characteristics

Transverse Mode	TEM <sub>00</sub>
Longitudinal Modes	Many (No Control)
Pulse Width	30 ns FWHM
Polarization	Linear
Time Interval Between Pulses	7 - 10 minutes
Energy Output	5 - 12 Joules
Beam Diameter at Position of Glass Sample	~ 1.8 mm
Repeatability of Energy Output	± 10%

Figure 1 shows the arrangement used to calibrate the energy density of the sample. In order to minimize any self-focusing effects the sample position was chosen to be at the waist of the focused laser beam. A specially designed 1 mm diameter aperture was placed at this chosen position in front of a thermopile. The aperture was moved across the beam until a maximum reading was obtained from the thermopile. Filters were added in the path of the beam until no plasma was detected around the aperture. This was ascertained by photographing the aperture with an open shuttered camera during the laser shot. That there was no plasma which might have interfered with the passage of the laser pulse through the aperture was further verified by changing the transmission of the filters by a given factor and noting that the energy passing through the aperture changed by the same factor. Prior to this the filters were checked

for bleaching during the laser pulse and no such bleaching was noted. Several thermopiles were checked for use in these measurements. Readings among these varied by  $\pm 10\%$ . Even recent calibration did not insure readings more consistent than this.

In summation, the possible sources of error, other than the thermopile used, in the energy density calibration described above are as follows:

1. Undetected bleaching of the neutral density filters during the laser pulse.
2. Undetected absorption of the pulse by a plasma around the aperture.
3. Positioning of the aperture off beam center.

Note that any of these errors would result in an underestimation of the energy density.

The arrangement of figure 1 was also used to monitor and control energy on the samples during damage tests, the only difference being that the aperture and thermopile were replaced by the sample. In all shots the pulse width, transverse mode, and energy out the laser were monitored. The laser was always pumped at the same level, the energy on the sample being controlled by changing filters. Because the transmission of the filters was changed in nominal steps of 10% and the repeatability of the laser output was  $\pm 10\%$ , the thresholds measured are relatively accurate to within 20%. All damage thresholds reported in this paper are based on the average energy density across the 1 mm aperture used for calibration. Calculations based on the approximately Gaussian cross section of the beam indicate peak energy densities 25% higher than these average numbers.

The occurrence of damage is defined in this report as the appearance of a visible plasma at the sample surface. Although the sample was carefully examined after each shot, no change in the surface was noted without the appearance of a plasma. Conversely, a visible change in the surface was observed with every occurrence of a plasma. This change was sometimes very minute and difficult to see, but it was always present. Thus we find the occurrence of a visible plasma is a necessary and sufficient condition for surface damage in glass.

### 3. Damage of Untreated Samples

One-half inch glass cubes of ED-2 laser glass were prepared for damage testing by polishing two opposite faces to normal commercial specifications. Several cleaning procedures were tried before settling on one which seemed to give satisfactory results. This final procedure consisted of ultrasonic cleaning in a soap and water solution, a rinse in distilled water, and cleaning in the vapors of boiling isopropyl alcohol. Final examination for cleanliness consisted of a careful visual examination under a bright microscope light. Great care had to be exercised in the cleaning process before the sample could pass this inspection. It is worth noting that these samples were much cleaner than the components of most laser systems. Nevertheless, inspection of the samples in a HeNe laser beam showed obvious non-uniformity of scattering over the cleaned surfaces. Immediately after cleaning of a particular sample damage tests were begun. For a given sample these tests typically required between 1.5 and 2 hours, the sample being subjected to pulses of gradually increasing power densities. Thus the condition of the sample was representative of surfaces in a carefully cleaned laser system.

The exit and entrance damage thresholds of 5 typical samples are given in table 2:

Table 2. Entrance and exit damage threshold for normal incidence beam

Sample	Entrance Damage Threshold J/cm <sup>2</sup>	Exit Damage Threshold J/cm <sup>2</sup>	Entrance Threshold	Entrance Threshold
			Exit Threshold	Exit Threshold
15	195 - 230	111 - 120	1.6 - 2.1	1.9
16	187 - 204	86 - 124	1.5 - 2.4	2.0
17	125 - 130	90 - 105	1.2 - 1.4	1.3
18	160 - 209	120 - 146	1.3 - 1.7	1.5
21	150 - 179	100 - 110	1.4 - 1.8	1.6



The thresholds of both surfaces vary over a wide range, the exit threshold generally lying between 80 and 120 J/cm<sup>2</sup> (2.7 - 4 GW/cm<sup>2</sup>) and the entrance between 120 and 200 J/cm<sup>2</sup> (4 - 6.7 GW/cm<sup>2</sup>). There are two plausible reasons for this wide range. First, the process which triggers the damage might be inherently probabilistic.[1]<sup>1</sup> In connection with this it should be remembered that the beam diameter used here is much larger than that used in the experiments described in [1]. Second, the condition of the surface undoubtedly plays a role in determining the damage threshold. By purposely scratching the entrance surface it is possible to cause it to damage at much lower levels than it normally would.

Damage near threshold on both the entrance and exit surfaces typically takes the form of a ring (figures 2 and 3). The diameter of this ring varies but is usually larger than the damaging laser beam, 3 mm being a nominal value. When viewed under a microscope the ring appears to be a layer of material. This material cannot be removed by hard rubbing with water or acetone. On the entrance surface the material inside the ring generally exhibits no change in appearance after damage. On the exit face a slight ripple is often seen inside the ring. Pitting is rarely seen near threshold.

Since the damage ring is larger than the laser beam, it is obvious that it is due to the plasma which accompanies damage and not to the laser beam. This plasma normally spreads over the surface to a distance of several millimeters from the beam center. Aside from the ring structure, a slight permanent darkening of the glass surface is often seen several mm from the area irradiated by the laser beam. This again is due to the plasma.

Events leading to the ring deposition were theorized to be as follows: A plasma is formed in the area exposed to the laser beam. The temperature of this plasma in its incipient stage is 10<sup>4</sup> - 10<sup>5</sup> K.[2] The plasma expands, remaining in close contact with the surface, until it becomes cool enough for its components to condense on the cooler surface. Thus the ring is a condensation of certain components of the plasma. If we assume this explanation is correct, the ring should be rich in the most volatile component in the glass surface, whether this be from the polishing compound or the glass per se.[3] In the case of ED-2 laser glass, the most volatile compound is Li<sub>2</sub>O. In order to test this hypothesis an elemental analysis of the ring was made using Auger spectrometry. Compared with undamaged glass, the only element detected in excess in the ring was lithium.

#### 4. Ion Exchanged Samples

Since some theories of surface damage involve mechanical breakage, a strengthening of the surface presents itself as a possible method of increasing resistance to damage. We have used an ion exchange process on ED-2 glass to examine this approach. In this process lithium atoms in the surface are replaced by sodium atoms. This results in a "crowding" of atoms on the surface, leading to a surface compression layer. In the work described here this layer is about 200 microns deep. Glass so treated exhibits greatly increased mechanical strength.

No experimentally measurable increase in the damage threshold was noted for these ion exchanged samples. However, the characteristics of the damage are quite different from that seen on untreated glass. The damage is initially much like that described above for the untreated samples. In particular, the ring structure is present immediately after the damaging shot. Within a few minutes after the shot no damage can be seen inside this ring. However, over an extended period of time, ranging up to two days, the surface inside the ring often gradually develops a tessellated pattern. Figures 2 and 4 show respectively exit damage a few minutes and one day after the occurrence of damage. Out of fifteen damage sites examined on ion exchanged samples, eight exhibited this cracking phenomenon. The same thing is sometimes seen on untreated samples but much less often and only after exposure to very high power levels. For example, out of thirty damage sites on untreated samples only two showed tessellation.

It is of interest to note that cracking of the surface is due to the hot plasma and not the laser pulse. These cracks often fill the interior of the several millimeter diameter ring, but they never extend outside the ring. This is consistent with the theory presented above explaining the origin of the ring. The plasma inside the ring is hot enough to cause cracking of the surface, while outside the ring it has cooled to the point where it no longer causes damage. This cooling might in part be attributable to the partial condensation of the plasma as the ring forms.

---

<sup>1</sup>Figures in brackets indicate the literature references at the end of this paper.

A possible reason why ion exchanged glass exhibits delayed failure to a greater extent than does untreated glass is that the thermal expansion coefficient of a glass is a strong function of the quality and quantity of its alkali content. A sodium containing glass has a greater coefficient than the same glass with lithium. Thus heating the Na rich surface of an ion exchanged sample results in much greater stresses than in the case of an untreated Li containing surface. Still another and perhaps more plausible reason for the delayed failure in strengthened glass is the difference between stress in the surface layer and stress in the glass immediately below the surface. This stress difference could be increased greatly through the heating by the plasma and subsequent cooling.

## 5. Relation Between Entrance and Exit Damage Thresholds

In the 4th column of table 2 are listed the ranges of possible ratios of entrance to exit damage thresholds based upon the numbers in columns 2 & 3. In the 5th column the averages of these ranges are given. Although these averages vary, because of the variation of the thresholds themselves, they are balanced about a ratio of approximately 1.5.

The reason for the asymmetry in the exit and entrance damage thresholds has been a subject of speculation for several years, asymmetric plasma growth,[4] and stimulated Brillouin scattering being examples of hypotheses which have been presented in explanation. This asymmetry can, however, be quantitatively and qualitatively explained in terms of Fresnel reflections from the surfaces.[5] At the entrance face the reflected wave is  $\pi$  radians out of phase with the incident wave, resulting in electric field at the entrance surface lower than the electric field of the incident laser beam. At the exit surface the reflected wave is in phase with the incident wave, thereby leading to an increased electric vector at the surface. The ratio of the powers at the two surfaces is given by:

$$\frac{[E_{\text{exit}}]^2}{[E_{\text{ent.}}]^2} = \frac{4n^2}{(n+1)^2} \quad (1)$$

where  $n$  is the index of refraction of the glass. For ED-2,  $n = 1.55$  and the ratio of eq (1) is 1.48, in good agreement with the data of table 2.

If the above explanation of exit and entrance damage asymmetry is correct, then there should be no difference between the entrance and exit damage thresholds of samples whose faces are at Brewster's angle to an appropriately polarized laser beam, since no reflection waves occur in this case. Several glass samples were subjected to this test and no experimentally determinable difference between entrance and exit thresholds was found. Table 3 shows this:

Table 3. Entrance and exit damage threshold for beam incident at Brewster's angle

Sample	Entrance Damage Threshold J/cm <sup>2</sup>	Exit Damage Threshold J/cm <sup>2</sup>	Entrance Threshold	Entrance Threshold
			Exit Threshold	Exit Threshold
B	105 - 120	92 - 117	0.9 - 1.0	1.0
E*	52 - 57	57 - 60	0.9 - 1.0	1.0
F	83 - 88	83 - 88	0.9 - 1.0	1.0
G	112 - 130	112 - 130	0.9 - 1.2	1.1

\*This sample was observed to have poor surface quality.

This hypothesis is also satisfying from a phenomenological point of view. It is reasonable to assume that the strength of the electric field at a surface is related to damage at that surface. Further, these results emphasize the importance of paying attention to what is happening at the surface of interest in measurements of damage threshold. The true damage threshold is not necessarily given by the energy density in the incident laser beam, but rather must be calculated for the surface under investigation. In the case presented here the calculation is straightforward. In the case of dielectric coatings, for example, the calculations can be more involved.



Finally, it should be pointed out that Fresnel reflections explain only the difference in damage threshold between the entrance and exit surfaces. The development of damage after the threshold is reached is itself asymmetrical, the exit surface being prone to pitting and the entrance surface to less extensive damage. Further work is needed to explain this asymmetry but is quite possible that it can be explained by an extension of the reflection theory presented above.

## 6. Conclusions and Discussions

The surface damage thresholds given in this paper for untreated glass are generally higher than reported by other investigators working with glass. Care has been taken to insure that these thresholds are not falsely high. Any source of error in the measurements tends to make the actual values larger than those given herein. These relatively high thresholds could be due to the laser used in their measurement. For example, it has been reported that the surface damage threshold in some instances appears to be a function of the beam diameter.[6] However, the most probable reason for the large threshold values is the glass itself. Previous measurements on the same glass with a multimode laser emitting several tens of joules yielded thresholds consistent with those reported here.[7] It is our intention to measure the damage threshold of ED-2 with a laser having a much smaller beam than was used here. Perhaps in this way it can be learned whether damage thresholds depend on parameters such as beam size.

From a practical point of view, the experiments described here were performed under conditions which can, with care, be reasonably duplicated in practical laser systems. The samples were cleaned in a straightforward manner and tested over long periods of time in the laboratory environment. The laser beam was free of "hot spots" and had a relatively large diameter. Consequently, in working systems power densities of  $2 \text{ GW/cm}^2$  (in 30 ns) can easily be achieved without concern for surface damage, and with care  $3 \text{ GW/cm}^2$  should be safely attainable on a normal operation basis. These numbers apply to the local energy density at the exit surface. Self-focusing of the beam, for example, can of course raise the surface energy density in an uncontrollable manner.

Ion exchange strengthening of glass does not appreciably affect the damage threshold. In fact, damage when it does occur, is more likely to spread than in the case of untreated glass. This process, then, shows no promise of alleviating the surface damage problem. However, this negative result does suggest that shock waves of any sort are not primarily responsible for surface damage near threshold. In this sense the results are instructive.

The asymmetry of exit and entrance surface damage thresholds can be readily explained in terms of Fresnel reflections at the surface. This result suggests that it is particularly important to consider the strength of the local electric field in damage studies of coatings, mirrors, etc.

This work was supported by the Advanced Research Projects Agency of the Department of Defense under Contract No. DAHC 15-69-C-0303.

## 7. References

- [1] Bass, M., Barrett, H. H., and Holway, L. H., Jr., "Experimentation and Investigation of Optical-Irradiation-Induced Surface Damage in Optically Nonlinear Materials," Scientific Report No. 1, Feb. 1972, ARPA Order No. 1434AMD#1.
- [2] Boling, N. L., and Beck, R. W., "Damage in Laser Materials," 1971, Glass, A. J., and Guenther, A. H., Eds., National Bureau of Standards Spec. Pub. 356 November 1971.
- [3] Haller, W., and Winogradoff, N. N., "Explosive Vapor Release as Cause of Laser-Induced Surface Damage of Glass," Journal of The American Ceramic Society, 54, No. 6, 314, June 1971.
- [4] Fersman, I. A., and Khazov, L. D., Sov. Phys.-Tech. Phys. 15, 834, 1970.
- [5] Crisp, M. D., Boling, N. L., and Dube', G., "Importance of Fresnel Reflections in Laser Surface Damage of Transparent Dielectrics," Submitted June 1972 to Applied Physics Letters.
- [6] Newman, B. E., and DeShazer, L. G., "Spot-Size Dependence of Laser-Induced Damage Thresholds of Dielectric Thin Films," Digest of Technical Papers, VII International Quantum Electronics Conference, Montreal, Canada, May 1972.
- [7] Beck, R. W., "Laser Glass Damage Testing at Owens-Illinois" 1970, Glass, A. J., and Guenther, A. H., Eds. National Bureau of Standards Spec. Pub. 341, December 1970.



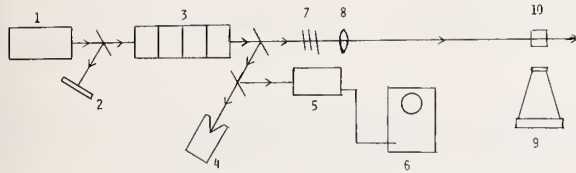


Figure 1. This figure shows the apparatus used for the damage threshold measurements. The components are: (1) laser oscillator; (2) polaroid film; (3) laser amplifier chain; (4) thermopile; (5) photodiode; (6) Tektronix 519 oscilloscope; (7) neutral density filters; (8) 1.5 m focal length lens; (9) camera; (10) sample.

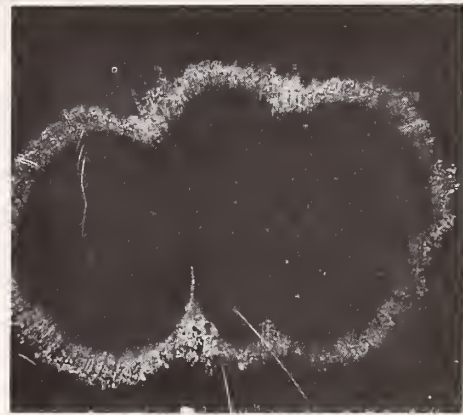


Figure 2. Typical damage ring new threshold. 40X magnification. Ring is 4mm in length. This particular ring is on a chemically strengthened sample immediately after damaging shot.



Figure 3. Section of damage ring near threshold 100X magnification.

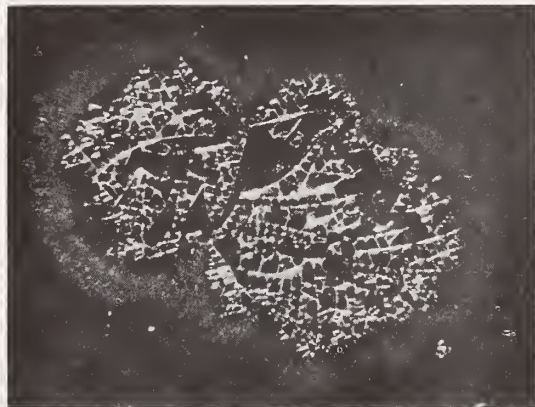


Figure 4. Damage on chemically strengthened sample one day after damaging shot.

# The Relation between Surface Damage and Surface Plasma Formation\*

Concetto R. Giuliano

Hughes Research Laboratories  
Malibu, California 90265

A number of experiments are described in which entrance and exit surface laser-induced damage on sapphire samples are studied. Damage thresholds are measured as a function of beam size and divergence at the surfaces. Temporal evolution of surface plasmas is studied using a streaking camera, and spatial differentiation of surface plasmas is accomplished by allowing the light to strike the surfaces away from normal incidence. It is found that the entrance surface has two plasma components, an air plasma which is directed along the light beam and an "explosion" plasma which is directed normal to the surface. The exit surface has only the explosion plasma. It is concluded that surface plasmas are a result of rather than a cause of surface damage.

Key Words: Entrance and exit surface damage, sapphire, spatial and temporal plasma resolution, streak camera experiments, surface plasmas.

## 1. Introduction

It has been known for some time that laser-induced surface damage has distinctly different physical characteristics, depending on whether the entrance or exit surface is damaged. [1-4]<sup>1</sup> To a certain extent the conditions under which the damage is generated (e.g., focusing, surface finish) are important in determining some of the details of the appearance of the damage, but as a general rule entrance surface damage is less extensive and more difficult to detect visually than exit surface damage, especially when generated under conditions of gentle focusing. Under such conditions for sapphire the distinguishing features are that exit surface damage can be most easily described as relatively deep fractured areas, while entrance surface damage is relatively shallow crazed areas. Scanning electron micrographs of both types of damage are presented in Figures 1 and 2.

The occurrence of laser-induced surface damage is known to be accompanied by a bright flash of light which comes from a spark or plasma at the surface. [1-5] (See fig. 3) In fact, the occurrence of a visible spark has been held to be a criterion for surface damage. [4] Spectra taken of exit surface plasmas show that the light contains spectral lines characteristic of the material being irradiated. [1] The connection between the surface plasma and the damage was not established in the early work. Whether or not the plasma is a result of or a cause of the surface damage or whether it is an independently occurring phenomenon that simply accompanies the damage phenomenon was not determined.

---

\* Work supported by the Advanced Research Projects Agency under ARPA Order No. 1434 with Air Force Cambridge Research Laboratories.

<sup>1</sup> Figures in brackets indicate the literature references at the end of this paper.

Fersman and Khazov [3] have suggested that the surface damage is caused by a plasma-surface interaction and have explained the difference between entrance and exit surface damage using a model in which both the plasmas grow in an upstream direction as they develop in time, an extension of the observations for air breakdown plasmas. [6] The exit damage would then be expected to be more extensive than entrance damage because the exit plasma grows into the surface, while the entrance plasma grows away from the surface. Fersman and Khazov observe a compressional wave which propagates inwardly from the exit surface. Compressional waves arising from damage sites in solids have been observed by others using both schlieren and holographic techniques. [7-8] While the above picture can predict a difference between the entrance and exit damage, it was not experimentally confirmed.

Another possible explanation for the difference between exit and entrance damage is that exit damage might be somehow influenced by self-focusing of the beam in the material, while the beam at the entrance would not be so affected.

We have carried out a number of experiments in an attempt to determine more explicitly the connection between the surface damage and the plasmas and to clarify the nature of the damage mechanism or mechanisms.

All the experiments described in this paper were carried out using a single longitudinal and transverse (TEM<sub>00</sub>) mode Q-switched ruby laser. The laser and associated monitoring apparatus are described in detail elsewhere. [2] Typical laser pulse width and peak power are 20 nsec (FWHM) and 1 MW, respectively.

## 2. Damage Threshold as a Function of Beam Size and Divergence

One of the questions which arises in the consideration of exit surface damage is concerned with the possibility that the damage at the exit surface might be influenced by what the beam does in the bulk of the material. For example, if some self-focusing or other nonlinear phenomenon takes place, it might affect the beam so that the intensity at the exit face will be different from that expected on the basis of linear propagation theory. Also, some phenomenon which might cause the generation of acoustic waves directed toward the exit surface would be affected by how the beam propagates inside the sample before reaching the exit surface. A series of experiments on sapphire was carried out in which the sample was moved relative to the focusing lens, so that the spot size at the surface would vary over a wide range and also so that the beam could be either converging or diverging at the surface, depending on whether the beam waist lay downstream or upstream from the surface.

The result of these experiments is shown in fig. 4. In these experiments a 19 cm lens for focusing the light from the mode-controlled ruby laser was used. The sapphire samples were moved in 5 mm increments relative to the lens, and surface damage threshold was measured for each location. The data on the left half of the figure correspond to the case of rays converging at the exit surface and the data on the right half to diverging rays. The beam area at the surface is also plotted as a function of distance in the figure.

Figure 4 shows that the results for exit surface damage threshold power in sapphire sample L134 fall very close to the beam area curve. The fact that they fall so closely is a coincidence of the scale and the units chosen, but the fact that they have the same functional dependence on distance is significant in that it strongly indicates that the damage threshold is a power density phenomenon. Also, the fact that the threshold is independent of whether the beam is converging or diverging at the exit surface indicates that the damage seems to be strictly a surface or near-surface phenomenon. The exit surface damage threshold for this sample is about 1 GW/cm<sup>2</sup>. The data for entrance surface damage for sapphire sample C129 are shown in fig. 5. A similar dependence on lens-to-sample distance is seen in the plot but in this case the scatter in the points is somewhat greater. Here the beam area curve is plotted on a different scale than in fig. 4 to show that the dependence of threshold power with distance is essentially the same as the dependence of beam area with distance, again indicating that damage threshold is a power density phenomenon. The entrance damage threshold for this case is about 1.5 GW/cm<sup>2</sup>.

## 3. Surface Damage without Plasma Formation

We have carried out a few experiments in which surface damage was generated without observing an accompanying plasma. These experiments were conducted on sapphire samples, and the observations apply only to the exit surface (entrance damage was not



pursued in this series of experiments). In these experiments we observed the exit surface during laser irradiation both visually and photographically under different conditions of optical filtering and exposure. It was found that when the sample was exposed to focused radiation very close to the threshold, damage could be generated in the form of a series of micropits without the simultaneous accompaniment of a detectable plasma or spark.

A series of experiments was initiated in which the sample was irradiated well above damage threshold, and the plasma observed as the power was gradually reduced, each time exposing a fresh area of the surface. During this series, the accompanying plasma was seen to decrease in size and brightness as the laser power was reduced, until a power point was reached at which the spark was no longer visible. On a number of occasions after laser irradiation at a level just below that for generating a visible plasma, it was possible to detect damage in the form of a number of micropits when the sample was carefully examined through a microscope with properly chosen illumination. This micropitting, which is seen only very close to threshold, is less extensive than the single fracture crater that occurs more often at slightly higher powers when the plasma is clearly visible. It should be noted that at the times when no plasma is visible, it is possible to see small amounts of laser light scattered from the tiny surface pits which are being formed.

The results of these observations suggest that it is possible to obtain exit surface damage without plasma formation. Of course, the nonobservability of a plasma does not necessarily imply that it is not present, and these results alone do not allow us to form any definite conclusions regarding the connection between the damage and the plasma.

#### 4. Time Evolution of Surface Plasmas

One reason for the interest in studying the temporal evolution of the surface plasmas has been to determine the direction of growth of the plasmas relative to the crystal surface, which would lead to a possible explanation of the differences between exit and entrance damage and to test the mechanism proposed by Fersman and Khazov.

We have employed an STL image converter camera operating in the streaking mode for observing the growth of the entrance and exit surface plasmas (see fig. 6). For these experiments, the output from our single-mode ruby laser was focused with a 19 cm lens on the desired surface of the sapphire sample being examined. Typical laser output is about 20 mJ in a 20 nsec pulse, which gives a power density at the focus of approximately 10 GW/cm<sup>2</sup>, about 10 times above damage threshold. For the streak camera experiments, a portion of the incident laser light was allowed to enter the camera directly to serve as a marker streak for synchronization purposes.

Streak photographs showing the temporal development of the surface plasmas are shown in figs. 7 and 8. Because the photographic setup is such that the camera views the surface at an angle less than 90° to the normal (see fig. 6), both the plasma and its reflection in the surface are often seen. The fact that there are indeed reflections was confirmed by placing an appropriately oriented Polaroid filter in front of the camera, in which case the reflection from the dielectric surface disappears as expected.

Essential features of these streak photographs to be noted are

- The plasmas grow away from the surfaces in both cases, the entrance plasma growing in the upstream direction and the exit plasma in the downstream direction.
- The entrance plasma has two temporal components, whereas the exit plasma has one temporal component.
- The extent of growth and luminosity of the faster growing component of the entrance plasma depends on the incident laser pulse in that it ceases to expand and to emit light when the laser terminates.
- The slower growing, longer lived component of the entrance plasma expands at about the same rate as the exit plasma. These plasmas continue to expand outward and emit light long after the laser has terminated.
- Typical velocities of expansion of the luminous plasma fronts are  $\sim 2 \times 10^6$  cm/sec for the short-lived entrance component and  $\sim 1 \times 10^6$  cm/sec for the long-lived entrance component and for the exit plasma.

Several ideas are suggested by these observations. First, the fact that both entrance and exit plasmas grow away from the surfaces suggests that the mechanism proposed by Fersman and Khazov is incorrect. From the time dependences of the plasmas relative to the incident laser pulse it can be inferred that the short-lived entrance component is a plasma supported in the ambient atmosphere and sustained directly by the laser beam itself, while the longer-lived components at both surfaces result from a kind of micro-explosion caused by the deposition and subsequent release of energy at or near the surface.

## 5. Spatial Differentiation of Surface Plasmas

To test these hypotheses further, we devised additional experiments that were designed to allow a spatial differentiation of the plasmas. The reasoning behind these experiments is as follows. A plasma sustained directly by the light beam would be expected to exist only where the light is present and to be directed along the light beam independent of the angle at which the light enters the material. A plasma which results from a surface explosion caused by a deposition of energy at the surface would be expected to extend in a direction normal to the surface no matter at what angle the light should enter the material.

Figure 9 shows time-integrated photographs of the entrance plasma formed when the light is allowed to strike the surface at angles other than normal incidence. The photographs show the separation of the plasma into different spatial components. One component extends along the direction of the light beam; this apparently is the short-lived air plasma. Another component that extends normal to the surface can be seen; this is the component resulting from the surface explosion. A third more diffusely defined plasma component can be seen, extending in the direction of the light reflected from the surface and is presumably additional air plasma sustained by the reflected light. Figure 10 shows a time-integrated photograph of the exit plasma formed when the light leaves at an angle of  $45^\circ$  to the surface. This photograph shows a single plasma component directed normal to the surface, as expected if a surface explosion were taking place.

As a final confirmation of assignments for the different plasma components, we looked at the entrance plasma in a vacuum. Figure 11 shows photographs of the entrance plasma for a sample tilted  $26^\circ$  from the incident light both at 1 atm pressure and at about 1 Torr pressure. Because of the shape and size of the container, it was impossible to perform the experiment at angles larger than  $26^\circ$ . As a result, the two spatial components are not distinguishable in figure 11(a) and (b). However, note that when the air is removed from the system (fig. 11(c) and (d)), the plasma component which extends along the light beam is no longer seen; the plasma visible in vacuum is directed normal to the surface, i.e., only the explosion plasma remains.

## 6. Conclusions

As a result of these experiments, the following conclusions are reached. First, the surface plasmas are a result rather than a cause of the surface damage. Second, two kinds of plasmas occur at the entrance surface, one which is sustained by the light beam in the ambient atmosphere and another which arises from a micro-explosion at or near the surface. The exit surface plasma is of the explosion type. While it may be true that some of the features seen on the surface of a material that has been subjected to damaging laser radiation might be caused by the interaction of the plasma with the surface, the primary cause of the damage is not the plasma. Rather, the surface plasmas are a result of the process or processes, whatever they may be, that give rise to the surface damage.

It is still not clear why the exit damage is physically so different in appearance than entrance damage. If the mechanism of energy deposition were simply one of surface absorption, it would be expected that the damage would be very similar on both surfaces. For some reason, there seems to be a distinct directionality to the surface damage mechanism. Since the exit surface damage threshold appears to be power density phenomenon and since it is not apparently dependent on whether the beam is converging or diverging before it reaches the surface, one would be inclined to conclude that the damage mechanism does not depend strongly, if at all, on phenomena which take place in the bulk of the material. It appears to be strictly a surface or near-surface phenomenon. The possibility that a directed intense acoustic wave [1] is involved in the damage mechanism is still open, although Stimulated Brillouin Scattering (SBS) is not likely since there seems to be no correlation between SBS thresholds and damage thresholds for a number of different solids. A mechanism of the type proposed by Hellwarth for bulk damage [9] might be a valid surface damage mechanism. The end result of this mechanism is the generation of intense acoustic phonons, but whether one would expect the acoustic wave to be directed in any particular way is not known at this time.

## 7. Acknowledgement

The author wishes to acknowledge the skilled technical assistance of G. R. Rickel.

## 8. References

- [1] Giuliano, Concetto R., "Laser-induced damage to transparent dielectric materials," *Appl. Phys. Letters* 5, 137-139 (1964).
- [2] Giuliano, C. R. and L. D. Hess, "Damage threshold studies in ruby and sapphire," in Damage in Laser Materials, edited by A. J. Glass and A. H. Guenther, U. S. National Bureau of Standards Special Publication No. 341 (U.S. GPO, Washington, D.C. 1970), pp. 76-89
- [3] Fersman, I. A. and L. D. Khazov, "Damage of transparent dielectric surfaces by a laser beam," *Sov. Phys.-Tech. Phys.* 15, 834-838 (1970).
- [4] Bass, Michael, "Nd:YAG laser-irradiation-induced damage to  $\text{LiNbO}_3$  and KDP," *IEEE J. Quantum Electron.* QE-7, 350-359 (1971).
- [5] Khazov, L.D., A. N. Shestov, and G. P. Tikhomirov, "Luminous discharge on non-absorbing surfaces produced by a single pulse laser," *Sov. Phys.-Tech. Phys.* 13, 1112-1114 (1969).
- [6] Ramsden, S.A. and W. E. R. Davies, "Radiation scattered from the plasma produced by a focused ruby laser beam," *Phys. Rev. Letters* 13, 227-229 (1964).
- [7] Belikova, T. P., A. N. Savchenko, and E. A. Sviridenkov, "Optic breakdown in ruby and related effects," *Sov. Phys.-JETP* 27, 19-23 (1968).
- [8] Boling, N.L. and R. W. Beck, "Laser glass damage threshold studies at Owens-Illinois," in Damage in Laser Materials, edited by A. J. Glass and A. H. Guenther, U. S. National Bureau of Standards Special Publication No. 356 (U. S. GPO, Washington, D. C., 1971), pp. 15-23.
- [9] Hellwarth, "Role of photo-electrons in optical damage," in Damage in Laser Materials, edited by A. J. Glass and A. H. Guenther, U.S. National Bureau of Standards Special Publication No. 341 (U.S. GPO, Washington, D. C., 1970), pp 67-75



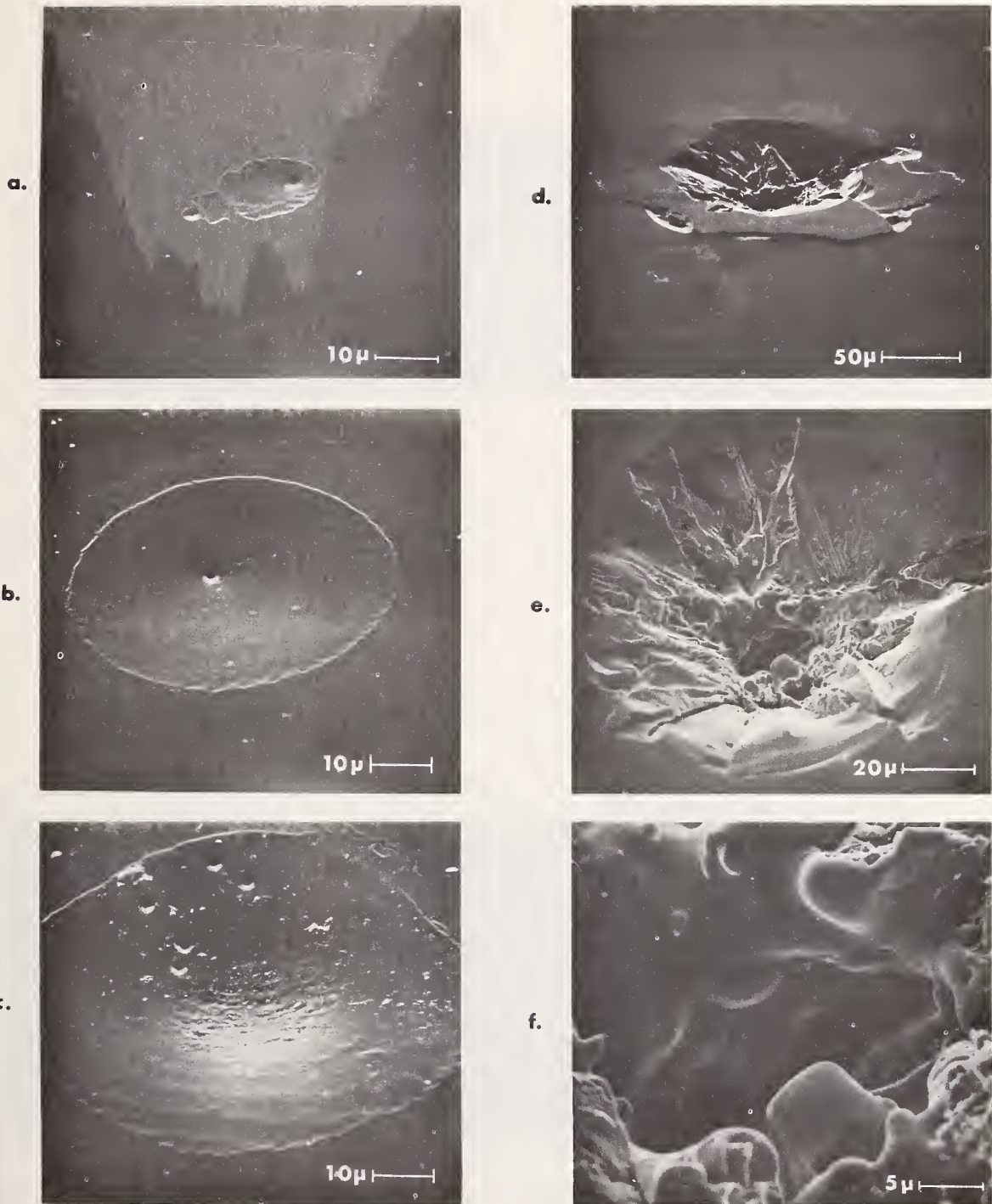
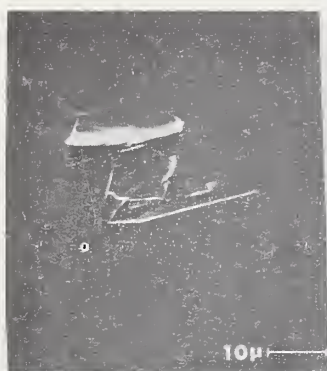


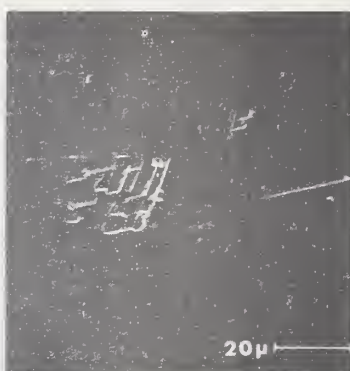
Figure 1. Scanning electron micrographs of exit damage sites for sapphire. Pulse energy increases from a-d; e and f are magnified views of site shown in d.



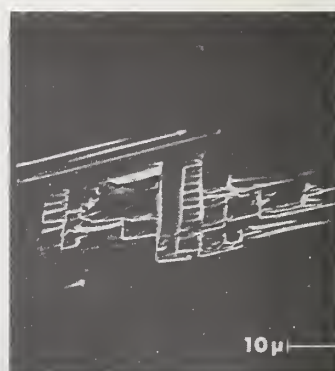
Figure 2. Scanning electron micrographs of entrance damage for sapphire. Pulse energy increases from a-c.



A.



B



C

Figure 3. Example of entrance and exit surface plasmas formed when light from a Q-switched ruby laser passes through a sample. Sample length - 3 in. Light is travelling from left to right.

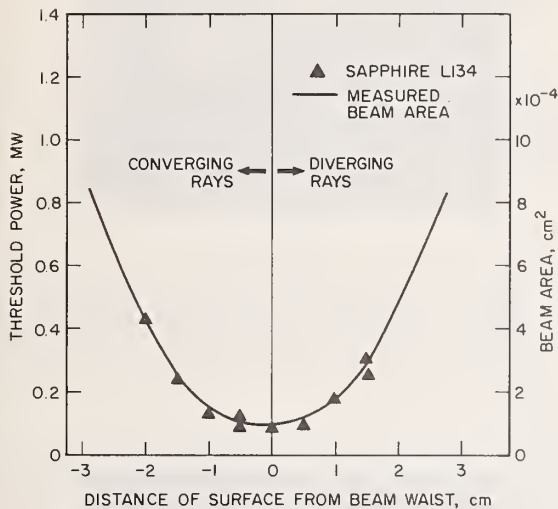


Figure 4. Exit surface damage threshold power for sapphire sample as a function of surface distance from beam waist for 19 cm lens. Beam area is also plotted.

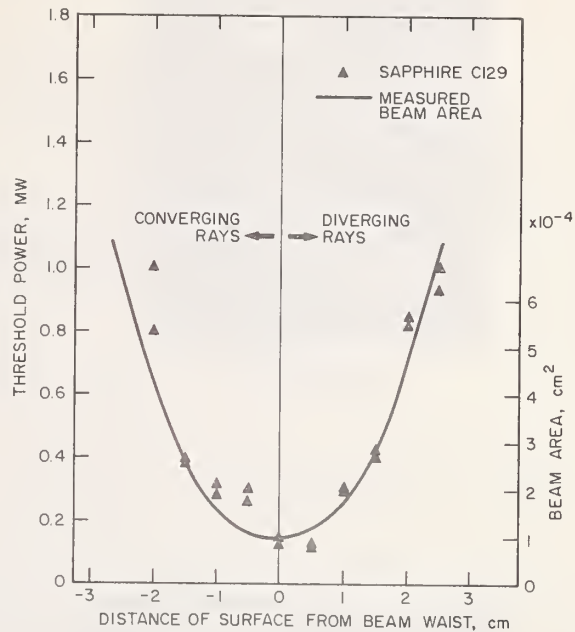


Figure 5. Beam area and entrance surface damage threshold as a function of surface distance from beam waist for 19 cm lens.

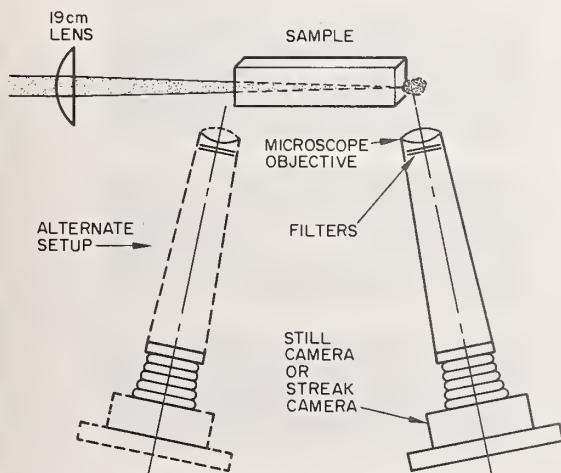


Figure 6. Schematic diagram showing setup used for photographing surface plasmas both for still and streak photography.

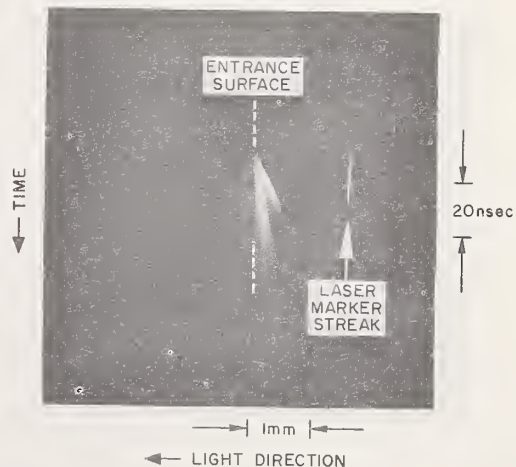


Figure 7. Streak photograph of entrance plasma on sapphire surface showing two temporal components.



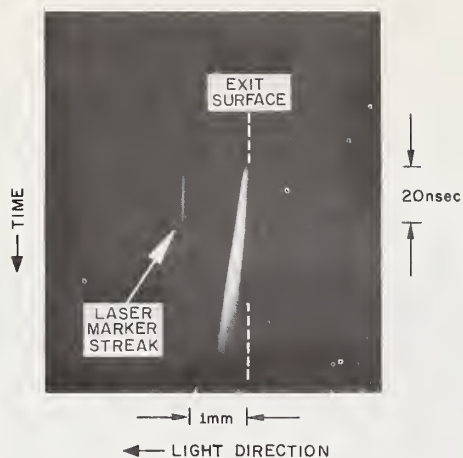


Figure 8. Streak photograph of exit plasma on sapphire surface.

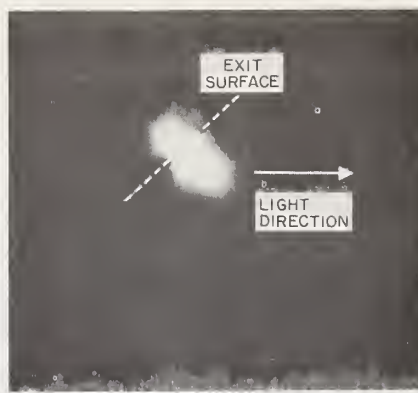


Figure 9. Time-integrated photographs of entrance plasma at sapphire surface tilted with respect to incident beam direction. Angle between light direction and surface normal (a)  $45^\circ$ ; (b)  $60^\circ$ .

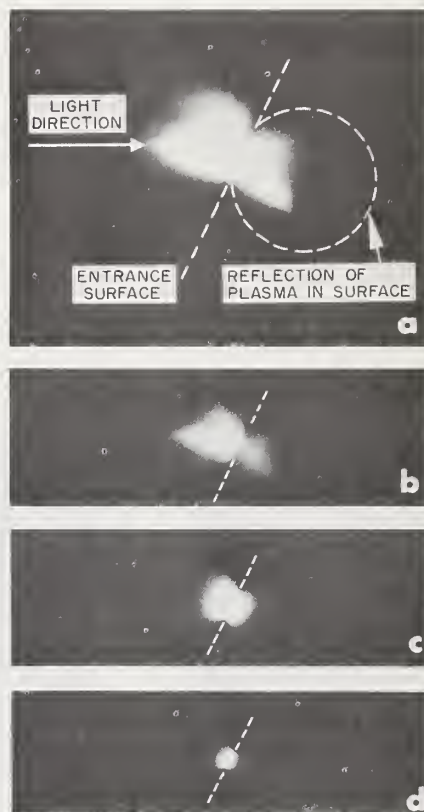
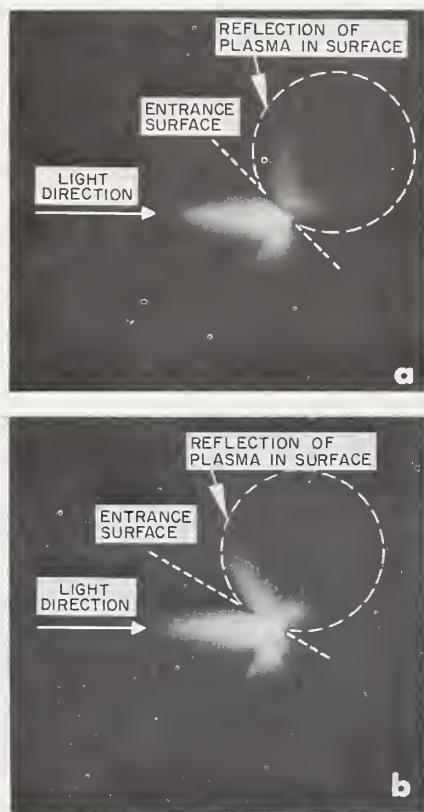


Figure 10. Time-integrated photograph of exit plasma at sapphire surface tilted  $45^\circ$  with respect to light propagation direction.

Figure 11. Time-integrated photographs of entrance plasma at sapphire surface tilted  $26^\circ$  from beam direction for different optical attenuations at camera, (a) and (b) taken at 1 atm pressure in air, (c) and (d) taken at 1 Torr pressure. Optical attenuation at camera (a) N.D. 1.0, (b) N.D. 1.7, (c) N.D. 0.7, (d) N.D. 1.7.

# Ion Beam Polishing as a Means of Increasing Surface Damage Thresholds in Sapphire\*

Concetto R. Giuliano

Hughes Research Laboratories  
Malibu, California 90265

Polishing of sapphire surfaces with energetic  $\text{Ar}^+$  ion beams is shown to result in a substantial increase in laser damage threshold over that for conventionally polished surfaces. Data for both entrance and exit damage are presented. The results are interpreted in terms of an increase in surface strength with ion beam polishing.

Key Words: Ion beam polishing, sapphire, surface damage, threshold increase, threshold measurement.

## 1. Introduction

It is a generally accepted fact that the threshold for laser induced surface damage of transparent dielectrics is a function of the condition of the surface being irradiated. Any foreign material on a surface subjected to high optical fluxes can cause catastrophic damage to occur at levels well below those which can be sustained by clean surfaces. The quality of surface fabrication has also been recognized as being important in influencing the damage resistance of materials. For example, it is known that a frosted surface damages more easily than a surface with a good optical polish. [1]<sup>1</sup> Various chemical surface treatments have been tried on different materials [2-3], some of which have shown improvement but often the effect is only temporary.

We have found that polishing of sapphire surfaces with ion beams results in a marked increase of surface damage threshold compared with that for abrasively polished samples.

Experiments were carried out using a single transverse and longitudinal mode ruby laser whose output is focused on either the entrance or exit surface of a sapphire sample. The samples are sapphire bars 3 in long by 0.25 in square cross section. The laser and associated monitoring apparatus are described in detail elsewhere. [4] Typical laser pulse width and peak power are 20 nsec (FWHM) and 1 MW, respectively. The area of the focused spot has been measured using a modified multiple lens camera technique [5] to be  $10^{-4} \text{ cm}^2$  at the  $1/e^2$  intensity points. The beam profile was measured to be gaussian down to 8% of the peak. The power incident on the sample is varied by rotating the first of a pair of air-spaced polarizers, the second being held at a fixed orientation.

A typical series of measurements is carried out as follows. The laser is fired at a particular spot on the desired surface at a power below damage threshold. The sample is then examined through a traveling microscope without disturbing the sample between shots. If no damage is observed the incident power is increased (by  $\sim 10\%$ - $20\%$ ) and again the sample is examined. The procedure continues until damage is observed; then the sample is moved and the process repeated on an undamaged spot. Typically 10-20 damage thresholds are measured in this way for a given surface.

Abrasively polished samples were used as obtained from the manufacturer (Union Carbide). They were fabricated with the "laser finish" specifications typical for ruby laser rods. Ion polished samples were exposed after mechanical processing to an  $\text{Ar}^+$  beam (7 kV,  $300 \mu\text{A}/\text{cm}^2$ ) for periods from 2 hrs to 4 hrs. The beam strikes the surface at an angle of  $20^\circ$  from the surface plane. An estimated 200 Å/min is removed from the sapphire surface under these conditions giving a total of from about 2.5 to 5  $\mu\text{m}$  of material removed in a given exposure.

\*Work supported by the Advanced Research Projects Agency under ARPA Order No. 1434 with Air Force Cambridge Research Laboratories.

<sup>1</sup>Figures in brackets indicate the literature references at the end of this paper.

## 2. Experimental Results

The results of a series of measurements on abrasively polished and ion beam polished samples are shown in Fig. 1. In Fig. 1(a) and (b) the results for entrance surface damage are shown. For the abrasively polished sample most of the damage thresholds occur between  $1 \text{ GW/cm}^2$  and  $2.5 \text{ GW/cm}^2$  with a few higher values occurring. For the ion polished case (Fig. 1(b)) we see a few damage thresholds ranging from  $2 \text{ GW/cm}^2$  to  $9 \text{ GW/cm}^2$  with a large fraction ( $>50\%$ ) above  $10 \text{ GW/cm}^2$ . (The dashed portion of Fig. 1(b) indicates that we were unable to reach damage threshold with the maximum output from our laser under the focusing conditions of our experiment.) Fig. 1(c) shows the exit damage thresholds for the abrasively polished sample. Here the bulk of the points are clustered between  $1 \text{ GW/cm}^2$  and  $2 \text{ GW/cm}^2$ . For the ion polished case (Fig. 1(d)) the values are again spread over a wide range (up to  $9 \text{ GW/cm}^2$ ) but for this case no damage thresholds lower than  $2 \text{ GW/cm}^2$  are observed. The data in Fig. 1(d) were obtained from samples which were ion polished for 2 hrs and 4 hrs. No noticeable change in the distribution was observed between the 2 hr and 4 hr case and the data are presented together in the figure.

Fig. 2 shows examples of x-ray reflection topographs for sapphire samples which were abrasively polished (Fig. 2(a)) and ion beam polished (Fig. 2(b), (c)). The depth of the region being probed in these topographs depends on the angle of incidence and energy of the x-rays as well as other experimental conditions and sample properties. An estimated region  $10\text{--}20\mu$  thick is being probed in the above topographs. We see in Fig. 2(a) a number of deviations from crystallinity which appear to follow scratch lines from the mechanical polishing process. In Fig. 2(b) the topograph for a different sample shows that some of the mechanical damage appears to have been "erased" after 2 hrs of ion beam polishing. Fig. 2(c) shows a topograph taken after 4 hrs of exposure to the ion beam and, although evidence of damage still is seen, there is a marked difference between this and the previous topographs. We present these topographs to point out that a distinct change in surface topography is brought about by ion beam polishing. A detailed correlation between the changes in the topographs and the damage thresholds is not possible at this time.

## 3. Conclusions

The main conclusion reached by these preliminary results is that a distinct increase ( $\sim 2\text{--}6\times$ ) in surface damage threshold can be realized by ion beam polishing. Although there is a wide scatter of results in measured thresholds for ion polished samples, we see that even the low values for the ion polished samples are generally higher than those for the abrasively polished samples. We interpret the scatter in the threshold data for the ion polished samples to indicate a variation of surface strength from place to place over the sample. It is very likely that the influence of mechanical damage due to abrasive polishing, although somewhat lessened, has not been completely removed under the conditions of our experiments. This is suggested by the x-ray topographs, although as yet no definite correlation between topograph details and threshold variations has been established. We choose to interpret the data as reflecting a variation of threshold from spot to spot on the surface rather than in a probabilistic manner as described by Bass and Barrett. [6] It is apparent from the topographs that the surface crystallinity varies considerably from place to place over the sample and that the surface is not uniform all over. A possible interpretation of the difference between the abrasive polish and ion polish results is that in the former case the surface is "uniformly weak" and the damage thresholds are found to have a relatively narrow range of values whereas in the latter case a distinct toughening of the surface has taken place but the influence of mechanical damage from the abrasive polishing still exists.

A final point worthy of mention is that the damage when it occurs at a high threshold is generally much more extensive than when it occurs at a low threshold. For example, exit surface damage in abrasively polished samples is generally characterized by a small fractured crater or pit about  $10 \mu\text{m}$  in diameter when it occurs near threshold. On the other hand, the high threshold damage seen in the ion polished samples is more severe; the damage craters are usually several times larger and more extensively fractured. This fact suggests that the effect of ion polishing is to toughen or strengthen the surface in some way rather than to change the basic damage mechanism whatever it may be. It seems that the surface is able to sustain a larger deposition of energy before catastrophic breakdown occurs but when the surface does let go it goes with a bigger bang.



#### 4. Acknowledgement

The author wishes to acknowledge critical suggestions by V. Evtuhov, as well as the aid of H. L. Garvin who performed the ion beam polishing and K. T. Miller who provided the x-ray topographs.

#### 5. References

- [1] Khazov, L. D., A. N. Shestov, and G. P. Tikhomirov, Sov. Phys.-Tech. Phys. 13, 1112 (1969).
- [2] Swain, J. E., IEEE J. Quantum Electron. 4, 362 (1968).
- [3] Davit, J., in Damage in Laser Glass, edited by A. Glass, A. Guenther, C. Stickely, and J. Myers, American Society for Testing and Materials Technical Publication No. 469 (ASTM, Philadelphia, PA, 1969), p. 100.
- [4] Giuliano, C. R. and L. D. Hess, in Damage in Laser Materials, edited by A. J. Glass and A. H. Guenther, U. S. National Bureau of Standards Special Publication No. 341 (U. S. GPO, Washington, D. C., 1970) p. 76.
- [5] Winer, I. M., Appl. Opt. 5, 1437 (1966).
- [6] Bass, M. and H. H. Barrett, IEEE J. Quantum Electron. 8, 338 (1972).

#### 6. Figures

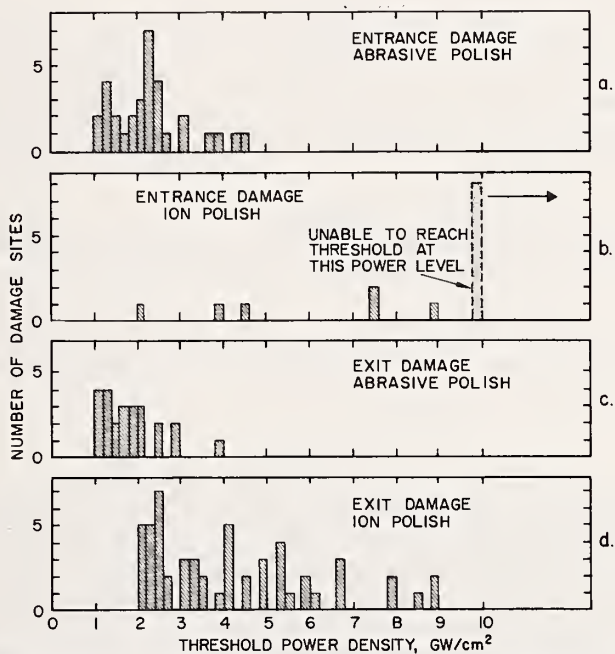


Figure 1. Number of damage sites as a function of threshold power density at entrance and exit surfaces of sapphire crystals for abrasively polished and ion beam polished samples.

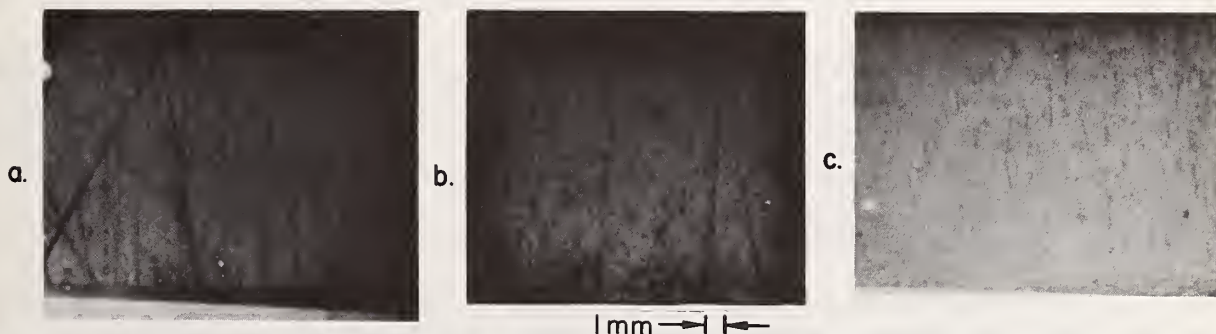


Figure 2. Examples of x-ray diffraction topographs taken for (a) abrasively polished sample, (b)  $\text{Ar}^+$  ion polished for 2 hours ( $7\text{kV}$  @  $300 \mu\text{A}/\text{cm}^2$ ), (c) same conditions as (b), but for 4 hours.

Michael Bass and Harrison H. Barrett

Raytheon Research Division  
Waltham, Massachusetts 02154

Measurements of the laser-induced surface damage process at both ruby and Nd:YAG laser wavelengths are reported in which the laser pulse and beam parameters were carefully held constant for both sources. This resulted in the first directly comparable measurements of laser damage at two different wavelengths. The most striking feature of the data is that all the materials studied are harder to damage at 0.69  $\mu\text{m}$  than at 1.06  $\mu\text{m}$ . In addition, the relationship between the damage probability and the optical electric field strength at 0.69  $\mu\text{m}$ , though similar to that at 1.06  $\mu\text{m}$ , suggests that more than one damage mechanism may be operative.

The probabilistic nature of the laser-induced damage process at 1.06  $\mu\text{m}$  was explored further by measuring the distribution of breakdown starting times with the image-converter streak camera. For a particular laser pulse a threshold-like damage process would result in a very sharp distribution of breakdown starting times. Instead, a large spread is found, with the most likely starting time occurring before the laser intensity reaches its maximum. The observed distribution is described by the compound probability that breakdown occurs at a particular time, given that it has not occurred before that time.

In addition, several possible connections between the probabilistic and threshold-like interpretations of laser-induced damage are discussed. It is shown that these points of view are not totally incompatible.

Key Words: Breakdown starting time, electron avalanche, probabilistic nature of damage, surface damage, wavelength dependence of damage.

## 1. Introduction

The first direct comparison of damage in transparent media produced by ruby and Nd:YAG lasers was performed using experimental techniques described previously. [1]<sup>1</sup> These studies have shown that a material is less likely to damage when subjected to a particular optical field at 0.69  $\mu\text{m}$  than at 1.06  $\mu\text{m}$ . Comparison of the 0.69  $\mu\text{m}$  data with that recorded at 1.06  $\mu\text{m}$  also shows that the relationship between the damage probability,  $p_1$ , and the applied optical electric field strength,  $E$ , though still generally of the form  $p_1 \propto \exp(-K/E)$ , has changed to a greater degree than predicted by a very simplified avalanche breakdown model. [1,2] In fact, for at least two materials studied,  $K$  is so large at 0.69  $\mu\text{m}$  that the damage process at this wavelength might properly be characterized by a well defined threshold field. The inadequacies of the simplified optical-frequency avalanche-breakdown model [1,2] are discussed and the possibility that more than one damage mechanism may be operative is examined in view of the experimental data.

A very fast image-converter streak camera was used to study the distribution of starting times for 1.06  $\mu\text{m}$  laser-induced surface breakdowns. If the breakdown or damage process were completely described by a well defined threshold, then this distribution should be very narrow and no breakdowns should occur after the laser field reached its maximum. The data, however, shows broad distributions, particularly when the applied field is such that  $p_1 < 1$ . In all cases the most probable time for breakdown is before the time of maximum field, though some breakdowns do occur later. The properties of the measured distributions are described by the compound probability that breakdown occurs at a particular instant, given that it has not occurred before that time and, as such, are added evidence for the probabilistic interpretation of the 1.06  $\mu\text{m}$  damage process.

\* This research was supported by the Advanced Research Projects Agency of the Department of Defense and was monitored by the Air Force Cambridge Research Laboratories under Contract No. F19628-70-C-0223.

<sup>1</sup> Figures in brackets indicate the literature references at the end of this paper.

Several possible connections between the probabilistic and threshold-like interpretations of laser induced damage are also discussed. It is shown that these two points of view are not totally compatible. The possibility that fluctuations in the laser pulse which were not detected experimentally caused the statistical nature of the damage data is considered. We show experimentally, however, that such fluctuations were not present.

## 2. Comparison of Ruby and Nd:YAG Laser Induced Damage

### 2.1 Experiments

An examination of the available literature reveals that due to variations in experimental conditions there are no directly comparable published results for 0.69 and 1.06  $\mu\text{m}$  laser induced damage. In the experiments described below the same sample was studied at both wavelengths. Self-focusing was eliminated by studying surface damage only and the critical laser beam parameters were carefully held constant as shown in table 1. Under these conditions and using a slightly modified version of the experimental techniques described previously [1] directly comparable laser damage data was obtained.

Table 1. Laser parameters

Wavelength	Nd:YAG <u>1.06 <math>\mu\text{m}</math></u>	Ruby <u>0.694 <math>\mu\text{m}</math></u>
Max. Energy TEM <sub>00</sub> Mode	1.8 mJ	5.0 mJ
Longitudinal Mode	1-5	1-5
Beam Diameter at Output Mirror TEM <sub>00</sub> Mode	1 mm	0.75 mm
Polarization	Linear	Linear
Pulse Repetition Rate	1 pps	1 pulse/5 sec
Pulse Duration in TEM <sub>00</sub> Mode	12 nsec (FWHP)	12 nsec (FWHP)
Pulse to Pulse Energy Reproducibility	$\pm 7\%$	$\pm 7\%$
Focal Spot Size	0.003 cm	0.003 cm

The general experimental arrangement of reference 1 was modified as shown in figure 1. The laser focusing optics was unchanged but an automated pulse monitoring and damage detection system was installed. One pen of the dual-pen chart recorder was driven with a signal proportional to the laser pulse energy and the other pen monitored the intensity of a beam of light transmitted through the region which was exposed to the laser pulses. This arrangement was sensitive to the appearance of surface damage craters  $\sim 0.003$  cm in diameter and  $\sim 2000$   $\text{\AA}$  deep, the smallest damage observed by earlier monitoring techniques [3]. A typical recording, derived from this arrangement, is shown in figure 2 where a ruby laser at  $\approx 9$  GW/cm<sup>2</sup> was used to irradiate an x-cut crystalline quartz sample. Note the  $\pm 10$  percent laser pulse energy variation. The first pulse to strike the sample is marked with an arrow and the 99th pulse, marked with a star, is the one which produced damage. This is indicated by the sharp reduction in the transmitted monitor intensity. The laser trigger signal was picked up by the photomultiplier and so resulted in a fiducial marker on the record of the transmitted light intensity.

The data in figure 2 shows that at this level of irradiation the sample does not have to damage when exposed to any particular pulse. In fact, preceding the damaging pulse (no. 99), there were several more energetic pulses which, according to the "threshold point of view," should have been the ones to cause damage.

The data in figure 3, while similar to that in figure 2, show the improved pulse-to-pulse energy reproducibility of the ruby laser achieved by more careful tuning of the laser cavity components. Alignment of the flat, parallel rod faces with the cavity mirrors was found to be critical. Proper rod alignment was always accompanied by a dramatic smoothing of the pulse waveform as recorded by a high-speed photodiode and a 519 oscilloscope. Figure 4 shows this effect for the TEM<sub>00</sub> ruby laser. Similar results were obtained by aligning the Nd:YAG rod in its laser cavity.

The detection of a smooth pulse by a limited bandwidth detector may be the result of either single-frequency output or the simultaneous oscillation of many randomly phased modes. In order to resolve this question the lasers' output spectra have been studied with Fabry-Perot interferometers. The lasing



bandwidth narrowed significantly as the rod was aligned to achieve smoother pulses. Unfortunately, our interferometers lacked sufficient finesse to resolve individual laser cavity modes ( $\Delta\nu \approx 300$  MHz). The longitudinal mode content of a perfectly smooth laser pulse can be inferred, however, by combining the interferometer and pulse waveform data. The observed interferometer limited bandwidth of a smooth ruby laser pulse was  $\approx 1.5$  GHz, implying that a maximum of  $\sim 5$  modes could have been oscillating. Since the photodiode-oscilloscope combination could detect frequencies as high as  $\sim 3$  GHz, the presence of five oscillating modes would have been detected through the presence of mode beating as in figure 4b. Therefore, our perfectly smooth ruby laser pulses, as shown in figure 4c, were caused by single longitudinal mode lasing. In support of this conclusion we note that Giuliano et al. [4] reported that perfectly smooth pulses correspond to single mode oscillation while non-smooth waveforms were always associated with two or more oscillating modes.

Single longitudinal mode oscillation is generally obtained by placing an intracavity resonator in the laser with sufficient finesse to limit the number of modes [4]. In the present experiments intracavity resonators were created by aligning the plane parallel faces of the laser rods with the plane parallel cavity mirrors as shown in figure 5. The finesse of each of the indicated resonators is very low because the rod faces were antireflection coated for less than 0.25 percent reflectivity at the laser wavelength. However, when lasing occurs, resonators  $M_1$ -A, B-A, and A- $M_2$  contain a medium with gain. Thus the effective reflectivity of the rod face in these resonators is increased and so is the effective finesse. Resonator  $M_1$ -A which includes the 100 percent reflecting laser cavity mirror has the highest finesse and is felt to be responsible for limiting the number of oscillating modes. For example, in the ruby laser, we used a 10 cm long rod with a gain coefficient of  $\approx 0.25 \text{ cm}^{-1}$  [5] resulting in an effective finesse of  $\sim 6$ .

The possibility that subnanosecond fluctuations in the laser field during a single pulse which were not detected by the photodiode-oscilloscope combination caused the statistical nature of the damage data had been suggested [6]. However, the study of the frequency content of the smooth laser pulses showed that the experimental data given here and in references 1 and 2 was obtained with a single longitudinal mode laser pulse or, at worst, with one containing only a few oscillating modes. Therefore, such fluctuations could not have been present and could not have been the source of the form of the damage data. In addition, the data for  $\text{SrTiO}_3$  in reference 1 covers a range in power of 36 to 1 and fluctuations of this magnitude in a laser pulse would certainly have been noticed.

Using the smooth-pulse, reproducible lasers the damage data for 0.69 and 1.06  $\mu\text{m}$  summarized in table 2 was obtained. As shown therein the lowest power density required to always produce damage in a single pulse,  $P_1$ , is generally higher at 0.69  $\mu\text{m}$  than at 1.06  $\mu\text{m}$ . In addition, the quantity K in the relation

$$P_1 \propto \exp(-K/E) \quad (1)$$

is larger for ruby irradiation.

Table 2. Comparison of damage properties at 1.0645  $\mu\text{m}$  and 0.6943  $\mu\text{m}$ .

Laser Wavelength ( $\mu\text{m}$ )	K( $10^8 \text{ V/M}$ )		$P_1$ ( $\text{GW/cm}^2$ )	
	1.0645	0.6943	1.0645	0.6943
X-Cut Crystal Quartz	33.0	60.5	5.4	20.2
KDP	28.5	92.8	16.6	27.6
$\text{LiNbO}_3$	16.6	> 200	11.1	11.1
$\text{LiIO}_3$	7.1	16.3	2.8	3.9
$\text{SrTiO}_3^*$	8.7	> 500	0.8	15.3

\* This  $\text{SrTiO}_3$  was sample No. 2 and was cut from a different boule than the one used in references 1 and 2.

## 2.2 Discussion

In references 1 and 2 a model for the damage mechanism based on electron avalanche breakdown was proposed for two main reasons: 1) It gave the experimentally observed relation between damage probability and optical electric field; and 2) It did not require material properties inconsistent with transparent, insulating dielectrics. This model was fashioned on the assumptions that the statistics of the

avalanche breakdown process were largely determined by the first one or two ionizations and that the fraction of collisions which the accelerating electron could make and remain acceptable in phase with the optical field,  $f$ , was independent of electron energy. It was also assumed that the collision rate,  $\tau_{coll}^{-1}$  was independent of electron energy. In this very simplified model, in contrast to the data,  $K$  has a weak dependence on the optical frequency and large changes in  $P_1$  are not predicted. However, because of the successes of the avalanche breakdown mechanism mentioned above a re-examination of its dependence on optical frequency is in order.

If, as in our simplified model, the steps in the avalanche are all highly likely after the first one or two, then the statistics of these early steps will dominate and the process will appear probabilistic. If, on the other hand, the probability for each step in the avalanche is the same, damaging avalanches will not be possible until a field is applied which is large enough to make the probability for each step near unity. In this case the process will appear threshold-like.

Consider the sequence of events whereby an electron in an optical field is accelerated to ionizing energies. Since the field direction reverses periodically the electron must undergo collisions at the proper times to be able to efficiently extract energy from the field. At low energies inelastic optical phonon collisions dominate the electron-lattice interaction [7] and are, in effect, a frictional force on the electron's motion. This means that there is some "friction barrier" to the electron's energy which is determined by the energy range over which optical phonon interactions dominate. At higher energies elastic collisions with acoustic phonons dominate and it is much easier for the electron to accelerate further to ionizing energies. Therefore electrons with initial energies greater than this "friction barrier" can dominate the avalanche process.

Now assuming an electron reaches the ionization energy,  $\epsilon_I$ , it cannot undergo an ionizing interaction until it gains some additional energy since the ionization cross section is zero at  $\epsilon_I$ . The probability for ionization, however, increases rapidly with electron energy [8]. Ionization is most likely to occur, then, when there is a substantial excess energy over  $\epsilon_I$ , with this extra energy divided between the two ionization products. If the energy of these products exceeds the "friction barrier" then they can be more easily accelerated to produce the next step in the avalanche and so on for each succeeding step until damage occurs. The ionization products dominate the avalanche. On the other hand, if the excess energy is small, the ionization products may have energies less than the "friction barrier" and be virtually indistinguishable from the rest of the free electrons. Each step in the avalanche then must follow the same course as the first, requiring large fields to produce damage.

In figures 6 and 7 the 1.06 and 0.69  $\mu\text{m}$  electric field required to accelerate an electron to a particular energy is plotted. The curves are numbered according to the number of half cycles of the field required to accelerate the electron to that energy assuming an optimally lucky collision occurs each time the field reverses. This number is also the number of the collision which must occur if the electron is to continue to accelerate. For example, 12 collisions are required to reach the curve labeled 13. Perfectly lucky collisions are those which exactly reverse the electron momentum. The results show that in a Nd:YAG laser field an electron will gain more energy through fewer collisions than if the same field were due to a ruby laser. Both the collision rate,  $\tau_{coll}^{-1}$ , and  $f$  decrease with increasing electron energy. In fact, above 2-4 eV the cross section for acoustic phonon scattering is strongly peaked in the forward direction which means that "lucky" collisions at high energies are very unlikely [7]. Thus, since fewer collisions are required, the energy of an electron in a 1.06  $\mu\text{m}$  field which causes ionization will, in general be further in excess of  $\epsilon_I$  than when ionization is caused by a 0.69  $\mu\text{m}$  field. In the 1.06  $\mu\text{m}$  field then the ionization products have less of a "friction barrier" to clear than in the latter and an avalanche can proceed with high probability. In the 0.69  $\mu\text{m}$  case the ionization products are less distinguishable from other free electrons and an avalanche may not develop. Larger fields should then be necessary to produce ionization at 0.69  $\mu\text{m}$  and the mechanism of producing a damaging avalanche should exhibit higher  $K$  value or be more threshold-like than at 1.06  $\mu\text{m}$ . This very speculative interpretation is presented only because it agrees with the most important experimental facts and in order to stimulate interest in further theoretical study of the avalanche breakdown process in optical frequency fields.

Figures 6 and 7 also show that between 3 and 5 more "lucky" collisions are required to reach a particular energy in a ruby laser field than in a Nd:YAG field. Thus if  $f$  is a constant, say 0.1, [1,2] the probability for damage at 0.69  $\mu\text{m}$  is between  $10^{-3}$  and  $10^{-5}$  times less than at 1.06  $\mu\text{m}$ . However, as stated above,  $f$  decreases with increasing electron energy and so the probability for ionization in a given field at 0.69  $\mu\text{m}$  is even smaller. We have therefore an additional reason for the fact that damage with the ruby laser always requires higher fields.

It appears reasonable from the preceding discussion that the electron avalanche breakdown process, which gives a qualitatively good picture of 1.06  $\mu\text{m}$  laser induced damage, will be observed only at much higher optical fields at 0.69  $\mu\text{m}$ . However, as the ruby laser field is increased to find avalanche breakdown damage, it is possible that some materials may display damage due to another mechanism. In  $\text{LiNbO}_3$  and  $\text{SrTiO}_3$ , both of which absorb strongly at 0.35  $\mu\text{m}$  and have well defined experimental damage thresholds for 0.69  $\mu\text{m}$  irradiation, this mechanism may be two-photon absorption.



Both the 1.06 and 0.69  $\mu\text{m}$  data in table 2 for  $\text{SrTiO}_3$  were taken for sample No. 2 so that direct comparison is possible. In references 1 and 2, the value of K for  $\text{SrTiO}_3$  at 1.06  $\mu\text{m}$ , obtained using a sample cut from a different boule, was about one fourth that in table 1. This is the first instance yet encountered where so large a sample-to-sample variation in K was observed. On checking with the manufacturer [9], however, we found that sample No. 2 was doped with tungsten while sample No. 1 was not. Tungsten had been added to make the material visually clearer and satisfy our order for "optical quality  $\text{SrTiO}_3$ ." The two samples therefore were not the same material and so differences can be expected. More experimental data will be obtained on other samples as soon as possible.

### 3. Distribution of Breakdown Starting Times

Since the observation of a visible spark upon laser irradiation is always followed by the detection of damage in the irradiated area, a study of the temporal development of such sparks was initiated over one year ago. The initial observations of this study were concerned with self-focusing and its relation to the internal damage process [1]. More recent work has been concerned with measuring the distribution of surface breakdown starting times and the interpretation of such data.

Using the high speed image converter streak camera technique described previously [1] and the TEM<sub>00</sub> mode Nd:YAG laser, the distributions shown in figures 8 and 9 were obtained. Twenty-five different measurements of starting times were made to obtain each distribution. Plate glass and  $\text{SrTiO}_3$  were studied because they have very different K values and because at convenient optical field strengths  $p_1 \leq 1$  could be obtained.

The most obvious feature of these distributions is that, except for the highest field applied to plate glass, a high K material, they are not very sharp. Assuming constant pulse shape and material properties, as implied by the excellent fit of the measured distribution of N (the number of pulses required to damage) to the binomial distribution assuming a constant  $p_1$ , [1] a process described by a well defined threshold would yield distributions of breakdown starting times which ranged over an interval of time much less than the laser pulse duration. In addition, such a process would not permit any breakdowns to occur after the time of maximum field strength: If breakdown did not occur in the most intense field it would certainly not occur when the field was weaker. Both of these requirements for the distribution of breakdown starting times of a threshold like process are violated by the data and so an interpretation based on the probabilistic point of view is sought.

Consider an ensemble of samples, each subjected to the same laser pulse,  $E(t)$ , such that  $E(t) = 0$  for  $t \leq 0$ . Let  $\nu(t)$  be the fractional number which have not damaged at time t and let  $g(t)$  be the fractional rate with which the surviving samples breakdown. Note then that, within a scale factor,  $g(t)$  is the distribution of breakdown starting times. The applied laser field results in a probability per unit time that breakdown occurs,  $h(t)$ , and so

$$g(t) = - \frac{d\nu(t)}{dt} = \nu(t) h(t) \quad (2)$$

Solving the second part of this equation gives

$$\nu(t) = \exp \left( - \int_0^t h(t') dt' \right) \quad (3)$$

which satisfies the obvious initial condition that  $\nu(0) = 1$ .

Thus we have for the form of the distribution of breakdown starting times

$$g(t) = h(t) \exp \left( - \int_0^t h(t') dt' \right). \quad (4)$$

Initially  $g(t)$  grows as  $h(t)$  but the influence of the exponential term rapidly becomes dominant and eventually  $g(t)$  decreases towards zero. The time interval over which  $g(t)$  is not negligibly small (the time width of the distribution) depends on the precise form of  $h(t)$  for the particular material and laser pulse. This interval, however, need not be very small compared to the laser pulse duration and can include times after the peak field is reached.

The most probable time for breakdown to begin is the time,  $t_M$ , when  $g(t)$  is maximum. Thus we consider



$$\frac{d(g(t))}{dt} \Big|_{t_M} = \left( \frac{d(h(t_M))}{dt} - (h(t_M))^2 \right) \exp \left( - \int_0^{t_M} h(t') dt' \right) = 0. \quad (5)$$

Since  $\exp \left( - \int_0^{t_M} h(t') dt' \right) \neq 0$ , eq. (5) holds when

$$\frac{d(h(t_M))}{dt} = (h(t_M))^2. \quad (6)$$

The solution for  $t_M$  is then found during the interval when

$$\frac{dh(t)}{dt} > 0. \quad (7)$$

Since the applied field,  $E(t)$ , determines the time dependence of  $h(t)$ , we have

$$\frac{dh}{dt} = \frac{dh}{dE} \frac{dE}{dt}. \quad (8)$$

It is physically reasonable to require that the damage rate increase as  $E$  increases and decrease as  $E$  decreases so that

$$\frac{dh}{dE} > 0 \text{ for all } t. \quad (9)$$

Thus  $g(t)$  reaches its maximum at a time when

$$\frac{dE}{dt} > 0 \quad (10)$$

or before the peak field strength is reached. This result agrees with the experimental data in figures 8 and 9 where the most probable time for breakdown to occur is always found before the time at which the optical field strength is maximum.

Further evidence for a probabilistic interpretation of the damage process is shown in figure 10. In this case a TEM<sub>00</sub> mode ruby laser pulse was focused inside a NaCl crystal and the transmitted laser intensity monitored with a fast photodiode-519 oscilloscope combination. As will be discussed in a later paper [10] the laser power was such that no self-focusing was likely. The photos in figure 10 are representative samples of the many that were taken and show that damage does not have to occur for every pulse. In addition, they show that when ruby laser induced internal damage does occur, it can begin before, at, or after the peak of the laser pulse.

The use of the breakdown or damage starting time to study the probabilistic nature of laser damage is especially important for materials with large  $K$ 's. In such cases one may not have sufficiently fine control over the laser pulse parameters to confidently resolve the region of intermediate damage probabilities. Thus data such as that in figure 10 can be used to assist in identifying such important characteristics of the damage mechanism as its statistics.

#### 4. Comments on the Probabilistic and Threshold Points of View

The last paragraph of the preceding section indicates just one of the problems involved in distinguishing between probabilistic and threshold-like phenomena. For all practical purposes, materials having large  $K$ 's can be considered to have a damage process which is governed by a well-defined threshold. It is possible however, as shown above, to perform studies of the damage dynamics which reveal some probabilistic properties.

The experiments described in this paper and in references 1 and 2 employed the techniques of irradiating a particular region of the sample until either damage occurred or 500 pulses spaced by a 1 or 5 second interval had been tried. A new region was then studied in the same manner at the same level of irradiation. Having done this at least 25 different times an estimate of the damage probability was obtained by dividing the number of damages by the total number of laser pulses. We then always examined the set of values obtained for the number of pulses required to damage at each region,  $N$ , to see if this set is distributed according to

$$f_N = p_1 (1 - p_1)^{N-1}. \quad (11)$$

If good agreement is found, then it is fair to say that the probability for damage in each region and for each pulse was always  $p_1$  even though damage did not always occur. Data of this sort, obtained from sets of  $\sim 100$  values of  $N$  for two different materials, fused quartz and  $\text{SrTiO}_3$ , are shown in figures 11 and 12 respectively.

If the fluctuations in  $N$  values which led to the probabilistic interpretation of damage represented local variations in the threshold for damage due to dirt, stresses or other material imperfections then the distribution of  $N$  values would not be given by eq (11). Instead,  $f_N$  would be determined by the density of the regions which had damage thresholds less than or equal to the maximum optical field strength. Suppose, for example, that the maximum optical field strength is such that 20 percent of the material could be damaged. Our experimental procedure would then generate approximately 5 places where  $N = 1$  and  $\sim 20$  where  $N = 500$  pulses with no damage, were recorded. We would then obtain a damage probability of  $p_1 \approx 5 \times 10^{-4}$ . Since the probability that 25 samples of numbers distributed according to eq (11) with  $p_1 = 5 \times 10^{-4}$  contain five 1's and twenty 500's is very small, the set of measured  $N$  values and the resulting  $p_1$  would not be accepted. This type of disagreement for the  $N$  value distribution would indicate material variations or laser fluctuations. We feel that these are minimal in view of figures 11 and 12. However, as in the case of the  $\text{LiNbO}_3$  sample discussed in reference 1, instances where such disagreements occurred would be reported separately from more reliable measurements of  $p_1$ .

Following a suggestion of E. Bliss we now consider the effect of varying the irradiated area on the rate of change of damage probability with applied optical power density. If the optical field is kept constant and the irradiated area is increased, then the number of electrons in the sample subjected to the optical field is increased. Thus if  $p = p(E)$  is the probability for breakdown when one initial electron is present, then

$$p'(E) = Np(E) \quad (12)$$

is the probability for breakdown when the area is increased and  $N$  initial electrons are now sampled. Here we assume that  $N \neq N(E)$ . If  $Np(E) > 1$  we must obviously set  $p'(E) = 1$ . From our damage data [1,2]

$$\frac{d(\ln p(E))}{d(1/E)} = -K \quad (13)$$

and so, from eq (12),

$$\frac{d(\ln p'(E))}{d(1/E)} = -K \quad (14)$$

Thus the two cases will appear in a log of probability vs  $1/E$  graph as sketched in figure 13. From this we find that

$$\Delta \left( \frac{1}{E} \right) = \Delta \left( \frac{1}{E'} \right) \quad (15)$$

where  $E$  and  $E'$  are defined in figure 13. Now, in arbitrary units

$$P = E^2 \quad (16)$$

where  $P$  is the power density. By differentiation we find

$$\Delta \left( \frac{1}{E} \right) = - \frac{\Delta P}{P} \frac{1}{2E} \quad (17)$$

and

$$\Delta \left( \frac{1}{E'} \right) = \frac{-\Delta P'}{P'} \frac{1}{2E'} \quad (18)$$

Therefore, the required fractional changes in power density necessary to achieve a change in damage probability from say  $p_i$  to  $p_j$  are related by

$$\frac{\Delta P'_{i \rightarrow j}}{P'_i} = \frac{E'_i}{E_i} \frac{\Delta P_{i \rightarrow j}}{P_i} \quad (19)$$

But  $E'_i/E_i < 1$  and so

$$\frac{\Delta P'_{i \rightarrow j}}{P'_i} < \frac{\Delta P_{i \rightarrow j}}{P_i} \quad (20)$$

$$\Delta P'_{i \rightarrow j} < \Delta P_{i \rightarrow j} . \quad (21)$$

In words, by increasing the irradiated area while maintaining a constant field one is performing many experiments at once and so to the extent that different regions are independent, the probability for at least one breakdown must increase with area. As a result, for example, if the area is large enough so that the damage probability changes from say  $10^{-3}$  to 1 over a small range in power density then it is possible therefore to perform experiments where the probabilistic nature of the damage process could be overlooked. (See figure 14).

The preceding consideration of the case of increasing the area irradiated while maintaining the electric field strength shows that the probability of at least one breakdown occurring also increases. However, the probability for damage per unit area is independent of the irradiated area and would be a useful quantity for describing a material's damage properties.

If the area of the beam is increased while the total pulse power is kept constant, the electric field,  $E$ , decreases and the damage probability decreases.

We see from this treatment that it is essential to maintain constant irradiated area or volume when comparing laser damage properties with different lasers or when comparing different materials. It is also critical to take this into account when comparing the work of different researchers.

In the probabilistic view a report of a damage threshold could correspond to 1) a very high value of  $K$  in eq (1), 2) a study of a much larger volume of material than that which is small enough to reveal the probabilistic properties of damage, 3) an experiment in which the intermediate range of power densities (power densities where  $0 < p_1 < 1$ ) was missed due to experimental procedure or 4) an experiment in self-focusing always produced an intensity so high that the intermediate range was never studied. It is also possible that there is more than one damage mechanism and that some mechanisms, such as avalanche breakdown, are probabilistic while others are threshold-like.

## 5. Summary

The first direct comparison of damage in transparent media produced by ruby and Nd:YAG lasers revealed that: 1) A material is less likely to damage when subjected to a particular optical field at  $0.69 \mu\text{m}$  than at  $1.06 \mu\text{m}$ ; and 2) The relationship between damage probability,  $p_1$ , and applied optical electric field strength,  $E$ , though still generally of the form  $p_1 \propto \exp(-K/E)$ , has a value of  $K$  at  $0.69 \mu\text{m}$  which is substantially greater than at  $1.06 \mu\text{m}$ . A tentative interpretation of these changes based on a modified optical frequency avalanche breakdown model was proposed. In addition the possibility that in some materials more than one damage mechanism may be operative was discussed.

The distribution of damage starting times was studied experimentally for two different materials. In contrast to the very small spread expected for a threshold process, broad distributions were found. Each distribution showed, in addition, that the most likely starting time for damage is before the time of maximum field. The properties of the measured distributions were described by the compound probability that breakdown occurs at a particular time, given that it has not occurred before that time and, as such, provided added evidence for the probabilistic interpretation of the  $1.06 \mu\text{m}$  damage process.

Several possible connections between the probabilistic and threshold-like interpretations of laser-induced damage were considered and the two points of view were shown not to be totally incompatible. Unnoticed, subnanosecond fluctuations in the laser pulse as the source of the statistics in the experiments were ruled out by evidence showing that only one or at most a very few longitudinal modes could oscillate in our lasers. This meant that shortest possible duration of any fluctuation was still long enough to have been detected by our fast photodiode-519 oscilloscope monitor system.

## 6. Acknowledgements

The authors wish to acknowledge the invaluable experimental assistance of D. Bua. The work of D. Bua in automating the data recording and along with D. Fradin in establishing and interpreting the procedure which results in smooth laser pulses is especially gratefully acknowledged. Valuable discussions were held with E. Bliss, D. Milam, D. Fradin and F. Horrigan.



## 7. References

- [1] Bass, M. and Barrett, H. H., NBS Special Publication 356 (1971) p. 76 and IEEE J. Quant. Elect. QE-8, 338 (1972).
- [2] Bass, M., Barrett, H.H. and Holway, Jr., L.H., Scientific Report No. 1 for Contract No. F19628-70-C-0223 (February 1972).
- [3] Bass, M., IEEE J. Quant. Elect. QE-7, 350 (1971).
- [4] Guiliano, C. R., Hellwarth, R. W., Hess, L.D. and Rickel, G. R., Semiannual Report No. 2 for Contract No. F19628-69-C-0277 (July 1970).
- [5] Evtuhov, V. and Neeland, J. K., "Pulsed Ruby Lasers," Lasers, Vol. 1, ed. A. K. Levine (M. Dekker, Inc., New York, N.Y.) (1966).
- [6] Yablonovitch, E., Ph.D. Thesis, Harvard University (June 1972).
- [7] Seitz, F., Phys. Rev. 76, 1376 (1949).
- [8] Kane, E. O., Phys. Rev. 159 624 (1967).
- [9] Merker, L. and Cobb, J., N. L. Industries, private communication.
- [10] Fradin, D. W., Yablonovitch, E. and Bass, M. "Comparison of Laser Induced Bulk Damage in Alkali-Halides," 4th ASTM-NBS Symp. on Damage in Laser Materials (1972).

## 8. Figures

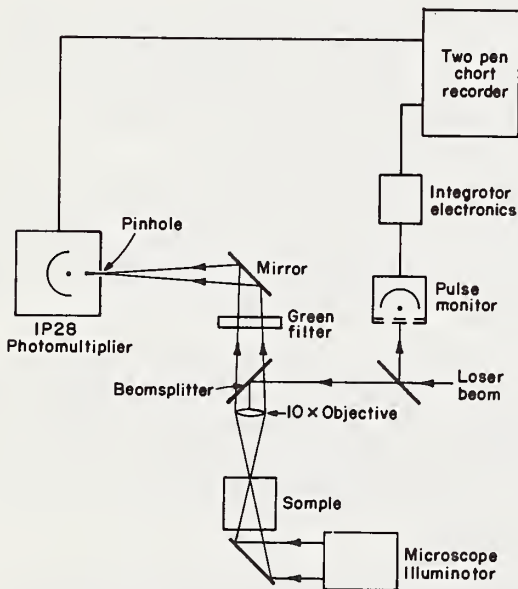


Figure 1. Schematic diagram of automatic pulse and damage monitoring apparatus.

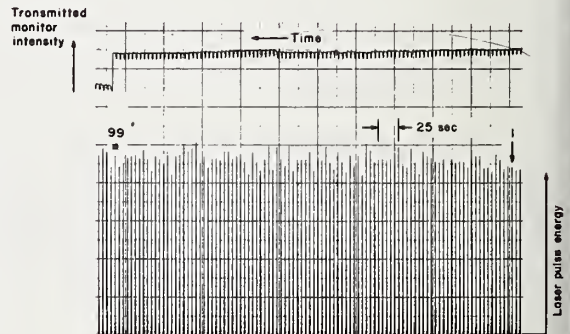


Figure 2. Record of exposures of X-cut crystalline quartz to pulses of ruby laser light  $\sim 9 \text{ GW/cm}^2$ .

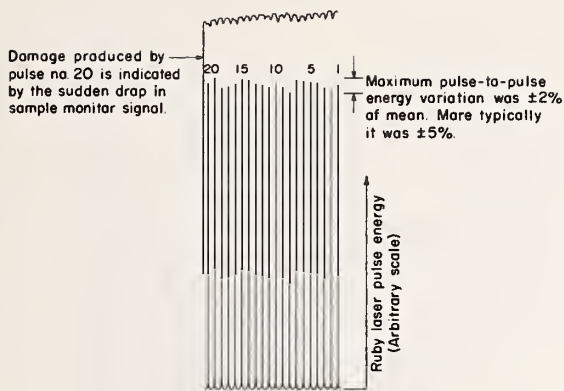


Figure 3. Ruby laser energy recording showing best pulse-to-pulse stability.

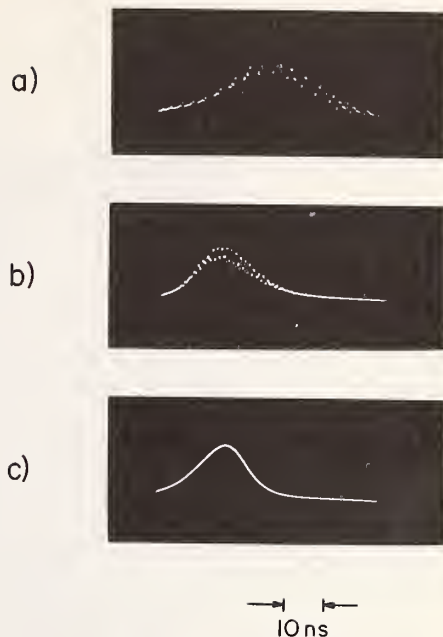


Figure 4. Effects of rod alignment on output pulses for Q-switched ruby. a) rod badly misaligned, b) rod coarsely aligned, c) cavity finely tuned.

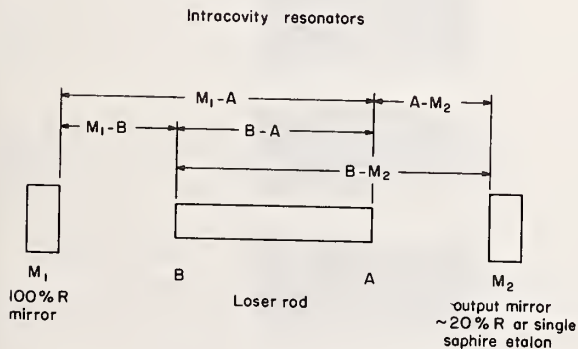


Figure 5. Schematic diagram of a laser cavity showing potential mode selecting intracavity resonators.

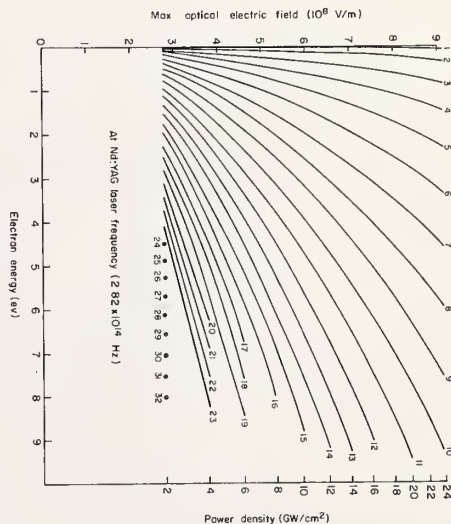


Figure 6. Electric Field at  $1.06 \mu\text{m}$  required to accelerate an electron to a particular energy. Each curve is numbered according to the number of half cycles of the field required to accelerate the electron assuming only perfectly lucky collisions occur. The number then is also the number of the collision which must occur for the electron to continue to gain energy from the field.

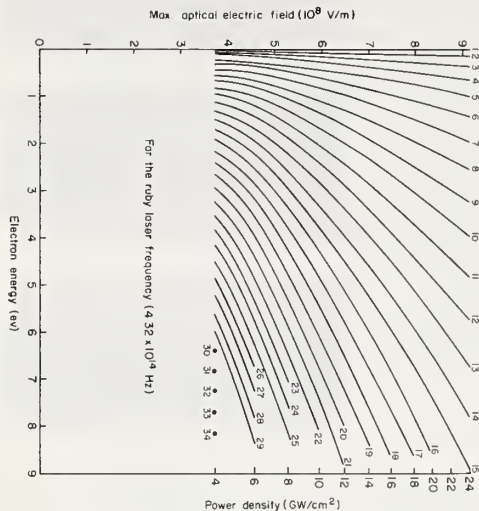


Figure 7. Electric field at  $0.69 \mu\text{m}$  required to accelerate an electron to a particular energy. Each curve is numbered according to the number of half cycles of the field required to accelerate the electron assuming only perfectly lucky collisions occur. The number then is also the number of the collision which must occur for the electron to continue to gain energy from the field.

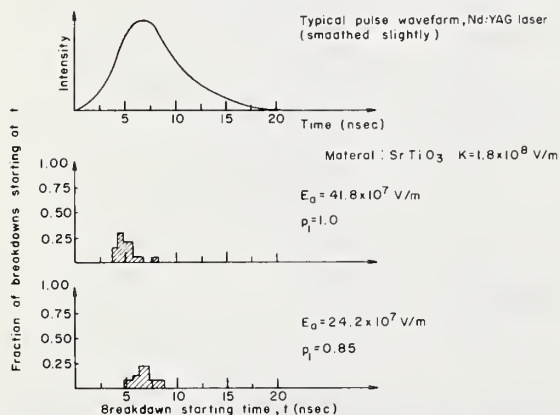


Figure 9. Distribution of surface breakdown starting times for  $\text{SrTiO}_3$  for two different damage probabilities.

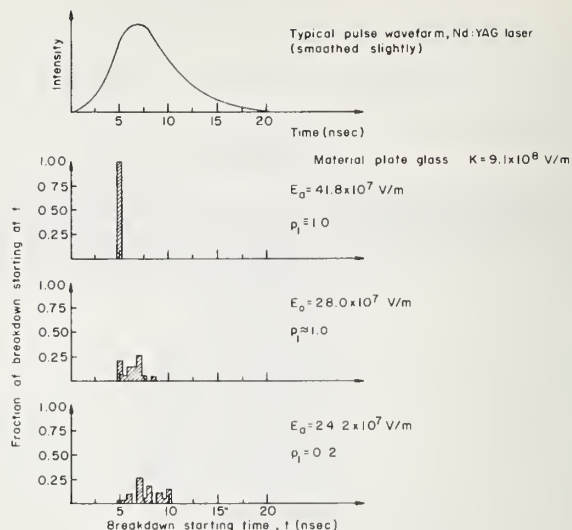


Figure 8. Distribution of surface breakdown starting times for plate glass for three different damage probabilities.

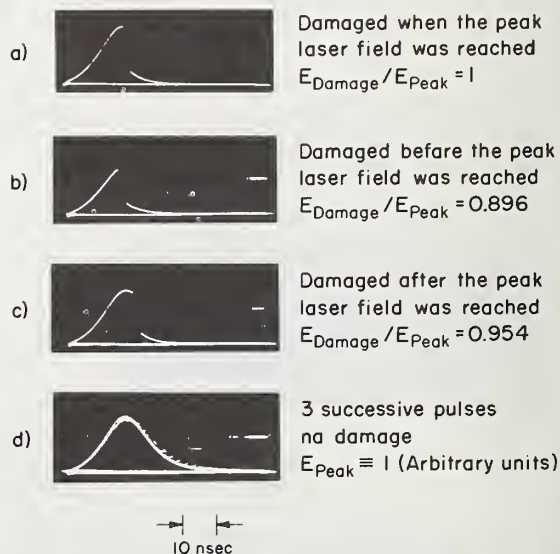


Figure 10. The occurrence of internal damage in  $\text{NaCl}$  due to ruby laser irradiation. The laser intensity transmitted through the sample is shown in these photos.



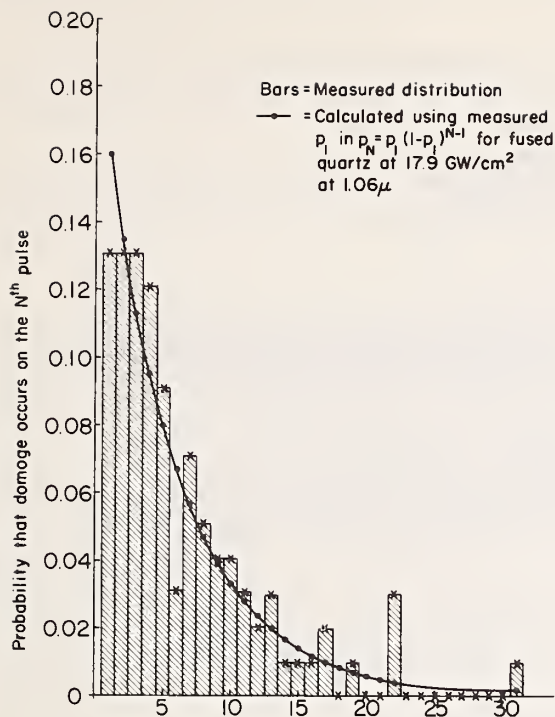


Figure 12. Probability that damage occurs on the Nth pulse versus N for SrTiO<sub>3</sub>. A 0.5 GW/cm<sup>2</sup> TEM<sub>00</sub> mode 1.06 μm beam was used.

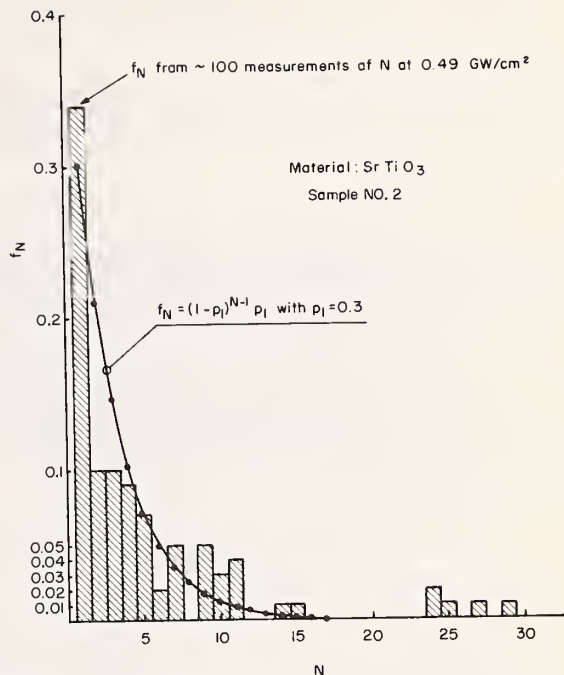


Figure 13. Sketch of a plot of the log of damage probability versus the inverse optical electric field for two different irradiated areas.  $p'(E)$  is the result for an irradiated area larger than used to obtain  $p(E)$ .

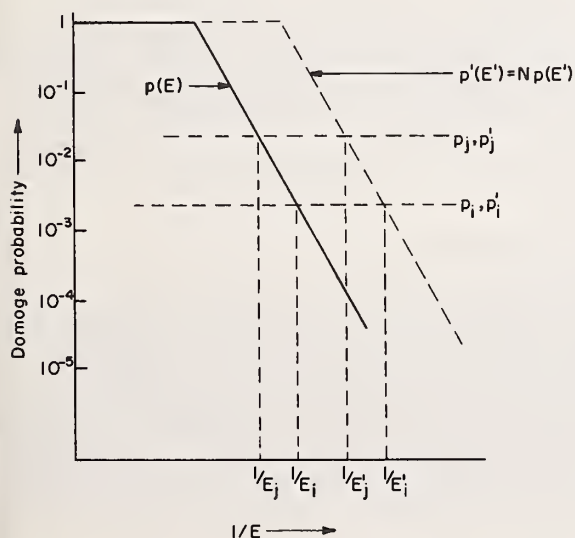


Figure 11. Probability that damage occurs on the Nth pulse versus N for fused quartz. A 17.9 GW/cm<sup>2</sup> TEM<sub>00</sub> mode 1.064 μm beam was used.

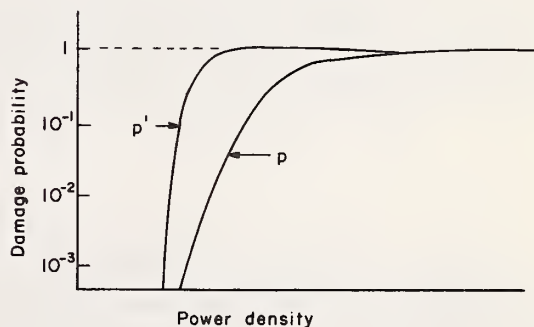


Figure 14. Sketch of a plot of the log of damage probability versus power density for the same two cases as in figure 13.

J. Lynn Smith

Physical Sciences Directorate  
U. S. Army Missile Command  
Redstone Arsenal, Alabama 35809

Surface damage of GaAs due to 0.694- and 1.06-micron beams from ruby and Nd-glass lasers has been investigated. The wavelengths employed represent photon energies above and below the bandgap of GaAs. For laser operation in the conventional mode, Ga-rich material developed on the surface to a greater extent than for Q-switched operation. Surface damage from Q-switched beams did not appear to depend on the absence, presence or type of doping, although the nature of the surface preparation was important. The damage threshold for Nd-glass laser illumination was approximately  $10^7$  W/cm<sup>2</sup>, only a little higher than that for ruby laser illumination. For Q-switched, Nd-glass laser beam exposure, the damage occurred in highly localized regions and appears to be connected with material flaws near the surface.

Key Words: GaAs, doping, laser induced damage, photoconductivity, surface surface finish.

## 1. Introduction

Damage induced in GaAs by both ruby and Nd-glass laser light has been investigated by Grasyuk and Zubarev [1]<sup>1</sup>. However, they did not look for a possible correlation between the type of damage or damage threshold and the type of dopant in the GaAs or the nature of the GaAs surface. Furthermore, their criterion for damage was cracking of the sample which they attributed to thermal shock, but experience shows that other types of damage occur before cracking which have important implications concerning the damage mechanism.

This paper summarizes a study [2]<sup>2</sup> in which GaAs was exposed to intense ruby and Nd laser light, both in the conventional and Q-switched modes. For the conventional mode work, a photoconductivity signal was obtained from n-type samples for correlations with damage, and an electron microprobe scan of regions which acquired high reflectivity was made. For the Q-switched mode operation, n-type, p-type, and undoped samples were exposed for surface damage studies. The effect of surface type on the damage threshold and the appearance of damage were studied using mechanically polished, chemically polished, and cleaved surfaces.

## 2. Experimental

### 2.1. Conventional Mode Experiments

The photoconductivity (PC) response to laser exposure in GaAs decreases dramatically if microcracks occur. Thus, the PC response was recorded to confirm that surface damage is not necessarily accompanied by bulk fracture. Raw data for the PC response to conventional mode ruby laser radiation (0.694  $\mu$ m) were recorded on dual trace oscillograms. One trace displayed laser power, and the other displayed the corresponding PC signal. Before and during laser exposure, current through the GaAs sample was kept practically constant. Thus, the voltage change was proportional to the change of inverse effective conductivity. The conventional mode pulse contains laser spikes of various heights. Therefore, only a few selected oscillograms yielded sufficient data for a plot of PC response vs laser power for a given range of total energy deposited. Curves were then plotted for different ranges of exposure. Visual examinations of the samples were performed throughout the experiment for correlation of PC response and sample

---

<sup>1</sup>Figures in brackets indicate the literature references at the end of this paper.

<sup>2</sup>Although some results discussed have not been submitted for journal publication, most will appear in greater detail in reference [2].

damage. Later, each sample was placed under a microscope and photographed. Analysis for Ga and As non-stoichiometry with an electron microprobe was performed on one degraded sample.

The Si-doped, n-type samples used for PC response measurements were about 0.23 cm wide, 0.009 cm thick, and 1 cm long. Electrical contacts were attached 0.45 cm apart by melting on In at 400°C for 5 min in a vacuum. The laser beam was incident upon the middle of the sample and focused to a 0.18-cm diam half-power circle.

No PC signal could be detected when Zn-doped, p-type GaAs was exposed to ruby laser light. For Nd-glass laser radiation (1.06  $\mu\text{m}$ ), a two-photon process is probably necessary to cause direct band-to-band excitation; therefore, the PC signal was too weak even with n-type GaAs for detection in this experiment.

## 2.2. Q-Switched Mode Experiments

Damage thresholds for surface damage of n-type, p-type, and undoped GaAs samples were measured by both Q-switched ruby and Nd-glass laser pulses of 20- and 60-nsec duration, respectively. Bulk material characteristics are shown in table 1. Little, if any, external beam focusing was necessary with these

Table 1. Bulk properties of GaAs used

Type and dopant	Carrier density ( $\text{cm}^{-3}$ )	Mobility ( $\text{cm}^2/\text{V}\cdot\text{sec}$ )	Preparation technique
n, Si	$1 \times 10^{18}$	3000	Czochralski
p, Zn	$2.5 \times 10^{19}$	74.3	Czochralski
n, Te	$2 \times 10^{18}$	$\geq 2800$	Czochralski
n, undoped	$\leq 5 \times 10^{16}$	$\geq 4500$	Czochralski
n, undoped <sup>a</sup>	$7 \times 10^{12}$	2910	Gradient freeze
Etch pit count on 100 surface of all materials approximately $10^4/\text{cm}^2$ .			

<sup>a</sup>Obtained from Monsanto Chemical Company. Other materials obtained from Bell and Howell Electronic Materials Division.

high power pulses ( $\sim 20$  MW). The beam area was several times that of the samples, and often two or more samples of different type were mounted together and simultaneously exposed to ascertain the relative merit of each type material. Threshold values obtained were averaged over several measurements for each material. Photomicrographs of surface damage were made for comparison. Q-switched operation was attained with passive dye cells for both ruby and Nd-glass lasers. Photographs of the sample during exposure to laser light were made to confirm the existence of a luminescent plasma or spark.

## 3. Results

### 3.1. Damage from Conventional Mode Operation

The PC-laser power data showed that cumulative surface damage reduces the PC response gradually. Most samples were not exposed sufficiently to produce the cracking which causes large, abrupt decreases of PC. The conventional mode pulse of  $\sim 1/2$ -msec duration was adequate for dissociation of GaAs, regardless of the dopant. For both 0.694- and 1.06- $\mu\text{m}$  laser flux, the damage appearance was similar on all samples and exhibited highly reflecting regions (figure 1a) which were investigated with the electron microprobe. The highly reflecting regions were found to be rich in Ga and depleted in As. Cracking occurred along cleavage planes for samples repeatedly subjected to high energy pulses ( $\gtrsim 5 \text{ J}/\text{cm}^2$  for the ruby laser).

### 3.2. Damage from Q-Switched Laser Light

The average power density at which surface damage is just observed (slight diffuseness in reflection, no cracking generally) for the Q-switched ruby or Nd-glass laser pulse is shown for various samples in table 2.



Table 2. Damage threshold for GaAs samples

Type and dopant	Surface orientation	Surface finish <sup>a</sup>	Threshold	
			0.694 $\mu\text{m}$ (MW/cm <sup>2</sup> )	1.06 $\mu\text{m}$ (MW/cm <sup>2</sup> )
n, Si	100	Chemical polish	8 $\pm$ 2	13 $\pm$ 5
p, Zn	100	Chemical polish		
n, Te	100	Chemical polish		
n, undoped	100	Chemical polish		
n, undoped	110	Cleaved	-	13 $\pm$ 5
n, undoped	100	Mechanical polish	-	10 $\pm$ 5

<sup>a</sup>All except cleaved surfaces prepared by supplier. Chemical polish utilizes Bromine methanol etchant.

Of importance is the fact that the damage threshold for 1.06  $\mu\text{m}$  laser flux is not much greater than that for 0.694  $\mu\text{m}$  laser flux. Yet the former has photon energy below the  $\sim 1.45$  eV bandgap and the latter has photon energy above the bandgap.

It is very significant that damage to the best GaAs surfaces for 1.06- $\mu\text{m}$  radiation occurs in highly localized regions (figure 1c). These regions are often only 2 or 3  $\mu\text{m}$  in diameter and appear to have even smaller origins. Inhomogeneity of the laser beam cannot account for this degree of localization since, for geometry used, diffraction and interference patterns at the sample from inhomogeneous near-field laser emission could have spacial periods no smaller than about 50  $\mu\text{m}$ .

It is also significant that the damage is independent of whether the GaAs is n-doped, p-doped, or the purest undoped material available. Noteworthy, too, is the fact that the damage is strictly an input surface effect. No internal damage was seen upon inspection with an optical microscope and an infrared converter.

Major variations in the appearance of surface damage shown in figure 1 are as follows: (1) Unlike the case for conventional mode pulsing (figure 1a), Q-switched pulsing does not produce any great amount of the highly reflecting, Ga-rich phase during 20-60 nsec exposure time; however mechanical deformation appears to extend deeper beneath the surface. (2) Surface damage features are smoother (suggesting overall melting) for 0.694- $\mu\text{m}$  radiation than for 1.06- $\mu\text{m}$  radiation (figures 1b and 1c). (3) Although the damage threshold is not much lower, damage from 1.06- $\mu\text{m}$  radiation is more extensive on mechanically polished surfaces (figure 1d) than on cleaved or chemically polished surfaces. Whereas damage runs along mechanical scratch lines on the mechanically polished surface, it occurs as highly localized craters on both cleaved and chemically polished surfaces.

#### 4. Discussion

No damage threshold is calculated for the conventional mode (as is for the Q-switched mode) since the laser radiation is spiky and damage is cumulative over the  $\sim 1/2$ -msec duration. The gradual decrease of PC signal with repeated laser beam exposure of that n-type GaAs which did not acquire microcracks is interpreted as shielding by the Ga-rich phase found to develop on the surface.

##### 4.1. Theories for Catastrophic Damage

The 0.9- $\mu\text{m}$  internal emission from GaAs laser diodes lies between the 0.694- and 1.06- $\mu\text{m}$  wavelengths employed in this study. During lasing, population inversion in the active region of the GaAs diode allows very little absorption of internal emission. Similarly, absorption at 1.06  $\mu\text{m}$  is slight, although the reason is that the 1.06- $\mu\text{m}$  photon energy is slightly below the  $\sim 1.45$ -eV bandgap of GaAs. The obvious similarities between the physical situation presently studied and that of GaAs laser junctions are of practical importance. Therefore, the two main theories for catastrophic surface damage of GaAs laser diode junctions are of relevance here. These theories are briefly presented and discussed in what follows.

Dobson and Keeble [3] have proposed that optical energy is absorbed by inhomogeneities near the surface which causes heating. According to their view, resulting hot spots cause local decreases of bandgap which further increase absorption. Thus, local heating increases until Ga and As dissociate,

leaving a Ga-rich phase on the surface. They suggest the initial inhomogeneities may be local doping variations. On the other hand, Kressel and Mierop [4] propose that the optical flux is absorbed through stimulated Brillouin scattering (SBS) which results in the formation of destructive acoustical waves.

There are several reasons why catastrophic surface damage in GaAs is unlikely to result from stimulated Brillouin scattering: (1) Laser damage thresholds for quartz, sapphire, and glass which show evidence of SBS [5,6] are two or more orders of magnitude higher than that for GaAs. (2) Grasyuk and Zubarev [1] designed an experiment to observe the existence of laser induced SBS in GaAs and could find no such effect, although the material degraded. (3) Damage observed by Giuliano [6] in glass was mostly on the output face, whereas damage in the present study always occurred on the input face. (4) For 1.06- $\mu\text{m}$  laser radiation, the present study shows damage craters on GaAs which are much smaller than regions where the optical flux is coherent and reasonably uniform. (5) Although general melting appears to occur between craters with 0.694- $\mu\text{m}$  laser radiation, the craters themselves no doubt originate the same way as when 1.06- $\mu\text{m}$  radiation is used. (The damage thresholds are not greatly different.) Yet the penetration for 0.694- $\mu\text{m}$  light is only on the order of 1  $\mu\text{m}$ , hardly enough for SBS to occur.

Evidence from the present study lends general support to the theory of Dobson and Keeble, but differs by minimizing the role of doping inhomogeneities. As previously mentioned, the 1.06- $\mu\text{m}$  radiation damage thresholds for n-type, p-type, and the purest undoped GaAs available were about the same, and the appearance of damage (excluding mechanically polished surfaces) was the same. As seen in figure 1d, the mechanical flaws associated with polishing greatly increase susceptibility to damage. No assertion is made that the presence of minor doping inhomogeneities cannot play a role, but simply that it is not the most influential factor in damage from  $\sim 10^7$  W/cm<sup>2</sup> laser pulses. Calculations for the upper-limit energy absorption of a free electron during a half cycle of the electric field associated with  $10^7$  W/cm<sup>2</sup> gives only  $\sim 10^{-4}$  eV, much less than the GaAs bandgap. Thus, the breakdown cannot result from an electron avalanche in the classical sense. This in itself, however, does not imply that collision ionization due to hot conduction electrons excited by inverse Bremsstrahlung does not take place. Yet each free electron in GaAs excited to ionization energy with 1.06  $\mu\text{m}$  light by inverse Bremsstrahlung would have to reach this energy through more than one event. The reason for this is that the photon energy is less than the bandgap, momentum must be conserved, and the electron also undergoes lossy collisions. The lack of detectable influence on the damage threshold by degenerate n-type or p-type doping behooves any damage theory involving free electrons to explain the insensitivity of the threshold to initial free electron concentration and to the possible influence of hole density on free electron lifetime.

The high localization of damage sites with Q-switched laser light indicates inhomogeneity of material susceptibility. It cannot be concluded from this study whether the intrinsic threshold is much higher. Generally speaking, however, the results of this study clearly suggest that for pulsed, near-bandgap photon flux, where gross, direct electron-hole pair creation and recombination are minimal, the flux limit ( $\sim 10^7$  W/cm<sup>2</sup>) is due to material flaws made more susceptible to damage by properties inherent to a surface.

## 5. Acknowledgments

Appreciation is expressed to P. P. Budenstein of Auburn University who acted as consultant, to C. W. Austin for electron microprobe work, and to R. A. Shatas for comments on writing the manuscript.

## 6. References

- |  |   |
|--|---|
| [1] Grasyuk, A. Z. and Zubarev, I. G., Sov. Phys.-Semicond. <u>3</u> 576 (1969).       | [4] Kressel, H. and Mierop, H., J. Appl. Phys. <u>38</u> 5419 (1967).                           |
| [2] Smith, J. L., J. Appl. Phys. (scheduled for August 1972).                          | [5] Chiao, R. Y., Townes, C. H., and Stoicheff, B. P., Phys. Rev. Letters <u>12</u> 592 (1964). |
| [3] Dobson, C. D. and Keeble, F. S., Proc. Internat. Symp. GaAs, Reading, 1966, p. 68. | [6] Giuliano, C. R., Appl. Phys. Letters <u>5</u> 137 (1964).                                   |

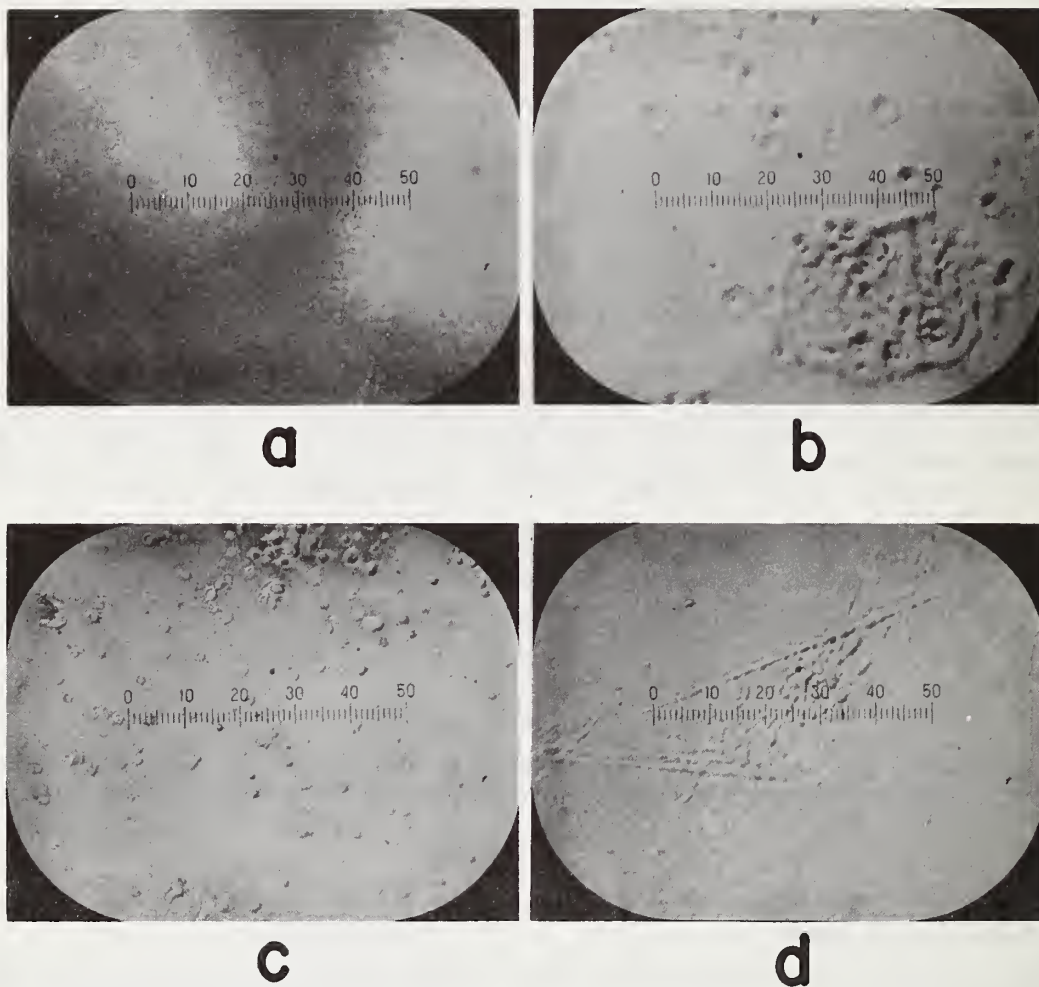


Figure 1. Photomicrographs of different types of laser damage on GaAs surfaces. (The scale in each figure is  $2.5\text{ }\mu\text{m/division}$ . Damage is from (a) conventional mode pulses, (b)  $0.694\text{-}\mu\text{m}$  Q-switched pulses, (c)  $1.06\text{-}\mu\text{m}$  Q-switched pulses, and (d)  $1.06\text{-}\mu\text{m}$  Q-switched pulses on mechanically finished surface.)



Jhan M. Khan

Lawrence Livermore Laboratory  
Livermore, California 94550

The relatively new field of Surface Science is concerned with the measurement of physical and chemical properties of well characterized surfaces. The ability to characterize these surfaces has been steadily increasing due to the development of new tools, or the application of older techniques to surface interrogation. The overwhelming result of surface investigation is to draw attention to the difficulty of obtaining such well-characterized surfaces. With this realization in mind, it is highly instructive to review the conventional methods of creating surface conditions. The assumptions involving the conditions at prepared surfaces or interfaces must be reexamined. New procedures may have to be evolved to control conditions to even assure reproducibility. Only when this has been accomplished can measurements of surface damage thresholds be taken as intrinsic characteristics of prepared surfaces.

Key Words: Laser damage, surface science, thin films

## 1. Introduction

The purpose of this survey is to show how the tools of surface analysis might provide some answers to our current concerns of predictability and reliability of optical elements in high power laser applications. The lack of predictability of the index of refraction and growth characteristics of coated optics is well established and accepted in thin films. Although not as well established, reliability seems also to be affected by the surface condition. This paper will attempt to convey the diagnostic techniques necessary to characterize the near surface of solids.

In section 2, selected examples are employed to establish the tentative relevance of surface effects to reflectivity of metallic surfaces and the index of refraction of disordered surfaces. In section 3 is presented a brief development of materials from the simplest form, the monocrystalline solid, to impurity effects in polycrystalline films.

Section 4 contains a review of the commonly employed surface diagnostic methods and the basis of their operation. Section 5 attempts to point out the advantages and disadvantages of the common surface preparation methods, including thin film deposition. These considerations only concern themselves with characterization, not application.

The conclusion that is drawn by the author is that in almost all practical situations, there is only the crudest knowledge of the structure and composition of the surfaces employed in optical elements. If this is a problem, then surface analytical methods and instruments exist that can be used to supply such knowledge. Such exercises in characterization are generally time-consuming and require expensive, sophisticated technology. The semiconductor industry has felt this has been justified. In addition to analysis, certain of the tools have been incorporated into the production procedures as on-line monitors. Perhaps this may also become the case in the area of high power laser optics.

## 2. Optical Predictability and Reliability

Predictability and reliability are both necessary when considering energy absorption in optical elements. These both imply a knowledge of the surface characteristics of the system in terms of physical, chemical and optical properties. Failure due to excessive energy absorption may take place as a result of the departure of the system from initial design parameters or a change in the system after initial preparation. These general comments apply to both simple terminations of a bulk material and

---

\*Work performed under the auspices of the U. S. Atomic Energy Commission

structures resulting from a coating operation. The effects of the surface condition will vary from material to material. It would be unwise to generalize extensively.

A question that remains to be answered is "Are variations in surface characteristics responsible for low reliability or low damage thresholds of surfaces?". The reported results of Swain (1)<sup>1</sup> and Divit (2) in altering surface thresholds by mechanical/chemical treatments suggest a possible importance. These treatments are being reexamined by various experimenters.

The importance of the surface condition in influencing the reflectivity of metallic surfaces has been established by Bennet.(3) In addition, there is ample evidence that the complex index of refraction of solids can be strongly effected by the surface structure. (4).

## 2.1 Reflectivity and Index of Refraction

Bennet (3) has studied the reflectivity of surfaces of silver, gold, and aluminum. In this work the effect of overcoats, tarnish, and surface roughness were investigated. Bennet has shown that there are changes in the fundamental absorption characteristics of the metal surface due to the changes in the electronic states at the surface. In addition, surface roughness in the A range were observable in its effect upon the scattering characteristics of the surface for 10.6  $\mu\text{m}$  light.

In a recent ellipsometric study of the surface of silicon, Vadam (4) has observed the effect of surface preparation methods on the index of refraction. He was able to determine the cause of variations in the index of refraction from bulk values and connect this cause with structural disorder of  $\mu\text{m}$  depth for mechanically polished, ion-bombarded, and cleaved surfaces. The index resulting from this disorder was comparable with that observed for some amorphous surfaces produced by vapor deposition. These latter values, however, show variations that indicate there is no unique "amorphous" index of refraction.

## 2.2 Surface Integrity

The observations noted in 2.1 clearly indicate that if structure and surface chemistry can effect the optical properties, then changes in these two quantities will also alter the system characteristics. In practical applications, optical surfaces are exposed to varying and potentially hostile environments. Further study should be made of methods creating stable surfaces of the desired optical properties.

## 3. Solid Surfaces

The term "surface" has no unique meaning when applied in the field of surface science. The depth of influence of a surface very strongly depends upon the particular phenomena that is being studied. It is fair to say, however, that most influences subside in dimensions greater than 10  $\mu\text{m}$ . To attempt to clarify this somewhat, the following portions of this section will consider a few cases.

### 3.1 Monocrystalline Solids

This is the purest and simplest case we can choose. Even here there exists some complexity. Let us consider several examples of different depth dependences.

#### 3.1.1 Influence of Surfaces on Electron Motion

The characteristic distance of unimpeded motion is termed the mean free path (MFP). The MFP is a function of the energy of the electron and the solid in which it resides, as well as the temperature of the solid. When the electron is farther than several MFP's, it should not be influenced by the boundary condition imposed by the surface. This would typically be of the order of 500 A. (5) Therefore, coupling of energy to electrons less than this depth should show some effect on the surface.

#### 3.1.2 Atomic Lattice Constant

Distortions of the atomic lattice result from the lack of symmetry in the crystalline field at the surface. There will be effects upon the vibration amplitude near the surface. In addition, there may be the appearance of two-dimensional structure on the surface that does not reflect the bulk structure. These general effects may evidence themselves in altered chemical reactivity on the surface. The dimension of these effects may be as much as 100 A.

---

<sup>1</sup> Figures in parenthesis indicate literature references at the end of this paper.

### 3.1.3 Surface Optical Reflection

This refers to the attenuation of the field of a reflected electromagnetic wave (photon) at the surface of a metal or under total external reflection from a dielectric. These dimensions may range from the skin depth to the wavelength of the light, i.e., 500 Å to 10,000 Å, depending upon the conductivity of the solid. (3)

### 3.2 Polycrystalline Solids

The statements made in 3.1 must be modified to include the effect of grain boundaries and variation in crystal orientation of the grains. Many crystalline materials are not isotropic with respect to the properties noted in 3.1. Therefore, these properties will be effectively averaged over all angles. In addition, the grain boundaries will represent scattering sites for any conduction electrons, and may well influence energy absorption characteristics.

### 3.3 Thin Films

Typical thin films are comparable to or thinner than grain dimensions. These, then, may be looked upon as a special case of the polycrystalline solid. The thin film has structural characteristics that are a result of the method of fabrication. The conditions of deposition will strongly influence the crystalline structure, void size and shape, and surface topography. This is a result of nucleation and growth phenomena that is well documented. Up to this point we have assumed all of the ideal conditions, i.e., purity and stoichiometry. When these conditions are relaxed, matters become less predictable.

### 3.4 Role of Impurities

Two classes of impurities exist: surface and bulk. There is a liberal interchange between these, in practice. Burton (6) modeled the equilibrium concentration of impurities on crystal surfaces. In his model he generated the following expression:

$$S = B \exp \left( -\Delta F / kT \right)$$

where S and B are the surface and bulk impurity concentrations, respectively, and  $\Delta F$  is the change in free energy of the crystal when the impurity atom is moved to the surface. By considering surface sites, and substitutional and interstitial sites he concluded that at temperatures below the melting point, impurity atoms that are strongly bound to the solvent atoms will move to the bulk, while impurity atoms for which the impurity-solvent bond is weaker than the solvent-solvent bond will concentrate on the surface. Rate constants will, of course, be determined by diffusion constants. For the surface concentrating impurity, the bulk may represent a semi-infinite reservoir just waiting for conditions to become favorable for mass transport, such as temperature rise or radiation damage (radiation enhanced diffusion). This temperature could be due to the repeated exposure of the surface to high power laser radiation.

Bulk impurities may supply low lying donor electron levels in the case of dielectrics. This phenomena is exploited in the semiconductor industry. These impurities may also influence mechanical properties, as they can affect defect motion. These impurities may be important for some damage mechanisms.

At surfaces of grains or on the air-solid interface, impurities may significantly influence physical, chemical, and mechanical properties in what may appear to be unpredictable ways.

### 3.5 Nonstoichiometry in Chemical Compounds

We are specifically interested in deviations from the Law of Definite Proportions. These deviations occur most predominately in solids. The observations of variable composition were put on a firm theoretical basis by Wagner and Schottky (7) in 1931 in a statistical thermodynamic analysis which established the relation between lattice defects and nonstoichiometry, and showed that all crystalline inorganic compounds are inherently nonstoichiometric. (8)-(12) In any real crystal above absolute zero, there is a finite concentration of point defects. Let us consider one case to illustrate.

For a binary compound MX, there are six simple types of point defects (assuming no impurities):

- a) M vacancies
- b) X vacancies
- c) Interstitial M atoms or ions
- d) Interstitial X atoms or ions
- e) M atoms on X lattice sites
- f) X atoms on M lattice sites



In any given crystal, all six types may be present. Of these types b, c, and e will lead to an excess of M atoms in the crystal, while types a, d, and f will lead to an excess of X atoms. The concentrations of these defects will not in general be equal, and the crystal will be nonstoichiometric.

The above observations apply to the "perfect" single crystal. In practice, the materials that are commonly available have additional complicating factors. These include impurity concentrations, grain boundaries (precipitation sites), and for thin films a potential dominance of purely surface effects (surface states, structural irregularities, etc.)

The importance of deviations from stoichiometry lies in the changes in optical absorption that may accompany them. This has been observed in  $\text{As}_2\text{S}_3$ , where excess sulphur produces absorption bands in the 10  $\mu\text{m}$  wavelength range (13).

#### 4. Surface Characterization Methods

In this section a variety of techniques will be presented that are commonly used to determine the properties of solids in the first few  $\mu\text{m}$  or less. No single measurement is able to characterize the surface. The current trend in surface analysis is to combine more and more of the methods into one experimental system to allow complimentary characterizations.

##### 4.1 Techniques Based upon Scattered Primary Electrons

An incident beam of electrons may interact with a solid in two ways reflecting the wave-particle duality of quantum mechanics. As a wave the electron may be diffracted by an orderly array of atoms to give information related to atomic arrangement. In addition the electron may lose energy to the solid by collisions. In resonant processes the energy loss may be associated with excitation of specific levels within the atoms or excitation of collective motion of electrons in the conduction band of metals (plasmons). A special case of the collision case is elastic scattering where the electron loses no significant portion of its initial energy.

###### 4.1.1 Low Energy Electron Diffraction (LEED) (14)(15)

This technique observes the two-dimensional structure on the surface of monocrystalline solids. It employs a primary beam of monoenergetic electrons of energy less than several hundred electron volts energy. LEED is used to study nucleation and growth phenomena for adsorbed or deposited species on crystal surfaces.

This technique is limited in applicability by the need for preparing clean, well-ordered surfaces. Many materials undergo phase transitions during the cleaning process that leave the surface in a disordered state when averaged over beam dimensions of the order of a millimeter.

###### 4.1.2 Inelastic Electron Scattering (IES) (16)

By measuring the energy loss spectrum of these scattered electrons information may be obtained regarding electronic excitations. These excitations play an important role in the absorption of laser photons in metallic reflectors. The technique may be combined with LEED. Detailed information may be obtained for collisions involving specific energy and momentum loss within the solid.

##### 4.2 Techniques Based on Secondary Electron Emission

For purposes of surface analysis, attention is focused upon the characteristic portion of the secondary electron spectrum. These characteristic electrons emitted are produced by specific transitions within the atoms of the solid. They are somewhat analogous to x-ray fluorescence. The characteristic electrons studied here are generally quite low in energy and originate in the first 100 Å of the surface or less. Surface contamination is a very serious problem for these measurements.

###### 4.2.1 Auger Electron Spectroscopy (AES) (17)(18)

The AES technique employs an electron beam to excite the atoms that emit the auger electrons. Under most circumstances AES gives an elemental analysis of the first several atom layers of the surface with a sensitivity of 1/10 of an atom layer (i.e., about  $10^{14}$  atoms/cm<sup>2</sup>). In general the results are qualitative or at most semi-quantitative.

ESCA also looks at characteristic electrons, but these are photo electrons. An intense source of characteristic x-rays is employed. The principle difference between AES and ESCA lies in the sharpness of the electron spectrum observed. For AES the full width at half maximum (FWHM) is of the order of 1 eV, while for ESCA it may be as low as 0.1 eV. This latter value of the FWHM allows ESCA to observe chemical shifts in a number of cases. With information of this sort, it is possible to identify the binding state of an atom on the surface, thereby shedding light upon the surface chemistry of the system.

## 4.3 Techniques Based on Scattered Positive Ions (20)

Ions incident upon a solid sample lose energy by a variety of interactions: electronic excitation and ionization and nuclear scattering. The latter may be either elastic or inelastic. Elastic scattering implies a conservation of momentum and kinetic energy. Three quantities are of interest: 1) energy of recoil of the incident particle, 2) the cross section or probability of scattering the incident particle into a specific element of solid angle, and 3) the probability that the incident particle is charged after the scattering event. We will wish to look at two regimes of scattering, i.e., high energy ( $E_0 \gg 10$  keV) or low energy ( $E_0 \ll 10$  keV). In both cases the recoil energy,  $E_1$ , from a two-particle event is given by:

$$\frac{E_1}{E_0} = \frac{M_1^2}{(M_1 + M_2)^2} \left[ \cos \theta + \left( \frac{M_2^2}{M_1^2} - \sin^2 \theta \right)^{1/2} \right]^2 \quad (2)$$

where  $M_1$  and  $M_2$  are the masses of the primary ion and the target atom respectively, and  $\theta$  is the scattering angle in laboratory coordinates.

## 4.3.1 High Energy Scattering (21)(22)

Typically, the incident energies are of the order of 1 MeV and the incident ions are low mass ( $H^+$ ,  $He^+$ ,  $C^+$ ,  $N^+$ ,  $O^+$ ). The detection systems are usually only energy sensitive, so the charge state is irrelevant. The application of this technique yields:

1. Mass analysis.
2. Depth distribution to the order of 0.5  $\mu m$  with a resolution of 300 Å or greater.
3. Spatial distribution with typical resolution of 1 mm.
4. Sensitivity:  $M_2 > M_s$  (bulk masses):  $10^{14}$  atoms/cm<sup>2</sup>

$$M_2 < M_s : 10\% \text{ of } M_s$$

From the above it is clear that the mass analysis is averaged over a minimum depth of 300 Å or so.

## 4.3.2 Low Energy Ion Scattering (23)(26)

Typical incident energies are of the order of several keV. Under these conditions only incident ions that are scattered from the outermost atoms of the solid remain charged. If the detection system uses electrostatic or magnetic analysis (as is usual) then only these charged species are detected. Therefore, this technique gives a mass distribution of those atoms in the first atom layer of the solid.

## 4.4 Technique Based on Optical Reflection (Ellipsometry)

This optical technique is based upon the measurement of the reflectivity of the components of light with planes of polarization perpendicular and parallel to the plane of incidence (4)(27)(31). The power of this technique is illustrated by its application to a reflecting silicon substrate having a damaged surface layer covered by a transparent film. The method was employed to characterize surfaces subjected to a variety of treatments: mechanical polishing, chemical etching, sputtering by argon ions, cleavage and annealing. The resulting reflectivities and indices of refraction obtained were very sensitive to treatment. This sensitivity indicates that ellipsometry is a technique that may have a valuable place in the laboratory which studies optical surfaces.

## 4.5 Scanning Electron Microscopy (SEM)

The SEM conventionally displays the intensity of the low energy secondary electron spectrum and the high energy elastically scattered electrons. In the former case surface topography is observed

due to changes in efficiency of emission. The latter case utilizes the increase in the probability or cross section for scattering with charge on the scattering atom. Thus a display is presented of a relative distribution of "light" versus "heavy" atoms on the surface.

The SEM may be upgraded to allow incorporation of auger analysis (SEM-AES) (32). The changes are most associated with improvement in the vacuum environment. The partial pressures of condensible, reactive species should be very much below  $10^{-8}$  torr. Under these conditions, the AES-SEM systems allows the study of surface composition with a spatial resolution comparable to the beam dimensions, i.e., 100 Å.

Table 1.

Analysis method	Qualit.	Quant.	Elemental	Chemical	Structural	Depth	Depth resoc.	Surface resoc.	Comment
LEED <sup>(a)</sup>		X			X	3 Å	---	mm	2-D surface structure
IES <sup>(b)</sup>	X	X	X			3 Å	---	mm	Collective electron oscillation
AES <sup>(c)</sup>	X		X			10 Å	---	mm	Difficult to apply to dielectrics
ESCA <sup>(d)</sup>	X		X	X		100 Å	---	cm	Difficult to apply to dielectrics
HEBS <sup>(e)</sup>		X	X			5000 Å	300 Å	mm	
LEBS <sup>(f)</sup>		X	X			3 Å	---	mm	
ELL <sup>(g)</sup>		X			X	100 Å	---	mm	Determine index of refraction-films on substrates
SEM <sup>(h)</sup>	X		X		X	100 Å	----	100 Å	
SEM-AES	X		X		X	100 Å	---	100 Å	

(a) Low Energy Electron Diffraction

(b) Inelastic Electron Scattering

(c) Auger Electron Spectroscopy

(d) Electron Spectroscopy for Chemical Analysis

(e) High Energy Ion Backscattering

(f) Low Energy Ion Backscattering

(g) Ellipsometry

(h) Scanning Electron Microscopy

#### 4.6 Summary

Table I shows a comparison of the surface characterization methods currently available. Many of these exist as commercially available tools, some as purely experimental research instruments.

#### 5. Surface Preparation Methods

Although surface preparation is usually associated with cleaning, the term will be expanded in its meaning here to include the creation of surfaces or interfaces by deposition methods.

As a general statement all surfaces must be considered reactive. That is, the surface is prone to the accumulation of impurity atoms, whether they be chemisorbed or physisorbed. The origin of the impurities may be internal or external to the bulk.



As a result of the foregoing, all operations involving the surface should be accompanied with some experimental test of the surface condition. In the extreme, as many of the operations as possible should be performed in a controlled environment so that the full history of the surface is known. In practical circumstances, this may not be possible on a routine basis. Under these conditions the systems employed should be fully understood prior to their use, so that limits may be placed on the contributions of different sources of imperfections.

## 5.1 Preparation of Solid Surfaces

The starting point for preparation of a surface is the bulk material. In view of the discussion in section 3.4, the chemical composition of the bulk should be ascertained prior to any surface preparation. This is crucial! In addition, the completeness of the chemical analysis must also be assured. Given confidence in the bulk composition, then a variety of surface preparation methods may be applied.

Each method or sequence of methods of surface preparation has its own set of advantages and disadvantages, so that the techniques to be used for a given application should, in principle, be the result of systematic study of the different preparation methods on the desired physical and chemical properties of the finished surface.

### 5.1.1 Mechanical Operations

The act of cutting, grinding, or polishing will inherently cause disorder in mono or polycrystalline solids. In addition, the polishing agents will be present in or on the surface. The depth of these effects will vary but may extend many microns in general.

The principal purpose of mechanical operation is to give the sample an overall shape and smoothness. Typically, after cutting and grinding of hard material, polishing is employed. The last stages of polishing usually employ a succession of finer and finer abrasive powders in a suspension. The last particle size may be a fraction of a micron. Disruption and contamination may be expected to be found to depths of 3 to 5 times the particle diameter. It will be necessary to remove this portion of the surface to remove such effects, if they are found to be detrimental.

### 5.1.2 Chemical Etching

To remove surface material, a chemical etch is frequently employed. The particular etch employed will vary with the solid. Again, care must be taken. Some of the problems encountered are:

- 1) Concentration of less soluble impurities at the surface,
- 2) Impurities in the etchant remaining bound to the surface,
- 3) The etchant may partially decompose on the surface, leaving reactive elements behind (such as flourine),
- 4) Selective action by the etchant that will partially destroy the smoothness left by the final stage of polishing. As in all cases of surface preparation, the surface should be characterized following the etching operation.

### 5.1.3 Ion Bombardment

A recent technique that has been used to clean surfaces is inert ion bombardment at low energies (10 keV). Typical ions are  $\text{Ar}^+$ ,  $\text{Ne}^+$ ,  $\text{Xe}^+$ . Material removal may be effected with reasonable efficiency. Two potential problems arise: 1) implantation of the ion into the surface and 2) production of a highly reactive surface in the case of dielectrics. Disorder produced in the surface by low energy ion bombardment is well documented. Frequently, annealing may be used to remove disorder and drive off residual inert gas atoms from the surface region.

### 5.1.4 Annealing

Annealing to remove disorder and impurities is well known. However, impurities may diffuse to the surface as a result of this operation, as discussed in section 3.4. In cases such as the preparation of atomically clean ordered silicon surfaces, many cycles of ion bombardment and annealing in an ultra-high vacuum environment may be required to reduce the impurity level to an acceptable value.

### 5.1.5 Cleaving

This technique is deemed the best for obtaining an atomically clean surface. Recent experiments (4) show that stress-strain fields may exist in the cleaved surfaces up to microns in depth. If it is necessary to obtain a strain-free surface, annealing may be employed. The final surface should be characterized, however, to ascertain the impurity level.

## 5.2 Surfaces Prepared by Coating

The process of preparing a thin film coating on a solid is one of the more complex surface processes. For a film of 1  $\mu\text{m}$  or less, it should be looked upon as two surfaces, back-to-back. More rigorously, there is no region of the film that does not feel the influence of an interface. As a result, the properties of a film are not readily comparable with bulk characteristics of the same material. For optical applications, this disparity with bulk properties requires the measurement of indices of refraction for each film and are highly desirable.

It would be inappropriate in a survey of this sort to discuss in detail vaporization, condensation, nucleation and growth of thin films. It is reasonable to identify the basic components in an evaporation system. These components are coupled in such a way that the vacuum coater and sample must be viewed as a system.

### 5.2.1 Coating Environment

Sources of contamination are 1) residual gases (at their respective pressures), 2) residual coating materials from previous processes, 3) condensable material supplied by the vacuum envelope. To illustrate the importance of contamination, it requires approximately  $2 \times 10^{-6}$  torr-min exposure to a typical vacuum environment to saturate an aluminum film. (33)

### 5.2.2 Substrate

The topography, surface chemistry, impurity concentration and temperature all affect the growth of the film, and its physical, chemical and optical properties.

### 5.2.3 Vapor Source

The vapor source does much more than supply the coating material. A compound may be vaporized in elemental ratios different from the stoichiometric ratio of the ideal compound. In addition, the vapor source is also a source of radiant energy. The influence of this on the substrate surface should be ascertained. Impurities and ionized species may also be present.

## 6. Conclusion

There is a reasonable indication that knowledge of the composition, structure and the electronic and chemical character of surfaces may be necessary before the desired level of predictability and reliability in laser optics may be achieved. The careful application of surface science techniques may be able to isolate the factors most influential in reducing predictability in coated optics and reliability in both coated and uncoated optics. Given a knowledge of these factors, it should be possible, then, to modify production practice in a way to mitigate or eliminate their effects. Much work remains to be done in these areas if the requisite understanding is to be acquired.

## 7. References

- (1) Swain, J. E., Damage in Laser Glass, ASTM STP 469, American Society for Testing and Materials, 1969, pp. 69-78.
- (2) Davit, J., J. Appl. Phys. **39**, 6052 (1968).
- (3) Bennet, H. E., Damage in Laser Materials, ASTM STP 356, American Society for Testing and Materials, 1971, pp. 153-167.
- (4) Vedam, K. and So, S. S., Surface Science **29**, 2 (1972).
- (5) Kanter, H., Phys. Rev. B **1**, 522 (1969).
- (6) Burton, J. J., Phys. Rev. **177**, 1346 (1969).
- (7) Wagner, C. and Schottky, W., Z. Physik. Chem. **B11**, 163 (1931).
- (8) Anderson, J. S., Natl. Physical Lab, Symposium No. 9, Paper 7A (1959).
- (9) Ehrlich, P., Z. Elektrochem. **45**, 362 (1939).
- (10) Hauffe, K., Reaktionen in und an Festen Stoffen, Springer-Verlag, Berlin (1955).
- (11) Kroger, F. A. and Vink, H. J., Solid State Physics, Vol. 3, Academic Press, New York, pp. 307-435 (1956).
- (12) Libowitz, G. G., Progress in Solid State Chemistry, Vol. 2, Pergamon Press (1965).
- (13) Frerichs, R., U. S. Patent 2,979,382 (1961).
- (14) Haas, T. W., Dooley, III, G. J., and Grant, J. T., Prog. in Surface Sci. **1**, Part 2 (1971).
- (15) MacRae, A. U., Surface Sci. **13**, 130-3 (1969).
- (16) Porteus, J. O. and Faith, W. N., Phys. Rev. B, **2**, 1532 (1970).

- (17) Jenkins, L. H. and Chung, M. F., Surface Sci. 28, 2 (1971).
- (18) Taylor, N. J., J. Vac. Sci. Technol. 6, 241-5 (1969).
- (19) Siegbahn, K., et al, Nova Acta Regiae Societatis Scientiarum Upsaliensis IV, 20, (1967).
- (20) Rutherford, Sir Ernest, Geiger, H. and Marsden, E., Phil. Mag. 21, 669 (1911).
- (21) Davies, J. A., Denhartog, J., Eriksson, L. and Mayer, J. W., Can. J. Phys. 45, 4053 (1967).
- (22) Rubin, S., Nucl. Inst. Methods 5, 177 (1959).
- (23) Ball, D. J., Buck, T. M., MacNair, D. and Wheatley, G. H., Surface Sci. 30, 1 (1972).
- (24) Goff, R. F. and Smith, D. P., J. Vacuum Sci. Technol. 7, 72 (1970).
- (25) Smith, D. P. J. Appl. Phys. 38, 340 (1967).
- (26) Smith, D. P., Surface Sci. 25, (1971).
- (27) Fehlner, F. P. and Mott, N. F., Oxidation of Metals 2, 59, (1970).
- (28) Frankl, D. R., J. Appl. Phys. 34, 3514 (1963).
- (29) Heavens, O. S., Optical Properties of Thin Solid Films, Academic Press, New York (1955).
- (30) Kruger, J., in: Ellipsometry in the Measurement of Surfaces and Thin Films, Symposium Proceedings, Eds. E. Passaglia, R. R. Stromberg and J. Kruger (Natl. Bur. Std., Misc. Publ. 256, Washington, D. C., 1964).
- (31) Paik, W. and Bockris, J.O.M., Surface Science 28, 1 (1971).
- (32) MacDonald, N. C., Appl. Phys. Lett. 16, 76 (1969).
- (33) Kruger, W. H. and Pollack, S. R. Pollack, Surface Sci. 30, 2 (1972).



# Self-Focusing with Elliptical Beams

John Marburger\*

Departments of Physics and Electrical Engineering  
University of Southern California  
Los Angeles, California 90007

The time independent self-focusing of beams whose constant intensity contours are ellipses has been studied in the paraxial ray-constant shape approximation. This approximation leads to equations for the principal  $1/e$  intensity diameters versus axial distance which have been analysed previously by Vorob'yev by a different method. Our method allows the treatment of non-gaussian intensity profiles. The solutions are employed to find expressions for the critical powers and self-focal lengths of nonaxially symmetric beams under a variety of initial conditions. The critical power can be greatly enhanced by astigmatic focusing, even if the beam shape is initially axially symmetric. This theory implies that bulk damage thresholds arising from self-focusing depend strongly on beam shape, in agreement with experimental results of Giuliano.

Key Words: Bulk damage, damage threshold, elliptical beams, enhancement, self-focusing.

## 1. Introduction

Most studies of self-focusing of intense optical beams assume that the incident beam has circular, or axial, symmetry. However, many important laser systems produce a beam which is more nearly elliptical than circular in cross section, and it is therefore important to understand how the performance of the system depends upon distortions of the beam shape. We show below that self-focusing is rather sensitive to such distortions, and that the critical power for self-focusing, and thus to some extent the bulk damage threshold, can be enhanced by employing elliptical beams. This conclusion was reached experimentally by C. Giuliano [1]<sup>1</sup> independently of the theoretical analyses of Vorob'yev [2], Shvartsburg [3] and Vlasov, et al., [4]. In this paper we sketch a simple theory of the self-focusing of elliptical beams, and use it to derive formulas for the behavior of the self-focal point under a variety of incident beam conditions. Some of our results have been obtained previously in [2]-[4], but this work is not yet available in English translation, and we feel that it is worthwhile to repeat some of it here.

In addition to departures from axial symmetry, we shall also briefly consider the influence of non-gaussian and acentric intensity profiles on self-focusing. The experimental verification of theory developed here is by no means complete, but what data exist are consistent with our results [1].

## 2. The Motion of the Principal Axes of Elliptical Self-Focusing Beams

We shall develop our theory only for linearly polarized beams propagating in a lossless medium with nonlinear dielectric constant

$$\epsilon = \epsilon_0 + \epsilon_2 \langle E^2 \rangle \quad (1)$$

where  $\langle \dots \rangle$  denotes a time average over many optical cycles, and  $E$  is the peak instantaneous electric field. This form is appropriate for a nonlinear polarization which responds instantly to changes in the

---

\* Research sponsored by the Joint Services Electronics Program through the Air Force Office of Scientific Research under Contract F 44620-71-C-0067.

<sup>1</sup> Figures in brackets indicate the literature references at the end of this paper.

applied field, and therefore we are ignoring the slowly responding mechanism of electrostriction. We use gaussian cgs units.

Writing the electric field strength as

$$E = \frac{1}{2} E' \exp i(Kz - \omega t) + \text{c.c.} \quad (2)$$

(all vectors will be assumed parallel to  $\underline{E}$  which is approximately parallel to the x axis), we may derive the following equation for  $E'$

$$2iK \frac{\partial E'}{\partial z} + \nabla_T^2 E' + \frac{1}{2} K^2 (\epsilon_2/\epsilon_0) |E'|^2 E' = 0. \quad (3)$$

This may be obtained from the usual wave equation in the presence of matter, with the approximation

$$|\partial^2 E' / \partial z^2| \ll |K \partial E' / \partial z| \quad (4)$$

which means that most of the z dependence of E is in the factor  $\exp iKz$ , and therefore  $E' = E'(x, y, z)$  is a slowly varying "envelope" function of z. The time dependence has been suppressed here. As long as we assume instantaneous response, the time dependence can be inserted a-posteriori into the solutions by allowing the "initial" conditions at  $z = 0$  to depend upon time. (See reference [6] for an account of this approach.)

If we let

$$E' = E_0 \exp i\phi \quad (5)$$

we find from the real and imaginary parts of (3)

$$K \partial E_0^2 / \partial z + \nabla_T \cdot (E_0^2 \nabla_T \phi) = 0 \quad (6)$$

$$K \partial \phi / \partial z + \frac{1}{2} (\nabla_T \phi)^2 - \frac{1}{2} (\nabla_T^2 E_0) / E_0 - \frac{1}{4} (K^2 \epsilon_2 / \epsilon_0) E_0^2 = 0. \quad (7)$$

Here  $\nabla_T^2 = \partial^2 / \partial x^2 + \partial^2 / \partial y^2$  and  $\epsilon_0 \omega^2 = c^2 K^2$ .

Equation (7) is the Hamilton-Jacobi equation for a particle of unit mass moving under the influence of the potential

$$-\frac{1}{2} (\nabla_T^2 E_0) / K^2 E_0 - \frac{1}{4} (\epsilon_2 / \epsilon_0) E_0^2 \quad (8)$$

if the quantity  $Kz$  is interpreted as the time, and  $Kx, Ky$  as the particle coordinates. The equations of motion for these coordinates can be cast into a convenient form if we assume that

$$E_0 = E_m(z) \exp -\frac{1}{2} \left( \frac{x^2}{a^2} + \frac{y^2}{b^2} \right) \quad (9)$$

where a and b are both functions of z. This is the constant shape approximation which forces the intensity contours of the beam to be elliptical at any axial distance z, although the ellipticity and size of the ellipse may vary with z. If we use (9) to evaluate (8) for the particle (ray) passing through the paraxial point  $(\alpha a, \beta b)$ , where  $\alpha, \beta \ll 1$ , then we find the components of "force" in the x and y directions:

$$\frac{\alpha}{K^2 a^3} - \frac{\epsilon_2}{2\epsilon_0} E_m^2 \frac{\alpha}{a} \quad (10)$$

$$\frac{\beta}{K^2 b^3} - \frac{\epsilon_2}{2\epsilon_0} E_m^2 \frac{\beta}{b} . \quad (11)$$

The function  $E_m^2$  may be eliminated from these formulas by using the relation between  $E_m^2$  and the total power in the beam

$$E_m^2 = (8P/nc ab) \quad (12)$$

where  $n^2 = \epsilon_0$ . This leads finally to the following equations for the principal axes of the ellipse formed by the  $e^{-1}$  intensity points in the transverse plane:

$$2K^2 \frac{d^2 a}{dz^2} = \frac{2}{a^3} - \frac{2\eta}{a^2 b} \quad (13)$$

$$2K^2 \frac{d^2 b}{dz^2} = \frac{2}{b^3} - \frac{2\eta}{ab^2} \quad (14)$$

where  $\eta = P/P_1$ , and  $P_1 = n^3 c/4\epsilon_2 K^2$ . These equations were first derived by Vorob'yev [2] who obtained them using a variational method. The quantity  $P_1$  is the power required in a circularly symmetric beam in a self-focusing medium to cause the initial curvature of the on-axis intensity versus distance curve to vanish. It is less by the factor 0.273 than the critical power  $P_2$  above which a "strong" or catastrophic self-focus forms at  $z = \infty$ . (See reference [7].) In our approximate theory, however,  $P_1$  plays the role of a critical power for circular beams, as we shall see below.

Equations (13) and (14) are formally equivalent to the equations of motion of a particle of mass  $2K^2$  moving in the conservative two-dimensional potential well

$$U = \frac{1}{2} + \frac{1}{2} - 2\eta \frac{1}{ab} \quad (15)$$

The equipotential curves of (15) are shown for several values of  $\eta$  in figures 1 - 5. Notice that as  $\eta$  increases from 0 to 1, the potential well remains repulsive for all positive values of  $a$  and  $b$  (corresponding to diffractive spreading of the beam), but develops a "trough" along the line  $a = b$  which finally acquires a flat bottom at  $\eta = 1$ . For  $\eta > 1$ , there are two straight lines  $U = 0$  between which the potential surface drops steeply to  $-\infty$  at the origin.

Obviously the path of a particle moving in such a potential can be complicated, but the form of equations (13) and (14) allows a simple expression for the quantity  $a^2(z) + b^2(z)$ , as shown first by Vorob'yev. The reader may easily verify that

$$\frac{d^3}{dz^3} (a^2 + b^2) = 0 \quad (16)$$

and therefore

$$K^2(a^2 + b^2) = \left[ K^2(\dot{a}_0^2 + \dot{b}_0^2) + \frac{2}{a_0 b_0} (\eta_c - \eta) \right] z^2 + 2K^2(a_0 \dot{a}_0 + b_0 \dot{b}_0) z + K^2(a_0^2 + b_0^2) \quad (17)$$

Here  $a_0, b_0$  are the axes of the ellipse formed by the  $e^{-1}$  points of the transverse intensity profile at  $z = 0$ , and

$$\eta_c = (a_0^2 + b_0^2)/2a_0 b_0 \quad (18)$$

The quantities  $\dot{a}_0, \dot{b}_0$  are the initial rates of change of these axes, and are simply related to the principal radii of curvature  $R_a, R_b$  of the incident phase front:



$$R_a = a_o / \dot{a}_o, \quad R_b = b_o / \dot{b}_o. \quad (19)$$

Equation (17) provides the starting point for the derivation of many interesting formulas regarding the self-focusing of elliptical beams.

### 3. Useful Equations for Self-Focusing Elliptical Beams

If the phase fronts of the wave at  $z = 0$  are plane, then  $\dot{a}_o = \dot{b}_o = 0$ , and (17) becomes

$$\frac{a_o^2 + b_o^2}{a_o^2 + b_o^2} = 1 + (1 - \eta/\eta_c) \left( \frac{z}{K a_o b_o} \right)^2 \quad (20)$$

where  $\eta = P/P_1$ . If  $\eta > \eta_c$ , this function decreases to zero at the point

$$z_{fo} = \frac{K a_o b_o}{(\eta/\eta_c - 1)^{1/2}}. \quad (21)$$

At this point the intensity  $ncE_m^2/8\pi = P/\pi ab$  becomes infinite because  $ab \leq \frac{1}{2}(a^2 + b^2)$ . A glance at the potential curves shows that  $a$  and  $b$  must vanish together so that whenever  $ab = 0$ , we also have  $a^2 + b^2 = 0$ . Thus the quantity

$$P_c = \eta_c P_1 = \frac{1}{2} \left( \frac{a_o}{b_o} + \frac{b_o}{a_o} \right) P_1 \quad (22)$$

must be regarded as the critical power for self-focusing for this case, and  $z_{fo}$  is the self-focal length for  $P > P_c$ .

When  $P = P_c$ , then  $a^2 + b^2$  remains constant (for plane incident phase fronts). Vorob'yev has pointed out that in this case the equations of motion can be integrated in a closed form involving elliptic integrals [2]. The trajectory of the analogous particle in the  $(a, b)$  plane is the arc of a circle, concentric with the origin, of radius  $(a_o^2 + b_o^2)^{1/2}$  and contained between the lines  $U = 0$  as indicated in figure 4. The beam shape changes from an ellipse to a circle with lower axial intensity, and back to an ellipse with interchanged axes, then repeats the cycle. This is the closest possible analogue to a self-trapped beam for an incident elliptical cross section.

If the initial phase fronts have finite curvature, then equation (17) implies that when  $\eta$  exceeds a certain value  $\eta_{cc}$ , the beam intensity becomes infinite at

$$z_f = \frac{z_o}{1 + \frac{z_o}{K a_o b_o} \left( \frac{\eta - \eta_{cc}}{\eta_c} \right)^{1/2}} \quad (23)$$

where

$$\eta_{cc}/\eta_c = 1 + \left[ \frac{K a_o b_o}{2\eta_c} \left( \frac{1}{R_a} - \frac{1}{R_b} \right) \right]^2, \quad (24)$$

and  $z_o$  is the distance at which the self-focus first appears as the power is increased to  $P = \eta_{cc} P_1$ . It satisfies

$$-\frac{(a_o^2 + b_o^2)}{z_o} = \frac{a_o^2}{R_a} + \frac{b_o^2}{R_b}. \quad (25)$$

When  $\eta$  is less than  $\eta_{cc}$ , there is still an on-axis intensity maximum near the real part of  $z_f$  given by (23):

$$z_{\max} = \operatorname{Re} z_f = \frac{z_o}{1 + \left( \frac{z_o}{K a_o b_o} \right)^2 \left( \frac{\eta - \eta_{cc}}{\eta_c} \right)} \quad (26)$$

We say "near  $\operatorname{Re} z_f$ " because we can only compute the minimum of  $a^2 + b^2$  versus  $z$  from (17), whereas the intensity maximum occurs at the minimum of  $ab$ .

Notice that  $z_o$  given by (25) is negative for diverging beams ( $R_a, R_b$  are positive for diverging beams) and therefore a self-focus first appears at  $z = \infty$  for such beams only at the critical power  $P = \eta_{cd} P_1$ , where

$$\eta_{cd} = \eta_{cc} + \frac{1}{2} K a_o b_o \left( \frac{a_o}{b_o R_a} + \frac{b_o}{a_o R_b} \right). \quad (27)$$

The critical power enhancement predicted by (24) for astigmatically focused beams ( $R_a \neq R_b$ ) can be quite large. Thus in Guiliano's recent experiment [1],  $a_o = 0.179$  mm,  $b_o = 0.232$  mm,  $R_a = 4.05$  cm,  $R_b = 7.04$  cm, and  $K a_o b_o = 66.1$  cm. For these values,  $\eta_c = 1.03$ , but  $\eta_{cc} = 12.7$ . This is consistent with the observed increase in threshold.

#### 4. Formulas for Non-Gaussian Intensity Profiles

Our starting assumption (9) for the shape of the incident beam is rather restrictive, and it is useful to know how the results of the preceding section must be modified to account for deviations from this form. If we start with the more general form

$$E_o = E_m(z) g_1(x/a) g_2(y/b), \quad (28)$$

we may still find simple results for the self-focusing parameters. The functions  $g_1$  and  $g_2$  must be even, and therefore we may write

$$g_1(x/a) = 1 - \frac{1}{2} \frac{x^2}{a^2} + \left( \frac{2\rho + 1}{24} \right) \frac{x^4}{a^4} + \dots \quad (29)$$

$$g_2(y/b) = 1 - \frac{1}{2} \frac{y^2}{b^2} + \left( \frac{2\sigma + 1}{24} \right) \frac{y^4}{b^4} + \dots \quad (30)$$

We shall also require the "normalization" integrals

$$\int_{-\infty}^{\infty} g_1^2(x/a) d(x/a) = r \quad (31)$$

$$\int_{-\infty}^{\infty} g_2^2(y/b) d(y/b) = s. \quad (32)$$

For gaussian beams,  $\rho = \sigma = 1$ ,  $r = s = \sqrt{\pi}$ . Beams which are flatter and broader than gaussians have larger values of these parameters.

If the derivation of the equations of motion for  $a$  and  $b$  outlined in Section 2 is repeated for the more general shape of equation (28), one finds equations exactly analogous to (13) and (14), but with new forces derivable from the potential

$$U' = \frac{\rho}{a^2} + \frac{\sigma}{b^2} - 2\eta' \frac{1}{ab}, \quad (33)$$

where

$$\eta' = \frac{\pi}{rs} \eta = \frac{\pi}{rs} \frac{P}{P_1} . \quad (34)$$

The quantity  $d^2(a^2 + b^2)/dz^2$  is still a constant of the motion, and  $a^2 + b^2$  may be written as before with  $\eta_c$  replaced by

$$\eta'_c = \frac{1}{2} \left( \sigma \frac{a_o}{b_o} + \rho \frac{b_o}{a_o} \right) . \quad (35)$$

Thus all previous formulas can be corrected for non-gaussian beams by replacing  $\eta_c$  everywhere with  $\eta'_c$ .

One might object that (28) is still a rather restrictive assumption, but unfortunately more general forms lead to systems of differential equations for the beam parameters which have no simple solutions such as those given here. The value of our treatment is that it gives simple formulas for the important self-focusing parameters which might be expected to give at least their qualitative dependence on incident beam conditions. Since our theory correctly describes only rays very near the axis, we cannot rely on its results too heavily for quantitative information.

## 5. Acentric Beams

In this section we simply wish to draw attention to the work of Kaplan [8] which shows that acentric beams will follow a curved path in a self-focusing medium. This bending of the path occurs because the rays comprising the beam see an induced prism proportional to the nonlinear index and the degree of acentricity in the beam.

A ray propagating in a linear inhomogeneous medium will possess a local radius of curvature,  $R$ , given by

$$R^{-1} = \hat{N} \cdot \frac{\nabla n}{n}$$

where  $\hat{N}$  is the principal normal of the ray, and  $n$  the refractive index. In our case, the inhomogeneity in  $n$  is induced by intensity variations within the incident beam. The simplest variation leading to beam bending in the  $x, z$  plane is obviously

$$\begin{aligned} E_o^2 &= E_m^2 \left( 1 + \frac{2\Delta}{W} x \right), \quad \frac{W}{2} \leq x \leq \frac{W}{2} \\ &= 0, \quad \frac{W}{2} < |x| \end{aligned}$$

The corresponding intensity profile along the  $x$  axis is shown in figure 6. For this shape, the initial radius of curvature of the beam is

$$R = \frac{2n_o^2 W}{\epsilon_2 \Delta E_m^2} = \frac{n_o^3 c W^2 a}{4 \Delta \epsilon_2 P}$$

where we have assumed that the total beam power is

$$P = \frac{n_o c E_m^2}{8\pi} \cdot \pi a W .$$

This radius of curvature gives an angle of deflection of  $\phi/s = R^{-1}$  radians per cm of path length  $s$  in cgs units. For  $\epsilon_2 = 10^{-13}$  (esu),  $P = 10^{10}$  W/cm<sup>2</sup> =  $10^{17}$  erg/cm<sup>2</sup> sec,  $n_o \approx 1.5$ , and  $a = W = 0.1$  mm, we find

$$\phi/s \approx 0.4 \Delta \text{ radians per cm} .$$

This is a remarkably large angle for these not unreasonable beam parameters, and one might expect to be able to see such a deflection experimentally. Notice that self-focusing causes the beam dimensions to decrease with path length which implies that  $R$  also decreases with path length. Thus we expect the path of an acentric beam in a self-focusing medium to be a spiral terminating at the self-focus.



## 6. References

- [1] Giuliano, C., Marburger, J., Yariv, A., Appl. Phys. Letters, July 1972, "Enhancement of Self-Focusing Threshold in Sapphire with Elliptical Beams."
- [2] Vorob'yev, V. V., IVUZ Radiofiz. 13, 1905 (1970), "Self-Focusing of Non-Axisymmetric Optical Beams."
- [3] Shvartsburg, A. B., IVUZ Radiofiz. 13, 1775 (1970), "Self-Focusing of a Beam of Electromagnetic Waves with an Ellipsoidal Phase Front." (In Russian.)
- [4] Vlosov, Petrichen and Tallanov, J. Radio Fizika, 14, 1354 (1971). (In Russian -- reference incomplete.)
- [5] Reference not used in text.
- [6] Marburger, J. "Theory of Self-Focusing for Fast Nonlinear Response," in Damage in Laser Materials: 1971, A. J. Glass, A. H. Guenther, eds. NBS Special Publication 356, 51 (1971).
- [7] Dawes, E. and Marburger, J., Phys. Rev. 179, 862 (1969), "Computer Studies of Self-Focusing."
- [8] Kaplan, A. E., JETP Letters 1, 33 (1969), "Bending of Trajectories of Asymmetrical Light Beams in Nonlinear Media."

## 7. Figures

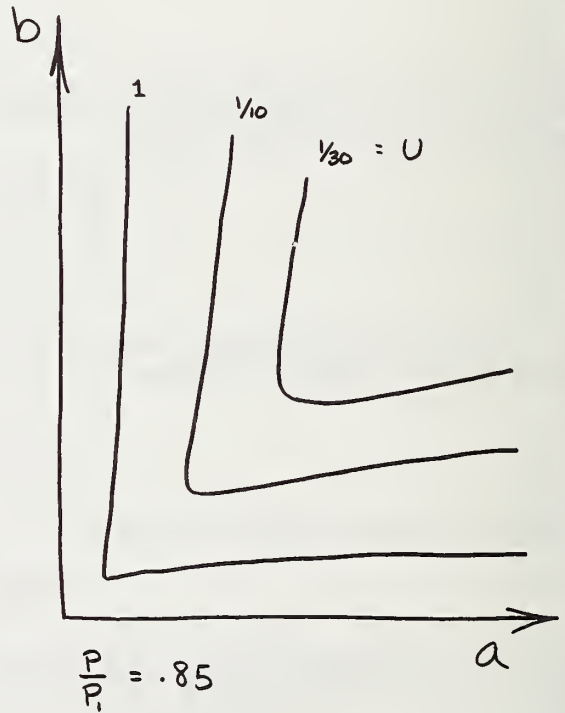
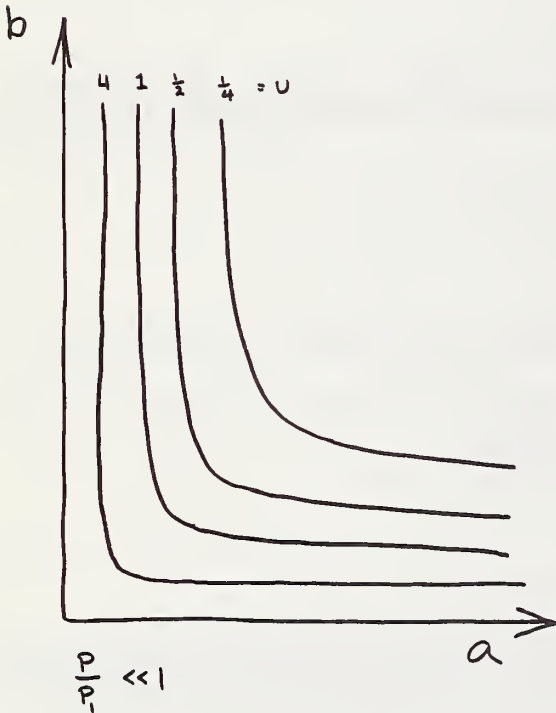


Figure 1. Equipotential curves in the  $a, b$  plane for the potential of Equation (15) in the text, where  $\eta = P/P_1$  is negligible.

Figure 2. Same as figure 1, but  $\eta = .85$ .

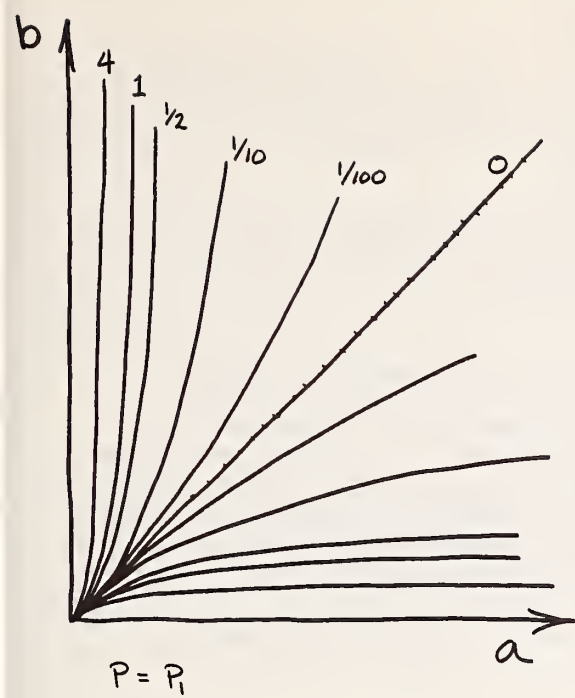


Figure 3. Same as figure 1, but  $\eta = 1.0$

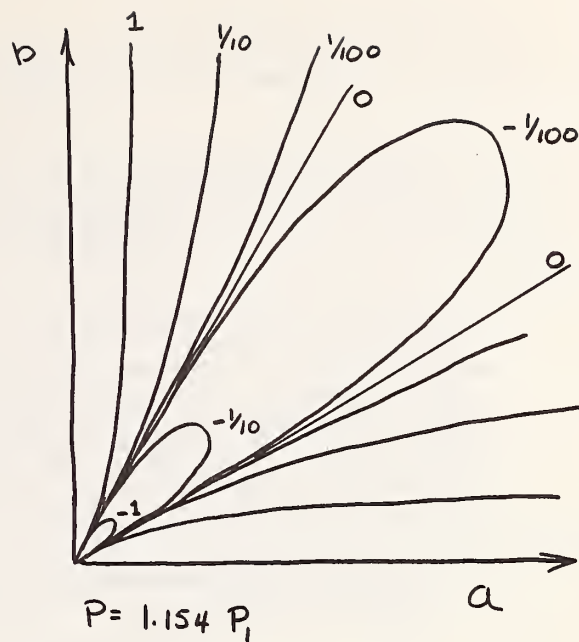


Figure 4. Same as figure 1, but  $\eta = 1.54$

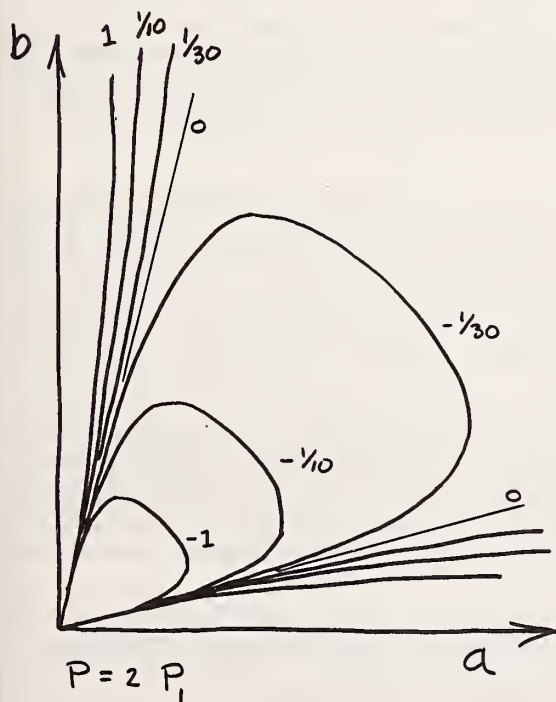


Figure 5. Same as figure 1, but  $\eta = 2$

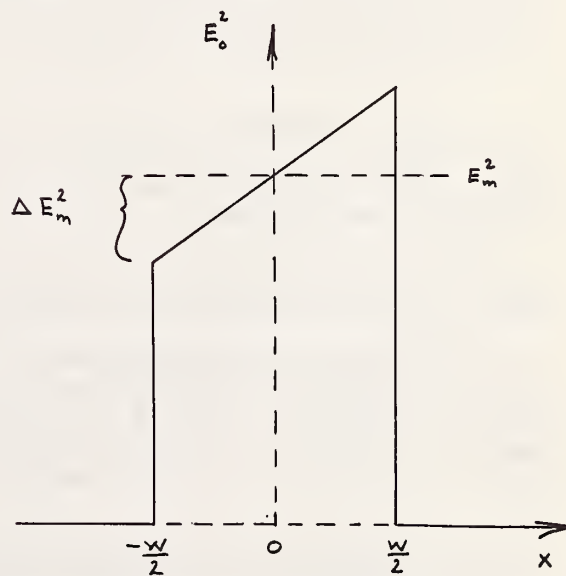


Figure 6. Notation for intensity distribution of simple acentric beam.

# Relative Contribution of Kerr Effect and Electrostriction to Self-Focusing\*

Albert Feldman, Deane Horowitz, and Roy M. Waxler

National Bureau of Standards  
Washington, D. C. 20234, U. S. A.

The ratio of damage thresholds for circularly polarized radiation to linearly polarized radiation was found to be  $> 1$  in borosilicate crown glass, fused silica, and dense flint glass. A Q-switched Nd:glass laser operating in the TEM<sub>00</sub> mode was used. The damage was assumed to result from self-focusing. The fractional contributions of electrostriction and the Kerr effect to the nonlinear index  $n_2$  are estimated from the threshold ratios calculated for each mechanism in the absence of the other and assuming no other self-focusing mechanism. The high damage threshold of fused silica is attributed to its relatively small Kerr effect. Measurements of self-focusing lengths as a function of peak power give qualitatively good agreement with theory.

Key Words: Damage threshold, electrostriction, Kerr-effect, laser damage in glasses, optical glasses, self-focusing.

## 1. Introduction

The mechanism responsible for the self-focusing of laser beams with pulse widths of  $\sim 25$  ns has not been uniquely identified. Three mechanisms have been proposed to explain the effect [1]<sup>1</sup>: electrostriction [2-6], Kerr effect [2-4,7], and thermal self-focusing [8-10]. Up to the present time there has been insufficient data to judge the comparative importance of the proposed mechanisms. Self-focusing in liquids is known to be caused by the Kerr effect because of the large contribution of freely rotatable molecules or ions to the nonlinear index coefficient  $n_2$ . Because solids lack freely rotatable molecules, it was thought that electrostriction [2-4] was the dominant mechanism. Duguay and Hanson have calculated the nonlinear index of refraction due to the Kerr effect  $n_2(K)$  from measurements of induced birefringence in borosilicate crown glass using picosecond pulses [11,12]. They find that the value obtained is of sufficient magnitude to cause self-focusing and are of the opinion that the Kerr effect is the predominant mechanism for all pulse widths.

E. L. Kerr [6] has developed the theory of electrostrictive self-focusing to explain the data of Steinberg [13], who used 55-ns pulses from a ruby laser to measure damage thresholds in several optical glasses. Kerr is of the view that electrostriction is the principal self-focusing mechanism for pulse widths  $> 10$  ns. For pulses less than 10 ns, on the other hand, the electrostrictive mechanism has insufficient time to take effect.

For the glasses such as we are considering, thermal self-focusing is not thought to be important. Quelle [10] in a sample calculation showed that the threshold for thermal self-focusing would be two orders of magnitude greater than for electrostriction.

We have made self-focusing measurements in borosilicate crown glass (BSC 517)<sup>2</sup>, fused silica, and dense flint glass (SF 55 formerly SFS 5). Self-focusing lengths were measured as a function of beam power [14] and compared with the theory of Dawes and Marburger [15] which assumes an instantaneous self-focusing mechanism. Additional measurements were made which showed that the damage threshold is higher for circular polarization than for linear polarization. From these measurements we estimate the relative importance of the proposed mechanisms to self-focusing. In liquids, similar measurements helped to confirm that the Kerr effect is the predominant mechanism [16,17].

\* Research supported in part by the Advanced Research Projects Agency of the Department of Defense.

<sup>1</sup>Figures in brackets indicate the literature references at the end of this paper.

<sup>2</sup>Certain commercial materials are identified to specify adequately the experimental procedure. In no case does such identification imply recommendation or endorsement by the National Bureau of Standards.



## 2. Experimental Procedure

The experimental apparatus is shown in figure 1. The oscillator consists of a Nd:glass rod pumped by a helical flash lamp. It is Q-switched by means of a KD\*P Pockels cell. There is an aperture in the cavity 2.44 mm in diameter for producing a beam in the TEM<sub>00</sub> mode. The output from the oscillator is a pulse whose width at half the maximum power is 25 ns as measured by a high-speed photodiode.

The beam profile of the laser beam at the focusing lens is obtained from burn patterns on developed unexposed black (Polaroid)<sup>3</sup> film [14]. The output of the laser is maintained at a constant pulse energy but is attenuated from pulse to pulse by interposing calibrated attenuation filters between the oscillator and the film. Figure 2 shows a set of burn patterns used for determining the beam profile. The radius of the outermost burn ring for each pattern is plotted as a function of beam energy. The result is fitted to a Gaussian curve  $H = H_0 e^{-r^2/a^2}$ . The constant  $H_0$  is obtained in units of J/cm<sup>2</sup> from

$$E = 2\pi H_0 \int_0^\infty \exp(-r^2/a^2) r dr, \quad (1)$$

where E is the total pulse energy (99 mJ in this case). Figure 3 shows a plot of the beam profile together with the Gaussian which is fitted to the data by eye.

The energy output at a given pumping level was constant to within  $\pm 2\%$  as measured by the thermopile. During the damage tests each shot was monitored by the photodiode. The energy of the beam was varied in 20% increments with calibrated attenuation filters. Finer increments of energy were obtained by varying the oscillator pump energy.

## 3. Self-Focusing Length Measurements

Recent experiments [18-21] have shown that the filamentary damage observed when solids are exposed to high-intensity laser radiation is due to self-focusing of the laser beam and that the self-focused spot moves toward the laser source as the pulse power rises. Dawes and Marburger [15] have made a detailed computer calculation which predicts the self-focusing length as a function of beam power assuming that the nonlinear index coefficient  $n_2$  responds instantaneously to the laser pulse shape.

We have produced damage filaments in optical glasses by focusing the laser beam at different power levels P into samples using a 181-mm focal length lens. A length  $z_f$  was measured from the upstream end of the damage track to the sample entrance face. The self-focusing length z was calculated from the formula [22]

$$z^{-1} = z_f^{-1} - R^{-1} \quad (2)$$

where R is the radius of curvature of the laser wavefront at the sample entrance face. R is calculated from the measured focal spot of the lens and the propagation characteristics of Gaussian beams. The critical power for self-focusing  $P_c$  is taken to be the lowest power which produced damage in the sample. The normalized inverse self-focusing length  $(z^*)^{-1}$  is plotted as a function of  $(P/P_c)^{1/2}$  in figure 4 together with the theoretically calculated curve of Dawes and Marburger (our  $P_c$  is equivalent to their  $P_2$ ), where  $z^* = z/2ka^2$  and  $k = 2\pi n_0/\lambda$ ;  $n_0$  is the refractive index of the medium;  $\lambda$  is the wavelength of the laser beam in air; a is the 1/e intensity point at the sample face. There is good qualitative agreement between the data and the theory. The deviations are attributed to electrostrictive self-focusing. Because of the low threshold in the SF 55, we can compare experiment with theory over a large range of values. The fact that the slope of the data matches the experimental slope confirms that the laser beam had a Gaussian profile. We believe the data demonstrate that the theory provides a good description of self-focusing in solids.

<sup>3</sup>Certain commercial instruments and materials are identified in this paper in order to specify adequately the experimental procedure. In no case does such identification imply recommendation or endorsement by the National Bureau of Standards, nor does it imply that the instrument or material identified is necessarily the best available for the purpose.

## 4.1 Experimental

Damage threshold measurements for linearly and circularly polarized light were made by focusing the laser beam into the samples using lenses of 76 mm and 181 mm focal length. The oscillator output was linearly polarized in the horizontal plane with the ratio of horizontal to vertical polarization being greater than 200:1. Circularly polarized light was produced by inserting a quarter-wave plate into the beam. The quarter-wave plate consisted of a plate of fused silica under uniaxial compression [23]. The linear polarization damage measurements were made by relaxing the stress in the plate. Measurements were also made with the plate stressed to a half-wave retardation; the results were consistent with the unstressed plate measurements.

Figures 5 and 6 show the damage threshold data obtained. The solid points represent pulses that produced damage; the open points represent pulses that did not produce damage. The scatter in the data is due to sample variability, laser energy variations, and the statistical nature of the actual damage process [20]. In all cases, the threshold for circularly polarized light  $P_t'$  is higher than for linear polarization,  $P_t$ . (Unprimed symbols refer to linear polarization and primed symbols to circular polarization.) Table 1 lists the ratios  $P_t'/P_t$ . The error limits represent the full scatter in the data.

Table 1. Parameters for calculating electrostriction and Kerr effect in optical glasses.

	BSC 517	Fused Silica	Dense Flint
$n_o$ (1.06 $\mu\text{m}$ )	1.507	1.450	1.733
$q_{11}$ ( $10^{-13}\text{cm}^2/\text{dyn}$ )	$a_{0.315}$	$b_{0.418}$	$c_{1.7}$
$q_{12}$ ( $10^{-13}\text{cm}^2/\text{dyn}$ )	$a_{1.92}$	$b_{2.71}$	$c_{2.2}$
$P_{11}$	$a_{0.115}$	$b_{0.120}$	$c_{0.21}$
$P_{12}$	$a_{0.221}$	$b_{0.270}$	$c_{0.23}$
$n_2^t(\text{es})$ ( $10^{-13}$ esu)	0.62	0.81	2.5
$n_2^t(\text{es})$ ( $10^{-13}$ esu)	0.56	0.72	2.5
$n_2(\text{es})/n_2^t(\text{es})$ (theory)	1.11	1.13	1.00
$n_2(K)/n_2^t(K)$ (theory)	1.50	1.50	1.50
$P_t'/P_t = n_2/n_2^t$ (experimental)			
Reference d	$1.18 \pm 0.07$	$1.09 \pm 0.09$	$1.25 \pm 0.08$
Reference e	$1.26 \pm 0.12$	$1.24 \pm 0.11$	$1.32 \pm 0.07$
$\alpha$			
Reference d	$0.8 \pm 0.2$	$1.15 \pm 0.35$	$0.40 \pm 0.13$
Reference e	$0.6 \pm 0.3$	$0.7 \pm 0.3$	$0.27 \pm 0.13$

<sup>a</sup>R. M. Waxler and C. E. Weir, J. Res. Natl. Bur. Std. (U. S.) 69A, 325 (1965),  $\lambda = 587.6$  nm.

<sup>b</sup>W. Primak and D. Post, J. Appl. Phys. 30, 779 (1959),  $\lambda = 546.1$  nm.

<sup>c</sup>This work,  $\lambda = 632.8$  nm.

<sup>d</sup>Data obtained with 76-mm focal length lens. Error limits represent full scatter in the data.

<sup>e</sup>Data obtained with 181-mm focal length lens. Error limits represent full scatter in the data.

The mechanisms of electrostriction and the Kerr effect are associated with the quadratic dependence of refractive index on electric field  $E$ :  $n = n_0 + \frac{1}{2}n_2 E^2$ ;  $n_2 = n_2(es) + n_2(K)$ . [es  $\equiv$  electrostriction, K  $\equiv$  Kerr effect.] The self-focusing threshold  $P_t$  is inversely proportional to  $n_2$ . The relative contributions of the above mechanisms to the self-focusing can be calculated from the experimental data if we make several assumptions: (1) The damage is assumed to result from self-focusing; (2) thermal self-focusing can be ignored; (3) the ratios  $n_2(es)/n_2^1(es)$  and  $n_2(K)/n_2^1(K)$  can be calculated.

In calculating  $n_2(es)/n_2^1(es)$ , we assume the material responds to a D. C. field obtained from a time average of the optical electrical field tensor  $E_i E_j$ . It is assumed that the  $E$  field is uniform within a cylinder and zero outside. The result will be the same on the axis of a Gaussian beam. Detailed dynamical calculations are not expected to change the ratio  $n_2(es)/n_2^1(es)$  even though they would affect the absolute index changes. Steady-state conditions are assumed.

In the presence of an intense uniform electric field all solids undergo a strain [24]

$$\epsilon_{k\ell} = \frac{1}{2} \gamma_{ijkl} E_i E_j. \quad (3)$$

From thermodynamics we can show that

$$\gamma_{ijkl} = - \kappa_{im} \kappa_{jn} q_{mnkl} / 4\pi, \quad (4)$$

where  $\kappa_{ij}$  is the dielectric tensor and  $q_{ijkl}$  is the stress-optical coefficient. If we assume a freely expanding cylinder, we obtain the expressions

$$n_2(es) = n_0^7 (p_{11}q_{11} + 2p_{12}q_{12}) / 8\pi \quad (5)$$

$$n_2^1(es) = n_0^7 (p_{11}q_{11} + 3p_{12}q_{12} + p_{12}q_{11} + p_{11}q_{12}) / 16\pi, \quad (6)$$

where the  $p_{ij}$  are the elasto-optic coefficients; the Voigt notation is used. Values for the above constants are given in table 1. Although the numbers quoted were obtained at visible wavelengths, we do not expect them to differ significantly at 1.06  $\mu\text{m}$ .

For the Kerr effect we assume only an electronic contribution [11,12,25-27]. Recent experimental work suggests this is indeed the case [28]. For an isotropic material the nonlinear polarization will be [29]

$$\vec{P}^{NL} = 3C_{1122} (\vec{E} \cdot \vec{E}) \vec{E}. \quad (7)$$

If we insert the field for a linearly polarized wave  $\vec{E} = [E_0 \cos(\omega t - kz), 0, 0]$  and a circularly polarized wave  $\vec{E} = [E_0 \cos(\omega t - kz), E_0 \sin(\omega t - kz), 0] / \sqrt{2}$  into eq (7) and calculate the Fourier component of  $\vec{P}^{NL}$  at frequency  $\omega$ , we obtain a ratio of 1.5 for  $n_2(K)/n_2^1(K)$ .

It is now possible to estimate the fractional contribution of electrostriction,  $\alpha = n_2(es)/n_2$ , and the Kerr effect,  $(1-\alpha) = n_2(K)/n_2$ , to the nonlinear index coefficient. Calculated values for  $\alpha$  are summarized in table 1.

One cannot attribute any significance to one value of  $\alpha$  being greater than unity for  $\text{SiO}_2$ . This value was obtained with a lens of short focal length. Because of the high self-focusing threshold for fused silica, it is probable that only a slight amount of self-focusing took place and the threshold measured was essentially the intrinsic damage threshold for which one might expect no difference between circular and linear polarization.



The data indicate that the Kerr effect is larger in BSC 517 than in  $\text{SiO}_2$ . This conclusion would explain why fused silica has a higher damage threshold than BSC 517 since, on the basis of electrostriction alone, BSC 517 would have the higher damage threshold. In dense flint glass the Kerr effect appears to make a greater contribution than electrostriction; the observed difference in damage threshold between circular and linear polarization must be ascribed to the Kerr effect since no difference is expected from electrostriction alone.

In all cases the value of  $\alpha$  is larger for the longer focal length data. This is reasonable since electrostrictive effects are expected to decrease with increase of the focal spot size while the Kerr effect is expected to remain unchanged. It is interesting to note that electrostriction makes a relatively smaller contribution in SF 55 vs the other glasses. This is to be expected since electrostriction depends on the parameter  $X = a_0/v\tau$  where  $\tau$  is the pulse width and  $v$  the velocity of sound in the medium [6]. As  $X$  increases, electrostrictive effects decrease. For SFS 55,  $v = 3000$  m/s, while for  $\text{SiO}_2$  and BSC 517,  $v = 6000$  m/s. Thus,  $X$  is twice as large for SF 55 as it is for the other glasses.

Figure 7 compares our data with the data of Steinberg [13] and E. L. Kerr's theory of electrostrictive self-focusing [6]. The figures were obtained from Kerr's work. The  $X$ 's represent values we measured. In order to compare the data, it was necessary to scale the power with  $\lambda^2$  and the beam radius with  $1/\tau$ . We find relatively good agreement for the fused silica and borosilicate crown data with that of Steinberg. The data for SF 55 do not agree, however. Our data seem reasonable in view of the previous results. In SF 55 the relative contribution of electrostriction is small, and hence one expects a small change in damage threshold for the different lenses used. In fused silica and BSC 517, where electrostriction appears to be more important, we observe a definite increase in damage threshold with a longer focal length lens.

The data presented suggest that the Kerr effect increases with refractive index. A large refractive index implies large charge displacements, and large charge displacements are more likely to lead to a nonlinear response to the electric field and, therefore, to a large Kerr effect. It is known that flint glasses exhibit increasing polarizability and refractive index with increasing lead content [30]. The data obtained are consistent with axis rotation measurements of elliptically polarized light [28].

## 5. Conclusions

Our self-focusing length measurements show that the theory of Dawes and Marburger provides a good description of self-focusing.

From threshold measurements using linearly and circularly polarized radiation we conclude that the Kerr effect and electrostriction are of comparable magnitude for the beam geometry used.

## 6. References

- [1] Akhmanov, S. A., Sukhorukov, A. P., and Khokhlov, R. V., *Usp. Fiz. Nauk* **93**, 19 (1967) [*Sov. Phys.--Usp.* **93**, 609 (1968)].
- [2] Chiao, R. Y., Garmire, E., and Townes, C. H., *Phys. Rev. Letters* **13**, 479 (1964).
- [3] Zel'dovich, Ya. B. and Raizer, Yu. P. *ZhETF Pis. Red.* **3**, 137 (1966) [*JETP Lett.* **3**, 86 (1966)].
- [4] Shen, Y. R., *Phys. Rev. Letters* **20**, 378 (1966).
- [5] Chaban, A. A., *ZhETF Pis. Red.* **6**, 487 (1967) [*JETP Lett.* **6**, 20 (1967)].
- [6] Kerr, E. L., *Phys. Rev. A* **4**, 1195 (1971).
- [7] Chaban, A. A., *ZhETF Pis. Red.* **5**, 61 (1967) [*JETP Lett.* **5**, 48 (1967)].
- [8] Litvak, A. G., *ZhETF Pis. Red.* **4**, 341 (1966) [*JETP Lett.* **4**, 230 (1966)].
- [9] Raizer, Yu. P., *ZhETF Pis. Red.* **4**, 124 (1966) [*JETP Lett.* **4**, 88 (1966)].
- [10] Quelle, F. W., "Self-Focusing in Glass," in *Damage in Laser Materials*, ASTM STP 469, American Society for Testing and Materials, 1969, pp. 110-116.
- [11] Duguay, M. A. and Hansen, John W., "Measurement of the Nonlinear Index  $n_2$  of Glass Using Picosecond Pulses," in *Damage in Laser Materials* (NBS Special Publication 341), p. 45.
- [12] Duguay, M. A., Hansen, J. W., and Shapiro, S. L., *IEEE J. Quant. Electron.* **QE-6**, 725 (1970).
- [13] Steinberg, G. N., *Phys. Rev. A* **4**, 1182 (1971).
- [14] Feldman, A., Waxler, R., and Horowitz, D., "Laser Induced Damage Studies," in NBS Technical Note 703, *ARPA-NBS Program of Research on High Temperature Materials and Laser Materials*, 1971, edited by A. D. Franklin and H. S. Bennett, p. 12.
- [15] Dawes, El. L. and Marburger, J. H., *Phys. Rev.* **179**, 862 (1969).

- [16] Wang, C. C., Phys. Rev. 152, 149 (1966).
- [17] Close, D. H., Giuliano, C. R., Hellwarth, R. W., Hess, L. D., McClung, F. J., and Wagner, W. G., IEEE J. Quant. Electron. QE-2, 553 (1966).
- [18] Zverev, G. M., Maldutis, E. K., and Pashkov, V. A., ZhETF Pis. Red. 9, 108 (1969) [JETP Lett. 9, 61 (1969)].
- [19] Giuliano, C. R., "Time Evolution of Damage Tracks in Sapphire and Ruby," in Damage in Laser Materials, 1971 (NBS Special Publication 356), p. 44.
- [20] Bass, M. and Barrett, H.H., "The Probability and Dynamics of Damaging Optical Materials with Lasers," in Damage in Laser Materials, 1971 (NBS Special Publication 356), p. 76.
- [21] Giuliano, C. R. and Marburger, J. H., Phys. Rev. Letters 27, 905 (1971).
- [22] Marburger, J. H., "Theory of Self-Focusing for Fast Nonlinear Response," in Damage in Laser Materials, 1971 (NBS Special Publication 356), p. 51.
- [23] Waxler, R. M. and Farabaugh, E. N., J. Res. Natl. Bur. Std. (U. S.) 74A, 215 (1970).
- [24] Nye, J. F., in Physical Properties of Crystals (Oxford University Press, London, 1957), p. 257.
- [25] Buckingham, A. D. and Pople, T. A., Proc. Phys. Soc. (London) A68, 905 (1955).
- [26] Buckingham, A. D. and Orr, B. J., Quart. Rev. (London) 21, 195 (1967).
- [27] Buckingham, A. D., and Orr, B. J., Trans. Faraday Soc. 65, 673 (1969).
- [28] Owyong, A. Hellwarth, R. W., and George, N. Phys. Rev. B 5, 628 (1972).
- [29] Maker, P. D. and Terhune, R. W., Phys. Rev. 137, A801 (1965).
- [30] Fajans, K. and Keidl, N. J., J. Am. Ceram. Soc. 31, 105 (1948).

## 7. Figures

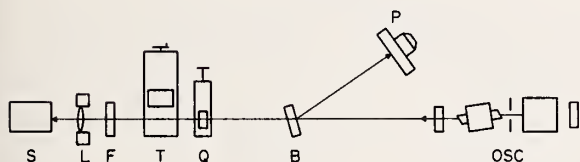


Figure 1. Apparatus for damage testing: OSC = oscillator; B = beam-splitter; P = high speed photodiode; Q = quarter-wave plate for circular polarization, zero or one-half-wave plate for linear polarization; T - thermopile energy meter movable into the beam; F = attenuation filters; L = focusing lens; S = sample.

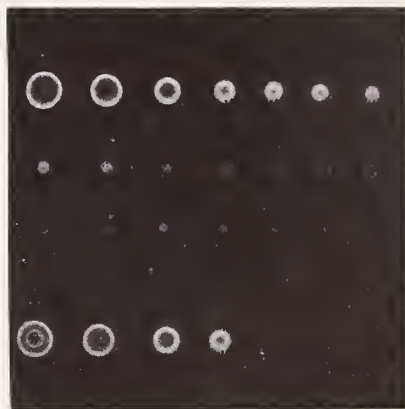


Figure 2. Burn patterns on unexposed (Polaroid) film used for determining beam profile.

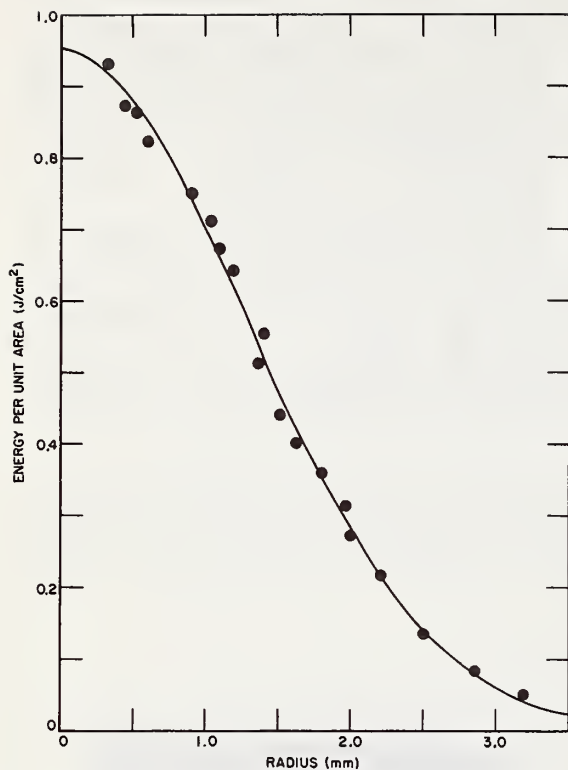


Figure 3. Beam Profile. Energy per unit area as a function of distance from laser beam axis as measured at the focusing lens. The solid line is a Gaussian fit to the data.

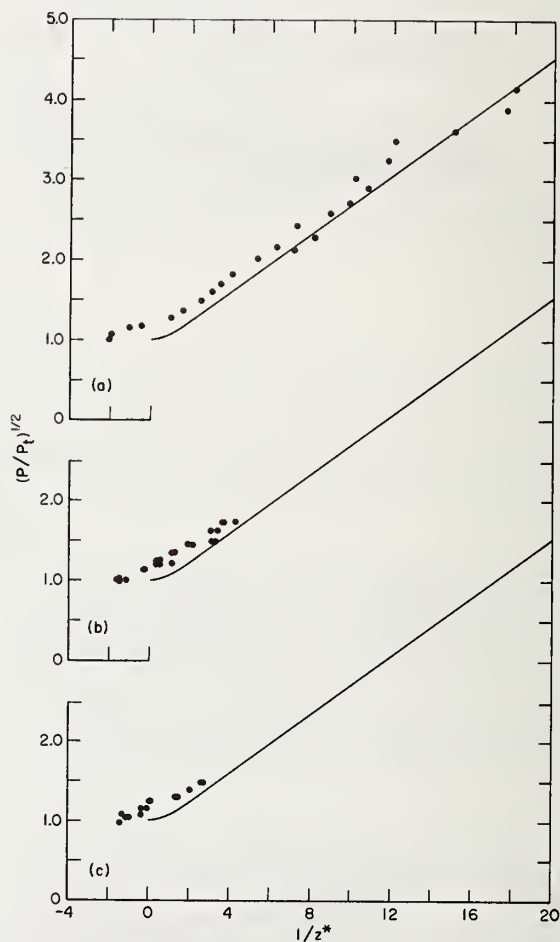


Figure 4. Self-focusing length as a function of the square root of normalized beam power. A lens of 181-mm focal length was used in obtaining the data. Samples used: (a) dense flint glass, (b) borosilicate crown glass, (c) fused silica. The solid curves are from the work of Dawes and Marburger [15].



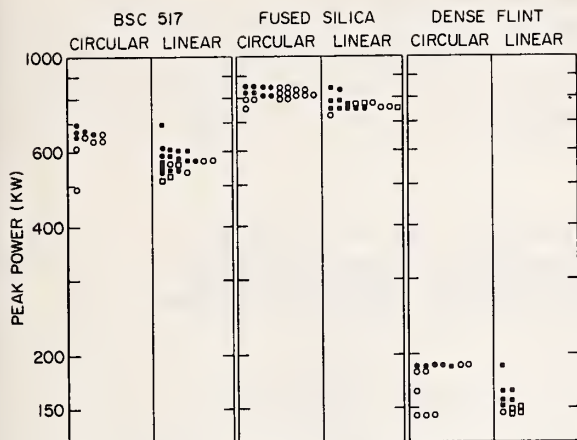


Figure 5. Damage threshold measurements in borosilicate crown glass (BSC 517), fused silica, and dense flint glass (SF 55) for linearly and circularly polarized radiation; wavelength =  $1.06 \mu\text{m}$ ; pulse width = 25 ns. The solid points represent shots which produced damage; the open points represent shots which did not produce damage. Data obtained using 76-mm focal length lens.

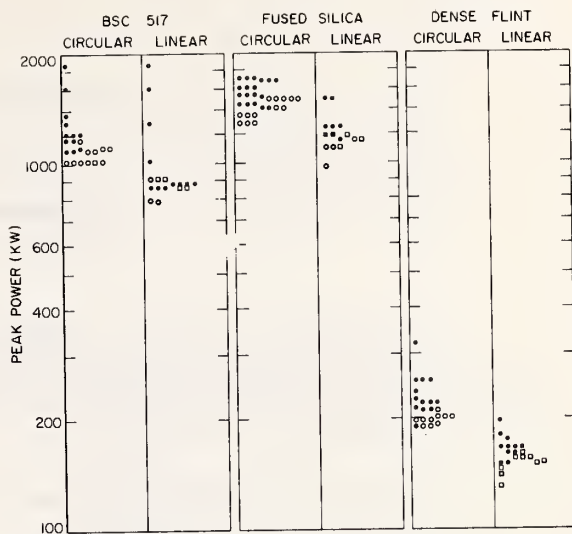


Figure 6. Damage threshold measurements in borosilicate crown glass (BSC 517), fused silica, and dense flint glass (SF 55) for linearly and circularly polarized radiation; wavelength =  $1.06 \mu\text{m}$ ; pulse width = 25 ns. The solid points represent shots which produced damage; the open points represent shots which did not produce damage. Data obtained using 181-mm focal length lens.

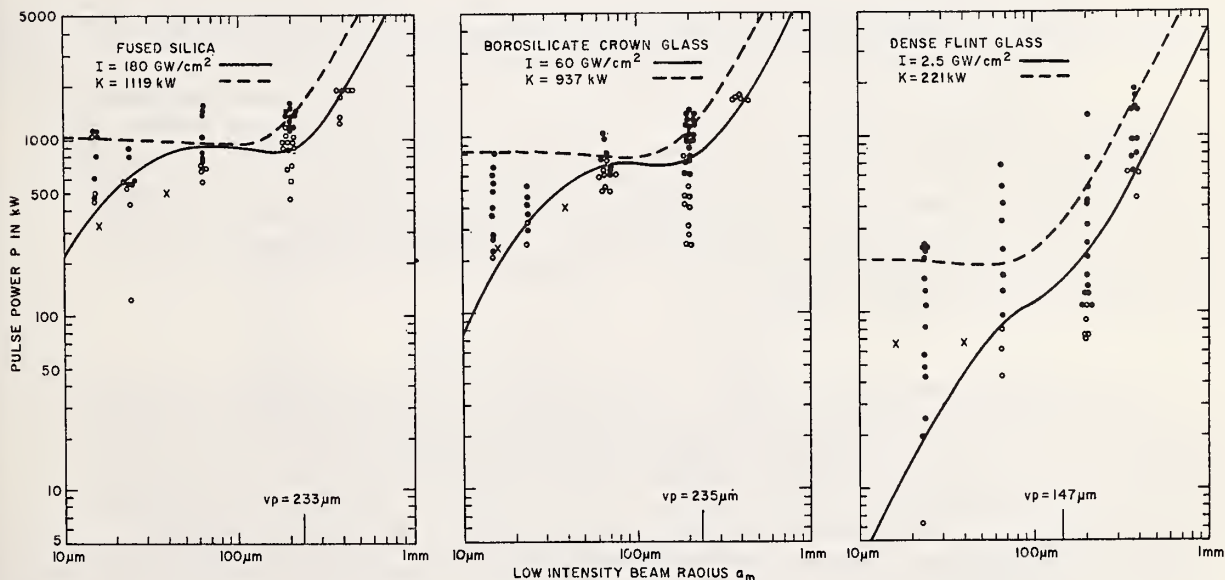


Figure 7. Track formation thresholds in borosilicate crown glass, fused silica, and dense flint glass from the work of E. L. Kerr [6] and G. N. Steinberg [13]. Also shown are data from the work depicted by X. It was necessary to scale our data as the wavelength and pulse width used differed from Steinberg's.

## Damage Measurements with Subnanosecond Pulses

John M. McMahon

Naval Research Laboratory  
Washington, D.C. 20390

The realization of high energy subnanosecond pulse lasers has been limited by self-focusing damage in laser rods. In this paper measurements on  $n_2$  for laser glasses with subnanosecond pulses are described. The systems aspects of using such glasses are also discussed since in practice this can have a dominant effect on the performance of a high energy short pulse device.

Key Words: Damage mechanisms in laser systems, disc amplifiers, Nd: YAG laser, self-focusing, subnanosecond pulses.

### 1. Introduction

There is currently a great deal of interest in generating intense subnanosecond pulses for laser CTR applications as well as for other purposes. Success in construction of relatively efficient solid state lasers which generate terawatt (or higher) level pulses and which operate reliably for many shots will require either that the pulse shape and intensity be tailored in time and spatial extent such that non-linear effects do not predominate or that geometries be chosen in which these effects can reasonably be expected not to occur.

Disc amplifiers, for example, appear to be relatively immune to self focusing (if only in that the surfaces will damage first). They however are somewhat unattractive from an efficiency and convenience standpoint compared to a solid rod system.

We have investigated the self focusing problem for three laser glasses in common use (Owens-Illinois ED-2; Soveril-MG 915 and Schott LG-56). Measurements of  $N_2$  are reported on unpumped rods for pulse durations between 20 psec and 250 psec. Measurement techniques for subnanosecond pulses are not presently as quantitative as might be desired. Pulse duration measurements by non-linear optical techniques may lead to erroneous results unless great care is taken. Energy measurements are complicated by plasma formation in the calorimeter at very low levels compared to q switched pulses ( $\approx 50 \text{ mJ/cm}^2$  on carbon) which reduces the signal to noise ratio to (typically) less than 20:1 and there are difficulties in measuring near and far field intensity distributions with a high precision and wide dynamic range at  $1 \mu\text{m}$ .

### 2. Measurement of $N_2$ in Laser Glasses

In the 1970 ASTM symposium, J. Davit[1]<sup>1</sup> of CGE and M. Duguay and J. Hansen[2] of BTL reported on measurements on  $N_2$  for several glasses by various methods. Duguay and Hansen reported some measurements at  $\sim 8 \text{ psec}$  on BK-7 and LASF-7 glasses and Davit on tests done at  $2 \text{ nsec}$  on LG-56 and MG-915 glasses. While BK-7 might be expected to behave in a similar fashion to the laser glasses Davit tested, the value of  $N_2$  was about an order of magnitude larger than the BTL value. This suggests the possibility that for very short pulses  $N_2$  might be smaller due to mechanisms important on the nanosecond time scale not being able to respond to short pulses. Another possibility was that since neither author used a laser which produced a time band width limited pulse, both measurements could be consistent with a model in which some of the pulse energy is in very short temporal spikes.

---

<sup>1</sup>Figures in brackets indicate the literature references at the end of this paper.

For the measurements reported here we used a mode locked Nd:YAG oscillator-amplifier which has been described elsewhere.[3] This system produces a TEM<sub>00</sub> spatial mode output single pulse with an energy adjustable from 1 - 200 mJ in a pulse whose width can be adjusted from 20 psec to 1.3 nano-seconds by the use of transmission etalons in the cavity. Our measurements and those of Carmen and co-workers at LLL indicate that the pulse is essentially time-bandwidth limited[4] with a smooth Gaussian spectral and temporal output. Figure 1 shows the geometrical arrangement of this device.

For the trapping measurements the beam was propagated ~ 3 meters to get rid of near field Fresnel fringes and the pattern checked and found to be a Gaussian down to below the e<sup>-3</sup> points. The beam was then run through a sample rod and the trapping length noted from the side during 10-20 shots for each sample. In all cases the start of the filament was characterized by the emission of blue light (presumably from plasma breakdown in the track). This was somewhat enhanced in the ED-2, presumably due to the ultraviolet pumping the cerium which then fluoresced in the region of 4000 - 5000 Å.

Table 1. Samples Tested

<u>Glass Type</u>	<u>l(cm)</u>	<u>γ(cm<sup>-1</sup>)</u>
ED-2	30	3 x 10 <sup>-3</sup>
MG 915 (cast)	30	7.5 x 10 <sup>-3</sup>
LG 56	50	3 x 10 <sup>-3</sup>
BK-7	6	3 x 10 <sup>-3</sup>

Table 1 lists the geometries and absorption coefficients of the samples tested. The Soveril glass tested was a rod made by the old process and had a significantly higher absorption coefficient than MG-915 made by the continuous flow process. The LG 56 rod was supplied by CGE with the NRL VD640 and had a low absorption coefficient for LG-56. We initially questioned whether this was LG-56 or LG-630 and were assured by CGE that it was LG-56.

In the actual sequence of experiments the laser was tuned to run at a given pulsewidth and then the samples were each irradiated to 10-20 shots and the mean trapping length, peak energy density, pulsewidth and spatial distribution determined. The laser was then tuned to the next pulsewidth and the sequence repeated. Table shows the results for pulse durations of 20 psec and 250 psec. The pulse peak powers and beam parameters were P<sub>0</sub> = 8 x 10<sup>10</sup> W/cm<sup>2</sup>, b = 1.1 mm and P<sub>0</sub> = 1 x 10<sup>10</sup> W/cm<sup>2</sup>, b = 1.5 mm, respectively.

Table 2. Relative Data on Trapping Length

<u>Type</u>	<u>Z(250 psec)</u>	<u>Z(20 psec)</u>
ED-2	24 ± 1	6.6 ± 1
MG-915	24 ± 1.5	6.1 ± 1
LG-56	21 ± 1.5	5.6 ± 1
BK-7	-----	6 + *

\* The 6 cm sample only trapped occasionally (≈ 30% of shots) and within 1 cm of the surface.

The difference in beam parameter was caused by the beginning of focusing in the YAG preamplifiers which was not severe enough to noticeably perturb the temporal or spectral structure of the pulse. The cone angle of the self-phase modulated light from the samples was ≈ 0.1 radian at 250 psec and ≈ 0.25 radian at 20 psec. Typically 3-10 filaments would be formed which would traverse the length of the rod.



Table 3. Trapping Data ED-2

$t(\text{psec})$	$P_o(\text{W/cm}^2)$	$b(\text{mm})$	$Z(\text{cm})$
20	$8 \times 10^{10}$	1.1	$6.6 \pm .5$
125	$1.2 \times 10^{10}$	1.2	$18 \pm 2$
250	$1 \times 10^{10}$	1.5	$24 \pm 1$
125*	$4.8 \times 10^{10}$	1.2	$9.2 \pm 1.6$

\* Etalon misaligned caused temporal beats with a four-fold enhancement of peak power.

Table 3 gives trapping data on ED-2 for a somewhat more complete set of experiments. Data sets were run for 20 psec, 125 psec and 250 psec "clean" pulses and also for a pulse 125 psec long with the etalon misaligned to give two spectral components of equal intensity. These interfered giving a peak intensity  $\sim$  four times the intensity for a non-structured pulse. This caused a reduction in trapping length of a factor of two.

Table 4.  $N_2$  Values (esu)

BK-7	$6 \times 10^{-14}$
ED-2	$(7 \pm 3) \times 10^{-14}$
MG-915	$(7 \pm 3) \times 10^{-14}$
LG-56	$(8 \pm 3) \times 10^{-14}$

Table 4 gives the calculated value of  $N_2$  for the glasses tested with an estimated absolute accuracy of  $\pm 40\%$ . The value of BK-7 should be taken as an upper limit since  $l_{\text{sample}} \approx Z_{\text{foc}}$ .

### 3. Discussion of the Results

The data all showed an excellent agreement with Kelley's formula for the parametric variation of self focusing length[5]

$$Z_{\text{foc}} = \frac{b}{4} \left( \frac{N_o}{N_2} \right)^{\frac{1}{2}} \frac{1}{E}. \quad (1)$$

Additionally, over the range of temporal values tested  $N_2$  for a particular glass was found to be sensibly constant.

It was additionally shown that  $N_2$  will follow temporal structure on the pulse. If we had assumed our structured pulse to be smooth, an  $N_2$  value four times the observed value would have been obtained.

Under a given set of conditions there did appear to be small but experimentally significant differences in self focusing length. That there is a difference between ED-2 and LG-56 is not too surprising since the two are dissimilar glasses, but the difference between the LG-56 and MG-915 is surprising, since they are essentially the same glass. These may be related to the difference in absorption coefficient of the two glasses.

### 4. Systems Considerations

Based upon the values of  $N_2$  reported here there appear to be no fundamental difficulties in amplifying pulses to high energies if the trapping length is long compared to the amplifier length and the pulse is temporarily and spatially smooth. Unfortunately, these conditions are rarely met (for more than a few shots).

Dust particles on surfaces can provide nuclei for wavefront disturbances which can then cause trapping in the next stage. Shot by shot this damage can then propagate through the system. This problem can be minimized if the amplifiers are spaced in the far field of any filaments generated in the previous amplifier.

It is also generally very difficult to avoid Fresnel fringes in the beam pattern. Based on the experiments of Guiliani [6], a Fresnel fringe itself may be expected to have a high threshold for trapping (since it would be a one dimensional process). However, in a circularly symmetric beam, the Fresnel fringes may accentuate damage by moving energy into the beam center where it may tend to form an intensity spike. We have seen such a spike forming at times and we understand that Bettinger [7] at CGE has seen such a spike form and then self-focus. This effect seems to be somewhat diminished if any apertures in the system are non-concentric.

Operating the CGE VD-640 amplifier train with 250 psec pulses outputs of 50-60 joules have been achieved with little or no degradation over  $\approx 100$  shots. A limited number of shots have been run at levels of 90-100 joules. No degradation has been observed to date.

## 5. References

- |  |   |
|--|---|
| [1]. Davit, J, NBS Special Publication 341, (1970) pp 37-44.   | [5] Kelley, P.L., Phys. Rev. Letters, <u>15</u> , 26 (1965), p. 1005.               |
| [2]. Duguay, M.A. and J. W. Hansen, NBS Special Publication 341, (1970) pp 45-50.                          | [6] Guiliani, IEEE Int. Quantum Electronics Conference, Montreal, Canada, May 1972. |
| [3] Emmett, J. et al, "Disc Lasers", IEEE Int. Quantum Electronics Conference, Montreal, Canada, May 1972. | [7] Bettinger, private communication.   |
| [4] Carmen, R., IEEE Int. Quantum Electronics Conference, Montreal, Canada, May 1972.                      |   |

## 6. Figures

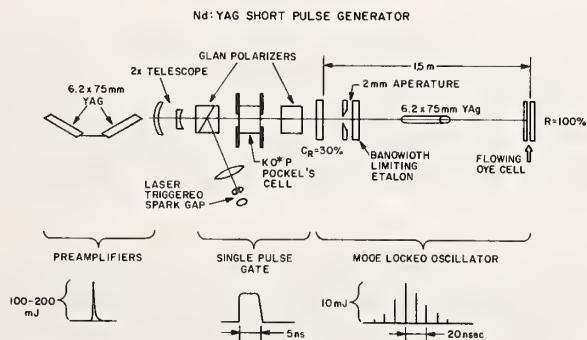


Figure 1. Nd:YAG Short Pulse Generator

## Time Resolved Damage Studies of Thin Films and Substrate Surfaces\*

J. H. Parks and N. Alyassini<sup>†</sup>

University of Southern California  
Los Angeles, California 90007

The time evolution of damage to thin films and substrate surfaces was observed by monitoring the intensity variation of a He-Ne beam reflected from the film or surface during irradiation by a Q-switched ruby laser. Monolayered films including ZnS, CaF<sub>2</sub> and NaCl on fused silica substrates were studied, as well as uncoated fused silica and LiF substrates. When the probe beam is reflected from the exit surface of a substrate sample, the reflected intensity was observed to decrease within the time-scale range of 20-200 nanoseconds to a final value significantly less than that prior to damage. When the probe is spatially offset from the damage region, the reflected intensity decreases and then returns to approximately the predamage value within 0.2-0.3  $\mu$  sec. This reversible effect was observed to be associated with a propagating disturbance on the substrate surface moving with approximately the speed characteristic of a Rayleigh surface wave. The risetime and duration of the plasma which accompanies surface damage was also measured.

The reflected intensity from thin films was observed to increase or decrease depending on the film index of refraction. The monolayer film samples exhibited reflectance changes on the timescale of the ruby pulse, however an offset probe position indicates this change can occur after a time delay of  $\sim 0.1$ - $0.2 \mu$  sec.

Key Words: Damage induced reflectivity change, laser induced damage, laser induced surface acoustic waves, surface, surface breakdown plasma, thin film, time resolved damage.

### 1. Introduction

Studies of surface damage in laser glasses, crystals and thin films usually characterize the damage in terms of the laser source used to induce the material breakdown. There has been considerable effort to correlate damage mechanisms with laser power threshold values, radiative pulse width, and the morphology of the damaged region. This work has led to a description of the conditions under which damage will happen and a clearer expectation of the resulting structural deformation. However, the present experimental techniques may not be particularly appropriate to reach a fundamental understanding of the primary physical processes, intrinsic to the material, which originate the sequence leading to irreversible, macroscopic damage.

We have developed an optical probe technique which allows the continuous time evolution of laser induced damage to be monitored on a timescale spanning 3 to 4 orders of magnitude. The time resolution can include effects occurring during the damage pulse and also be extended to observe phenomena existing well after the laser pulse has past. This experimental technique places emphasis on the study of physical processes in the time domain in an attempt to unravel the damage sequence and perhaps isolate a precursor time event which signals the onset of material breakdown.

A description of these time resolved damage measurements is presented in Section 2 and a summary of initial results observed in the damage of thin dielectric films and substrate surfaces in Sections 3 and 4. This presentation is intended as a progress report of a continuing research program rather than final results of a specific experiment. In the concluding Section 5, we summarize our findings and plans to extend these measurements.

\*This research was supported by Air Force Cambridge Research Laboratories and the Advanced Research Projects Agency of the Department of Defence under Contract No. 19628-71-C-0220.

<sup>†</sup>Departments of Physics and Electrical Engineering.



## 2. Time Resolved Damage Measurements

Figure 1 shows the experimental arrangement of the ruby laser, damage sample, and He-Ne probe laser. The passively Q-switched ruby laser is internally apertured to 6 mm and forms a uniform beam profile indicated by unexposed Polaroid film. Although the beam quality is not clean enough for detailed threshold measurements, it is adequate for the purposes of developing these techniques. The 15 cm focal length lens focuses the ruby beam at a point 2 cm past the sample exit surface and the ruby spot size is 1 mm diameter at this surface. The substrate sample position was adjusted slightly for thin film studies to produce a spot size of 0.6 mm diameter at the film surface. The laser power density used to damage substrate exit surfaces and thin films was  $\sim 2\text{GW}/\text{cm}^2$  and  $\sim 1\text{GW}/\text{cm}^2$  respectively. The ruby laser pulsewidth is 20 nsec.

During a damage pulse, the He-Ne probe beam is reflected from a point on the surface or thin film which is aligned with the ruby laser. As shown in figure 1a and 1b, the probe beam can be reflected either internally or externally from the surface to be studied. In the experiments described in Sections 3 and 4, the exit surface was observed via an internally reflected probe beam to avoid absorption of the probe radiation by the surface plasma. The He-Ne beam is focused on the damage region to a spot size of less than 0.5 mm diameter. A system of apodized lenses and apertures define the optical path of reflected probe and reduces plasma scattered light pickup. An RCA 7265 photomultiplier tube shielded by two 6328 Å narrow band filters detects the reflected probe intensity. The electronics risetime was 16 nsec which limited the time resolution in these experiments to the ruby pulsewidth. The He-Ne beam was polarized horizontally to allow near Brewster angle incidence on the substrate surface in order to avoid photomultiplier saturation by the reflected probe beam.

## 3. Substrate Surface Damage

Time resolved surface damage was observed in samples of fused silica (T13 Optical-2, T20 Suprasil-2 grades) and LiF ground and polished disks of 3 mm thickness. The probe focal spot could be spatially positioned with respect to the ruby spot by referencing to a second He-Ne laser beam used to align the ruby laser optics.

At the power densities used, the damage at the fused silica surface was in the form of pits 0.1 mm to 0.5 mm in diameter. Damage was generally weaker for LiF; leaving pits at most 0.2 mm in diameter. Using an optical telescope damage pits of 10 microns could easily be resolved visually. Figure 2a shows an example of the time response of the reflected probe intensity when the probe beam was positioned on the damage area. The general characteristics of the probe response under these conditions are shown in figure 3. When the damage pits are greater than 0.1 mm, a rapid decrease in intensity is observed during the ruby pulse timescale. However, for smaller pits corresponding to weaker damage, the intensity decrease begins within the ruby pulse width but only gradually reaches steady state long after the damage pulse has ended. These results are observed independent of probe polarization and appear to result from diffuse scattering of the probe beam by the damage pit.

When the probe beam is spatially displaced from the damage spot, a reversible intensity decrease is observed similar to the traces shown in figure 2b. When the spatial separation between damage and probe positions is increased a distance  $\Delta x$ , the intensity change is observed to occur at a delayed time  $\Delta t$  given by  $\Delta x = v \cdot \Delta t$  where  $v \approx 4 \times 10^5$  cm/sec for fused silica as shown in figure 3. The speed of this propagating effect is close to the speed of a Rayleigh acoustic surface wave,  $v = 3.4 \times 10^5$  cm/sec on fused silica. Such an effect has been observed previously [1]<sup>1</sup> to be generated by transient surface heating in metallic films. Holographic techniques [2] have also shown the presence of bulk and surface waves excited by laser induced damage in glass. In fused silica these propagating effects were observed when damage pits greater than 0.1 mm resulted. In LiF substrates, propagating intensity variations of comparable strength to fused silica were noted even when damage pits were less than 10 microns.

These techniques were also applied to time resolve the exit surface plasma. Passing the probe beam parallel to the exit surface at a distance of  $\sim 1$  mm from the substrate allows the plasma electron density to attenuate the probe beam by absorption. Figure 4 shows the probe intensity decreases for approximately a microsecond duration indicating the order of magnitude of the plasma timescale. It is important to note that the timescales of the propagating disturbance and the plasma duration vary by a factor of 10 which indicates that the propagator is not simply generated by the expanding plasma.

## 4. Thin Film Damage

Monolayer films of ZnS, CaF<sub>2</sub>, and NaCl were deposited on fused silica substrates in thickness of  $\lambda/4$  and  $\lambda/2$  at 6943 Å. These films were damaged by the ruby beam on the exit surface of the substrate and the probe beam was internally incident on the damage area. At the power densities used for the ZnS

---

<sup>1</sup>Figures in brackets indicate the literature references at the end of this paper.

and NaCl films, the fused silica surface showed no visible signs of damage. Figure 5a shows examples of the probe intensity changes resulting from thin film damage. In all cases the rapid intensity change occurred within the ruby pulse width. This transition was consistent with a reflectivity change from the relative index of the thin film boundary to the relative index of a fused silica-air interface. The film damage spot size was  $\sim 0.5$  mm diameter and the probe beam is measuring the timescale during which the film is leaving the substrate surface. When the probe is spatially offset from the damage area in NaCl films, a time delay has been observed. It is likely that this is a measure of the rate of an expanding heated region which is vaporizing the film. The  $\text{CaF}_2$  films were found to resist damage up to power densities for which the fused silica substrated became pitted.

Figure 5b indicates that the probe signal change can either increase or decrease consistent with the above interpretation of the probe time traces. Since the internal incidence angle was close to  $20^\circ$ , the Fresnel reflectivity is approximately given by the normal incidence dependence on relative refractive index  $n = n_2/n_1$ . The relative indices for fused silica to air, NaCl and ZnS boundaries are 0.69, 1.06 and 1.64 respectively which yield corresponding reflectivities of 0.034, 0.059 and 0.001 assuming normal incidence. This shows an increasing reflectivity of  $0.001 \rightarrow 0.034$  for NaCl film samples and a decrease  $0.059 \rightarrow 0.034$  for ZnS film samples, assuming the film is removed during damage leaving an uncoated fused silica surface to reflect the probe beam.

## 5. Concluding Remarks

The following points summarize conclusions drawn from these time resolved measurements:

1. Diffuse scattering at substrate exit surfaces, which arises from structural damage, can occur within the timescale of the ruby pulsewidth or continue well after the pulse, depending on the severity of the damage.
2. Damage at substrate surfaces can excite a propagating disturbance moving on the surface with speeds comparable to Rayleigh acoustic waves. This propagator can be detected by optical techniques; however, it has not been determined whether the fundamental process leading to changes in the reflected probe intensity are caused by a reversible diffuse scattering, absorption, or index variations.
3. LiF substrate surface damage appears to excite propagators with extremely small damage on the scale of 5-10 microns. This material offers the possibility of isolating a precursor mechanism for detailed studies of the damage physics.
4. Thin films exhibit damage primarily within the duration of the ruby pulse but it is possible to detect this rapid film destruction moving outward radially. No evidence of propagators has been detected optically in monolayer film structures.

It may be useful to indicate our immediate research plans to improve these time resolved damage measurements. In addition to increasing the time resolution of the probe beam detection electronics, and improving the ruby pulse optical homogeneity, the following experiments are being pursued:

1. The correlation of surface plasma formation and the initiation of structural damage by simultaneous optical probes.
2. A more detailed study of propagators on substrate surfaces and thin films as a possible precursor.
3. The use of acoustic surface wave techniques to detect damage phenomena with a greater sensitivity and time resolution than the optical methods provide.
4. These measurements will be applied to a wider variety of substrates and film materials; particularly those which have been carefully characterized by damage threshold studies.

## 6. Acknowledgements

We would like to acknowledge discussions with Prof. J. Marburger and Prof. R. W. Hellwarth. The film depositions were prepared by Mr. H. R. Owen.

## 7. References

- |   |   |
|---|---|
| [1] Lee, R. E. and White, R. M., Appl. Phys. Letters <u>12</u> , 12 (1968). | [2] Boling, N.L. and Beck, R. W., NBS Special Publication 356, Damage in Laser Materials: (1971). |
|---|---|

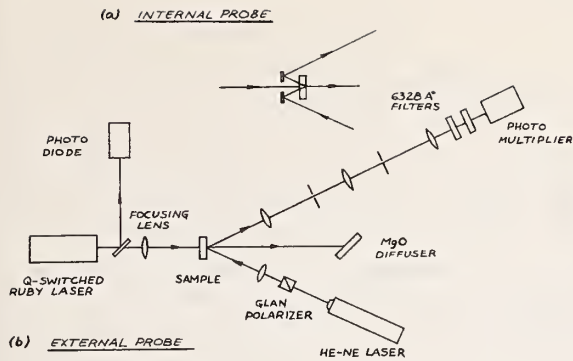


Figure 1. Experimental arrangement for sample irradiation and He-Ne probe optics.

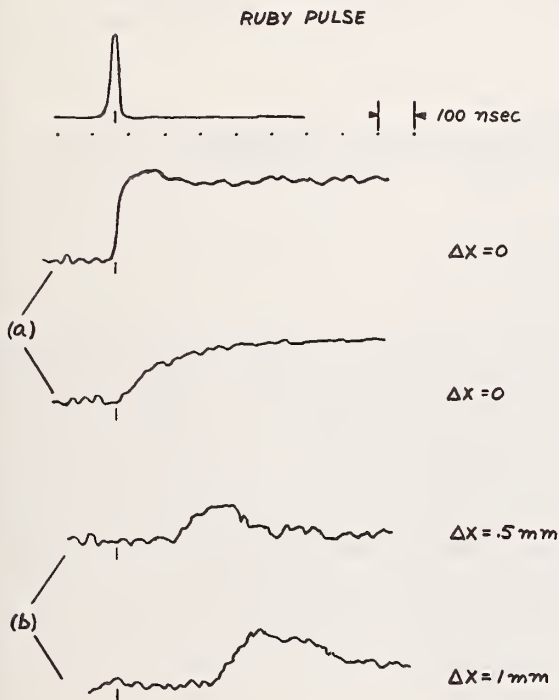


Figure 2. Oscilloscope traces showing: (a) decreases in reflected probe intensity during surface damage (b) reversible reflectivity changes associated with propagating surface waves observed when probe is offset a distance  $\Delta x$  from damage.

### SUBSTRATE EXIT SURFACE DAMAGE

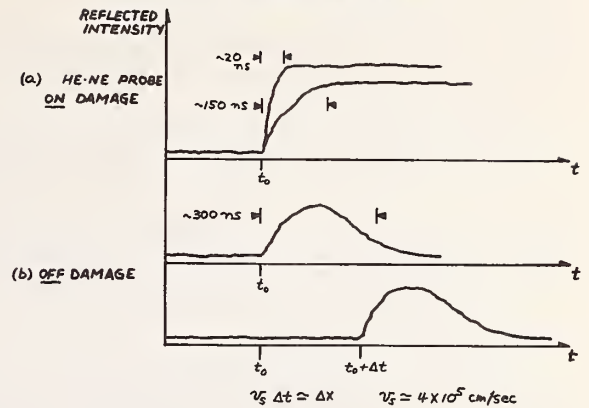


Figure 3. Characteristic time dependence of substrate exit surface damage observed by optical probe techniques. The timescales indicate an average range of many measurements. The ruby pulse position is indicated by  $t_0$ .

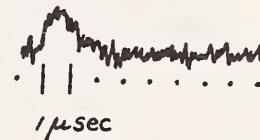


Figure 4. Exit surface plasma duration measured by optical probe absorption.

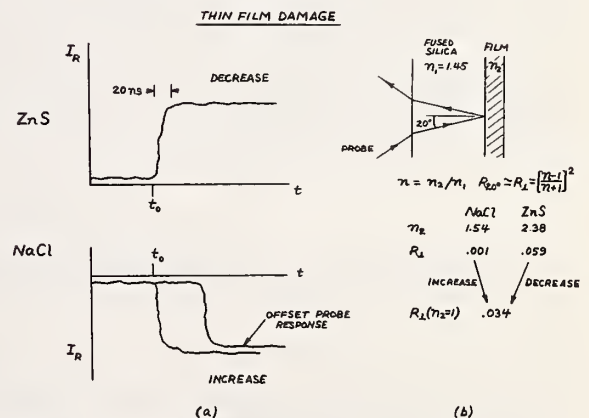


Figure 5. Film damage characteristics showing: (a) time dependence of reflected probe intensity for NaCl and ZnS films (b) analysis of reflectivity  $R$  which indicates an intensity decrease for ZnS and an increase for NaCl after film is removed during damage leaving  $n_2 = 1$ .



# Laser Induced Damage to Mirrors at Two Pulse Durations<sup>\*</sup>

E. S. Bliss and D. Milam

Air Force Cambridge Research Laboratories  
Hanscomb Field  
Bedford, Massachusetts 01730

The damage thresholds of eight, multiple layer dielectric, 95% reflecting mirrors have been measured for single pulses of 20 nanoseconds and 20 picoseconds duration. In both sets of measurements the pulse energy, an oscilloscope trace of the pulse, and the beam's transverse energy density profile at the surface being damaged are recorded for each shot. The variation of the threshold from mirror to mirror and as a function of pulse duration, beam radius, and appearance under microscopic examination is discussed in the context of possible damage mechanisms.

Key Words: Dielectric mirror, laser-induced damage, laser monitoring, laser damage mechanisms, electron avalanche, plasma production, scattering sites.

## 1. Introduction

For several years an effort has been underway at the Air Force Cambridge Research Labs to perfect a mode-locked ruby laser system capable of reliably producing single subnanosecond pulses with a smooth and radially symmetric energy density profile and enough energy to damage dielectric materials with spot sizes larger than 0.1 millimeter. Such a system is now in use and is described in detail in earlier publications. [1,2]<sup>1</sup> To complement the mode-locked system and to facilitate experimental identification of the laser-induced-damage mechanisms by determination of their pulse duration dependence [3], a standard Q-switched ruby laser system has also been constructed which meets the same reliability radial energy distribution, and total energy requirements and operates in a single longitudinal mode as well. Figure 1 contains block diagrams of both systems. This paper describes laser-induced-damage measurements performed on nine commercially produced dielectric mirrors using these two lasers.

## 2. Laser Damage Monitoring Apparatus

Meaningful laser-induced-damage experiments demand precise characterization of the laser pulse causing the damage. Accordingly, each pulse is scrutinized in unprecedented detail.

---

<sup>\*</sup>This research was supported jointly by the Air Force and the Advanced Research Projects Agency of the Department of Defense.

<sup>1</sup>Figures in brackets indicate the literature references at the end of this paper.

## 2.1 Q-Switched System Monitoring

Figure 2 is a schematic diagram of the monitoring apparatus for experiments using Q-switched pulses. The beam enters from the left and passes through two beam splitters. The first one deflects a portion of the beam to a fast diode which drives a Tektronix 454 oscilloscope and provides a filmed record of the temporal development of each pulse. The second beam splitter directs a known fraction of the beam to an EG&G radiometer, which is used to determine the energy of each pulse. Energy values measured by this instrument exhibit a random error of only a few percent. However, past experience and comparison with other radiometers and a Quantronix 500/504 calorimeter/energy-meter suggest that the absolute accuracy may be limited to 10 or 20 percent.

The beam then passes through a 50 cm focal length lens and, except for a small portion, is focused onto the damage sample. When the test sample is a high reflectivity mirror, the path shown beyond the sample is not used, and the mirror is tipped very slightly to avoid direct reflections back to the amplifier. The small reference beam which is split off after the focusing lens is identical to the damaging beam except for its energy content and it can be utilized for monitoring the focused radial energy distribution as follows: A calibrated reticle is inserted in the reference beam in the plane corresponding to the mirror surface in the main beam. An imaging lens is then placed such that the reticle is imaged onto the film in the multiple exposure-level camera. [4] For ruby lasers Polaroid film Type 55 is ideal since it provides a positive for visual examination and a negative for densitometer analysis. The magnification of the imaging system is determined by photographing the reticle with  $0.69\mu\text{m}$  light. Then the reticle is removed and the camera now records the radial energy density profile of each pulse in the damage plane. Examples of such photographs will be discussed in section 3.1. b.

## 2.2 Mode-Locked System Monitoring [1]

Figure 3 is a schematic diagram of the monitoring apparatus for experiments using mode-locked pulses. The principal features are the same as for the Q-switch pulse monitoring system, but there are some differences. The focusing is done by a lens pair whose effective focal length can be varied by changing the lens spacing (an effective focal length of approximately 1m was used for all the measurements reported in this paper). Both an EG&G radiometer and a Quantronix 500/504 calorimeter/energy-meter are used for energy measurement. Although the calorimeter is blocked when a high reflectivity mirror is used for a sample, measurements with both instruments and no sample show that the two devices, operating on entirely different physical principles, agree within 20% on the absolute value of the energy reaching the sample.

The fast diode drives a Tektronix 519 oscilloscope and examines light arriving along several paths simultaneously. A small portion of the oscillator output is picked off at the pulse selector [1] and enters the diode along the dotted path in figure 3. One percent of the amplified selected pulse is split off just ahead of the focusing optics and directed onto the diode with a delay appropriate to display it between pulses in the oscillator's mode-locked train. The remaining path to the diode is for monitoring the pulse after passage through a transparent damage sample and is not used for mirror studies.

The radial energy distribution in the damage plane is imaged into the multiple exposure camera by a lens pair instead of single lens. This allows the first lens to be well removed from the sample area and gives more flexibility for imaging different planes and changing magnification. As in the Q-switched monitoring system the energy density profile in the main beam is not monitored for mirror damage experiments and so no reference sample is required.

## 3. Output Properties of the Lasers

### 3.1 Q-Switched System

#### a. Temporal Profile

It is known that smooth, apparently single longitudinal mode oscilloscope traces obtained by spacially integrating over the whole beam on a diode do not guarantee that the temporal development

of the pulse is the same over the whole beam. [5] In order to determine whether deviations from ideal temporal behavior off of the beam axis might be related to deviations from the ideal radial energy distribution, a sequence of shots was fired in which the output mirror of the Q-switched oscillator was rotated by 4 sec. of arc about the vertical axis after each shot. After appropriate attenuation the oscillator output was directed into the multiple exposure-level camera without focusing, and each shot was photographed in turn. Figure 4a shows the results.

Each shot produces a vertical row of successively less exposed energy density profiles, and the shots on the left show a slightly elongated pattern with the top tipped to the right, while the shots on the right show a similar elongation with a tip to the left. When the temporal profile is examined through a pinhole on axis (fig. 4b, right) and through a vertically displaced pinhole (fig. 4b, left) for the mirror position giving no detectable tip (5th from the right), the off-axis temporal profile is found to be considerably different from that on axis. However, if the process is now repeated for mirror rotations about the horizontal axis, with 4 sec. rotations being made until the spot is no longer elongated but round as for the far right mirror position of fig. 5a, then the same temporal profile is found at both pinholes.

We conclude that a genuinely round output from the Q-switched oscillator implies uniform temporal behavior over the whole beam. Typically the preparations for a series of damage tests included an examination of the oscillator output, but it was not always done with the thoroughness demonstrated in figs. 4 and 5. Consequently, it is quite possible that some of the measurements to be described in sections 4. and 5. were performed with pulses whose off-axis temporal behavior was less than ideal. The effect of small temporal deviations off-axis on the results of our damage tests is assumed to be negligible.

In fig. 6 the spacially integrated temporal pulse profile as recorded by the monitoring apparatus in fig. 2 has been compared for three randomly selected pulses out of a series of some 220 shots. Pulse no. 217 is indicated by a solid curve and points measured from the scope traces of shots 11 (○) and 89 (□) are plotted on a normalized scale which forces the pulses to coincide at their peak power points. The fact that all three pulses fall on essentially the same curve demonstrates the high degree of repeatability obtained in the temporal shape of the pulse.

#### b. Spacial Profile

Figure 7a shows two examples of the Q-switched pulse's radial energy distribution in the damage plane as photographed by the imaging system described in section 2.1. Each pulse produces a horizontal line of spots in which adjacent exposures differ by a factor of two. The microdensitometer traces of three consecutive shots shown in fig. 7b verify the impression gained by visual examination of the photographs that the energy density varies smoothly with radius. Furthermore, we have determined by constructing energy density versus radius curves from the densitometer traces [6] that the radial dependence of the energy distribution is Gaussian.

### 3.2 Mode-Locked System

#### a. Temporal Characteristics

The mode-locked oscillator produces a train of short pulses separated by approximately 7 nsec. from which a single pulse is selected for amplification. In fig. 8 oscilloscope traces of four consecutive shots show the mode-locked train with the selected pulse missing and the amplified selected pulse displayed between the first two recorded pulses of the train. The extra little bump appearing just before the amplifier pulse in the bottom three traces is a stray reflection onto the diode and may be ignored.

The duration of the mode-locked pulses generated by the oscillator has been estimated from time-integrated two-photon fluorescence photographs to be approximately 20 psec. To check for the possibility that the pulse duration changes during amplification or that pulses from different parts of the pulse train have different durations, two-photon measurements of single amplifier pulses are planned, but have not yet been accomplished. Even without such measurements, however, it is known from the impulse response of the diode-oscilloscope combination that the pulse duration of the amplified pulses is less than 100 psec.. For the case of pulses selected from properly locked trains, the amplified pulse always gives the same impulse shape scope response as the oscillator output.



## b. Spacial Profile

The examples of focused radial energy density profiles for single mode-locked pulses shown in fig. 9 are similar to those shown for Q-switched pulses in fig. 7. Since the pronounced spike appearing on the left side of the first exposure in the bottom trace does not appear in the adjacent exposure, it is not an intensity spike in the beam and must be identified as a spot or a scratch on the film. Construction of energy density versus radius curves from these densitometer traces reveals some small departures from a true Gaussian profile, however the errors in damage threshold resulting from treating the profile as Gaussian are small compared to the uncertainty already existing in total energy measurement.

## 4. Mirror Damage Experiments

Using the lasers and monitoring techniques described above, experiments have been conducted on nine mirrors from five manufacturers. Basic information about the mirrors is given in table 1.

Table 1. Mirrors used for damage tests

Designation	Coating Composition	No. of layers	Reflectivity	Density of scattering centers
A-1	$\text{TiO}_2/\text{SiO}_2$	9	94.3%	Moderate
A-4	"	7	92.5%	Low
A-6	"	7	92.5%	Low
C-1	"	9	94.3%	Low
D-1	"	18	96.8%	Low
C-4	$\text{ZrO}_2/\text{SiO}_2$	13	95.6%	High
C-7	"	13	96.0%	Low
E-1	"	25	95.7%	High
B-1	$\text{ZnS}/\text{ThF}$	21	96.2%	Moderate

### 4.1 Observable Features Of The Damage Sites

When viewed under an optical microscope at a magnification of thirty, the most frequently observed form of damage has the appearance of one or more bright rings having the same shape as the beam's radial energy density profile. Sometimes one or more randomly located bright spots are observed within this overall pattern. Examination of such sites in a scanning electron microscope reveals considerably more detail. In figs. 10 and 11 the ring appearance is seen to be caused by a step inside of which one or more of the quarter wave layers have been removed. Since the sample is viewed from an angle in a scanning electron microscope, the round damage site appears to be compressed along the vertical axis. fig. 12 is a close-up view of the bright spot seen below and to the left of center in fig. 10. Since the position of this spot does not correspond with the position of maximum intensity in the beam, it is probably the result of a local absorbing center or other small scale mirror defect.

The photographs just described show damage sites caused by Q-switched pulses, but the physical characteristics of sites damaged by single mode-locked pulses are similar. In figs. 13, 14, and 15, for example, the same overall pattern of well defined rings with a randomly located little crater is observed. In figs. 16 and 17 a tendency toward smaller damage sites and removal of fewer layers is observed for less energetic pulses. fig. 16 also illustrates the fact that the transition from one layer to the next is not always a well defined step. Since the energy density profile of this pulse in the plane of the mirror is observed to be a smooth function of radius on the multiple exposure-level photograph taken during the experiment, the irregular pattern of material removal in the central region of this site suggests a degree of inhomogeneity in the coating itself.

In contrast to the damage site characteristics described above, the affected areas on some mirrors appear under the optical microscope to be made up of a large number of closely packed scattering sites. Two examples of this type of damage are given in the lower right portion of fig. 18. This mirror (E-1) has a generally high density of scattering centers even in areas not exposed to laser radiation, but it is not yet established whether they contribute to the characteristics of the damage sites themselves. The sites just described are produced by 20 psec. pulses and the ring type sites on the same mirror in the upper half of the figure are produced by 20 nsec. pulses. For mirror B-1 just the opposite is found: 20 psec. pulses produce rings and 20 nsec. pulses produce scattering centers

#### 4.2 Fogging Effects

Even when examination under the optical microscope reveals no obvious damage on a mirror, fogging the coating with one's breath often reveals clear evidence that the radiation has altered the surface in some way. The microscope photos a and b in fig. 19 illustrate this point. A striking feature of this effect is that an area much larger than the otherwise detectable damage region is affected. In c and d of fig. 19, for example, a region many times larger than the beam itself has different fogging properties. To some extent the effect is temporary as evidenced by the difference in appearance of the 20 hour old sites and the 1 hour old sites.

#### 4.3 Data Reduction

For each set of Q-switched damage measurements randomly selected pulses are quantitatively checked to verify the Gaussian radial dependence of the energy density and the reproducibility of the temporal pulse shape. These two important properties are also checked qualitatively for each shot by visual examination of the monitoring photographs. Any shots showing irregularities of either temporal or spacial profile are rejected. The Gaussian radius is measured for each remaining shot and combined with the pulse energy measurement to give a value of energy density on axis for each pulse. As will be shown, the diameter of each damage site is also of interest, and it is measured from optical microscope photographs of the damaged coatings.

Data reduction for the mode-locked pulse experiments is not quite so straightforward. Complications arise because of the limitations placed on energy measuring devices at this pulse duration. The calorimeter, for example, reads 100 mJ full scale on the most sensitive scale and its thermal sensitivity of  $3\text{J}/^\circ\text{C}$  makes compensation for ambient temperature changes very difficult. This leads to background variations which in the worst cases are on the order of the several mJ pulse energies being measured. The radiometer, which monitors a small fraction of the pulse energy on each shot, must also be used on its most sensitive scale (0.35 mJ full scale) where background noise is a problem. The seemingly expedient solution of putting a larger percentage of the laser output into the radiometer is risky since at such short pulse durations very little energy is required to cause saturation effects in the photodiode invalidating its calibration.

To circumvent these difficulties a series of shots is fired with no sample in place so that simultaneous calorimeter and radiometer readings as well as 519 scope traces are obtained. In a plot of calorimeter readings versus radiometer readings, the noise in both energy detectors scatters the points about a best straight line relating the absolute calibration of the two devices. It is found that the radiometer predicts 1.18 times the energy arriving at the sample location as that predicted by the calorimeter. Since neither measurement is known to be intrinsically more accurate than the other, the average of 0.924 times the radiometer reading is taken as the energy of a given pulse. Plotting the radiometer reading versus the height of the amplified pulse in the 519 scope trace provides a similar calibration curve of pulse energy versus 519 pulse height. The noise on the scope trace is typically much less than the noise on the radiometer; so the pulse height on the 519 scope makes a more consistent indicator of amplified pulse energy and when calibrated as described above, it is used as the primary energy measuring instrument. Radiometer readings are still taken throughout the run, however, to provide a constant check on the calibration curve.

An obvious difference between the Q-switched and mode-locked damage measurements is that no detailed analysis can be made of the temporal profile of the 20 psec. pulse. Any pulses longer than about 100 psec. can be rejected on the basis of the 519 trace, however, as can shots giving a double pulse or a poorly locked train.

A convenient way to display the mirror damage data is on a plot of damage site diameter versus the pulse energy density on axis. Fig. 20 shows such a plot for the Q-switch pulse damage tests on mirror A-4. For low enough energy densities no evidence of damage is found (O). For energy densities above 30 or 35 J/cm<sup>2</sup> some randomly located small scattering centers are created, but there is no well defined pattern to which a diameter can be assigned ( $\Delta$ ). Finally for energy densities above about 45 J/cm<sup>2</sup> well defined damage sites develop with diameters which are larger for more energetic pulses.

From such data two kinds of thresholds can be defined, the "practical damage threshold" below which no damage is caused by a single shot and a higher idealized threshold, a "perfect coating threshold", below which damage seems to be associated with local flaws of some sort rather than with inherent coating limitations. In fig. 20 the curve through the data is drawn to intersect the density axis at a point corresponding to the practical threshold. A curve drawn through the perfect coating threshold would intersect the axis at about 45 J/cm<sup>2</sup> and rise more steeply to pass through the remaining data points.

The simplest assumption which predicts an increase of site diameter with energy density on axis is that a coating damages only out to the radius at which the energy density drops below some critical value. The Gaussian energy distribution function can be solved for the diameter at which a given critical energy density is reached as a function of the on-axis energy density. The resulting curve is included in fig. 20 for a threshold value of 30 J/cm<sup>2</sup>. This curve does pass through two of the measurable - site data points but falls well below the data at higher energies. A similar curve for a threshold of 45 J/cm<sup>2</sup> would completely miss the data.

Plots of measured site diameter versus Q-switched on-axis energy density for six of the nine mirrors are shown (without data points) in fig. 21. The curves are drawn to cross the axis at the practical damage threshold, and in general the perfect coating threshold is higher as seen in table 2. All of these curves show damage sites which are larger at high energy than predicted by the simple constant energy density assumption discussed above.

Table 2. Measured threshold values

Mirror	Threshold at 20 psec. <sup>a</sup>	Threshold at 23 nsec. <sup>b</sup>	
		Practical	Perfect coating
	J/cm <sup>2</sup> on axis	J/cm <sup>2</sup> on axis	J/cm <sup>2</sup> on axis
A-1	1.6	43	46
A-4	2.2	30	46
A-6	-	-	26
C-1	1.8	30	30
D-1	1.6	33	38
C-4	1.9	23	31
C-7	1.8	58	60
E-1	2.9	47	47
B-1	0.6	16	24

a. For the mode-locked pulse the beam diameter at half the on-axis energy density is 197  $\mu$ m.

b. For the Q-switched pulse the beam diameter at half the on-axis energy density is 130  $\mu$ m.

Plotting the data from damage tests with single mode-locked pulses gives similar curves. There are some notable differences, however. First, all of the detected damage sites have measurable diameters, eliminating the distinction between the two threshold definitions discussed above. Second,



a sharp rise in the curve immediately above threshold is clearly established by the data for most of the mirrors. Finally, for all but two of the mirrors, the damage sites are smaller at high energy than predicted by the constant energy density assumption. The first two differences are evident in fig. 22, and the comparison with a constant energy density model may be made by sketching a curve through 0.0 mm at  $1.6 \text{ J/cm}^2$ , 0.2 mm at  $3 \text{ J/cm}^2$ , and 0.3 mm at  $8 \text{ J/cm}^2$ . This gives the diameter at which the local energy density is  $1.6 \text{ J/cm}^2$ .

Plots of measured site diameter versus the on-axis energy density of the 20 psec. pulse for seven of the mirrors are shown (without data points) in fig. 23. Mirrors B-1 and C-7 (not plotted) are exceptions in that they do fit a constant energy density curve quite well. Table 2 summarizes the results.

#### 4.5 Dependence Of Damage Threshold On Beam Diameter

To determine whether the observed damage threshold for 20 psec. pulses measured with a  $197 \mu\text{m}$  beam diameter can be meaningfully compared with the threshold for 23 nsec. pulses measured with a  $130 \mu\text{m}$  beam diameter, it is necessary to perform damage tests over a range of beam diameters at a fixed pulse duration. The results of such an investigation for mirror A-6 with 23 nsec. pulses are shown in fig. 24. As in fig. 20 two kinds of thresholds are evident, at least for the large diameter beams, and so two curves are drawn, the solid curve for the perfect coating threshold and the dashed curve for the practical threshold. These curves are simple fits to the data and do not represent any theoretically derived functional form. The decrease between 130 and  $197 \mu\text{m}$  should be taken into account when comparing the mode-locked and Q-switched data.

#### 4.6 Pulse Duration Dependence Of Mirror Damage Thresholds

Even allowing for possible 25% reductions of the Q-switched damage thresholds in table 2 if the measurements had been made with a  $197 \mu\text{m}$  beam diameter as the 20 psec. measurements were, the 23 nsec. values are from ten to thirty times higher than the 20 psec. energy density thresholds. Figure 25 illustrates this general observation with the results from mirrors A-1 and A-4. In this plot no adjustment for beam diameter dependence has been made since the size of such a correction could only be inferred from measurements on a different mirror. It is likely, however, that the Q-switched values should be recorded at a somewhat lower energy density. In this figure the functional form of the curves is suggested by theoretical considerations discussed in section 5.4.

#### 4.7 Accuracy And Reproducibility

##### a. Experimental Errors

For the Q-switched pulse data random errors in energy measurement and beam size determination can lead to uncertainties of plus or minus 10% in on-axis energy density measurements for single data points. As seen in fig. 20, however, either type of threshold can be determined to within about 5% for some of the mirrors.

For the mode-locked experiments, the uncertainties are somewhat larger because energy measurement is more difficult and there are small deviations from a true Gaussian energy density profile. Random errors in on-axis energy density for a single pulse may be as high as plus or minus 25% in this case. Again, however, threshold values are generally more accurately determined, as in fig. 22 where a reasonable estimate of uncertainty in threshold determination is plus or minus 10%.

In addition to the types of random error noted above, systematic error due to miscalibration of the energy measuring instruments must be expected. Comparison of the calorimeter and radiometer measurements as described in section 2.2 suggests that this error may be up to but probably does not exceed 20% for a given radiometer or calorimeter of the type used in this work.

##### b. Mirror Variations

It is important to observe that ordering ten mirrors coated with specified dielectric materials from a particular manufacturer does not guarantee that ten identical mirrors will be delivered. The thresholds recorded in table 2 for mirrors A-1, A-4, and A-6 and C-4 and C-7 illustrate the point. Decision concerning the relative capabilities of several manufacturers should not be based on the performance of a single mirror.

## 5. Possible Damage Mechanisms

### 5.1 Linear Absorption

Sufficient linear absorption in a coating can heat the film to its melting point. However, the thermal time constants for conduction losses from the irradiated spot on the film, either radially or into the substrate, are expected to be long compared to both pulse durations. Therefore a linear absorption model predicts the same energy density threshold over the whole pulse duration range and over the range of beam diameters tested as well. Neither prediction agrees with the experimental results. An additional observation is that the damage looks more like cracking than melting. Of course, thermal expansion resulting from linear absorption heating can cause fractures too, but the dependence on pulse duration and beam diameter is still wrong.

### 5.2 Local Defects

There is no doubt that small scale local defects can account for some of the damage features reported here. Figures 12 and 14 are examples of pits believed to be caused by the explosion of small absorption centers. It is likely that for mirrors exhibiting a large difference between the practical damage threshold and the perfect coating threshold, small absorbing centers are causing the low level damage. Possible defects include dirt, incompletely oxidized coating material, or some other form of non-uniform deposition. The decrease of practical threshold with increasing beam diameter may be related to the increased likelihood of finding a defect with a large beam.

### 5.3 Surface Plasma

On most shots which cause detectable damage a spark can be seen at the damage site. When a spark is not seen on damaging shots, the damage is small and the spark may just be too weak to detect by an observer looking through protective goggles. In any event, we believe the spark accompanies the principal damage event [7] rather than causing it, although the large area which is seen to have been affected when the coating is fogged may be an indication of some secondary plasma effect [8].

### 5.4 Electron Avalanche

Two conditions must be satisfied to cause damage by electron avalanche [3]. First, the intensity must be high enough that conduction electrons gain energy from the laser radiation faster than they lose it to the lattice. Second, the laser energy density must be high enough to create a critical number of conduction electrons within the duration of the pulse. Therefore, for very short duration pulses the limiting quantity is energy density while for long pulses it is intensity. The straight line segments of the curves in fig. 25 are drawn through the data points with the appropriate pulse duration dependence to give constant energy density and constant intensity thresholds.

If this mechanism is operating for the 20 psec. pulse damage, the intensity criterion is exceeded by a factor of about fifty, meaning that the electrons gain energy from the field much faster than they can transfer it to the lattice leaving many of the electrons to lose their energy to the lattice after the laser pulse has ceased. While they are returning to equilibrium with the lattice, however, there may be some tendency for electrons to drift away from the most intensely irradiated region and deposit their energy beyond the radius where damage would be expected on the basis of a constant energy density threshold. This does not lead to a larger damage site than expected, because the energy deposited at larger radii is not sufficient to cause damage. Rather, the fact that this energy was lost from the expected damage region will lead to a smaller than predicted damage site, as is observed for the mode-locked measurements for all but two mirrors.

If electron avalanche is causing the 20 nsec. pulse damage, intensity is the important variable, and the number of electrons grows more slowly since the field is smaller. As with the shorter pulse, electrons tend to drift to larger radii before they reach equilibrium, but in this case the laser pulse is still hitting the sample, and the presence of electrons at large radii makes damage there easier than expected. As a result the damage site is larger than predicted on the basis of a local energy density threshold. The dependence of threshold on beam diameter is qualitatively what is predicted by a probability formulation of electron avalanche theory [9], namely that the probability for finding "lucky

electrons" increases and the intensity needed to achieve a given probability for damage decreases for larger beams.

Some of the arguments in section 5.4 are admittedly speculative. Information about electron decay times and reasonable diffusion distances in thin dielectric films would help put the discussion on firmer ground.

## 6. Acknowledgment

The authors thank R. A. Bradbury for suggesting and obtaining the scanning electron microscope photographs used in this study. Technical and analytical assistance from E. E. Hoell, H. Miller, R. A. Clark, and C. C. Gallagher is also gratefully acknowledged.

## 7. References

- [1] Bliss, E. S. and Milam, D., AFCRL Report No. 72-0233 (1972). Available from the Defense Documentation Center, the National Technical Information Center, or the authors.
- [2] Milam, D., IEEE J. Quantum Electron. QE-7, 319 (1971).
- [3] Bliss, E. S., Proc. 2nd ASTM Symp. Damage in Laser Materials, NBS Spec. Pub. 341, 105 (1970); also Optoelectronics 3, 99 (1971).
- [4] Burnham, D. C., Applied Optics 9, 1482 (1970).
- [5] DeShazer, L. G. and Parks, J. H., Proc. 3rd ASTM Symp. Damage in Laser Materials, NBS Spec. Pub. 356, 124 (1971).
- [6] Winer, I. M., Applied Optics 5, 1437 (1966).
- [7] Giuliano, C. R., IEEE J. Quantum Electron., to be published (1972); also elsewhere in these proceedings (1972).
- [8] Boling, N. L., elsewhere in these proceedings (1972).
- [9] Bass, M. and Barrett, H. H., elsewhere in these proceedings (1972).

## 8. Figures

Q-SWITCHED LASER SYSTEM



MODE-LOCKED LASER SYSTEM

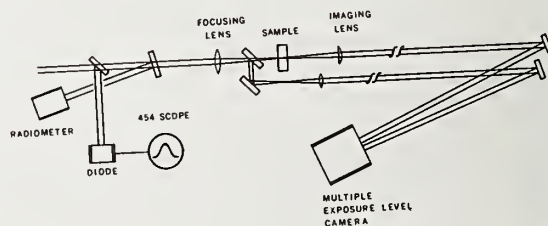
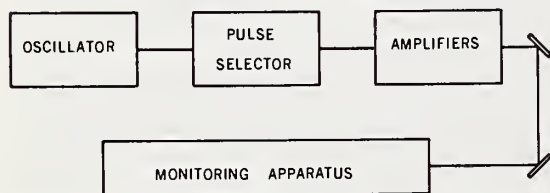


Figure 1. Block diagrams of the laser systems.

Figure 2. Monitoring apparatus for damage experiments with Q-switched pulses.



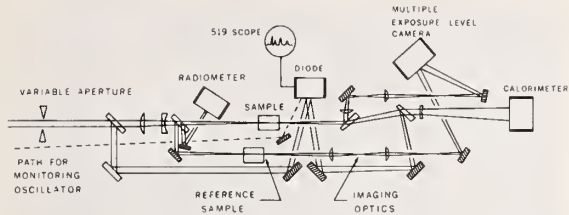


Figure 3. Monitoring apparatus for damage experiments with sub-nanosecond pulses.

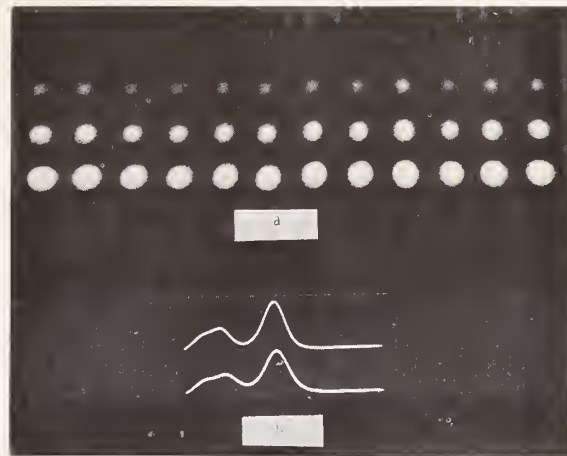


Figure 4. (a) Multiple exposure-level photographs of the oscillator output for a range of mirror rotations about the vertical axis. The output mirror was rotated by 4 sec of arc between successive exposures. (b) Temporal profile detected through a pinhole on axis (right) and through a vertically displaced pinhole (left) for the shot producing the fifth exposure from the right in (a).

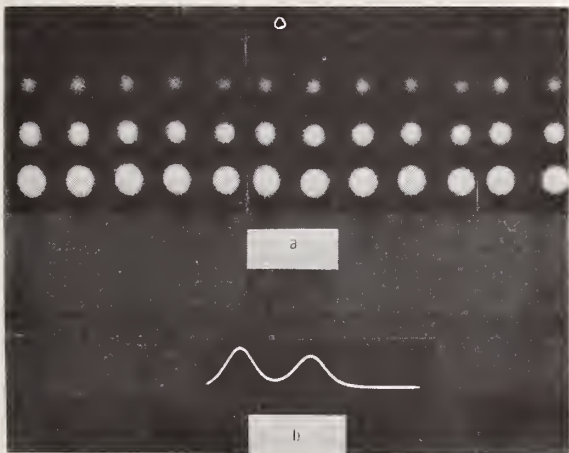


Figure 5. (a) Multiple exposure-level photographs of the oscillator output for a range of mirror rotations about the horizontal axis. The output mirror was rotated by 4 sec of arc between successive exposures. (b) Temporal profile detected through a pinhole on axis (right) and a vertically displaced pinhole (left) for the shot producing the far right exposure in (a).

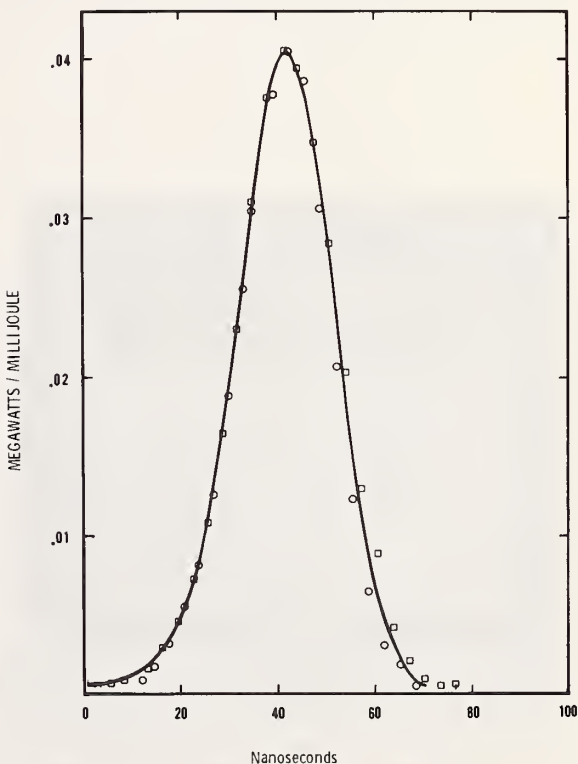


Figure 6. Spatially integrated temporal profile of three Q-switched pulses from a series of 220 shots: (O) shot 11, (□) shot 89, (—) shot 217.

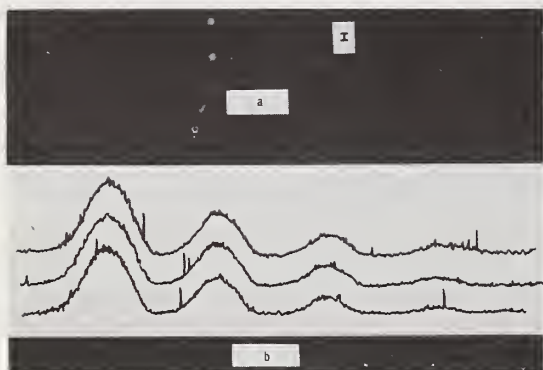


Figure 7. (a) Multiple exposure-level photographs showing the radial energy distribution in the damage plane for two Q-switched pulses. The dimension of the scale marker is  $100\ \mu\text{m}$ . (b) Microdensitometer traces of multiple exposure-level photographs for three consecutive Q-switched pulses. Adjacent exposures on each trace differ by a factor of two.

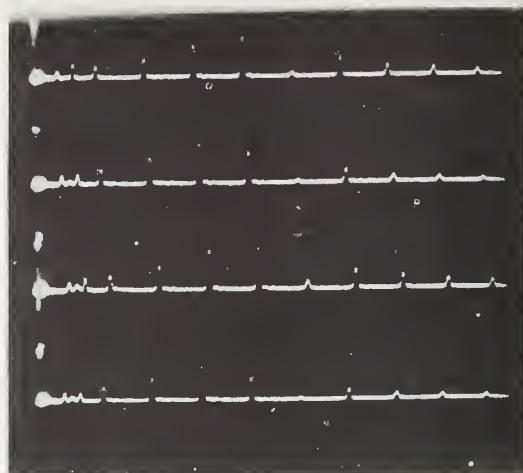


Figure 8. Oscilloscope traces for four consecutive firings of the mode-locked ruby laser. The selected pulse is missing from the train just to the right of center, and after amplification it is displayed between two early pulses of the train at the left.

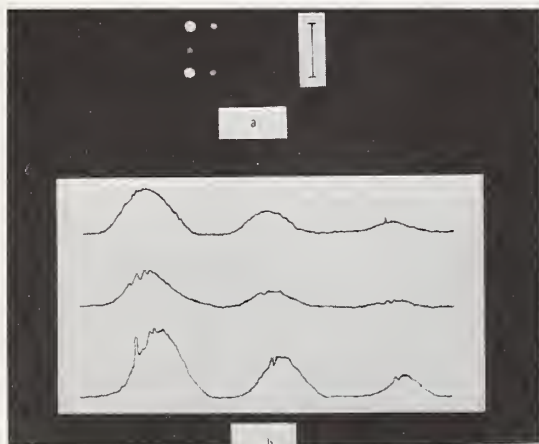


Figure 9. (a) Multiple exposure-level photographs showing the radial energy distribution in the damage plane for three 20 psec pulses. The dimension of the scale marker is  $1\ \text{mm}$ . (b) Microdensitometer traces of multiple exposure-level photographs for three consecutive 20 psec pulses. Adjacent exposures on each trace differ by a factor of 1.83.



Figure 10. Scanning electron microscope (SEM) photograph of a damage site produced by a Q-switched pulse. The site dimension is  $250\ \mu\text{m}$  from left to right.



Figure 11. SEM photograph of the edge of a damage site. The entire photo is 57  $\mu\text{m}$  wide.



Figure 12. SEM photograph of the bright spot seen below and to the left of center in figure 10. The width of the photo is 11  $\mu\text{m}$ .

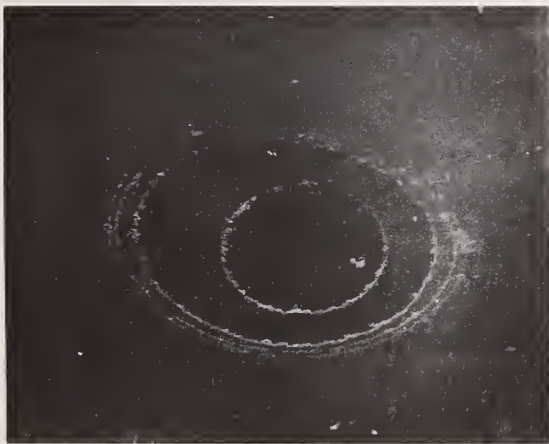


Figure 13. SEM photograph of a damage site produced by a 20 psec pulse. The width of the photo is 436  $\mu\text{m}$ .



Figure 14. SEM photograph of the steps seen in figure 13. The width of the photo is 180  $\mu\text{m}$ .



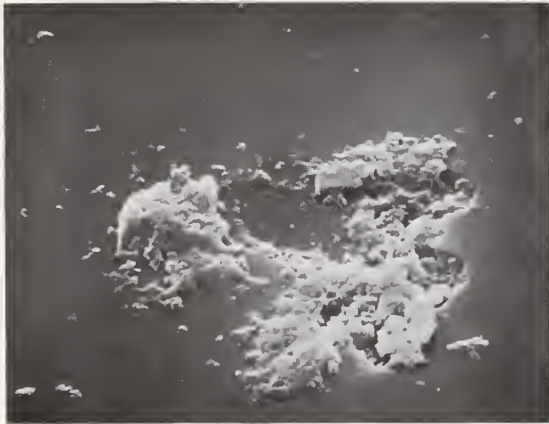


Figure 15. SEM photograph of the bright spot to the right of center in figure 13. The width of the photo is 18  $\mu\text{m}$ .

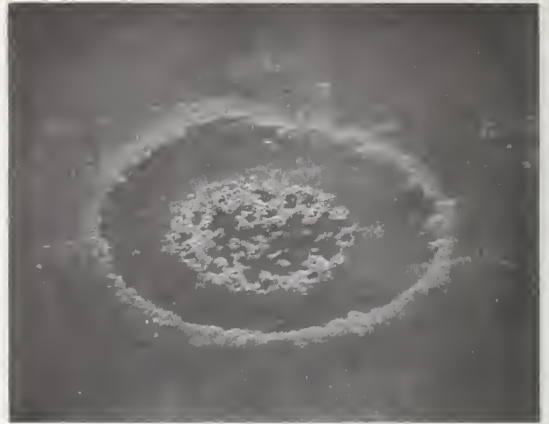


Figure 16. SEM photograph of a site damaged by a less energetic 20 psec pulse. An irregular pattern of material removal is evident in the central portion. The width of the photo is 456  $\mu\text{m}$ .

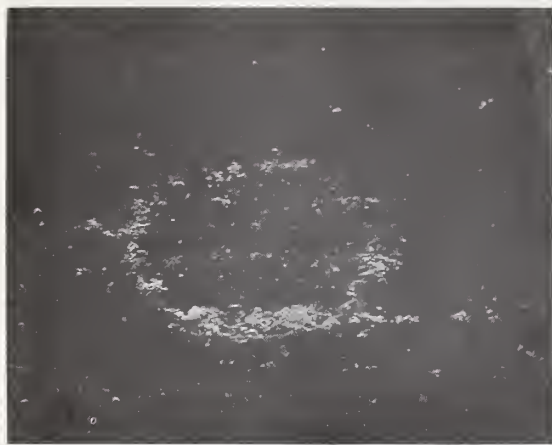


Figure 17. SEM photograph of a damage site produced by a 20 psec pulse having an energy density only slightly above threshold. The width of the photo is 98  $\mu\text{m}$ .

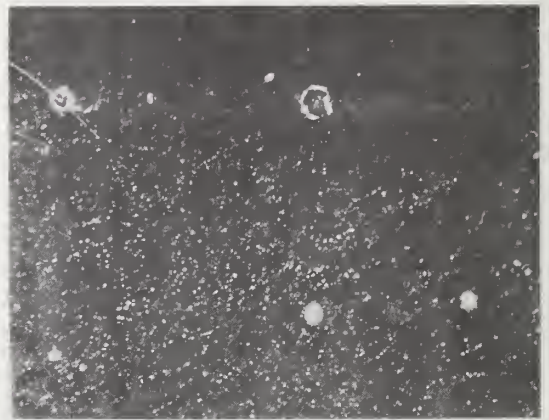


Figure 18. Optical microscope photograph of scattering site type of damage (lower row) caused by 20 psec pulse on mirror E-1, for which Q-switched pulses produced mostly ring type damage (upper row). The spacing between the two sites in the right side of the lower row is 1 mm.

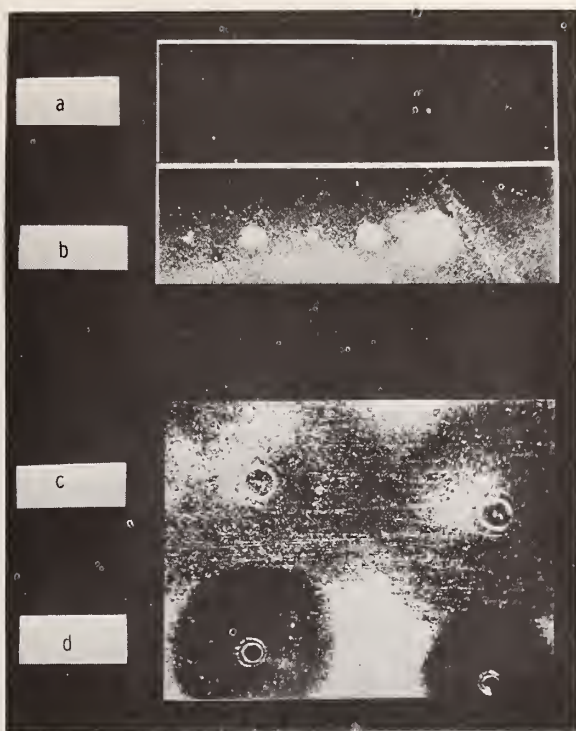


Figure 19. Optical microscope photographs of (a) a damaged unfogged mirror, (b) the same mirror after fogging with breath, (c) higher magnification view of some sites which were damaged twenty hours before the fogged photograph and (d) one hour before the fogged photograph.

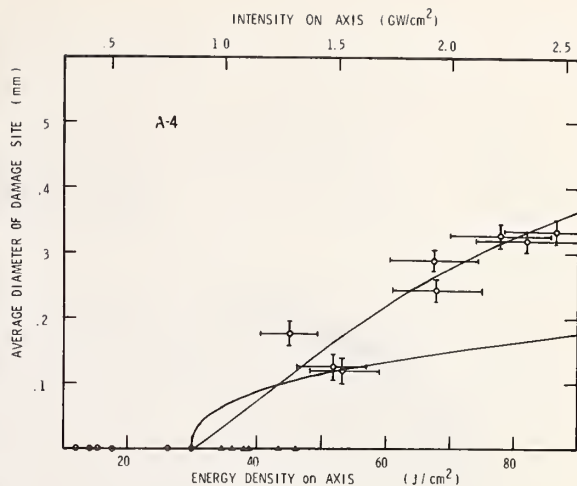


Figure 20. Damage site diameter versus Q-switched pulse energy density on axis for mirror A-4. Shots causing no detectable damage are indicated by ( $\circ$ ), those causing only randomly located small scattering centers by ( $\Delta$ ), and sites with well-defined diameters by ( $\circ$ ) at finite diameter values. A curve is drawn through the data points to intersect the axis at the practical damage threshold. The second curve gives the damage site diameter predicted on the assumption that any place on the coating will damage when subjected to an energy density of  $30 \text{ J/cm}^2$ .

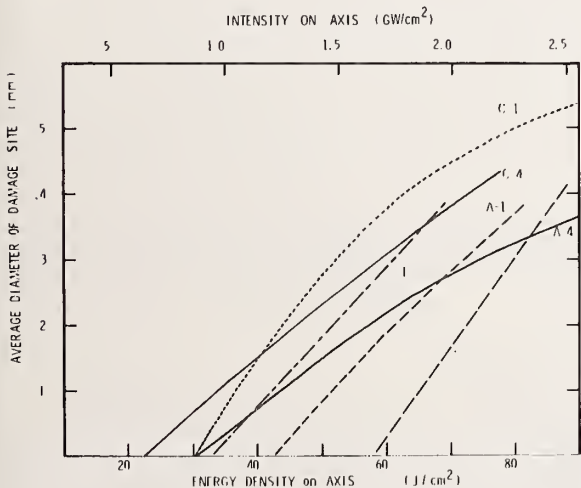


Figure 21. Damage site diameter versus Q-switched pulse energy density on axis for six mirrors. Curves with faded labels may be identified by reference to the practical threshold values recorded in table 2.

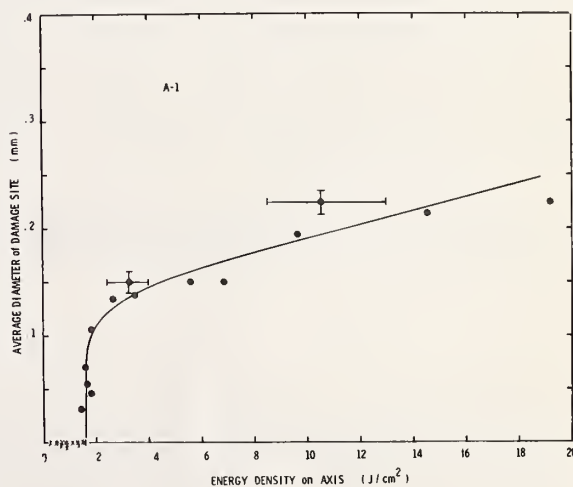


Figure 22. Damage site diameter versus 20 pic pulse energy density on axis for mirror A-1. Shots causing no detectable damage are indicated by ( $\times$ ) and those causing damage by ( $\circ$ ). The error bars shown are typical.

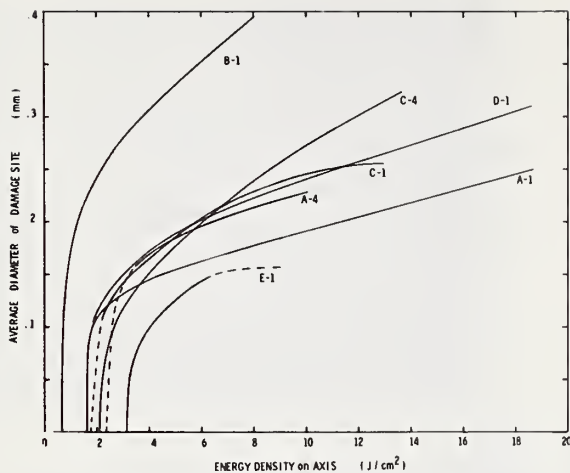


Figure 23. Damage site diameter versus 20 psec pulse energy density on axis for seven mirrors.

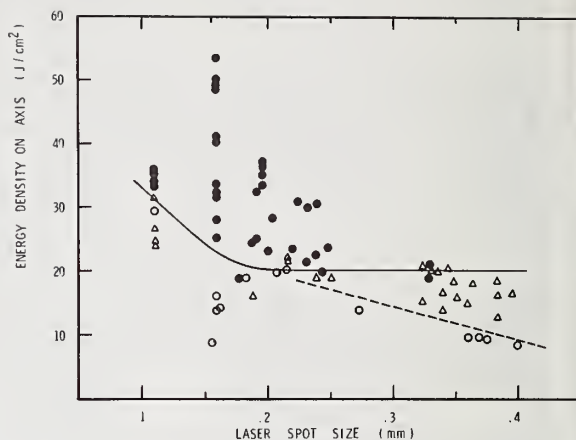


Figure 24. Q-switched damage threshold versus the beam diameter at half the on-axis energy density for mirror A-6. Shots causing no detectable damage are indicated by (○), those causing only randomly located small scattering centers by (△), and sites with well-defined diameters by (○). The solid curve indicates the best estimate for the variation of the perfect coating threshold, and the dashed curve the best estimate for the variation of the practical threshold.

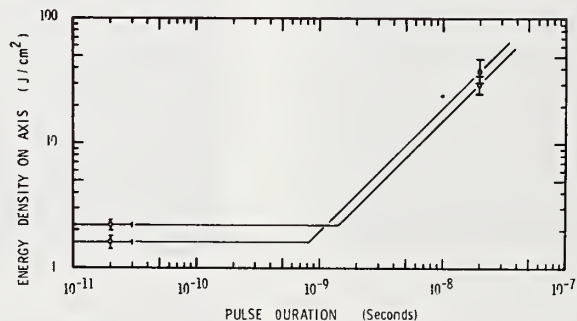


Figure 25. Single pulse damage threshold versus pulse duration for mirrors A-1 and A-4. The curves are drawn to fit the functional form suggested by theoretical considerations discussed in section 5.4.



## Study of Laser-Irradiated Thin Films

Brian E. Newnam and L. G. DeShazer

Departments of Physics and Electrical Engineering  
University of Southern California  
Los Angeles, California 90024

Laser damage to thin-film coatings was studied using a TEM<sub>00</sub> Q-switched ruby laser. Our study included mono-, bi- and multi-layered coatings of the materials TiO<sub>2</sub>, SiO<sub>2</sub>, ZrO<sub>2</sub>, MgF<sub>2</sub> and ZnS on substrates of glass, rocksalt and spinel. The samples included coatings for antireflection and reflection at the ruby wavelength, and were produced either at USC or by a commercial vendor. Damage threshold energy and power densities were measured with attention paid to dependences on laser beam spot-size, film material and thickness, substrate condition and incipient scattering of the film. Particular attention was given to the establishment of a threshold criterion for laser damage to thin films. Several effects attendant to damage were investigated, with the conclusion that film scattering induced by the laser was the most sensitive detector of film breakup. The laser induced scatter was observed prior to or at the threshold of spark formation at the film, depending on the film material.

Key Words: Damage morphology, damage thresholds, laser-induced scatter, ruby, spark thresholds, thin films, truncated Gaussian optics.

### 1. Introduction

During the past year we have been investigating laser-induced structural damage to dielectric thin films using a TEM<sub>00</sub> Q-switched ruby laser. The investigation concentrated on the measurement of damage threshold energy and power densities studying their dependence on film, substrate and laser parameters. The coatings tested were mono-, bi- and multi-layered films composed of various materials and thicknesses having differing initial film scatter. These coatings were on substrates of glass, rocksalt, spinel and YAG and were damaged while immersed in various liquids as well as air. The damage was studied as a function of laser beam spot-size, temporal pulsewidth and incidence direction. Also, several effects accompanying damage were investigated, with the conclusion that film scattering induced by the laser was the most sensitive indicator of film breakup. In addition, the damage thresholds, as determined from the laser-induced scatter, were correlated to the spark formation at the film, and the thin-film areas damaged at laser powers above and below the film's spark threshold were studied by optical microscopy.

In this report the study of the dependence of damage on the film parameters will be emphasized, leaving a fuller discussion of the laser and substrate dependences to a later time. Also, since the research effort up to the present time has been chiefly experimental, we will avoid speculating in theoretical models of damage mechanisms.

### 2. Experimental Configuration

A high-quality giant-pulse ruby oscillator-amplifier system, shown in figure 1, was the source of the laser beam used in the damage studies. This laser was Q-switched by cryptocyanine in methanol and operated in a single longitudinal and transverse TEM<sub>00</sub> mode. The single mode operation was important because a temporally and spatially smooth pulse is necessary for an accurate measurement of the damage thresholds. The time contour of the pulse was nearly Gaussian with pulsewidths (FWHM) from 9 to 35 nsec, and peak powers up to 10 MW when using the amplifier. For such Gaussian pulses, the peak power  $P_0$  is related to the total energy  $E$  by  $P_0 = (0.941E)/T$ , where  $T$  is the full width of the pulse at half maximum. Absolute energy calibration was performed using a ballistic thermopile (TRG 100) and agreed to within 5% of the calibration of another thermopile used by C. R. Giuliano at Hughes Research Laboratories. In the far field of the laser oscillator, the spatial intensity profile of the beam was close to a Gaussian

distribution as determined by a pinhole scan. At the distance of 100 cm (1.1 Rayleigh distance) from the oscillator, the intensity distribution at the temporal peak of the pulse is shown in figure 2. The amplified profile also had a similar near-Gaussian shape. The detailed operation of this apparatus was discussed at the Third ASTM-NBS Laser Damage Symposium [1].<sup>1</sup>

### 3. Truncated Gaussian Optics

The spatial intensity distribution of the laser beam cannot be exactly Gaussian since the single mode beam is coupled out of the laser through a circular aperture, resulting in the truncation of the aperture intensity illumination. This truncation produces rings in the far-field pattern and structure within the central disk in the near-field. Figure 3 shows the diffraction pattern of our laser in the far-field with three different exposures. The central disk is nearly Gaussian and in the overexposed pictures, the presence of the rings around the central disk due to truncation is strikingly evident. Now, the importance of recognizing the existence of truncation effects lies in the fact that if attention is not paid to these effects, calculations of the axial intensity may be in error by as much as 100%. Such discrepancies are particularly possible when truncated Gaussian beams are focused.

When a laser beam is focused by a lens the focused intensities can be simply predicted [2] only if the spatial profile of the beam has the ideal Gaussian distribution. Since an exactly Gaussian beam remains Gaussian throughout an optical system, only the calculation of the spot-size of the Gaussian beam with respect to the lens is required. The spot-size is the  $1/e^2$  radius of the intensity profile of a beam. The variation of the spot-size as the beam propagates along the axis of the lens is controlled by the spot-size  $W_0$  at the waist of the input beam and the distance  $d_1$  of the input waist from the lens as well as the geometric focal length  $F$  of the lens. The geometry of the input beam to the lens is illustrated in figure 4, and the value of the spot-size  $W_2$  at a distance  $d_2$  from the lens is determined from eq (1).

$$W_2 = W_0 \frac{d_2}{d_1} \left(1 + \frac{b^2}{d_1^2}\right)^{-\frac{1}{2}} \sqrt{1 + \frac{d_1^4}{b^2} \left(1 + \frac{b^2}{d_1^2}\right)^2 \left(\frac{1}{d_2} - \frac{1}{F} + \frac{1}{d_1 [1 + (b^2/d_1^2)]}\right)^2} \quad (1)$$

The parameter  $b$  is defined as  $\pi W_0^2/\lambda$  where  $\lambda$  is the laser wavelength. This eq (1) is the general expression giving  $W_2$  as a function of  $W_0$ ,  $d_1$  and  $F$ , and can be used to determine the peak power and energy densities anywhere in a focused beam provided the beam had an ideal Gaussian profile. Many experimenters using single transverse-mode lasers generally assume that this Gaussian description of focused beams applies to their laser setup. Truncation of the Gaussian beam can severely alter this calculation, though, and prevent a proper analysis of an experiment.

Truncation of the Gaussian distribution, which is infinite in extent, can never, of course, be avoided but it is generally unimportant in low-power lasers. In high-power Q-switched lasers, though, due to their resonator design requirements the truncation is usually not negligible. Figure 5 shows several possible intensity distributions in the aperture plane of a laser oscillator having a Fresnel number of 0.4, the Fresnel number of our oscillator. The profile for the fundamental stationary (Fox-Li) mode is a truncated Gaussian having a truncation parameter of 0.84. The truncation parameter is the ratio of the radius of the truncating aperture  $a$  to the spot-size  $W$ . This Fox-Li profile is flattened by saturation of the gain [3], which usually occurs in high-power pulsed lasers. Three examples are shown for initial numerical gains of 20, 12.2 and 7.4, all calculated assuming a uniform initial gain distribution. When the initial gain distribution is peaked symmetrically about the resonator axis due to the design of a particular pumping scheme the Fox-Li profile is sharpened, increasing the truncation parameter. A typical example of axisymmetric pumping is the elliptical focusing of pump light into a cylindrical laser rod. For the laser oscillator used in our investigations, the truncation parameter was near 0.6.

Since Campbell and DeShazer [4] have shown that diffraction effects due to truncation cannot be neglected when the truncation parameter is less than 2.0, the usual Gaussian description of focused beams does not apply to our laser experiment. Therefore, a calculation of focused truncated Gaussian beams is required for the analysis. A formula has been published [5] for the intensity variation along the optical axis for a special case of a truncated Gaussian beam where the lens is also the aperturing element. U.O. Farrukh [6] has calculated the diffraction effects in focused truncated Gaussian beams

<sup>1</sup>Figures in brackets indicate the literature references at the end of this paper.

for the more usual situation shown in figure 6. The source laser is represented by a collimated ideal Gaussian beam of spot-size  $W$  apertured by a diverging lens of geometric focal length  $f_1$  and radius  $a$ . A lens of geometric focal length  $f_2$  is placed a distance  $z$  from the lens  $f_1$  and the beam is viewed a distance  $y$  away from the lens. The axial intensity  $I$  at the distance  $y$  is determined from eq (2).

$$I = 2A^2 \left( \frac{y}{f_2} - 1 \right)^{-2} \left[ \frac{1}{f_1} \left( z - \frac{yf_2}{y-f_2} \right) - 1 \right]^{-2} \frac{\left( \frac{ka}{2g} \right)^2 e^{-a^2/W^2}}{\left( \frac{a}{w} \right)^4 + \left( \frac{ka}{2g} \right)^2} \left[ \cosh(a/w)^2 - \cos Q \right] \quad (2)$$

where  $k = 2\pi/\lambda$

$$\frac{1}{g} = \frac{1}{f_1} - \frac{1}{z - yf_2/(y - f_2)}$$

$$Q = \frac{ka^2}{2} \left( \frac{1}{z} - \frac{1}{f_1} \right) - ky \left( 1 - \frac{y}{h} - \sqrt{\frac{(h-y)^2}{h^2} - \frac{a^2}{z^2}} \right); \quad \frac{1}{h} = \frac{1}{f_2} - \frac{1}{z}.$$

Even though this is a rather complex expression, the axial intensities can be easily plotted by computer and the plots have predicted the experimental results.

In our experiment, a lens of 20.7 cm focal length was located 109.5 cm from the laser. Since the equivalent Gaussian and truncated Gaussian calculations of the axial intensity differ greatly near the focus, the axial intensity was directly measured and compared to the two calculations. The axial intensity of such small spots can be accurately determined by measurements of the damage threshold of Polaroid film. A microscope is required to examine the film. Fresh undeveloped Polaroid film (Type 410) was calibrated to have a damage threshold at  $50 \text{ mJ/cm}^2$ , which was independent of the laser beam spot-size. Figure 7 shows the measured axial intensity distribution after the lens and its comparison to both the equivalent Gaussian and truncated Gaussian laser beam calculations. The measured intensity value near the focus is about twice that predicted by the equivalent Gaussian calculation. The difference between the measured distribution and the truncated Gaussian calculation is not as large as indicated because the actual truncation parameter is near 0.6 and not the 0.5 as plotted.

Observation of the intensity profile of a truncated Gaussian beam after the focus reveals axial maxima and minima, unlike the smooth distribution before the focus. This is explained by recognizing that near-field axial extrema are present before the lens, which when the lens is used in the far-field ( $z > 2a^2/\lambda$ ), are transformed to locations after the focus. Figure 8 illustrates that the intensity distribution is not symmetrical about the focal plane for truncation parameters less than 2. Therefore, it is quite important to place the test samples before the focus in order to know the laser power densities incident to the samples.

#### 4. Laser Damage Detection

One of the important aspects of these current investigations has been the determination of a sensitive and reliable criterion for the onset of damage. Many investigators of laser-induced damage to surfaces of transparent dielectrics have observed a luminous surface spark whenever physical damage occurred. Some researchers have proposed that the spark is responsible for the observed damage. It has thus become a convenient practice to identify the spark threshold as the damage threshold. We have used three methods to monitor the onset of damage:

- 1) spark detection using a sensitive photomultiplier with a narrow band interference filter (4358 Å),
- 2) laser-induced increase in the scattering of 1mW He-Ne laser beam (visually observed), and,
- 3) optical microscopic observation of film breakup.

The interesting result which we wish to report is, that for monolayer films, the laser-induced scatter (LIS) of a He-Ne gas laser indicated that damage occurs before or at the detected spark threshold, depending on the film material. Multilayer coatings had an initial scatter level that was too high to obtain thresholds with the LIS technique. If the initial scatter levels were low enough, we would expect the same result for multilayer films also. The materials investigated, the energy density thresholds and the spark-to-LIS ratios are listed in table 1. It appears that laser-induced scatter occurs before spark initiation for films with high indices of refraction.



The film damage for all the tested samples was investigated by optical microscopy, and a certain pattern in the damage morphology was observed. The damage areas below spark threshold were much more irregular in shape than those considerable above spark threshold. Far above threshold the damage was circular, nearly following the intensity profile of the incident laser beam (figure 9). However, below threshold many small circular damage spots occurred in random clusters (figure 10) which may indicate localized points of absorption, optical breakdown or film inhomogeneities.

The damage in single and double-layer films was sufficient to remove the entire coating from the substrate. For multilayer reflectors the damage did not penetrate to the substrate. This is expected since the laser energy density decreases progressively due to the reflections at the multiple interfaces. At threshold only the top few layers were damaged.

## 5. Monolayer Dielectric Coatings

The damage thresholds for quarter-wave films of various materials are listed in table 1. The thresholds were determined by the onset of LIS using a He-Ne laser as a monitor of the scatter. In this paper, the thresholds are given as a range of values instead of a single number. This method of listing thresholds reflects more accurately the uncertainties in the threshold measurement. Ten to thirty laser shots were taken for each entry of a range in the tables. The damage, as observed by a certain film characteristic, is more or less identical within the reported range of values. Occasionally, a laser shot having an energy density higher than the determined threshold range will produce little or no damage; such shots were not included in the tables. It can be noted from table 1 that the damage thresholds were nearly inversely proportional to the refractive index of the film material. One possible explanation of the variation of damage with material involves the standing wave pattern of the electric field by the reflection at the film interfaces (figure 11). For most light-matter interactions, the absorption of energy is required. In terms of the electric field intensities the power absorbed per unit volume  $P_a = \alpha n |E/E_0|^2 I_0$  where  $\alpha = 4\pi\kappa/\lambda$ ;  $n$  and  $\kappa$  are the real and imaginary parts of the film's refractive index and  $I_0$  is the incident intensity (watts/cm<sup>2</sup>). Figure 11 illustrates that the absorption in a quarter-wave film is spatially dependent as shown by the variations of  $|E/E_0|^2$ . By examining the field variations in films of various thicknesses and for obverse and reverse laser incidence, and by correlating these with the respective damage thresholds, a determination of the appropriate causes of damage may be possible.

Table 2 gives the damage thresholds for various film thicknesses. In particular, note the variation of the thresholds for the three TiO<sub>2</sub> films. The damage threshold of the half-wave film was about one-third that of the quarter- and three-quarter-wave films. Figure 12 shows the calculated relative intensity distribution for these three film thicknesses of TiO<sub>2</sub>. For a high index film material, such as TiO<sub>2</sub>, between two lower index materials of air and glass, the net electric field has an antinode at the rear or glass-film interface. This rear reflected wave has an antinode (node) at the front or air-film interface in the case of a half- (quarter-) wave film. The higher net electric field at the front surface of the half-wave film may be the origin of the lower damage threshold of the half-wave film. It is interesting to note that the ratio of the intensities for the half- and quarter-wave films at the air-film interface is about three.

## 6. Multilayer Dielectric Coatings

We have studied damage to commercial antireflection coatings and reflectors. The antireflection coatings investigated were two-layer, non-quarter-wave films called "vee" coatings [7]. The damage thresholds measured for these coatings are listed in table 3. Like single layer films, LIS is the most sensitive method of detecting damage. For multilayer reflecting films, for which the initial He-Ne scatter level is quite high, spark detection is more sensitive. Table 4 lists the damage thresholds for sixteen reflectors. Samples 0103 and 0104 have the highest damage thresholds of any reflector tested in the program so far; both of these reflectors have spark threshold values near 120 J/cm<sup>2</sup>.

Another recent aspect of this study has been the investigation of a correlation between scattering (before damage) from thin-film coatings and their damage thresholds. The results from this experiment are shown in table 5. The scattering was measured by the intensity of light scattered at about 135° from the direction of the incident beam. Since there is a strong wavelength dependence for the diffuse reflectance from a dielectric film, we used a severely attenuated output from the single-mode Q-switched ruby laser as the measuring beam. This beam had a power density of 40 MW/cm<sup>2</sup> and did not produce any changes in the films. The scatter intensities listed in table 5 are averages of three measurements on each film and are normalized to the value obtained from the coating (0104) having the lowest scatter. From this preliminary study, there appears to be a good correlation between film scatter and damage threshold.

Table 1. Damage thresholds for quarter-wave single coatings  
(nominal pulsewidth, 11-13 nsec).

Sample	Material <sup>a</sup>	Refractive Index (6943 Å)	Spot size  mm	Peak energy density		Peak power density		Ratio of spark to LIS
				by spark J/cm <sup>2</sup>	by LIS J/cm <sup>2</sup>	by spark GW/cm <sup>2</sup>	by LIS GW/cm <sup>2</sup>	
O133	MgF <sub>2</sub>	1.38	0.055	111-131	111-131	8.2-9.3	8.2-9.3	1.0
O125	SiO <sub>2</sub>	1.456	0.055	>125	117	>10.5	10.5	> 1.1
O129	ZrO <sub>2</sub>	1.975	0.072	61-68	35-44	4.3-4.9	2.4-3.2	1.6
O121	TiO <sub>2</sub>	2.28	0.072	57-71	35-42	4.2-5.7	3.0-3.9	1.7
U203	ZnS	2.35	0.072	63	5.5-12.5	4.7	0.4-0.85	>5

<sup>a</sup> All substrates are BSC2 glass

Table 2. Damage thresholds for various film thicknesses<sup>a</sup>.

Sample	Film	Spot size	Peak energy density	Peak power density
		mm	J/cm <sup>2</sup>	GW/cm <sup>2</sup>
O133	MgF <sub>2</sub> , λ/4	0.055	111-131	8.2-9.3
O135	MgF <sub>2</sub> , λ/2	0.065	65-102	5.3-8.1
O125	SiO <sub>2</sub> , λ/4	0.055	117	9.8
O127	SiO <sub>2</sub> , λ/2	0.055	>111	>9.9
O129	ZrO <sub>2</sub> , λ/4	0.072	36-44	2.4-3.2
O131	ZrO <sub>2</sub> , λ/2	0.072	12-13	0.85-0.90
O121	TiO <sub>2</sub> , λ/4	0.072	36-42	3.0-3.9
O124	TiO <sub>2</sub> , λ/2	0.097	7-8	0.55-0.65
O137	TiO <sub>2</sub> , 3λ/4	0.072 0.122	17.5-25	1.4-2.2
O138	TiO <sub>2</sub> , 3λ/4	0.072	20-23	1.4-1.5

<sup>a</sup> Damage detected by laser-induced scatter

Table 3. Damage thresholds for bilayer antireflection coatings<sup>a, b</sup>

Sample	Description	Peak energy density		Peak power density		Ratio of spark to LIS
		by spark	by LIS	by spark	by LIS	
		J/cm <sup>2</sup>	J/cm <sup>2</sup>	GW/cm <sup>2</sup>	GW/cm <sup>2</sup>	
O143	ZrO <sub>2</sub> /SiO <sub>2</sub>	118-147	97-118	8.6-11.7	7.6-9.5	1.2
O147	TiO <sub>2</sub> /MgF <sub>2</sub>	84-85	60-65	5.8-6.1	4.0-4.3	1.4
O145	ZrO <sub>2</sub> /MgF <sub>2</sub>	64-92	54-57	5.1-6.8	3.5-4.0	1.5
O142	TiO <sub>2</sub> /SiO <sub>2</sub>	74-98	35-42	6.5-6.8	2.4-3.1	2.3

<sup>a</sup>Sample configuration is GHLA, where G is BSC2 glass (0.5mm thick), H is high index film ( $< \lambda/4$  thick), L is low index film ( $> \lambda/4$  thick), and A is air.

<sup>b</sup>Laser spot size is 0.062mm, and nominal pulsewidth is 11-14 nsec.

Table 4. Thresholds for multilayer reflectors  
(nominal pulsewidth: 12-15 nsec)

Sample	Description	Spot size	Peak energy density		Peak power density
			mm	J/cm <sup>2</sup>	GW/cm <sup>2</sup>
O103	TiO <sub>2</sub> /SiO <sub>2</sub>	0.056		121-126	9.1-9.3
O104	"	0.056		107-127	6.1-8.9
<sup>a</sup> O104	"	0.056		97-118	7.6-8.7
O101	"	0.062		83-103	5.5-8.4
O102	"	0.060		98-110	6.8-7.2
S101	"	0.062		43-56	3.0-4.0
S102	"	0.062		50	3.7
O107	ZrO <sub>2</sub> /MgF <sub>2</sub>	0.058		81-113	4.7-7.8
O108	"	0.062		90	6.1
O105	ZrO <sub>2</sub> /SiO <sub>2</sub>	0.13		18-20	1.2-1.6
O106	"	0.13		18.5	1.3
S103	"	0.12		7.5	0.52
SS103	CeO <sub>2</sub> /SiO <sub>2</sub>	0.14		17-19	1.4
SS102	"	0.14		14.5-17	1.1-1.2
SS101	"	0.14		11.5	1.1
SS101	"	0.072		14.5-19	1.0-1.4
U111	ZnS/ThF <sub>4</sub>	0.084		25-26	2.0-2.1

<sup>a</sup>Second test after 2½ months



Table 5. Comparison of weak-signal scatter and spark threshold for multilayer reflectors

Sample	Reflector	Normalized scatter intensities at 6943 Å	Peak energy density (spark)
			J/cm <sup>2</sup>
O104	TiO <sub>2</sub> /SiO <sub>2</sub>	1.0	107-127
O102	"	2.3	98-110
<sup>a</sup> U111	ZnS/ThF <sub>4</sub>	2.8	25-26
O101	TiO <sub>2</sub> /SiO <sub>2</sub>	3.5	83-103
O103	"	3.7	121-126
S101	"	6.5	44-56
O105	ZrO <sub>2</sub> /SiO <sub>2</sub>	9.3	18-20
SS103	CeO <sub>2</sub> /SiO <sub>2</sub>	14.3	17-19
O106	ZrO <sub>2</sub> /SiO <sub>2</sub>	16.7	18.5
SS101	CeO <sub>2</sub> /SiO <sub>2</sub>	24.5	11.5
<sup>a</sup> O108	ZrO <sub>2</sub> /MgF <sub>2</sub>	24.5	90
<sup>a</sup> O107	"	27.0	81-113
SS102	CeO <sub>2</sub> /SiO <sub>2</sub>	37.5	14.5-17
S103	ZrO <sub>2</sub> /SiO <sub>2</sub>	41.5	7.5

<sup>a</sup>Notable exceptions to the correlation

Figures 13 and 14 are microphotographs of two undamaged multilayer reflectors, showing the incipient film inhomogeneities. Figure 13 is a photograph of a TiO<sub>2</sub>/SiO<sub>2</sub> reflector which had low scatter and high damage threshold. Figure 14 is a photograph of a CeO<sub>2</sub>/SiO<sub>2</sub> reflector which had high scatter and low damage threshold. These pictures were taken with a Bausch & Lomb metalograph under dark field illumination.

Figures 15 and 16 are microphotographs of two laser damaged multilayer reflectors demonstrating the differing types of damage morphology with respect to initial film scatter. Figure 15 shows the damage area on a TiO<sub>2</sub>/SiO<sub>2</sub> reflector which had low scatter. The damaged area is approximately circular with a diameter near 0.7 mm. The depth of damage is uniform, probably at one of the initial layer interfaces. There are bubbles in the damage center which is indicative of heating, but otherwise the morphology shows a lack of microscopic inhomogeneities. Figure 16 is a photograph of the damage area on a ZrO<sub>2</sub>/SiO<sub>2</sub> reflector having high scatter. The damaged region is a granular area about 0.2 mm in extent. The granularity indicates that multiple weak points were present in the film and that damage nucleated on these points.

## 7. Damage Dependence on Laser Parameters

In a previous paper [8] we reported that the laser damage to three samples was dependent on the spot-size of the laser beam. To verify that result we continued to study spot-size dependence by using the laser output from the ruby oscillator focused by a 20.7 cm focal length lens. By placing the sample at various distances from the lens we could vary the spot-size at the film from 0.1 to 0.2 mm, never putting the test sample closer than 5 mm to the focus. In this manner we could accurately measure the spot-size by a pinhole scan. In addition, we amplified the oscillator output and used a 30 cm FL lens to obtain an even weaker converging beam. With this arrangement we were able to damage films at larger spot sizes (0.32 mm). The results are shown in figure 17, which demonstrates that the damage thresholds decreased with increasing spot-size. We also investigated the pulsewidth dependence of the energy density thresholds and these results for a single layer  $\text{ZrO}_2$  film are shown in figure 18.

## 8. Acknowledgements

The authors are grateful to the following companies and their thin-film experts who supplied test specimens for this study: 1) H.R. Owen of the University of Southern California, 2) L. Mott of Optical Coating Laboratory, Inc., 3) A. Zook of Herron Optical Company, 4) R. Mortensen of Spectra-Physics Corporation, and 5) G. Ash of Spectrum Systems Division of Barnes Engineering. Others receiving our gratitude are E. A. Maunders for microscopic photographs, C. R. Guiliano for discussions regarding beam focusing, U. O. Farrukh for theoretical analysis of focusing of truncated Gaussian beams, and A. G. J. Balbin Villa-verde for spark detection design.

This work was supported by the Advanced Research Projects Agency, ARPA Order No. 1738 and monitored by the Air Force Cambridge Research Laboratories under Contract No. 19628-71-C-0220 with the cooperation of R. A. Bradbury, contract monitor.

## 9. References

- [1] DeShazer, L.G. and Parks, J.H., in Damage in Laser Materials: 1971, edited by A.J. Glass and A.H. Guenther (NBS Special Publication 356, November 1971), pp. 124-136.
- [2] Dickson, L.D., Appl. Opt. **9**, 1854 (1970).
- [3] McAllister, G.L., Mann, M.M. and DeShazer, L.G., IEEE J. Quan. Elect. **QE-6**, 44 (1970).
- [4] Campbell, J.P. and DeShazer, L.G., J. Opt. Soc. Am. **59**, 1427 (1969).
- [5] Holmes, D. A., Korka, J.E. and Avizonis, P.V., Appl. Opt. **11**, 565 (1972).
- [6] Farrukh, U.O., USC, unpublished.
- [7] Catalan, L.A., J. Opt. Soc. Am. **52**, 437 (1962).
- [8] Newnam, B.E. and DeShazer, L.G., IEEE J. Quan. Elect. **QE-8**, 611 (1972).

## 10. Figures

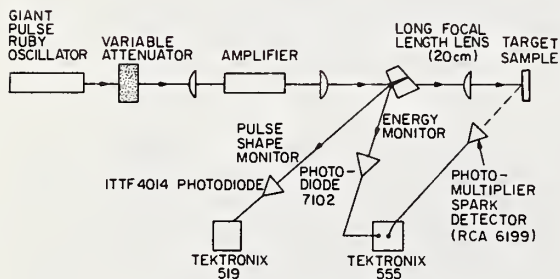


Figure 1. Schematic of Q-switched ruby laser system and spark detection electronics.

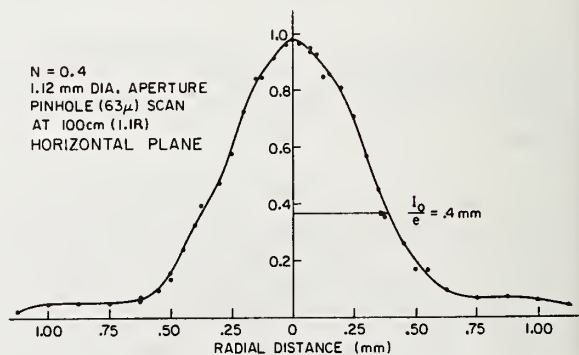


Figure 2. Normalized oscillator intensity distribution in the far field (100 cm) of the mode selecting aperture (1.12 mm dia.) for a cavity Fresnel number of 0.4. The profile was measured with a pinhole detector (64  $\mu\text{m}$ ).



Figure 3. Photographs of the diffraction pattern of the giant-pulse ruby laser oscillator (Fresnel No. 0.4) at 3 Rayleigh distances (far field) from the laser. The three photographs were exposed under three different beam attenuations.

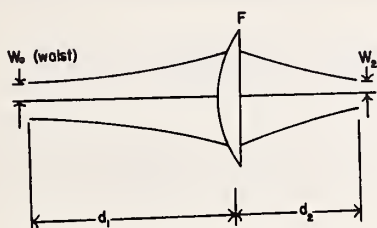


Figure 4. Focusing of a Gaussian beam.

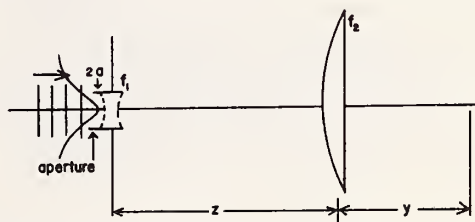


Figure 5 Aperture intensity profiles at the temporal peak of a passively Q-switched ruby laser oscillator with planar mirrors and Fresnel No. 0.4.

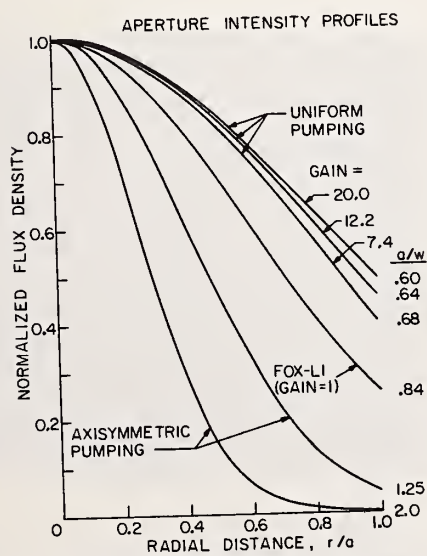


Figure 6. Focusing of a truncated Gaussian beam, described by the truncation parameter  $a/w$  and the initial divergence represented by a lens in the aperture lens  $f_1$ .

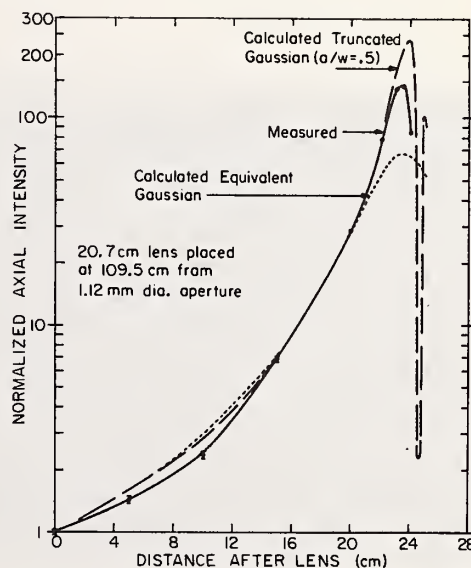


Figure 7. Axial intensities before the focus of a lens ( $F = 20.7$  cm) comparing the measured intensities to calculated equivalent and truncated Gaussian distributions.



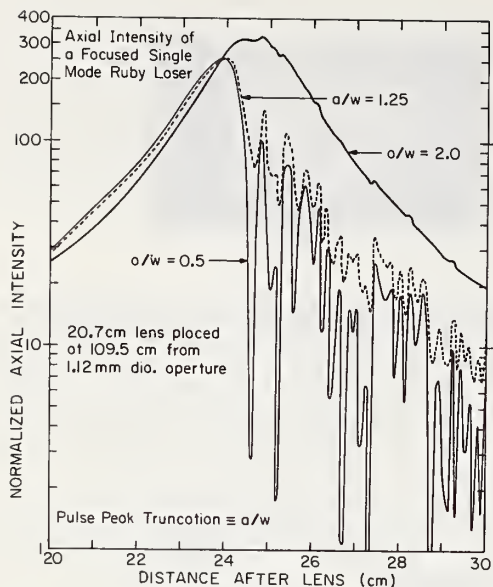


Figure 8. Axial intensity after the focus of a lens ( $F = 20.7$  cm) for truncated Gaussian beams with truncated parameters 0.5, 1.25 and 2.0.

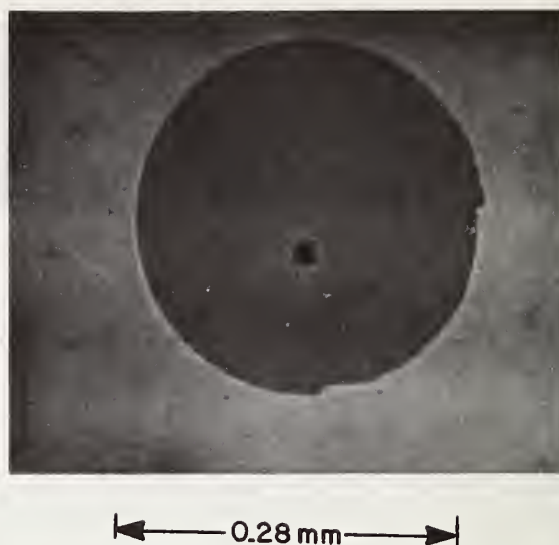


Figure 9. Laser-induced damage above the spark threshold for a 22 layer  $\text{TiO}_2/\text{SiO}_2$  reflector of configuration G(HL) $^{10}_{\text{HL}^2\text{A}}$ .



Figure 10. Laser-induced damage occurring before a detectable spark in a single quarter-wave film of  $\text{TiO}_2$ .

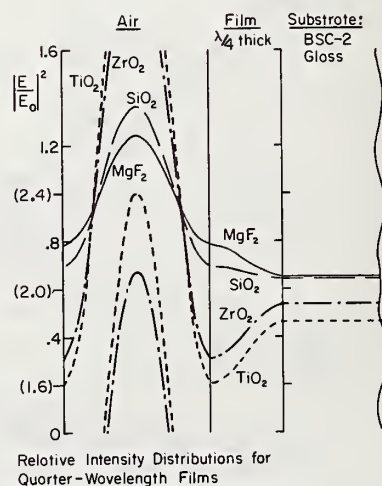


Figure 11. Relative intensity distribution for quarter-wave film on BSC-2 glass.

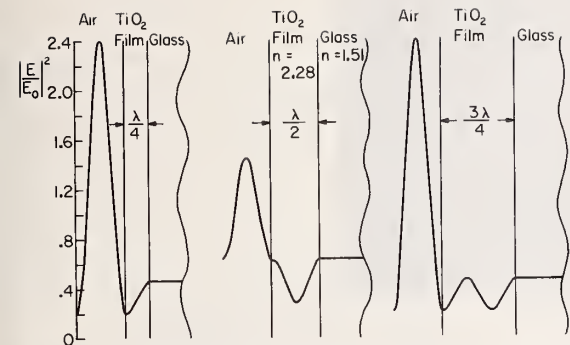


Figure 12. Relative intensity distribution for quarter-, half-, and three-quarter-wave  $\text{TiO}_2$  films.

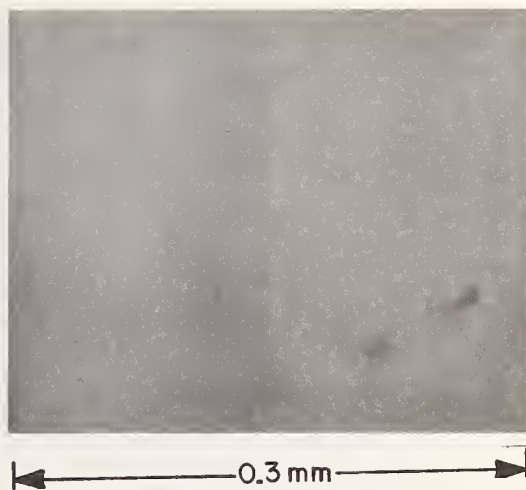


Figure 13. Surface of  $\text{TiO}_2/\text{SiO}_2$  multilayer reflector before irradiation which had a high threshold for damage. Note absence of defects.

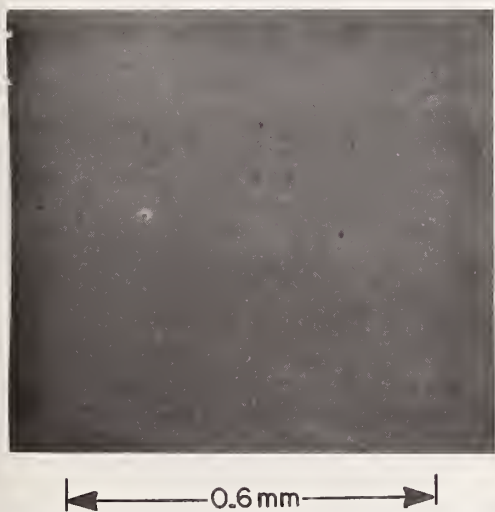


Figure 14. Surface of a  $\text{CeO}_2/\text{SiO}_2$  multilayer reflector before irradiation which had a very low threshold for damage. Note the great number of pinholes.

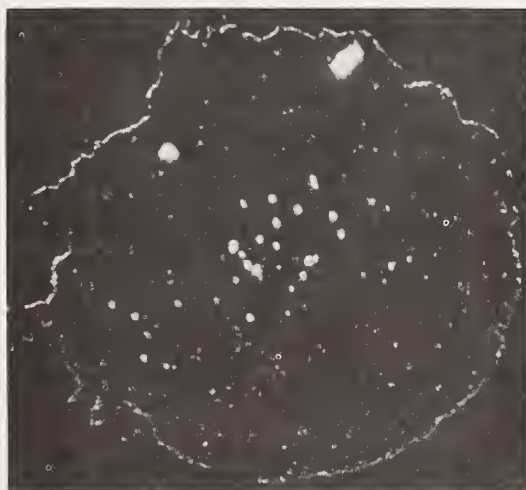


Figure 15. Laser-induced damage far above the spark threshold for  $\text{TiO}_2/\text{SiO}_2$  reflector. Note central bubbles.

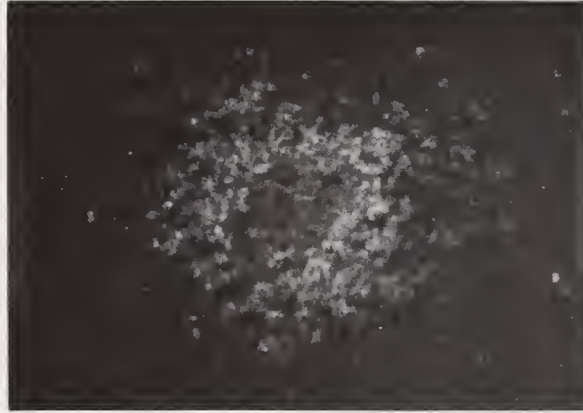


Figure 16. Laser induced damage above the spark threshold for a  $\text{ZrO}_2/\text{SiO}_2$  multilayer reflector. Note granular structure of the damage and the gradual decrease of damage penetration with radius.

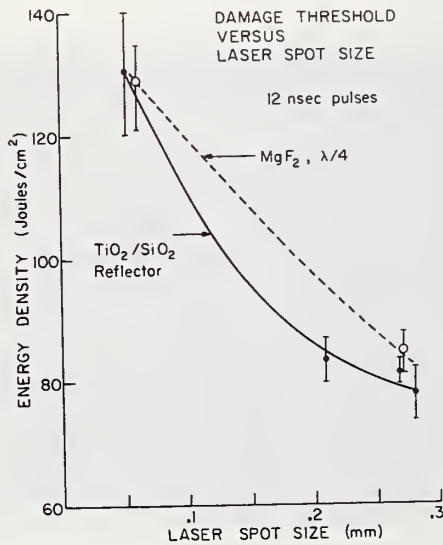


Figure 17. Damage threshold as a function of laser beam spot-size for a  $\text{TiO}_2/\text{SiO}_2$  multilayer reflector and a single quarter-wave thick  $\text{MgF}_2$  antireflection coating on BSC-2 glass.

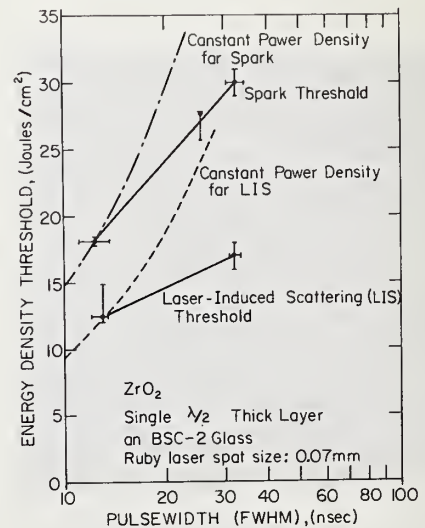


Figure 18. Laser pulse-width dependence of the damage thresholds for a single half-wave thick film of  $\text{ZrO}_2$  on BSC-2 glass. Damage was detected by both laser-induced scattering and spark formation. Deviation from constant power density thresholds is indicated by dashed curves.



Influence of Structural Effects on  
Laser Damage Thresholds of Discrete and Inhomogeneous  
Thin Films and Multilayers

R. Russel Austin and Raymond C. Michaud  
Perkin Elmer Corporation  
Norwalk, Conn. 06852

and

Arthur H. Guenther, Joseph M. Putman and Richard Harniman  
Air Force Weapons Laboratory  
Kirtland Air Force Base  
Albuquerque, N.Mex. 87117

The dependence of single shot damage threshold on certain film properties is discussed. Variable stress films are produced by mixing components with approximately equal damage thresholds but opposite stress characteristics a definite stress dependence is shown. Films formed from mixtures of high and low threshold components are investigated and found to have damage thresholds between the high and low component values. The damage threshold and damage mode of multilayer and periodic inhomogeneous film systems is compared. The results confirm that the damage threshold is almost entirely material dependent.

Key Words: Laser damage, optical coatings, inhomogeneous films, microscopy, thin film stress.

## 1. Introduction

A first examination of failure modes in various single and multiple layer anti-reflection coatings was undertaken by Austin and Guenther. [1]<sup>1</sup> In that work an attempt was made to relate damage levels and damage modes to some properties and structural parameters of the films and multilayers. Particularly interesting was the film stress effect and the conclusion was drawn that there were indeed some failure modes which could be explained on that basis. There were however insufficient experiments performed to clearly identify a relationship between stress and damage threshold.

Several instances of failure through delamination were evidenced by the study. These were sufficient to indicate the possibility of damage threshold effects due to film structure. The study also identified a weakness in anti-reflection coating design capability due to lack of medium index material with a high damage threshold. Additional studies were proposed which would allow property and parametric effects to be considered in more detail. Many of those studies are covered by this report.

## 2. Stress Effects on Laser Damage Threshold

In order to best examine this effect it was necessary to produce sample films in which the inherent stress was the only major variable. As in many other experiments with thin films it was not possible to exclude all other variables but by careful choice of film system these were reduced to levels which should be small compared with the gross effect of film stress.

### 2.1 Choice of Films

The stress in some film materials can be influenced by deposition conditions, and in other materials (particularly metals) the stress is a strong function of thickness. Aluminum for example forms films which begin as tensile stress films and become compressive with increasing thickness. A

---

<sup>1</sup>Figures in brackets indicate the literature references at the end of this paper.

condition of zero stress exists at a thickness of approximately 400 Å. Even though we are then able to produce a stress spectrum using a film of a single material many other properties of the film might be widely different. In the case of a luminum films the thickness would vary from a few angstroms to say 1000 Å, the reflectivity would vary from 5 percent to 90 percent; and the absorption would vary from 30 percent to 10 percent. Clearly then it would not be possible to isolate those effects purely due to stress in the presence of so many other variables.

Turner [2] studied the damage threshold of a number of common thin film materials and lists a hierarchy of resistance to laser damage as shown in table 1. Of the materials listed Magnesium Fluoride and Silicon Dioxide have damage threshold levels which are fairly similar. The refractive indices of the two materials are also fairly close. The stress properties of each material however are entirely different. Magnesium Fluoride forming films with a high tensile stress and Silicon Dioxide forming films with a high compressive stress. It was decided to use films which were a vapor phase mixture of these two materials for our investigation. By altering the relative proportions of the two materials in the mixture, films of different internal stress could be produced. Stresses could range from a very high tensile value through intermediate values and zero to a very high compressive value. Total film thickness could be maintained constant and there would be only small difference in refractive index from one mixture film to another.

Table 1. Observed Damage Thresholds, Single QW Films at  
Focus of f=42 mm Lens Glass Substrate Thickness 2.3 mm

Q-Switched Ruby Lasers	
<u>Material</u>	<u>Threshold <math>E_d</math> in J/cm<sup>2</sup></u>
ThF <sub>4</sub>	470
SiO <sub>2</sub>	360 - 420
SiO <sub>2</sub>	250
MgF <sub>2</sub>	300 - 360
MgF <sub>2</sub>	250 - 420
Al <sub>2</sub> O <sub>3</sub>	220 - 400
CaF <sub>2</sub>	50 - 300
ZrO <sub>2</sub>	130 - 160
ZrO <sub>2</sub>	200 - 280
ZrO <sub>2</sub>	115 - 240
5NaF .3AlF <sub>3</sub>	100 - 210
TiO <sub>2</sub>	115 - 180
SiO	115 - 150
LiF	100
MgO	100
CeO <sub>2</sub>	40 - 100
ZnS	30
ZnS	23

## 2.2 Film Preparation

The films were prepared by simultaneous evaporation of MgF<sub>2</sub> and SiO<sub>2</sub> from separate electron beam sources. Each source was provided with a separate rate of evaporation control, and the mixture proportions in the final film were obtained by control of the rate of evaporation of each source. The apparatus for the film deposition is described in detail in Appendix A. It was used for the generation of other experimental samples described later in this report.

Substrates for the films were 1" square fused silica pieces all of which were cut from a common wind blank. This ensured that the surface condition of the substrates was as similar as possible. The substrates were cleaned simultaneously in boiling methyl alcohol and in a methyl alcohol vapor degreaser prior to coating.

## 2.3 Experimental Results

### 2.3.1 General Film Properties

The general properties of the films are documented in table 2. The thickness of the films was held to minus 0 plus 4 percent of the intended thickness. Monitoring accuracy is not as high with mixture films as it is with films of single material because of the tendency to form inhomogeneous films. An estimate of this inhomogeneity is given in table 2. Inhomogeneity in thin films does not mean variation of composition but relates to variation in refractive index.

Table 2. Vapor Phase Stress Mixtures of  $\text{MgF}_2$  and  $\text{SiO}_2$

Sample Number	Percentage Composition $\text{MgF}_2:\text{SiO}_2$ (by weight)	Scatter (Percent)	Wavelength - at which films are $\lambda/2$ O.T. $\mu\text{m}$	Stress (Measured) ( $\text{Kg}/\text{cm}^2$ )	Refractive Index (Mean Value) ( $@ 2 \times \lambda_0/2$ )	Inhomogeneity @ $1.06 \mu\text{m}$
1	100 : 0	0.0030	1.08	2950 (T)	1.38	0
6	82 : 18	0.0031	1.06	520 (T)	1.39	0
5	76 : 24	0.0035	1.11	162 (T)	1.40	0
4	66 : 34	0.0032	1.08	312 (C)	1.41	+ 0.5%
3	50 : 50	0.0034	1.06	870 (C)	1.43	+ 0.4%
2	0 : 100	0.0030	1.10	2370 (C)	1.45	0

- NOTES: 1. Scatter measurements are taken directly from the samples without aluminum overcoating. Measurements are taken @  $6328 \text{ \AA}$  and are not normalized to account for the diffuse reflection component or scattering due to the influence of substrate quality.
2. Stress values (T) indicates tensile stress (C) indicates compressive stress. Measured using a stress interferometer [7].
3. The inhomogeneity value is the reflectivity difference (in percent) of the reflection from the film from the reflection of an uncoated substrate. A completely homogeneous film has an inhomogeneity value of zero. A positive value indicates an increase in refractive index in a direction from the substrate through the coating.

Figure 1 shows graphically the stress variation in the mixture films of  $\text{MgF}_2$  and  $\text{SiO}_2$  as a function of percentage composition. It can be seen that the relationship is not a simple one. Thirty percent of  $\text{SiO}_2$  in the mixture is sufficient to reduce the stress of the films to zero even though the single film of  $\text{SiO}_2$  in the same thickness as a  $\text{MgF}_2$  film is stressed less. This is indicative of some interaction possibly taking place between the  $\text{SiO}_2$  and  $\text{MgF}_2$ , in the deposition process.

There is no significant difference between the scatter values recorded for the mixture film-substrate combinations. The refractive index and inhomogeneity measurements for the films were made on substrates with  $n = 1.52$ . It was not possible to obtain good measurements of the homogeneity from the fused silica witness pieces because of the similarity of the film and substrate indices.

### 2.3.2 Experimental Procedure

The experimental configuration utilized in this investigation is in general similar to that reported last year.[1] For the laser damage threshold measurements, a high brightness  $1.06 \mu\text{m}$  glass laser was employed. The oscillator-amplifier system emitted in excess of 10 joules in a single 30 nsec FWHM pulse. The total beam intensity distribution is essentially flat topped with an rms intensity fluctuation of  $\sim 8\%$  over  $> 90\%$  of the total energy output cone.

An experimental arrangement as shown in Fig. 2 was used for all sample irradiation. The laser system was operated at a constant pump level to insure maximum stability in experimental exposure conditions. Under this restraint the laser output and beam quality as measured by its total divergence ( $\sim 5 \text{ mr}$ ) [3] and intensity distribution was reproducible to between 2 and 3%. The residual or aspheric portion of the beam divergence was  $\sim 0.1 \text{ mr}$  as determined by use of a Hartman diaphragm.[3] To vary the real power density, homogeneous Schott filters were inserted before the combination 4 m and 6 m focusing lenses.



In order to afford good sampling of surface imperfections, an irradiation area  $2.85 \pm 0.1$  mm in diameter was selected. Thus the irradiation area was  $0.061 \pm 0.002$  cm<sup>2</sup> at FWHM. This would insure that results would be representative of large area damage thresholds with a sufficient probability of occasionally encountering pinholes, dust particles or localized high stress regions. The 2.54 cm x 2.54 cm x 0.64 cm fused silica substrates with coating were inserted at an angle of  $\sim 5^\circ$  off normal to the incident laser beam to eliminate feedback into the laser. These dimensional conditions permitted nine (9) noninterfering exposures on each sample. Samples were only coated on one side and all exposures were accomplished with the laser radiation incident on the coated surface.

The intensity distribution from the rotating mirror Q-switched laser system is shown in Figure. From this known intensity distribution an average power density is calculated. To complete the experimental arrangement as shown in Fig. 2 a beam splitter was used to direct a portion of the beam to facilitate recording of the intensity distribution on each exposure. Since no apertures were used to limit the area as employed last year, a slightly different intensity distribution was obtained. This procedure eliminated to a large extent the occurrence of undesirable diffraction rings. All sample exposures were visually observed through a 1.06  $\mu$ m blocking filter to detect the formation of any visible plasma. In addition a visual spot check for damage was accomplished after each irradiation before microscopic inspection.

Before insertion in an adjustable x-y mount for exposure each sample was cleaned by pulling a Kodak lens tissue wet with spectral grade ethyl alcohol across each face once. No detectable water droplets or surface impurities were noted upon observing the evaporation of the residual alcohol film.

### 2.3.3 Damage Threshold Values

The evaluation of the single pulse damage threshold in this and later discussed experiments proved to be primarily qualitative and relative as opposed to quantitative and absolute. As in the case of last year's report, in general two exposures were recorded for the highest level without damage and two exposures at the lowest level with damage. The presented errors are due primarily to the insufficient selection of filters to further narrow down the uncertainty in the threshold value. Limited sample exposure areas prevented any systematic attempt at ascertaining the reproducibility of the damage threshold. Three criteria were used to determine the onset of damage and two opinions were sought to determine whether or not the criteria were satisfied. These criteria were:

1. The appearance of a visible breakdown during irradiation.
2. Microscopic evidence of damage.
3. Immediate visual observation of damage.

As usual there was always a plasma formed when damage was observable. However, when testing very damage resistant films plasmas would be formed at the surface which did not necessarily produce visual damage. In some cases there appeared to be a self-annealing taking place in which the immediately evident visual damage area would appear to lessen in a time period ranging from minutes to hours.

Figure 4 shows the damage threshold of the samples of varied film stress as determined by the spark criterion. This observation produced the least uncertainty in the overall results. It can be seen that all of the films that are mixtures show a higher damage threshold than the films of the pure materials, even though the trend of the measurements takes no immediately obvious form.

The threshold values for the discrete values were almost equal confirming the Turner results for the same materials. The actual levels for these materials however are lower than one might expect when compared with the levels for Zinc Sulphide and Thorium Fluoride generated in the mixture experiment discussed later. The damage levels for the mixture films are closer to the values that one might expect for discrete films in Turner's comparison.

The morphology of the observed damage areas is discussed later. It is more appropriate to present that analysis in conjunction with the observation of the damage evident in the other experiments where comparison between material and film properties can be made manifest.

### 2.4 General Comments on the Stress Investigation

Although it is difficult to ascribe any order to the damage threshold values compared with film stress the high magnification SEM pictures shows a progressive pattern of damage appearance and then an abrupt change in this appearance to another characteristic pattern as the SiO<sub>2</sub> content of the films reaches a certain level. It is significant however that the samples showing the highest threshold do not show the granularity and fail in the complete fusion mode without any evidence of cracking at the edge of the irradiated area.

### 3. Damage Threshold Value for Mixtures of High and Low Threshold Components

#### 3.1 Requirement for the Study

The data in section 2.1 shows that there is a tendency for the damage thresholds of low index materials to be higher than medium and high index materials. The obvious exceptions to this rule are Cryolite ( $5\text{NaF} \cdot 3\text{AlF}_3$ ) with a refractive index  $n$ , on the order of 1.35 and is fairly low on Turner's scale; and Alumina ( $\text{Al}_2\text{O}_3$ ) which is fairly high on Turner's scale, yet having an  $n_d$  in thin film form ranging from 1.65 to 1.75. It is noteworthy that films exhibiting high index values usually do so in the presence of some absorption and would therefore be more susceptible to laser damage.

In the design of multilayer anti-reflection coatings for either single wavelengths or broad bands of wavelengths there is frequently a requirement for a material with a refractive index lying in the range 1.80 to 2.0. Two materials in Turner's tabulation satisfy this requirement  $\text{MgO}$  (with an  $n_d \sim 1.86$ ) and  $\text{SiO}$  (with an  $n_d \sim 1.90$ ). Both materials would rate fairly low for damage threshold with values a factor of 3 to 4 less than good low index materials. There are two design devices which would allow the thin film designers to avoid the use of medium index films. One device is the Herpin equivalent multilayer approach wherein a symmetrical multilayer system of high and low index materials is substituted for the normally discrete layers in a multilayer film system. This would still pose a problem from the damage resistance standpoint because of the relatively poor damage resistance of the high index films.

The other device would be to use films which were formed by vapor phase mixture of the high and low index films as were the films prepared for the stress examination in Section 2. A second experiment was designed to investigate films of that type.

#### 3.2 Selection of Materials

It was decided that in order to obtain the best experimental results we should chose materials with widely differing damage thresholds. Thorium Fluoride and Zinc Sulphide occupy the top and bottom of the Turner scale, their damage thresholds differing by well over an order of magnitude. They are commonly used together in discrete films to form high efficiency reflectors and bandpass filters. The purpose of this second experiment was to determine mixture effects. This material pair was preferable to say  $\text{ZrO}_2$  and  $\text{SiO}_2$  where there is some overlap of the reported ranges of damage thresholds and the interpretation of the mixture effect would as a result be more difficult. It is probable that mixtures of  $\text{ZrO}_2$  and  $\text{SiO}_2$  would have produced a more damage resistant film for a given index than the  $\text{ZnS}$  and  $\text{ThF}_4$  mixtures.

The only problem anticipated was the modification of the result due to the stress range of the mixture films.  $\text{ZnS}$  is strongly compressive,  $\text{ThF}_4$  is strongly tensile and mixture films exhibit intermediate stress values. It was hoped that the stress effects would be sufficiently isolated by the previous experiments to make the appropriate allowances in the formulation of the results. Furthermore, the stress—composition behavior for this pair of materials is considerably different than  $\text{MgF}_2 - \text{SiO}_2$  previously studied. It is less composition sensitive to stress changes over a relatively large range of compositions resulting in low stress values for considerably different compositions.

#### 3.3 Sample Preparation

The samples were prepared by simultaneous evaporation, from two separate sources, of Zinc Sulphide and Thorium Fluoride. The apparatus was basically the same apparatus used for the preparation of the stress samples in the previous section with the exception that radiant heated thermal sources were used rather than electron sources.

All substrates were cut from the same window blank. The substrates were cleaned in boiling methyl alcohol and then in a vapor degreaser containing methyl alcohol. Each substrate was subjected to a glow discharge cycle at 2.5 KV/100 mA for a duration of 10 minutes prior to each evaporation.

It was attempted to maintain each film at a thickness (optical) of one half wavelength at  $1.06 \mu\text{m}$  in order that the reflection from the film system would be independent of the refractive index value. The films were difficult to monitor accurately because of inhomogeneity introduced by variations in evaporation rate from each source. This inhomogeneity does introduce some slight differences in the reflection values. In certain cases it was impossible to obtain any good information on the film properties because of gross inhomogeneity in the film systems.



### 3.4 Experimental Results

#### 3.4.1 General Film Properties

The general properties of the experimental films are listed in table 3. Samples #2,3, and 6 were grossly inhomogeneous to the extent where it was not possible to acquire any meaningful information on their refractive index values.

The apparatus used for the deposition of the films did not contain a film stress measuring interferometer so that it was not possible to measure the stress of the samples tested. It was necessary to generate a separate estimate of the stress versus composition of the films by supplementary measurements and by reference to existing data on these two materials. Figure 5 shows the estimated stress behavior of the mixture films. Typical response curves for a homogeneous and an inhomogeneous mixture film is shown in figures 6 and 7.

While the variation of refractive index of ZnS-ThF<sub>4</sub> mixture with composition is essentially linear (see table 3) the variation of refractive index with film stress takes the form of figure 8. Obviously this mixture film system allows great selectability of refractive index between 1.45 and 2.35 while exhibiting relatively low residual film stress over that range.

Figure 9 shows the dependence of damage threshold on the composition of the mixture. As expected a range of damage threshold values spread between the results for the discrete materials was obtained. The spread is such that it is possible to conclude at least tentatively a threshold versus mixture behavior. The data presented indicates the trend could either be a general increase in damage threshold as the ZnS% is decreased or once the mixture becomes at least 50% ThF<sub>4</sub> there is a step increase in damage threshold. Both types of behavior could be explained phenomenologically but additional data is warranted to elucidate the appropriate trend.

The results for the discrete material films indicate the possibility of over an order of magnitude difference in the thresholds of ThF<sub>4</sub> and ZnS which is in agreement with Turner's findings. It can also be seen that if these values represent the extreme of the damage threshold range, as they do in the Turner data then the values for the highly stressed discrete films of Magnesium Fluoride and Silicon Dioxide do not agree except in relation to each other. It is of note however that the actual values for the stress relieved mixture films of MgF<sub>2</sub> and SiO<sub>2</sub> do fall in the correct relative position on the damage threshold scale.

The morphology of damage will be presented later in which differences between the failure of homogeneous, inhomogeneous and various compositions will be discussed with the other experimental results.

Table 3. Vapor Phase Mixtures of ZnS and ThF<sub>4</sub>

Sample Number	Mixing Ratio ZnS:ThF <sub>4</sub>	Scatter (Percent)	Wavelength of $\lambda_0/2$ O.T. in $\mu\text{m}$	Refractive* Index	Inhomogeneity %	Stress (Estimated) kg/cm <sup>2</sup>
VPM 1	100 : 0	0.024	1.05	2.36	+ 0.6	2000 (C)
2	0 : 100	0.010		1.5 nominal	- 0.2	1500 (T)
3	13 : 87	0.008				670 (T)
4	23 : 77	0.010	1.15	1.59	- 0.6	500 (T)
5	31 : 69	0.024	0.8	1.72	+ 3.3	450 (T)
6	15 : 85	0.012				640 (T)
7	90 : 10	0.036	1.06	2.33	+ 1.0	540 (C)
8	80 : 20	0.040	1.06	2.15	+ 1.5	100 (C)
9	50 : 50	0.036	1.06	1.91	+ 5.0	100 (T)

\*Refractive index measured at the  $2 \times \lambda_0/2$  position.

O.T. = Optical Thickness =  $n \times d$

Films # VPM 2,3,6 are inhomogeneous in nature.



### 3.5 General Comments on the Mixture Experiment

The micrographs reveal no evidence to indicate the mechanism by which the threshold of a low threshold material is raised by adding a higher threshold component other than the progressive change in the appearance of the damaged areas from characteristics of one material to the other. Some pictures do reveal that the films may not have been as homogeneous as the spectral response data might indicate.

## 4. Damage Resistance Properties of the Periodic Inhomogeneous Film Systems

### 4.1 Description of the Periodic Inhomogeneous Film

The Periodic Inhomogeneous Film (PIHF) is a single film whose refractive index varies periodically with thickness according to some predetermined function [4]. By suitable choice of the function a film can be made to produce any spectral response characteristic that is possible with a discrete film system and some response characteristics that are difficult to produce in practice using solely discrete film systems.

The significant feature of the PIHF is that it has no discrete interfaces other than the interface with the surrounding media. There are no optical or mechanical discontinuities throughout the entire thickness of the film. The discrete film system by comparison does contain many interfaces where there are abrupt changes of mechanical stress or refractive index. The difference between the PIHF and the discrete film system is shown schematically on Figure 10.

### 4.2 Damage Patterns Occurring in a Discrete Film System

In a reflective film system comprising discrete quarter wavelength optical thickness films the standing wave pattern is such that electric field concentrations occur at every second interface in the system, as these interfaces are generally lines of abrupt change of mechanical weakness. Turner [2] observed in damage areas on multilayer reflections that delamination in certain instances occurred in layer pairs as shown schematically in Figure 11. The standing wave pattern in the multilayer system is shown schematically in Figure 12.

### 4.3 Philosophy of the Experiment Choice of Film System

It was decided that as part of this experiment that not only should we investigate the damage mechanism and damage resistance properties of the PIHF but also compare the same properties of the closest equivalent multilayer system.

The filming materials chosen were Zinc Sulphide and Thorium Fluoride. This choice was made not only because of the availability of design information for these systems from previous Perkin Elmer development programs but because of the availability of information on the damage resistance versus mixture data from the experiment described previously. This information was considered essential in the analysis of the experimental results.

The PIHF chosen for the experiment was an order suppression type filter optimized for transmission on the short wavelength side of the fundamental reflection band. The closest approach to this using discrete films of only two materials would be a short wavelength pass filter with a fundamental reflection band at the test wavelength. This design type does not have the order suppression property of the PIHF but this property has no particular significance from the damage standpoint, more important being the matching of total optical thickness in the discrete and PIHF designs.

Figure 13 shows the refractive index profile of one cycle of the PIHF chosen for the experiment. The profile of the discrete film equivalent cycle is shown on the same arbitrary thickness scale. In practice the mechanical thickness of the cycles is not exactly the same.

### 4.4 Preparation of Samples

Two coating facilities were employed in the generation of samples for this experiment. One of the plants was the dual source facility described in Appendix A. This system was used for the preparation of the PIHF samples. The other plant used for the deposition of the discrete film systems was a C.V.C. 18" Glass Bell Jar system equipped with a 6" oil diffusion pump system. As in the other experiments substrates 1' x 1' cut from a common window blank were used to eliminate the possibility of experimental variables associated with substrate surface conditions.

A total of 7 PIHF samples were prepared for the test, the maximum thickness samples having 4 cycle repetitions. Five discrete film reflectors having between one and four repetition groups were generated for comparison purposes. The design of these systems was of the general form.

$$(L/2 \text{ H } L/2)^n$$

where L = One quarter wave optical thickness of  $\text{ThF}_4$ .  
H = One quarter wave optical thickness of ZnS.  
n = An integer.

Table 4 describes the general properties of the experimental designs. It can be seen that the reflectivity of the discrete film reflectors is slightly higher than the equivalent PIHF reflector. There are two reasons for this: the basic constructional difference and the fact that the high and low index values in the PIHF never quite reach the value equal to 100 percent of either basic component. The controls being set for 5 percent of the lesser component at the extremes. To maintain control of the PIHF process, it is necessary to always have both sources at a finite evaporation rate, that is one not completely shut off allowing the film to contain 100 percent of the other component. Figures 14 and 15 show the spectral response curves of a 4 cycle PIHF and the equivalent discrete film reflector. One other point of note is the slightly larger spread of scatter values for the PIHF systems compared with the discrete films.

#### 5. Discussion of Damage Site Investigations by Optical and Electron Microscopic Techniques

Optical microscopy of the laser induced damage to the thin film coatings was performed on a Zeiss microscope employing Nomarski Differential Interference Phase Microscopy. This interference-contrast technique greatly enhances the contrast on a structured surface so that brilliant relief images can be obtained, as well as displaying reflective and transmissive anomalies manifest through interference effects. The photomicrographs obtained were taken using a variable intensity halogen source and a Polaroid film pack unit. Magnifications of 64 to 640 diameters were used in this particular analysis. The ultimate limit of this unit is  $\sim 2500$  diameters [5].

Table 4. Periodic Inhomogeneous and Discrete Film Systems of ZnS and  $\text{ThF}_4$

Sample Number	Design	Wavelength of Peak Reflection ( $\mu$ )	Reflectivity @ 1.06 $\mu\text{m}$	Scatter Percent
PIHF 4	1 cycle	1.20(R=0.29)	0.28	0.016
PIHF 5	2 cycles	1.02(R=0.69)	0.48	0.008
PIHF 6	2 cycles	0.80(R=0.53)	0.04	0.016
PIHF 7	3 cycles	0.97(R=0.68)	0.64	0.012
PIHF 8	4 cycles	0.95(R=0.80)	0.68	0.008
PIHF 9	4 cycles	1.16(R=0.82)	0.70	0.012
PIHF 10	4 cycles	1.08(R=0.81)	0.81	0.032
DF 6	$(\frac{L}{2} \text{ H } \frac{L}{2})$	1.26(R=0.32)	0.30	0.010
DF 2	$(\frac{L}{2} \text{ H } \frac{L}{2})^2$	1.02(R=0.59)	0.59	0.008
DF 3	$(\frac{L}{2} \text{ H } \frac{L}{2})^3$	0.98(R=0.80)	0.78	0.010
DF 8	$(\frac{L}{2} \text{ H } \frac{L}{2})^4$	1.13(R=0.89)	0.86	0.012
DF 4	$(\frac{L}{2} \text{ H } \frac{L}{2})^4$	1.03(R=0.89)	0.89	0.012



The Scanning Electron Microscopic (SEM) investigation of the samples was performed on an Advanced Metals Research Model 900 (SEM). The system was operated in the secondary electron emission mode using an acceleration potential 15 KV and a filament current of 100  $\mu$ A. The samples were vacuum coated with a 500 Å conductive layer of palladium-gold before analysis. The depth of focus or three dimensional aspect of the photomicrographs evident is a direct function of the secondary electron emission. Magnifications of 75 to 7500 diameters were used in this analysis while the ultimate limits of the system are 100,000 diameters magnification and 150 Å resolution. Polaroid photographs were obtained from an ancillary display cathode ray oscilloscope and records primarily surface cosmetics.

### 5.1 Comparison of Discrete Film Systems with Equivalent Periodic Inhomogeneous Film Systems

In the following section, the morphology of laser-induced damage in discrete, vapor phase mixture and periodic inhomogeneous film systems as elucidated from optical electron microscopy is presented. The notation employed in the following description is related to the assignment of specific samples of each set of tested film systems as given in the previous tables and denotes the method of observation. The notation gives the sample designation, magnification, and microscopic technique employed, e.g. D6-64X(N) indicated discrete film system D6; the next designator 64X gives the magnification for a standard Polaroid print while (N) refers to the use of a Normarski Phase Contrast Interference optical microscope.

### 5.2 General Comments on the Discrete Film Series

The low magnification Normarski pictures clearly show the increasing complexity of the damage sites with increasing number of layers. From the Scanning Electron Microscope pictures we are able to see that as the number of layers in the system increases it is clearly the weak component films that cause failure. The plots of damage threshold values versus number of layers, figure 16, tend to confirm this hypothesis, one can see that the failure threshold of the nine-layer systems are very close to the values for single films of Zinc Sulphide. It is intended to produce and test more multilayer systems, containing up to 22 layers, to further confirm these findings.

### 5.3 General Comments on the Periodic Inhomogeneous Film Samples

The PIHF systems did show a characteristic damage pattern which is significantly different from that observed in multilayer structures. The complexity of the pattern did increase with increasing thickness (number of function cycles).

The splitting of the films at certain levels was totally unexpected and a clear explanation is not readily available. If it were possible to estimate the level in the systems at which the failure occurred, then the composition of the film at that level could be estimated.

### 5.4 Damage Threshold Results for Multilayer and Periodic Inhomogeneous Thin Film Systems

The damage thresholds for the multilayer film systems are shown in figure 16. The results clearly show that the damage threshold does decrease as the total number of layers in the stack increases. The two different sets of results are for films deposited at near normal incidence on stationary substrates (DF6, DF7, DF8) and for films deposited at ~35 degrees vapor incidence angle in a rotating planetary fixture (DF1, DF2, DF3, and DF4).

The samples deposited at the higher incidence angle have a lower threshold overall than the samples deposited at near normal incidence. No attempt was made to observe the possibility of differences in the crystal structure of the two sets of films and in microscopic examination it was not possible to detect any significant difference in the damage patterns. A possible explanation for the difference may be that the stress in the films deposited at the high incidence angles is greater than the stress in the samples deposited at near normal incidence. The angle of incidence problem is certainly worthy of further study.

Both sets of results seem to form a trend to a leveling of the damage threshold at some periodic repetition number greater than 4. The actual level of the threshold for these more complex multilayers being much closer to the value for the low threshold component than the high threshold component.

Figure 17 shows the threshold results for the Periodic Inhomogeneous film systems. These systems were generated in the same chamber configuration as the discrete systems DF6, DF7, and DF8. There is no great difference between the discrete film and the periodic film results. The same trend towards the low threshold component level with increasing thickness was evident. One point worthy of note is the tendency for the damage threshold to be lower on consecutive evaporations of the same design. Examples are PIHF5 and PIHF6; and PIHF8, PIHF9, and PIHF10. This may possibly be related to an increase



in the finite size particle content of the films as the coating chamber becomes progressively more loaded with deposits from previous runs. Scatter measurements of the films which might have confirmed this hypothesis were however inconclusive.

In the three sets of Damage vs Thickness curves the most conclusive trend was the approach to the weak component threshold value with increasing complexity. Microscopic evaluation of the films confirmed this hypothesis as it was only possible to positively identify the damage origin in the more complex systems i.e. 3 or 4 groups.

## 6. Summary

There are numerous results that can be stated from the previously described experimental observations. Some results are quite conclusive, others indicate trends, while the remainder suggest the need for further work before laser induced damage effects can be elucidated. A few of the more positive results are:

1. In accord with Turner's remarks, the thicker, thin films are, the more damage sensitivity they exhibit. This is particularly evident as the number of cycles in the case of PIHF is increased as well as the number of periods in discrete multilayers. There are several possible explanations for this behavior including increased absorption, increased probability of encountering foreign particles, or, specifically in the case of reflecting multilayers, that an increasing percentage of the pulse is stopped by the film system as it's reflectivity increases.

2. Damage complexity increases as well with the number of periods or layers.

3. A most obvious conclusion is that laser induced damage resistance is film stress sensitive, and that vapor phase mixtures to relieve stress leads to improved film performance from a damage standpoint. In this light VPM films offer the optical design engineer greater opportunities for the design of low stress improved performance coatings.

4. Thermally induced damage can be observed outside the region of direct irradiation.

5. The angle of incidence of deposition is related to damage sensitivity. This is not surprising since it is also known to be related to the residual stress in the deposited film.

6. From the observation of the morphology of damage, pinholes are not necessarily low threshold initiating sites. The microscopic records show physical evidence of thermal and melting effects, surface tension stress relief, delamination of discrete films, and most surprising, the splitting of PIHF at regions of high concentrations of the low-damage component of such a film system.

7. The high magnification SEM records exhibits the vertical rod-like structure of the optical films which do not seem to vary periodically in PIHF or discrete films.

Concerning the less quantitative results which suggest trends and possible areas of future study specifically uncovered by this work,

1. The damage resistance of VPM films consisting of a high and low damage resistance material is definitely a function of the composition, whether there is a direct relation based upon composition or there are in addition structural effects (e.g. crystallinity, etc.) was not ascertained.

2. As a result of the several experimental observations, one could suggest that PIHF could be produced that were possibly more damage resistant than their discrete film analogs - particularly if these were made of two similar damage resistant materials. This certainly should be investigated further. However, one must realize that from an optical performance standpoint there are areas of both decreased as well as improved performance. The choice would have to be made upon specific requirements.

3. There are positive indications relative to the importance of coating geometry and procedures. The exact influence of substrate temperature, pressure, angle of incidence, chamber and substrate cleanliness, as well as the coating history of the deposition apparatus should be investigated further, particularly as these factors affect the residual film stress.

4. The degree of film homogeneity may have an effect on damage resistance as a result of the threshold values evidenced by these few observations of inhomogeneous VPM film behavior.

5. There is insufficient evidence to draw any conclusions or indicate trends based on the reflectivity or scattering of the film systems studied at the present time.

## 7. Suggested Areas of Future Study

Those areas which may have a profound influence on the damage threshold, besides the obvious one of material selection, and should be studied in specifically designed experiments are the effect of scatter, reflectivity or absorption, substrate finish, deposition method (i.e. R.F. sputtering, resistive evaporation or electron beam evaporation).

## 8. Acknowledgment

The authors would like to express their appreciation to Dr. A. Saxman, Air Force Weapons Laboratory, for his expert advice and assistance in the actual damage testing and laser operation.

## 9. Appendix A

1. A standard 18 inch VEECO coating plant with a Pyrex bell jar and a 4 inch oil diffusion pump, having a pumping speed of 400 liters/second was employed in this study. The system has a 0.8 liter capacity liquid nitrogen cold trap and is capable of reaching an ultimate pressure of  $10^{-7}$  Torr. To assist the 4 inch diffusion pump, the system contains a liquid nitrogen cryopanel with a surface area of approximately 270 square inches. The cryopanel is used primarily to reduce the water vapor content of the residual atmosphere.

Two Sloan Model BXV-6, 6KW, 180 degree bend electron beam guns with large capacity, water cooled hearths can be utilized for evaporating the individual materials. Each electron beam gun is equipped with electromagnetic beam positioning and programmed beam sweep controls. Both electron beam guns are powered by a single Sloan Model Six/Ten electron beam power supply. The Model Six/Ten is a constant voltage (10 KV), variable emission (0.600 ma) type power supply that incorporates a gun filament source and a two-gun magnet supply.

The power input and, therefore, the evaporation rate of each gun, is controlled by Sloan OMNI-II, Rate Controllers. Both OMNI-II's have low-rate measurement modification (0-30 cps) and can control the power input manually or automatically. A Lauda Model K-2 Constant Temperature Circulator is used to maintain both oscillator heads at 30°C, which is where the temperature coefficient of oscillation for a 5 MHz, AT cut quartz crystal is essentially zero. Optimum crystal performance is realized by minimizing the thermal effects associated with radiant heating from the electron beam source.

The two electron beam sources and the quartz crystal sensor heads are integrated with the rate control and electron beam gain electronics to perform coevaporation. The resistance source can be used as a direct or indirect source, automatically controlled by an OMNI-II or manually controlled by a Variac. Therefore, coevaporation can be accomplished with the two electron beam guns or with a resistance source and one gun. Shields are required in front of the crystals to ensure that they only "see" the evaporated vapor from the source being controlled. They are movable so that the different evaporation techniques can be used with little or no problems. In the VEECO 18 inch bell jar coating plant, the separation between the center of the gun hearths is 4.5 inches, while the vertical source to substrate distance is 17 inches. This particular geometry results in a maximum deposition incidence angle of 17.2 degrees over a centrally positioned 6 inch diameter flat, located at substrate level. The resulting film thickness variation over a 6 inch diameter, from a single displaced source, is 14 percent.

A combination of the Granville-Phillips' Series 236 Ionization Gauge Controller and the Series 213 Automatic Pressure Controller with servodriven bleed valve can be used to control the vacuum level at any desired value above the base pressure.

## 2. Equipment for Inhomogeneous Film Deposition

### 2.1 Vernistat Speed Control Section

Since the program function is provided by the output of a Vernistat interpolating potentiometer, it is necessary that the input shaft rotation be controlled with some degree of precision. A variable speed DC motor equipped with a tachometer is used in series with a multiratio speed reducer. This combination allows the Vernistat input shaft rotation to be accurately controlled at very low RMP's. An electric clutch coupling is used to start and stop the function interpolation cycle, while the motor drive maintains a uniform speed.

### 2.2 Function Generator Section

Perkin-Elmer Vernistat interpolating potentiometer and adjustable function generator are used to program the deposition rate controllers. The Vernistat requires eleven turns of its input shaft to go through one complete function cycle. The function generator has 34 adjustable sliders that are set to the desired function voltages. By rotating the shaft of the interpolating Vernistat, the output voltage curve conforms to a series of straight-line interpolations between voltages set up by the sliders.

### 2.3 Control Circuit

The control circuit is merely the necessary switch gear to stop and start the process. A timer is located in this section to monitor the elapsed time during the deposition. The timer also contains a 740 watt auxiliary relay, which can be used to activate a recorder-timer-marker circuit or energize a shutter in the vacuum chamber.

### 2.4 Deposition Rate Control Section

This section comprises two Sloan OMNI-II deposition rate controllers and thickness monitors. The signal from the Vernistat is interpreted as a rate, which signals an SCR module to increase or decrease filament power in order to maintain that rate.

### 10. References

- |  |   |
|--|---|
| [1] Austin, R. R., and Guenther, A. H., <u>Damage in Laser Materials</u> , NBS Spec. Pub. 356 (Nov. 1971) pp. 137-152; Austin, R. R. and Guenther, A. H., App. Opts. <u>11</u> pp. 695-697 (1972). | [4] Jacobson, R., Progress in Optics, E. Wolf, <u>5</u> , pp. 247-286.                            |
| [2] Turner, A. Francis, <u>Damage in Laser Materials</u> , NBS Spec. Pub. 356 (Nov. 1971).   | [5] Grifkins, R. C., Optical Microscopy of Metals, American Elsevier, New York (1970), pp. 94-97. |
| [3] Wick, R. V. and Guenther, A. H., Method of Test of Beam Divergence for Optically Pumped Lasers, ASTM Committee F-1.  | [6] Pearson, J.M., Thin Solid Films <u>6</u> , pp. 349-350 (1970).                                |
|  | [7] Ennos, A. E., App. Opts. <u>5</u> , p. 551 (1966).  |



# 11. Figures

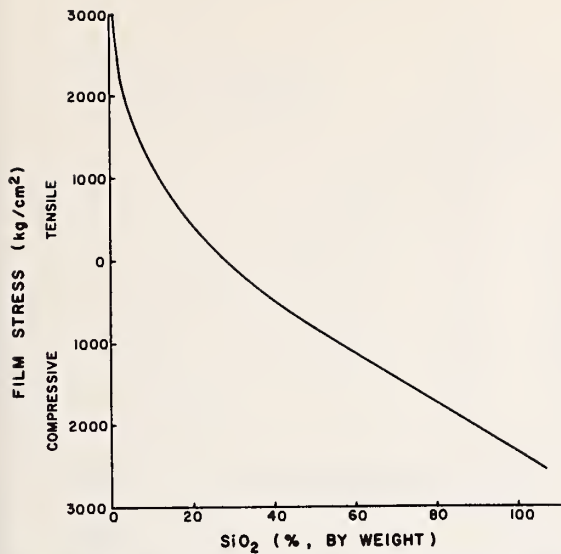


Figure 1. Variation of stress in mixture films of  $\text{MgF}_2 - \text{SiO}_2$ .

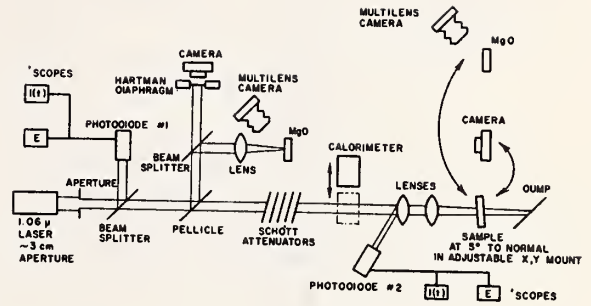
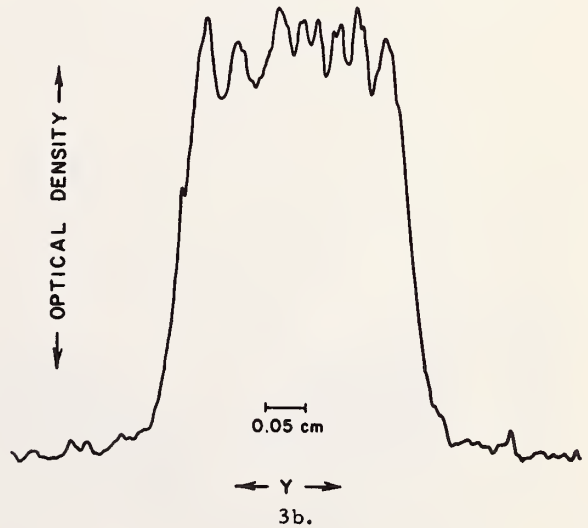


Figure 2. Experimental arrangement for damage threshold evaluation.



3a.



3b.

Figure 3. (a) Two dimensional intensity distribution at the entrance surface of the target as presented by an isodensitometer map. Increasing intensity is indicated by white-gray-black sequence. (b) Microdensitometer trace through center of focal area as recorded in 3 (a).

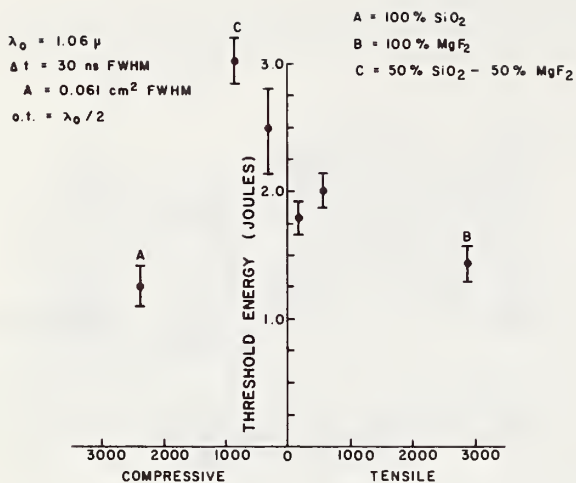


Figure 4. Damage threshold versus stress for mixture films of  $\text{MgF}_2$  -  $\text{SiO}_2$ .

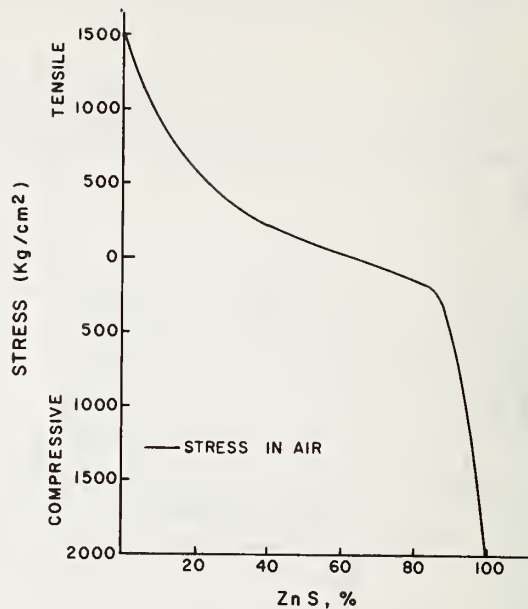


Figure 5. Variation of stress in mixture films of  $\text{ZnS}$  -  $\text{ThF}_4$ .

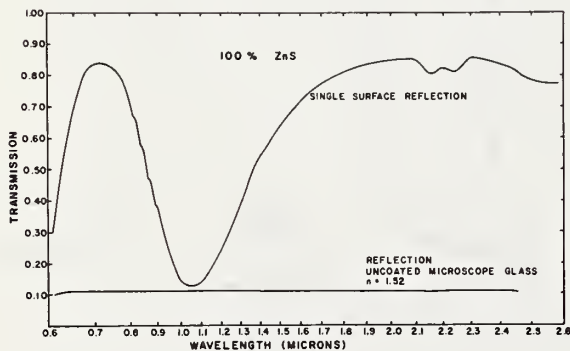


Figure 6. Typical spectral behavior (reflectivity vs wavelength) for a homogeneous film system.

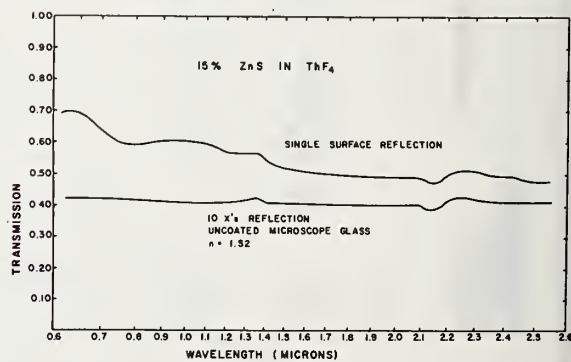


Figure 7. Typical spectral behavior (reflectivity vs wavelength) for an inhomogeneous film system.

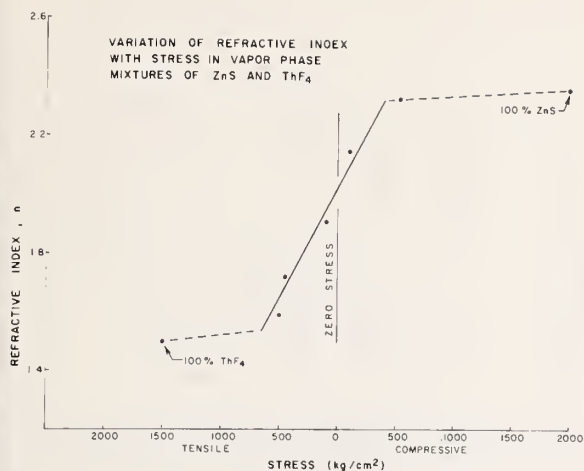


Figure 8. Variation of refractive index versus stress for mixture films of ZnS - ThF<sub>4</sub>.

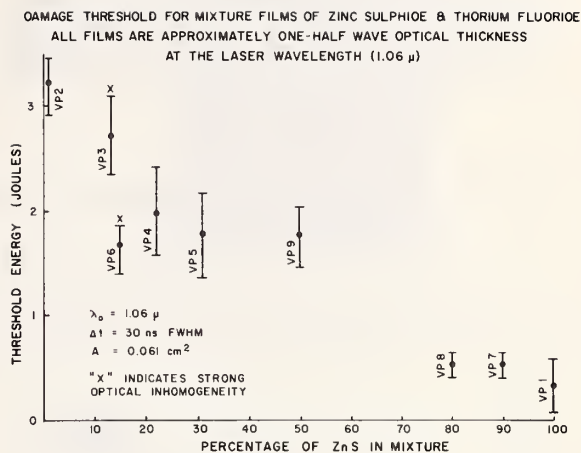


Figure 9. Damage threshold versus composition in mixture films of ZnS - ThF<sub>4</sub>.

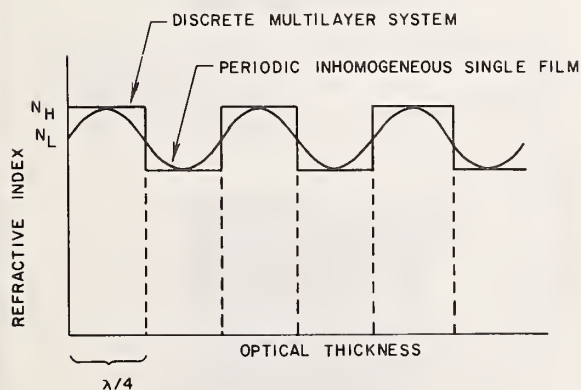


Figure 10. Comparison of refractive index-thickness profile of a discrete multilayer system and a periodic inhomogeneous single film.

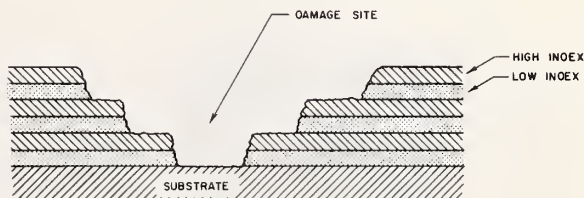


Figure 11. Schematic representation of a damage site in a discrete multilayer system indicating delamination occurring in layer pairs.



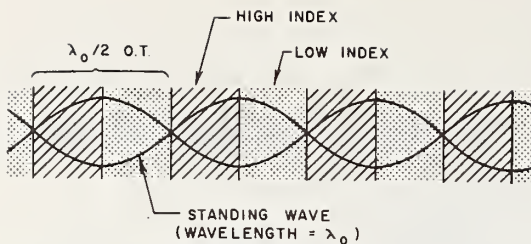


Figure 12. Schematic of the standing wave pattern in a multilayer system.

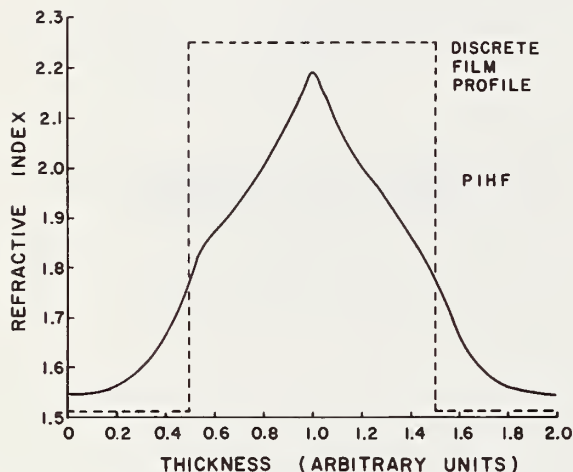


Figure 13. Refractive index profile for one cycle of a periodic inhomogeneous film system compared to one period of a discrete film system.

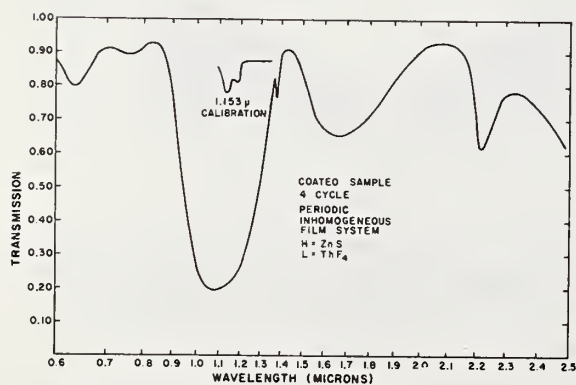


Figure 14. Spectral behavior of a four cycle periodic inhomogeneous film system.

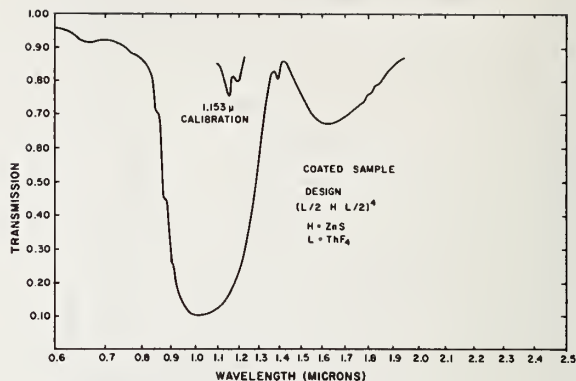


Figure 15. Spectral behavior of a four cycle discrete film multilayer system.

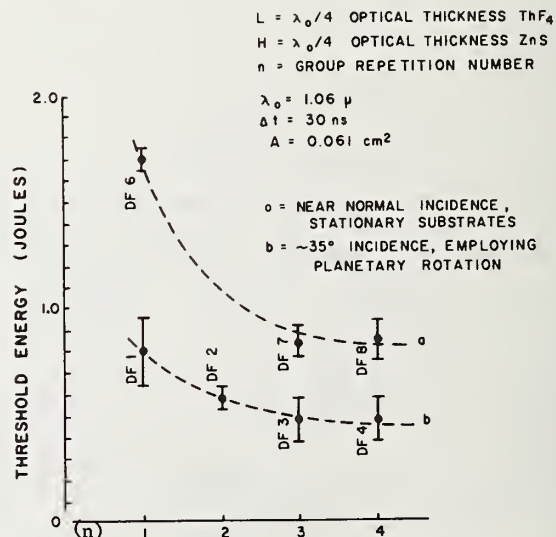


Figure 16. Damage threshold versus number of periods in a discrete film system of ZnS and ThF<sub>4</sub> at two differing angles of vapor incidence.

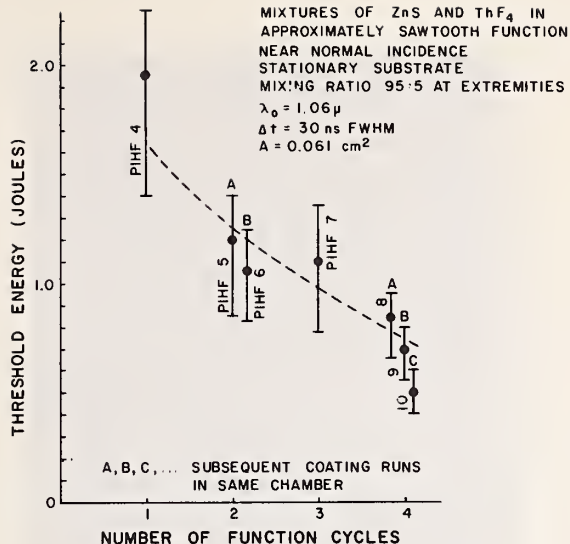


Figure 17. Damage threshold versus number of cycles in a periodic inhomogeneous film system of ZnS and ThF<sub>4</sub>.

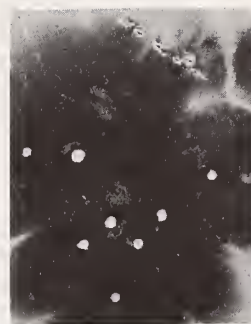


Figure 18. Shows a moderate to heavy damage area with a general onset of damage plus some areas of complete removal.



Figure 19. High magnification SEM picture of a removal area. The partially damaged film surrounding it shows a peculiar but uniform texture. Note the absence of fused materials around the removal site.



Figure 20. The edge of a damage area showing the same overall appearance as the previous sample but with some thermally induced cracks in the falloff region.



Figure 21. Damage onset in the general area, the same. Texture is evident as in the previous (100 percent MgF<sub>2</sub>) sample but with an increase in the size of the granularity.

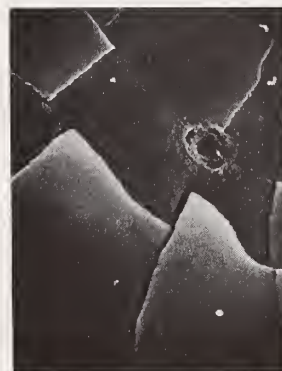


Figure 22. Thermal cracking damage in the falloff region: Note the absence of granularity.

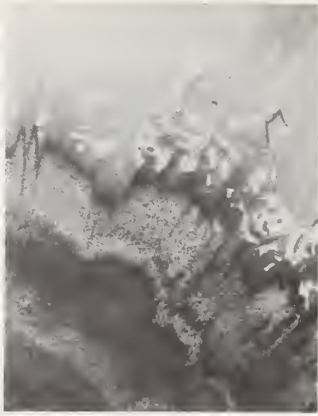


Figure 23. Damage in the same relative area as the previous sample. The appearance is generally the same.

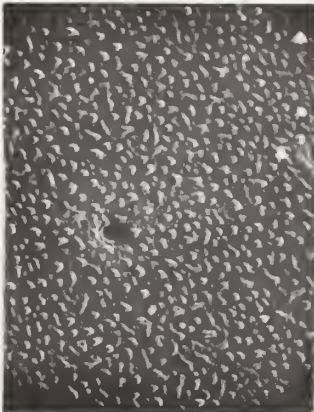


Figure 24. High magnification SEM picture from the central area. A further increase in granule size is evident.

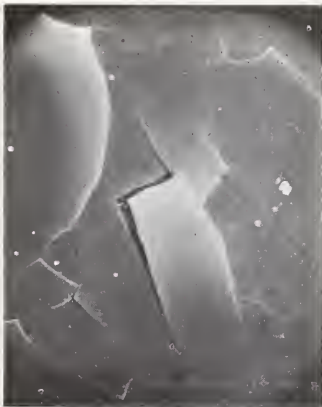


Figure 25. Stress cracking in the energy falloff region.



Figure 26. Edge of a moderate to heavy damage area. No stress cracks at the edge of the area are evident.

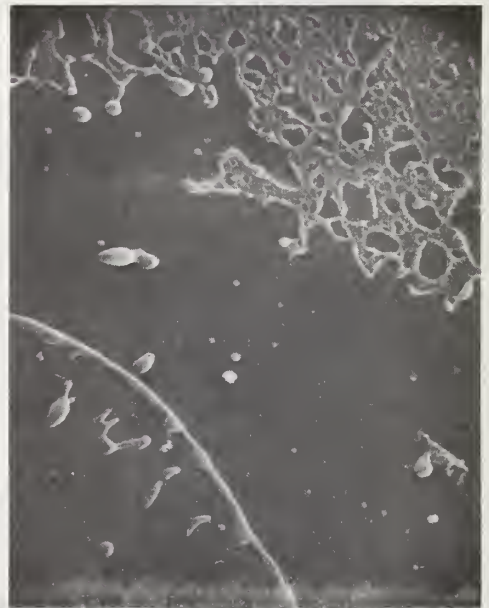


Figure 27. High magnification SEM picture of the dark to light transition region of VPS 4 - 7 - 512X (N). Complete fusion of the film is now evident.





Figure 28. Moderate damage area.

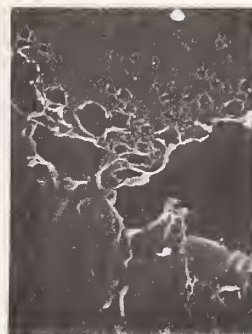


Figure 29. High magnification picture from the center of the area again showing complete fusion of the film.



Figure 30. Edge of a damage area in a 100 percent ZnS film. No evidence of fusion is present.



Figure 31. High magnification of a mechanically damaged area the columnar growth pattern of the film can be clearly seen.

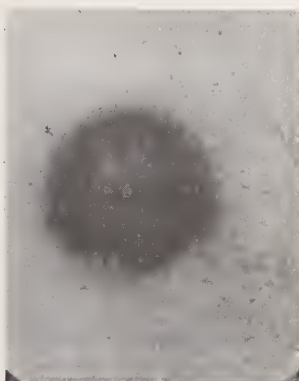


Figure 32. Damage site in a 100 percent ThF<sub>4</sub> film. No pertinent details are evident.

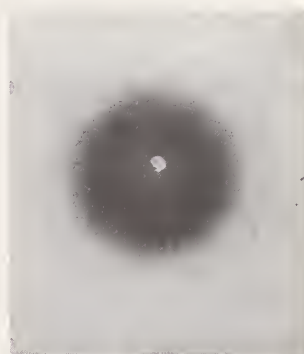


Figure 33. Damaged area showing a removal site. No cracking of the films is evident.



Figure 34. Detail of a removal site. A nucleus is evident but no evidence of fused material.

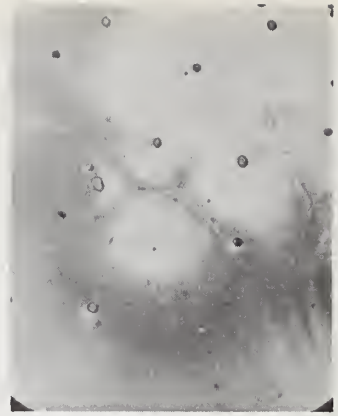


Figure 35. Shows damage in the form of pitting with lines showing the interaction of the thermal pulses for each pit.

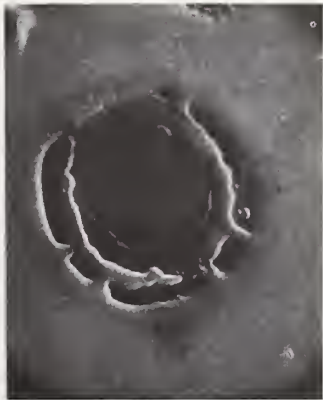


Figure 36. Detail of a damage pit. No nucleus is evident. It is not clear whether or not the crescent shaped cracks are in the film or in the substrate.

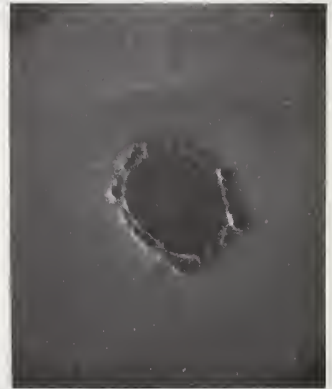


Figure 37. SEM picture showing a pit in the same area.



Figure 38. Damage occurring at two adjacent nuclei. Coalesced thermal areas are evident.

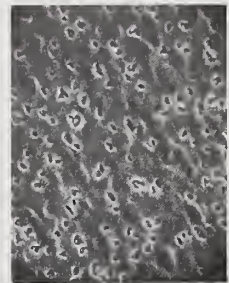


Figure 39. Peculiar granular damage area possibly the result of a mixing phenomenon between the two materials of the film.



Figure 40. Edge of a damaged area showing an area of uniform damage.

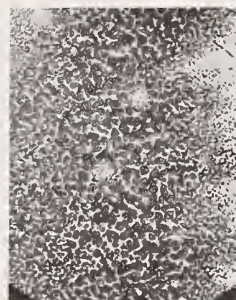


Figure 41. Detail of the damage area showing a pattern similar to that observed in 100 percent  $\text{ThF}_4$  films in previous studies.



Figure 42. Granular damage in the same area. Spacial frequency of the small pits is higher than in the VPM 5 samples.



Figure 43. Low magnification picture of a moderate to heavy damage site. The typical light damage annulus surrounds the main, heavy damage area.



Figure 44. Detail of the edge of a similar area in the same sample. Stress cracking is evident in the light damage area.



Figure 45. Detail of stress disruption. This characteristic is typical of the 100 percent  $\text{ZnS}$  films.



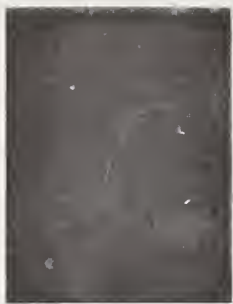


Figure 46. Detail in the same area showing some fusion but less evidence of cracking and disruption in the surrounding area.

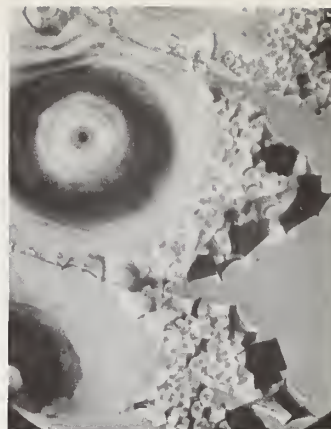


Figure 47. Shows damage at nuclei and also some mechanical disruption typical of ZnS films.

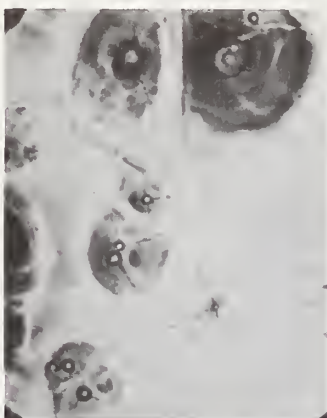


Figure 48. Shows nucleus damage but also the nucleus plus radiating crack damage characteristic of PIHF systems. This indicates that the film may not be completely inhomogeneous and may contain some stratification of the components.



Figure 49. Cracking and disruption similar to that observed in pure ZnS films. Some evidence of fused particles on the film surface is evident.



Figure 50. Damage occurring at nuclei with interacting thermal areas.



Figure 51. A small damage pit with some evidence of film cracking not necessarily extending throughout the film.

Figure 52. Detail of a fused particle on the film surface surrounded by a more extensively fused area more characteristic of 100 percent  $\text{ThF}_4$  films.

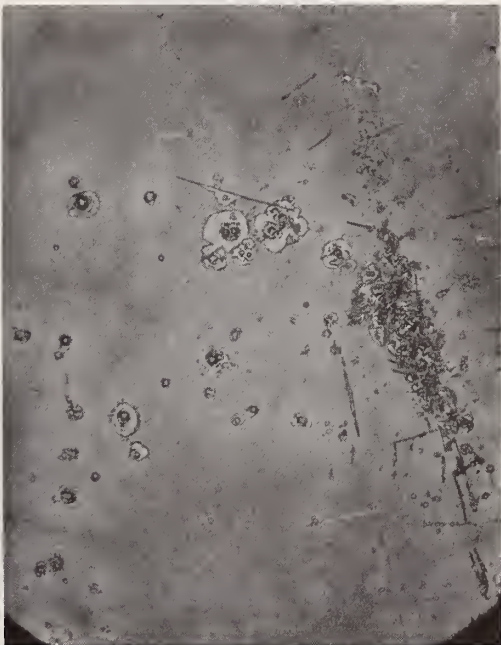


Figure 53. This photograph shows an overall view of a damage site in a one group multilayer reflector. Two types of damage are evident, first small craters emanating seemingly from a tiny nucleus, and secondly damage around a sleek in the substrate. It is not known which was the first to appear. The small crater damage will be seen to be the general damage pattern becoming increasingly complex as the complexity of the multilayer increases in subsequent records. The fact that the sites are clustered much more closely at the fault clearly indicates a possibility the damage nuclei in the film might be associated with substrate features. This may be true even if the nucleus is in the body of the film bearing in mind that substrate features are faithfully reproduced at every interface of a multilayer through as many as 24 layers.

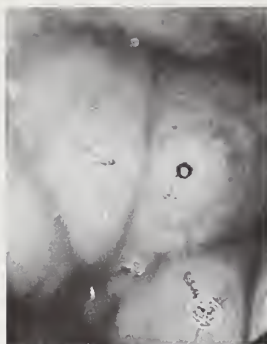


Figure 54. This shows damage sites from the same area as the previous photograph at higher magnification. The thermal wave effects surrounding each nucleus are clearly evident.



Figure 55. This is a view of damage sites which clearly indicates a crater type of delamination in the film.

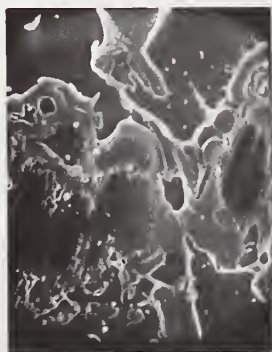


Figure 56. The same as described above. In both pictures it is difficult to tell whether one of the multilayer components is failing in preference to another.

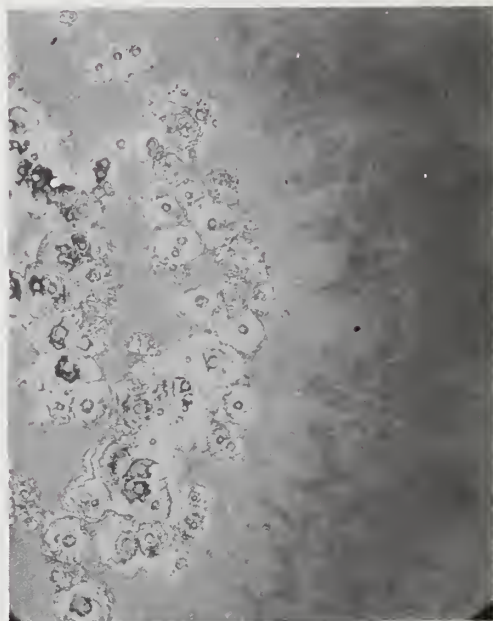


Figure 57. Crater type damage at the edge of a damage area. The sites have basically the same appearance as in the previous pictures but are bigger and in many places coalesced.



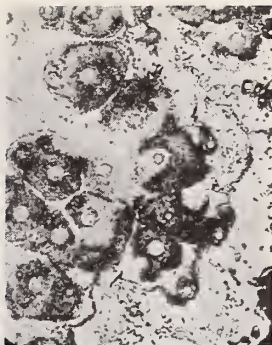


Figure 58. This is a higher magnification picture of the same area as D2 - 64X. The nuclei of the damage sites are very clear in this picture.

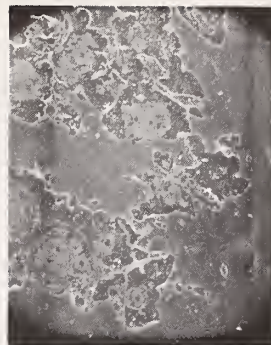


Figure 59. Low magnification SEM picture clearly showing film delamination.

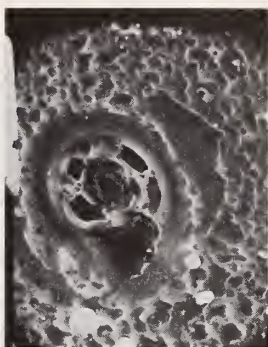


Figure 60. The picture shows a deep crater site extending right through the film system to the substrate; it is possible in this instance to see more extensive damage in some of the films than in others.

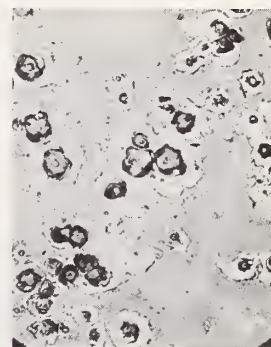


Figure 61. The crater damage pattern is still present in this 3 group (7 layer) multilayer system. It is still more complex than in the previous instances of systems with less layers.



Figure 62. High magnification picture from the same area as the previous picture.



Figure 63. Picture shows distinct evidence of at least one film having been completely fused causing cracks in the adjacent films. The molten film or films are presumably the much weaker ZnS films. The Thorium Fluoride films are cracked and split. Outer 3 films only are affected.

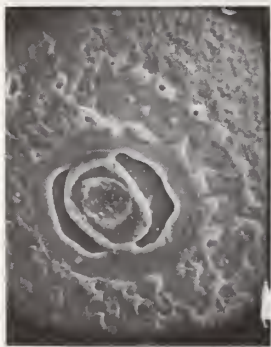


Figure 64. A crater type site showing evidence of preferential fusion of the ZnS films.

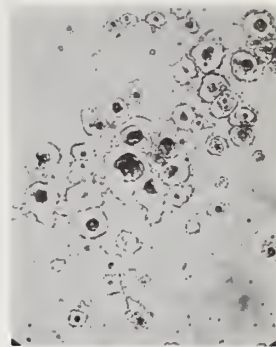


Figure 65. Nine layer system. Damage appearance is similar to D3 - 64X (N) except for the addition of fine cracks.

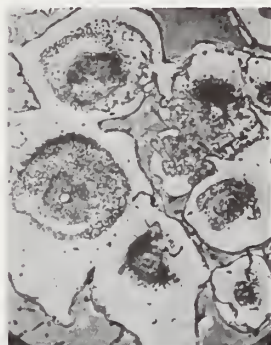


Figure 66. Similar appearance to D3 - 256X (N).

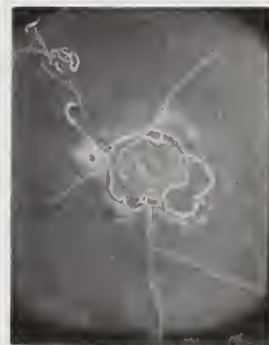


Figure 67. Clear evidence of the failure of internal ZnS films causing mechanical disruption of the outer  $\text{ThF}_4$  film and removal of some internal  $\text{ThF}_4$  films.



Figure 68. Higher magnification picture of the above site.

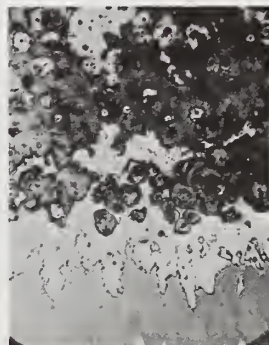


Figure 69. Heavy damage area in a 9 layer system. Many crater sites have coalesced to form a confused pattern.

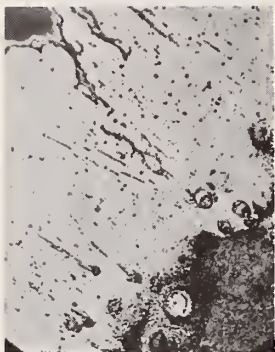


Figure 70. High magnification picture of the edge of the site showing the presence of molten material thrown from within the area.



Figure 71. Low magnification SEM picture of the above area; the ejected molten material is clearly shown.



Figure 72. High magnification SEM picture of the extreme edge of the area. Molten ZnS films and cracked  $\text{ThF}_4$  films can be clearly seen.

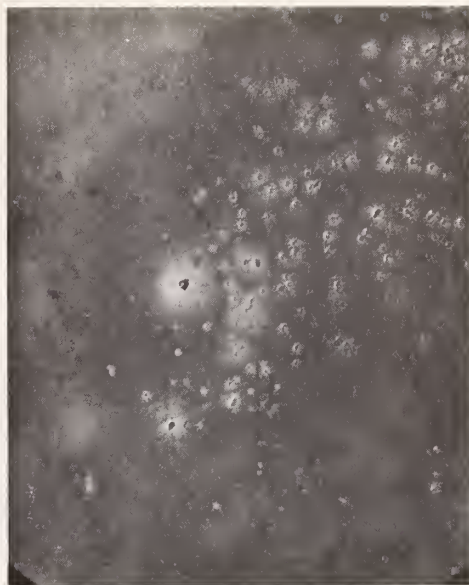


Figure 73. Appearance of damage sites of a 1 cycle PIHF optically equivalent to a one group discrete system. Instead of the crater sites peculiar to the multilayer we observe nuclei with a system of radiating cracks.



Figure 74. This high magnification picture clearly shows the nature of one of the nucleus/crack systems observed above. The nucleus is in fact a very small crater with smooth walls rather than the 'stepped walls' observed in multilayer structures. The remarkable feature of the crack is that it does not penetrate the whole thickness of the film and appears to extend only to the point where thermal failure occurred.





Figure 75. Nucleus crack systems in a 2 cycle film. Some evidence of 'swelling' of the film around the cracks is evident.



Figure 76. Gross damage in the 2 cycle film showing no evidence of the nucleus/crack systems but indicating some evidence of stratification.

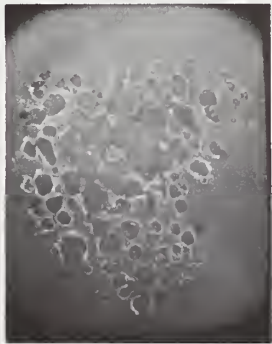


Figure 77. Low magnification SEM picture of an area which appears to show 'delamination' even though the film is continuous and has interfaces only at the substrate and air.



Figure 78. This shows clearly the peeling of an outer portion of the PIH film. It is evident that damage has occurred at a certain depth in the film completely removing any film above it as indicated by the bubbles under the peeling portion of the film which show how the removal is being affected.

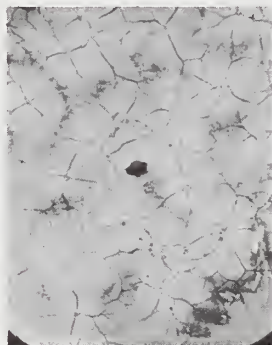


Figure 79. Shows a complex system of nuclei and cracks. It is not clear in this picture whether or not all of the cracks are at the same level in the film.

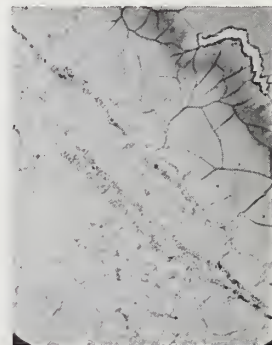


Figure 80. Appearance similar to the previous picture with the addition of concentration of damage sites along a probable fault.

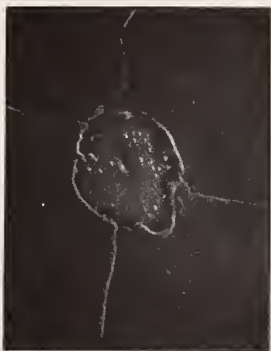


Figure 81. Detail of the nucleus again showing outer surface crack extending only to the level at which damage has occurred.



Figure 82. Detail of the fault time shown in PIHF 7 - 64X (N). The nucleus crack structure is complex and cracking at two different levels in the film is evident. This indicates that damage has occurred simultaneously at 2 different levels in the film.



Figure 83. Complex damage area. Complete removal of the film and complex crack patterns are evident.



Figure 84. Light damage area in the same system.

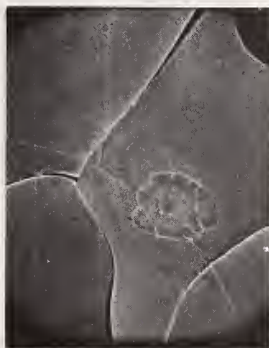


Figure 85. High magnification SEM picture of a portion of PIHF 9 - 64X (N). In addition to complete removal the multilevel damage and cracking is clearly evident.

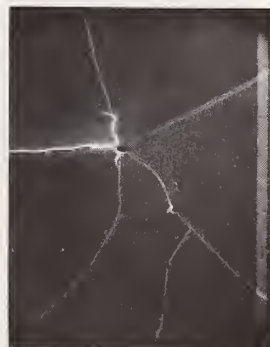


Figure 86. High magnification SEM picture of portion of PIHF 9-256 (N) showing details of fracture initiation sites.



Figure 87. Heavy damage in a 4 cycle PIHF [similar to PIHF 9 - 64X (N)].

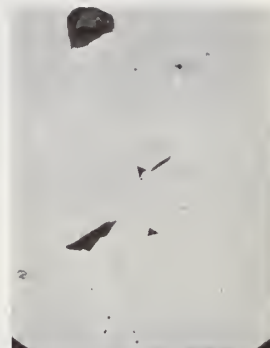


Figure 88. Light damage area in the same system.



Figure 89. Perfect illustration of shear of the PIHF due to damage occurrence at a lower level. The curling of the film demonstrates its tensile property clearly indicating that it is mostly  $\text{ThF}_4$ .



Figure 90. Beautiful illustration of a section of a 4 cycle PIHF. No evidence of stratification or periodicity can be seen. The columnar film growth characteristic is beautifully illustrated. This columnar growth in ZnS crysolite multilayer film systems has been observed by other workers. (6)



# Fundamental Absorption Mechanisms in High-Power Laser Window Materials<sup>\*</sup>

Robert Hellwarth

Department of Electrical Engineering  
University of Southern California  
Los Angeles, California 90007

The thermal deformation and damage to windows and lenses caused by their optical absorption poses serious limitations on the operation of high-power CW and long-pulse lasers. For example, no known materials have both low enough absorption coefficients and good enough mechanical and chemical properties to perform satisfactorily as windows in the large 10.6  $\mu\text{m}$  lasers being developed today. However, very many crystals and glasses would be good candidates for high-power IR windows, if their linear absorption coefficients could be made lower by at least an order of magnitude. Here we review what is known of the physical mechanisms that are responsible for, or may limit, the small residual absorption in the "transparent" wavelength regions of the best candidate window materials. From the primitive state of present knowledge, it seems likely that uncontrolled impurity effects are presently limiting performance in the best window materials, and that therefore their high-power performance can be improved further. We identify theoretical gaps whose filling would greatly improve our understanding of the mechanisms and limits of laser-window absorption.

Key Words: Absorption limit, extrinsic absorption, high-power laser window materials, intrinsic absorption, optical absorption mechanisms, thermal damage.

## 1. Introduction

When a light beam passes through a window (or other optical component), a small fraction of the beam energy is unavoidably deposited as heat in the window material or its coatings. If the beam power, and hence the heat absorbed, exceeds a certain critical value, the window will fail in its function. This failure can take the form either of a reversible thermal deformation which causes an unacceptable degree of phase distortion in the exiting beam, or of an irreversible deformation or even rupture in the window material or its coatings. The limitations on laser power and performance set by the thermal deformations in its windows are a serious problem in the high-power CW and long-pulse  $\text{CO}_2$  lasers presently under development. Given various physical characteristics of a window, one can predict these limitations. Reviews of how these predictions are formulated and their application to some 10.6  $\mu\text{m}$  window materials are given by Sparks in an accompanying paper and elsewhere [1].<sup>1</sup> A more exhaustive assessment of all interesting classes of window materials as potential high-power IR windows has recently been completed by an ad hoc committee of the National Materials Advisory Board [2]. It would appear that no material available at present could be fabricated into a satisfactory high-power 10.6  $\mu\text{m}$  window of the sizes desired ( $> 10$  cm diameter). It is also evident from this work that a critical factor in the performance of a material as a high-power laser window is its absorption coefficient  $\beta$  at the laser wavelength. The main hope for fabricating satisfactory high power windows, both presently at 10.6  $\mu\text{m}$  and probably at other wavelengths in the future, lies in producing materials with lower absorption coefficient than are presently available. At 10.6  $\mu\text{m}$  the best absorption coefficients in the mechanically satisfactory materials are around one percent per cm, and two-orders-of-magnitude lower absorption is desired.

In this paper we review the relatively little that is known of the physical mechanisms that are responsible for the small but troublesome residual bulk absorption in the "transparent" wavelength regions ( $\beta \lesssim 10^{-2}$ ) between the lattice absorption and electronic excitation frequencies. We emphasize the problems most pertinent to the fabrication of better laser windows in the infrared and especially at the  $\text{CO}_2$  laser wavelength of 10.6  $\mu\text{m}$ . In this examination, it is convenient to separate the mechanisms which give rise to this residual absorption into two classes, which we call "extrinsic" and

<sup>\*</sup>Refer to Section 6 at the end of this paper for Support and Acknowledgements.

<sup>1</sup>Figures in brackets indicate the literature references at the end of this paper.

"intrinsic". Extrinsic mechanisms are those associated with unwanted impurity atoms and molecules, deviations from stoichiometry, and also with those lattice imperfections (dislocations, twinning, grain boundaries, etc.) which constitute deviations from a thermal equilibrium state of a glass or crystal. The intrinsic absorption mechanisms are those which give rise to the electronic and vibrational absorptions that would exist in an ideal crystal or glass of some specified composition and possessing the structure and vacancy system appropriate to its ambient temperature. Generally speaking, extrinsic absorption mechanisms appear to be the more troublesome in the best contemporary materials. For example, despite much effort to achieve intrinsic materials for 10.6  $\mu\text{m}$  windows there is no clear-cut case at this writing in which the absorption of a promising window material is in fact intrinsic at this wavelength. Little effort has been applied to understanding the absorption mechanisms at shorter laser wavelengths.

In the next section (2) we review what is known of the dependence of the infrared absorption on extrinsic mechanisms. Then, in section 3 we review the as yet imperfect methods of estimating the intrinsic absorption well below the band gap and above the intrinsic vibrational resonance frequencies. In section 4 we comment on what is known of the corresponding mechanisms underlying the possibly troublesome absorption at surfaces, and also at thin anti-reflection or protective coatings. From these studies, we attempt to identify those areas where better physical understanding would aid in fabricating materials having lower absorption coefficients. These conclusions are given in the final part (5).

We have found that all the important examples of extrinsic and intrinsic absorption, in bulk or on surface, are of three general kinds: a) absorption by vibrational excitations without electronic change of state, b) free carrier absorption, and c) absorption by excitation of bound electrons. Usually, the relevant absorption by each mechanism is the "linear" absorption whose coefficient  $\beta \text{ cm}^{-1}$  is not dependent on the laser or ambient radiation intensity. However, some nonlinear free carrier absorption mechanisms may be important. We now proceed to discuss some of the outstanding problems in each of these areas.

## 2. Extrinsic Absorption Mechanisms

In crystals and glasses of near-ideal structure for a given composition, the small residual absorption due to impurities, dislocations, etc., can be considered as simply a superposition of the absorption from each such imperfection. That is, the absorption per cm  $\beta(\omega)$  is well-approximated at frequency  $\omega$  by

$$\beta(\omega) = \sum_i N_i \sigma_i(\omega), \quad (1)$$

where the sum is over the various types  $i$  of imperfections whose number densities are  $N_i$  and absorption cross sections are  $\sigma_i$ . The processes which give rise to the  $\sigma_i(\omega)$  may be divided into the aforementioned three types which we discuss below: 1) excitation of polar bond vibrations or local modes without electronic excitation, 2) absorption by free carriers donated by impurities, and 3) excitation of bound-electron impurity states.

### 2.1 Excitation of Polar Vibrations

There has been a great deal of experimental and theoretical work on the infrared absorption lines caused by the addition of various impurities to various crystals in various amounts. (See, for example, the review articles of Newman [3] and of Spitzer [4].) The impurities may enter the lattice singly or multiply in a number of different types of configurations. Unfortunately, the impurity atoms or molecules which appear to produce troublesome absorptions at 10.6  $\mu\text{m}$  and other IR laser wavelengths have not yet been studied adequately in the candidate materials for high-power windows. These impurities are primarily oxygen and hydroxyl radicals covalently bonded in various configurations. They typically produce absorption lines in the vicinity of 3, 9, and 13  $\mu\text{m}$  [5,6]. The cross sections  $\sigma_i$  at 10.6  $\mu\text{m}$  for metal-oxygen bond absorptions generally lie in the region of  $10^{-18}$  to  $10^{-20} \text{ cm}^2$ . The absorption cross section of an O-H bond around 3  $\mu\text{m}$  is likely to be of the same order of magnitude.

In any given material and at any specific frequency  $\omega$ , the cross sections of relevant vibrations of these and other impurity atoms, ions, molecules, vacancies, boundaries, precipitates, striations, etc., must be determined by experiment. An excellent review of current work on this is given in reference [7]. Theory can do little more than provide the phenomenological framework of eq (1) and suggest guidelines, such as that various covalent bond frequencies of a given atom or complex do not change much from one host to another.

There is another possible effect of impurities in the low absorption region of crystals, whose importance has not yet been assessed. This is the change in the coupling constants of the electromagnetic field to the intrinsic phonons, and also of the intrinsic phonons to each other, due to the disruption of the lattice periodicity. Since, as we discuss in the next section, the intrinsic



absorption at IR laser wavelengths in the "tail" of a fundamental reststrahl band commonly involves the creation of 4 to 100 optical phonons with the annihilation of one photon, these coupling alterations might well increase absorption. Most importantly, heavy-ion impurities could contribute to this effect as much as the lighter impurities. When an accurate theory of the intrinsic tail absorption becomes available, this type of impurity effect will be easier to assess.

## 2.2 Free Carrier Absorption

Free carriers donated by impurities contribute a term  $\beta_e$  to the optical absorption; this absorption can be correlated roughly with the dc conductivity. Except in very pure nonpolar crystals, the free carrier collision time  $\tau$  is of the order of an infrared period (i.e.,  $\omega\tau \lesssim 1$ ) in which case the infrared conductivity is not orders of magnitude different from the dc conductivity, and the absorption can be approximated by the Drude formula

$$\beta_e(\omega) = \left( \frac{30}{\rho n(\omega)} \right) / (1 + \omega^2 \tau^2) \text{ cm}^{-1}, \quad (2)$$

where  $\rho$  is the resistivity in ohm-cm and  $n(\omega)$  is the real part of the refractive index. Therefore, materials whose resistivity is less than, or of the order of,  $10^3$  ohm-cm usually have not been considered for high-power windows. An important exception is germanium whose  $\tau$  is so large that the best commercially available material (whose impurity concentration is around  $10^{14} \text{ cm}^{-3}$  and dc resistivity is around 20 ohm-cm) has an absorption of only  $0.017 \text{ cm}^{-1}$  at  $10.6 \mu\text{m}$  [8]. This absorption appears to be partly from extrinsic free carriers, but mainly from extrinsic vibrational absorption (probably of oxygen). However, new fabrication techniques for germanium may reduce these absorption components to their intrinsic values, as we discuss in section 3.2.

## 2.3 Excitation of Bound Electronic Impurity States

Heavy impurities generally have their vibration frequencies so low that the wing of their vibrational absorptions contributes negligibly at  $10.6 \mu\text{m}$  and shorter wavelengths. This would typically be the case if  $\sigma_v \lesssim 10^{-23} \text{ cm}^2$  for the vibrational cross section as the impurity density can be kept below  $10^{19} \text{ cm}^{-3}$  and  $\beta \sim 10^{-4} \text{ cm}^{-1}$  is often tolerable. However, heavy impurities might still absorb in the infrared via an electronic absorption tail. The electronic absorption cross section  $\sigma_e$  in the wing of a Lorentzian line of half width at half maximum  $\Delta\omega$  is given by

$$\sigma_e(\omega) = 4\pi f r_o c \Delta\omega [(\omega - \omega_o)^{-2} - (\omega + \omega_o)^{-2}] \text{ cm}^2, \quad (3)$$

where  $r_o$  is the classical electron radius  $2.8 \times 10^{-13} \text{ cm}$ ,  $c$  is the velocity of light, and  $f \sim 1$  is the f-number of the transition. In the infrared,  $\omega \ll \omega_o$ , and

$$\sigma_e \rightarrow 2f r_o \lambda_o \omega / (\omega_o Q) \quad (4)$$

where  $\lambda_o = 2\pi c / \omega_o$  and  $Q = \omega_o / \Delta\omega$  is the "Q" of the transition. It is well known that heavy-ion electronic excitations can have a small Q ( $\sim 10$  to 100, as do the  $\text{Cr}^{3+}$  "pump" transitions in pink ruby which have  $\lambda_o \sim 4000$  and  $5500 \text{ \AA}$ ). Therefore, an electronic "tail" absorption cross section  $\sigma_e$  might reasonably be of order  $10^{-18} \text{ cm}^2$  in the infrared if the line is Lorentzian in its low frequency tail. If so, the tail of the electronic absorptions of heavy-ion impurities might well be an important factor in the material absorption. This would depend largely on whether or not the absorption falls off much more rapidly than a Lorentzian line in the low frequency tail - a question which has not been studied sufficiently in solids.

How the extrinsic absorption of a typical material might dominate the transparent wavelength region of a crystal is shown schematically in the plot of  $\beta$  versus  $\omega$  in Figure 1. Whether or not there are actually bumps in the extrinsic portion of  $\beta$  versus  $\omega$  (as indicated in Figure 1) is not yet known; the absorption below  $10^{-2} \text{ cm}^{-1}$  is too low to have been scanned by conventional techniques. It would obviously be of great value to understanding window material absorption to know the absorption over a wide range of frequencies in this low-absorption region.

## 3. Intrinsic Absorption Mechanisms

At present, very little is known of the fundamental lower limit on the absorption of crystals at wavelengths where they are the most transparent to radiation, i.e., between their electronic absorption edge and their lattice vibration absorption bands. Similarly as for extrinsic absorption, the



mechanisms that may be important in setting the intrinsic absorption limit may be divided into three categories: 1) absorption by lattice vibrations, which the electrons follow adiabatically and in which there is no electronic transition involved; 2) free-electron or free-carrier absorption; and 3) bound-electron absorption. We shall review what is known of each of these mechanisms separately below for both ideal crystals and glasses.

### 3.1 Lattice Vibration Absorption

There have been a number of recent studies of how the infrared absorption drops off as the frequency becomes much greater than the fundamental lattice absorption frequencies, and also becomes much greater than the prominent overtone or combination absorption frequencies [8-10]. These studies have been mainly on the alkali halides and MF<sub>2</sub> crystals. In the more highly purified samples, it appears that the absorption coefficient  $\beta(\omega)$  universally exhibits an exponential fall-off over the lowest two-to-four decades of  $\beta$  that are measurable. That is, for  $\omega \gg \omega_{TO}$ ,

$$\beta(\omega) \propto e^{-\omega/\omega_0}, \quad (5)$$

where  $\omega_0$  is of the order of the reststrahl frequency  $\omega_{TO}$  and varies little with temperature at room temperature [11]. (For example,  $\omega_0 \sim 1/2 \omega_{TO}$  for KBr.)

In some crystals (e.g., Al<sub>2</sub>O<sub>3</sub>, SrF<sub>2</sub>, BaF<sub>2</sub>, LiF, and CaF<sub>2</sub>) the observed absorption at 10.6  $\mu$ m is clearly part of this tail, and therefore probably intrinsic. However, in these cases the absorption at 10.6  $\mu$ m is so high that the crystals are not good window material candidates. It is probable, though not certain, that the observed low absorption at 10.6  $\mu$ m in many of the more interesting candidate materials (KBr, Tl(Br,I), KCl, ZnSe, CdTe, GaAs, and Ge crystals, and chalcogenide glasses) lies above this intrinsic absorption tail, roughly as illustrated in Figure 1. This is certainly the case for the 2-5  $\mu$ m lasers.

Whether this exponential absorption tail is characteristic of all other classes of materials, including glasses and nonpolar crystals, is not yet known. Clearly, it would be desirable to establish some sort of theoretical basis for (5) to understand when, and to how low an absorption this very suggestive behavior obtains.

### 3.2 Free-Carrier Absorption

The theory of 2.2 above and the approximate equation (2) may also be applied to intrinsic free-carrier absorption. The only interesting material for which this may be an important limiting factor at 10.6  $\mu$ m is "ultrapure" Ge. Inch-size ingots of germanium, whose room temperature properties may be intrinsic, have recently become available on a limited basis [12]. Pure Ge has a hole concentration at room temperature of around  $1.5 \times 10^{13} \text{ cm}^{-3}$  and hence a free-carrier absorption of order  $10^{-2}$  at 10.6  $\mu$ m, about fifty percent lower than the best commercial germanium. Whether the total infrared absorption is correspondingly lower is not yet known because there may still be extrinsic or intrinsic lattice absorption of this order of magnitude in these "ultrapure" samples. That intrinsic free-carrier absorption may be reduced further in Ge by n-type compensation is pointed out in reference [11]. In fact the absorption of the best commercial Ge has been successfully reduced by such compensation [11].

It has been suggested that, even if free-carrier absorption is negligible, free-carriers may contribute significantly to absorption below the band gap by interband transitions in semiconductors [13]. The cross sections for such processes deserve further investigation. High intensities at laser and/or visible and ultraviolet frequencies may increase the free-carrier concentration by photo-excitation. The resulting intensity-dependent (nonlinear) absorption has not yet been analyzed.

### 3.3 Bound-Electron Excitation

We need consider only those materials which have a band gap (i.e., minimum nominal energy to excite bound electrons to a conduction band) that is much larger than the laser frequencies of interest. It is, therefore, only the low frequency tail of the fundamental gap absorption that might be of importance in a low-absorption laser window. This tail  $\beta_t(\omega)$  to the fundamental electronic absorption has been observed to be of the form

$$\beta_t(\omega) \propto e^{-\zeta \hbar \omega / k_B T} \quad (6)$$

in a wide variety of ionic, covalent, and amorphous materials. (Here,  $\zeta$  is a constant of the order

unity,  $k_B$  is Boltzmann's constant, and  $T$  the absolute temperature.) This dependence was first noticed by Urbach in alkali halides and has been found to be so widespread that it is called Urbach's rule [13,14]. The most recent and promising of many attempts to construct a theoretical basis for this general behavior is that of Dow and Redfield [15].

In any event, it would seem that we may estimate with some confidence the contribution  $\beta_t$  to the intrinsic absorption from electronic transitions by extrapolating measurements made just below the band gap [16]. The Urbach tail for a typical material is indicated in the  $\beta$  versus  $\omega$  plot of Figure 1. The Urbach tail is so steep that it could produce significant absorption only for those materials whose band gap is not more than  $\sim 20 k_B T$  above the infrared frequency one wishes to transmit.

#### 4. Surface and Coating Absorption

Surface and coating absorption can affect high-power window performance in several ways. The surface heating can cause thermal distortions of the optical phase front. If fragile surfaces, such as of the alkali halides, are subjected to high-power beams, the surface cracks and imperfections may propagate or enlarge, or become hygroscopic. When anti-reflection or passivating coatings are used, surface absorption may tend to dislodge or even evaporate the coatings. The theory of surface and coating absorption may be thought of in terms of the same six categories that we have used in discussing bulk absorption; by vibrational, bound-electronic, or absorption free-electronic excitations of either extrinsic or intrinsic types. We comment separately on problems in 1) surface and 2) thin-film coatings.

##### 4.1 Surface Absorption

There is some evidence that surface absorption by oxygen bonds has been observed near  $2.7 \mu\text{m}$  in various crystals [8]. In this case, we would, as in 2.1, assign an absorption cross section  $\sigma_i$  to the  $i$ th impurity bond type and write the fraction of the beam  $F_S$  absorbed at the surface as

$$F_S(\omega) = \sum_i M_i \sigma_i(\omega) , \quad (7)$$

where  $M_i$  is the number per unit surface area of this type of imperfection. For example, to estimate the surface absorption at  $10.6 \mu\text{m}$  due to a monolayer of oxygen, we suppose that the cross section  $\sigma_i$  is of the order of the bulk absorption cross section ( $\sim 10^{-18} \text{ cm}^2$ ) and the number per unit area  $M_i$  is the two-thirds power of the atomic density of the crystal ( $\sim 10^{15}$ ). In this case we estimate  $F_S$  to be of order  $10^{-3}$ . Although this is a significant fractional absorption in high power applications, it is very difficult to measure with existing techniques. Perhaps if the  $\sigma_i$  could be determined for the important impurities, the more easily measured surface density  $M_i$  would give a useful estimate for the surface absorption  $F_S$  of a given sample.

Both linear and nonlinear absorption by surface free-carriers and surface bound-electron states may well be important, but have received little attention to date.

##### 4.2 Thin-Film Coatings

In addition to introducing extra surfaces, and their associated absorptions, thin-film coatings have a "bulk" absorption that may often be allowed to be significant in order to obtain other characteristics required of a useful coating. Unfortunately, it has become evident that the absorption coefficient  $\beta$  in films is generally much larger than the  $\beta$  for the same nominal material in bulk (see, for example, the article 14 of reference [7]). The real part of the refractive index measured in a film is also different than that measured in bulk. These discrepancies have been observed to be a function of film preparation and the mechanisms responsible are not yet understood [17]. Nonlinear absorption processes are more likely to be important in films than in bulk, but estimates of these have not been made.

#### 5. Conclusions

It is probable that the low, but deleterious, infrared absorption that has been measured in the best candidate materials for high-power laser windows is extrinsic in origin. Therefore, the possibility exists that more careful preparation and purification of these materials will lower their absorption. Unfortunately, the materials with the best thermal and mechanical properties tend to need the most improvement in absorption. From our review of the gaps in theoretical knowledge of mechanisms of absorption, we conclude that a better theoretical grasp of the following facets of the absorption problem would aid the choice and fabrication of a satisfactory high-power infrared laser window. The list is arranged roughly as we see the relative priorities of the theoretical problems to window fabrication.

A practical limit to the improvement in window absorption that is possible in many cases of interest exists by virtue of the nearness of the laser frequency to intrinsic lattice vibrational frequencies and their overtones. The strength of this lattice-absorption tail has been traced experimentally so far mostly in polar crystals, where it has been found to fall exponentially with frequency over the lowest decades of absorption measured. This behavior should be given a theoretical basis from which to predict a) whether the exponential trend persists to lower absorptions, b) how the absorption tail behaves with changing temperature and composition, and c) if this tail is to be expected in other classes of materials, especially glasses and nonpolar crystals.

## 5.2

It is clear how various species of ionic impurities can vibrate to cause "local mode" or bond absorption resonances above the reststrahl bands. However, these impurities may cause a much less obvious raising of the background absorption by virtue of the anharmonicity, disruption of periodicity, and general change in phonon couplings, which they cause. An estimate of the changed background vibrational absorption from these effects should be made.

## 5.3

At the high levels of both the infrared beam intensity and the ambient visible and ultraviolet intensities that high-power infrared-laser windows may have to withstand, photoconductive free-carriers may introduce troublesome added (nonlinear) absorption. From existing data on the wavelength dependence of photoconductivity, theoretical estimates should be made of this effect in candidate materials. These effects of photoexcitation seem to deserve special attention at surfaces and in surface coatings.

## 5.4

Free-carriers, whether extrinsic, intrinsic, or photo-excited, may absorb by interband transitions. Such absorption might well peak near the laser frequency and exceed normal (intraband) free-carrier absorption at wavelengths of interest. Some straightforward band theory ought to provide a prediction as to when such an effect might be important.

## 5.5

The absorption by electrons localized on impurities usually peaks at much shorter than infrared wavelengths. Such absorption commonly has been observed to be so strong at its peak that it may well contribute a small but significant absorption far from resonance at the longer laser wavelengths of interest here. The theory of the shape of these electronic absorption tails on their low frequency side should be developed in analogy with the existing theory of the Urbach tail.

## 5.6

Although many of the discrepancies observed between values of absorption and refractive index in bulk and in thin film can be attributed to "dirt" effects, there may be some intrinsic change occasioned by the forced lattice distortions and proximity of surface states in the films. It would be helpful to the development of window coatings if some rules-of-thumb could be developed to predict the nature of these absorption and index discrepancies.

To this list many other potentially troublesome sources of absorption might be added. Studying such subjects as the formation of color centers, radiation damage, and light scattering from impurities might well expose some important contribution to the eventual amount of heat that will be deposited from a laser in the window material. We can only hope to have uncovered some of the more obvious problems and assessed them cursorily in a study so brief as this.

## 6. Support and Acknowledgements

This research has been supported in part by the Joint Services Electronics Program through the Air Force Office of Scientific Research under Contract F44620-71-C-0067 and in part by the Hughes Research Laboratories, Malibu, California. The results are based partly on work undertaken for the Ad Hoc Committee on High-Power Infrared-Laser Windows of the National Materials Advisory Board. A complete report of this committee's findings is to be published shortly as NMAB Publication 292 (see reference [2]).



## 7. References

- [1] Sparks, M., J. Appl. Phys. 42, 5029 (1971).
- [2] "High-Power Infrared-Laser Window," report of the Ad Hoc Committee on High-Power Infrared-Laser Windows of the National Materials Advisory Board. (Publication NMAB-292, National Academy of Sciences-National Academy of Engineering, to appear August 1972).
- [3] Newman, R.C., Advances in Physics, 18, 545 (1969).
- [4] Spitzer, W.G., Advances in Solid State Physics, (Festkörperprobleme) XI, 1 (1971).
- [5] Nielson and Savage, Infrared Physics, 5, 195 (1965): "Chalcogenide Glasses Transmitting in the Infrared between 1 and 20  $\mu\text{m}$ ."
- [6] Vasko, A., Lezal, D. and Srb, I., J. Non-Crystalline Solids, 4, 311 (1970): "Oxygen Impurities and Defects."
- [7] Proceedings of the Conference on High Power Infrared Laser Window Materials, (Oct. 1971). Ed. by C.S. Sahagian and C.A. Pitha (Air Force Cambridge Research Laboratories, Special Report No. 127, Dec. 1971).
- [8] Horrigan, F.A. and Deutsch, T.F., Final Technical Report, Contract No. DAAH01-70-C-1251, (Sept. 1971), "Research in Optical Materials and Structures for High-Power Lasers," Raytheon Research Division.
- [9] Genzel, L., Fest Körper Probleme, 6, 32 (1967), "Optische Absorption von Fest Körpern durch Gitterschwingungen."
- [10] Joos, G., reproduced in Introduction to Solid State Physics (4th edition) by C. A. Kittel, (John Wiley, New York, New York, 1970), p. 155, from FIAT Rev. Ger. Sci. (1939-1946) Part II: The Physics of Solids, "Optische Eigenschaften der Festen Körper."
- [11] Horrigan, F. A. and Rudko, R.I., Final Technical Report, Contract DAAH01-69-C-0038, Raytheon Research Division, (September 1969), "Materials for High Power  $\text{CO}_2$  Lasers."
- [12] Hall, R.N., General Electric Research and Development Center, Schenectady, New York. (Private Communication.)
- [13] Briggs, H.B. and Fletcher, R.C., Phys. Rev. 91, 1342 (1953); Kahn, A.H., Phys. Rev. 97, 1647 (1955); Wiley, J.D. and DiComenico, Jr., M.D., Phys. Rev. B3, 375 (1971).
- [14] Urbach, F. Phys. Rev. 92, 1324 (1953). For a review of Urbach's rule, see J.J. Hopfield Comments on Solid State Physics, 1, 16 (1968).
- [15] Dow, J. D. and Redfield, D., Phys. Rev. Letters, 26, 762 (1971), "Theory of Exponential Absorption Edges in Ionic and Covalent Solids."
- [16] Martienssen, W., J. Phys. Chem. Solids, 2, 257 (1957).
- [17] Young, P. A., Thin Solid Films, 6, 423 (1970); Young, P. A. and Thege, W. G., J. Phys. Soc., London, D4, 64 (1971).

## 8. Figures

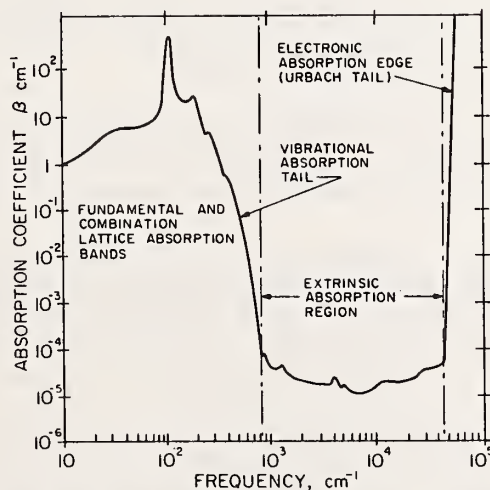


Figure 1. Schematic plot of the optical absorption coefficient  $\beta$  versus optical frequency for a typical material that would be a good candidate for a high-power-laser window by virtue of its low extrinsic absorption ( $\beta < 10^{-4}$ ). The extrinsic-absorption-region spectrum of a good window material has never been scanned and is drawn here entirely from imagination. As is discussed in the text, the exponential forms of the intrinsic vibrational absorption tail and the electronic absorption tail appear to be universal.

M. Sparks

Xonics, Incorporated, Van Nuys, California 91406

The problem of failure of high-power infrared laser-system windows involves low intensities (a few hundred to a few thousand  $\text{W/cm}^2$ ). Thermally induced distortion of the optical beam by a heated window and thermal fracture have been considered previously. Pressure-induced optical distortion is discussed. For large-diameter windows of weak materials, the minimum window thickness is determined by pressure-induced optical distortion, rather than by pressure-induced fracture. Previous figures of merit for rating candidate window materials assumed a constant thickness of 1 cm for all materials. New figures of merit, based on the minimum thickness required to withstand a given pressure, indicate a different preference for materials than that of the previous figures of merit.

It is not known if the measured values of the optical absorption coefficient  $\beta$  for candidate materials are extrinsic or intrinsic. The intrinsic value of  $\beta$  is needed in order to determine if material-improvement programs could produce materials with sufficiently low values of  $\beta$ . Information on extrinsic processes is needed in order to identify the sources of the extrinsic contributions to  $\beta$  so that they may be removed. Measurements of  $\beta$  over ranges of frequency and temperature should be invaluable in obtaining this information. Feasibility studies indicate that emissivity measurements should yield the required values of  $\beta$ , which cannot be obtained by current transmission or calorimetric measurements.

Key Words: Infrared absorption, infrared laser systems, thermal fracture, window materials.

The availability of high-power infrared lasers during the last few years has caused a shift of interest in infrared window material. For low-power applications, previous interest was in the so-called cut-off wavelength, at which a material becomes opaque, roughly speaking. For a 1 cm-thick sample, absorption becomes measurable in transmission when the optical absorption coefficient  $\beta$  reaches a value of  $\beta \cong 0.01 \text{ cm}^{-1}$  (approximately one percent absorption). For low-power applications, the absorption of several percent of the incident power usually is tolerable.

For currently envisioned high-power applications, the absorption of even a small fraction of one percent of the incident power can cause the window to melt, fracture, distort the laser beam or otherwise cause the system to function improperly. Thus, values of  $\beta$  at least as low as  $10^{-4} \text{ cm}^{-1}$  are of current interest. As more powerful lasers become available, even smaller values of  $\beta$  will be needed.

The chief current interest in high-power infrared window materials is in obtaining a sufficiently low value of  $\beta$  for materials that are otherwise satisfactory. Alkali halides have the lowest values of  $\beta$ , but they have poor physical, thermal, and chemical properties. Semiconductor materials have good physical, thermal, and chemical properties, but only fair optical properties, while glasses have good chemical and physical properties, but poor thermal and optical properties.

Before considering several interesting results from the past year, recall the effect of thermally induced optical distortion.<sup>[1]</sup> As illustrated in figure 1, an incident laser beam having greater intensity at the center of the window causes a greater temperature rise at the center than at the rim of

---

\*This research was supported by the Advanced Research Projects Agency of the Department of Defense and was monitored by the Defense Supply Service - Washington under Contract No. DAHCl5-72-C-0129.

<sup>1</sup>Figures in brackets indicate the literature references at the end of this paper.

the window. The bulging of the window and the change in the index of refraction cause the window to become a lens with finite focal length and nonzero aberration. This effect is severe in long-focal-length systems since small angular deviations (10 microradians in figure 1) can cause significant degradation in the intensity at the target.

A similar effect is caused by a pressure differential across the window. The bowing of the window caused by the pressure gives rise to optical distortion. At the suggestion of H. V. Winsor [2], M. Sparks and M. Cottis [3] examined the pressure-induced optical distortion-problem. A simple solution of the mechanical-deformation problem indicates that the window displacement  $w$  contains terms proportional to  $\rho^2$ ,  $\rho^4$ , and  $\rho^6$ , where  $\rho$  is the radial coordinate (see figure 2). The  $\rho^2$  and  $\rho^4$  terms were considered because the optical distortion for these terms is known. [1] The effects of the two terms are of the same order of magnitude, but the  $\rho^4$  term causes slightly more distortion. The  $\rho^6$  term was formally neglected since the optical analysis for this term has not been made. A straightforward calculation was performed to determine the values of thickness  $l$  at which an originally diffraction-limited target spot is reduced in intensity by a factor of two.

The results are illustrated in table 1. The first column of figures on the left shows the value  $l_f$  of window thickness required to keep the window from fracturing under pressure  $P = 7.3$  psi with a safety factor of 4. The values of  $l_o$  in the three right-hand columns are those required to keep the pressure-induced optical distortion from halving the target intensity. The minimum value of  $l$  is the greater of  $l_f$  and  $l_o$ . An underscored value of  $l_o$  indicates that  $l_o > l_f$ . For example, in order to prevent optical distortion from halving the target intensity, a 100 cm-diameter window of GaAs must be 3.18 cm thick, which is larger than the value of 1.65 cm required to keep the window from fracturing. The minimum value of  $l$  is 3.18 cm. A 1 cm-diameter window of GaAs must be at least 0.165 cm thick, which is larger than the value of 0.126 cm required to keep the pressure-induced optical distortion from halving the target intensity. The thickness of large-diameter windows of strong materials is limited by pressure-induced optical distortion, while the thickness of small-diameter windows of weak material is limited by pressure-induced fracture. Great thicknesses are required for the alkali halides; a 100 cm-diameter window of KBr with minimum thickness of 18.5 cm weighs 880 lbs.

A second effect of pressure is to modify the previous figures of merit of window materials. In the figures of merit for thermally induced optical distortion, it was assumed that all materials were 1 cm thick. [1] C. M. Stickley [4] pointed out that weaker materials require greater thicknesses, thereby causing greater optical distortion. New figures of merit have been obtained by replacing the value of  $l = 1$  cm by  $l_f$  or  $l_o$ , whichever is larger. The results are given in table 2. Here the figure of merit is defined simply as the average value of intensity the window can withstand without thermal fracture (second column of figures) or undue thermally induced optical distortion (last three columns). The listed values of the figures of merit apply only under the following conditions: diameter  $D = 10$  cm,  $P = 7.3$  psi, wavelength  $\lambda = 10.6$   $\mu\text{m}$ , and safety factor  $F_s = 4$ . The underscored value of 3.76  $\text{kW/cm}^2$  for ZnSe indicates that the intensity which can be transmitted without undue thermally induced optical distortion is less than the intensity at which the window fractures thermally. The underscored value of 3.02  $\text{kW/cm}^2$  for KCl indicates that a 10 cm-diameter window of KCl fractures thermally before the thermally induced optical distortion becomes severe.

The materials in table 2 are arranged in the order of decreasing magnitude of these underscored values. This preference of materials is different from the previous one which was based on the values of intensity for 1 cm-thick materials. For example, ZnSe is first in the current rating compared with fourth in the previous rating. Potassium bromide is on the bottom of the present list because the demonstrated value of  $\beta$  has been used. If the estimated value of  $5 \times 10^{-5} \text{ cm}^{-1}$  is used, KBr is at the top of the current list. It should be emphasized that in general the rating is changed when the values of diameter, wavelength, pressure, and safety factor are changed. For example, increasing the diameter from 10 to 100 cm and the pressure from 7.3 to 14.7 psi and decreasing the safety factor from 4 to 1 increases the ratio  $\langle I \rangle_{l_f} / \langle I \rangle_{t_f}$  by a factor of 28.

There has been an increased interest in alkali-halide materials based on the belief that these materials can be strengthened and coated to protect them from the atmosphere. There are several methods of increasing the strength of the alkali halides, including fabrication of polycrystalline materials with small grains and internally formed grain boundaries, using solid solutions such as KCl-NaCl, or adding impurity ions such as Sr to crystals such as KBr. Assuming that the strengthening and coating is successful, the crucial question remaining is whether these processes will increase the optical absorption to unacceptable values.

Large ( $\sim 15 \times 15$  cm) samples of chemical-vapor-deposited polycrystalline ZnSe with  $\beta = 0.004 \text{ cm}^{-1}$  were grown by Raytheon under contract to the Air Force Materials Laboratory. [5] This value of  $\beta$  is an order of magnitude lower than the previous experimental value but is still not sufficiently low for many high-power applications. There are three cardinal questions concerning ZnSe. Is the value of  $\beta = 0.004 \text{ cm}^{-1}$  intrinsic (already at the basic physical limit) or extrinsic? If it is extrinsic, what imperfection causes  $\beta$  to be greater than its intrinsic value? If extrinsic, what is the intrinsic value? If the current value of  $\beta$  is intrinsic, no material-improvement program to reduce the value of  $\beta$  can succeed. If the value is extrinsic, an estimate of the intrinsic value is needed in order to determine if a material-improvement program could in principle yield the value of  $\beta$  required in a particular application.



Table 1. Minimum Window Thickness

Material	Fracture $10^{-2} \ell_f/D$	Pressure-induced optical distortion $10^{-2} \ell_o/D$		
		D = 1 cm	D = 10 cm	D = 100 cm
ZnSe	3.00	1.23	1.96	<u>3.10</u>
CdTe	8.03	1.66	2.63	4.17
GaAs	1.65	1.26	<u>2.00</u>	<u>3.18</u>
Ge	2.01	1.24	1.96	<u>3.10</u>
KCl	12.9	1.40	2.21	3.51
KBr	18.5	1.49	2.36	3.74
NaCl	12.5	1.25	1.99	3.15
KRS-5 (TlBr-TlI)	3.80	2.23	3.53	<u>5.60</u>
Ge <sub>28</sub> Sb <sub>12</sub> Se <sub>60</sub> glass	4.27	1.84	2.92	<u>4.63</u>

Table 2. Figures of merit for pulse mode in 10 cm diameter windows

Material	Measured values of $\beta$ in $\text{cm}^{-1}$	Thermally induced optical distortion			
		Thermal fracture $\langle I \rangle_{\text{tf}}$ $\text{kW}/\text{cm}^2$	$\ell$ by pressure fracture $\langle I \rangle_{\ell_f}$ $\text{kW}/\text{cm}^2$	$\ell$ by pressure distortion $\langle I \rangle_{\ell_o}$ $\text{kW}/\text{cm}^2$	$\ell = 1 \text{ cm}$ (previous f of m) $\langle I \rangle_{1\text{cm}}$ $\text{kW}/\text{cm}^2$
ZnSe	$5 \times 10^{-3}$	20.4	<u>3.76</u>	5.76	1.13
KCl	$4.8 \times 10^{-4}$	<u>3.02</u>	37.8	220.	48.8
CdTe	$1.5 \times 10^{-3}$	14.6	<u>1.07</u>	3.25	0.859
NaCl	$1.3 \times 10^{-3}$	<u>0.971</u>	23.1	145.	29.0
GaAs	$5 \times 10^{-3}$	40.5	1.15	<u>0.949</u>	0.190
KRS-5	$5 \times 10^{-3}$	3.62	<u>0.377</u>	0.406	0.143
Ge <sub>28</sub> Sb <sub>12</sub> Se <sub>60</sub> glass	0.02	1.56	<u>0.171</u>	0.251	0.073
Ge	0.025	4.9	<u>0.149</u>	0.154	0.030
KBr	$4 \times 10^{-3}$	<u>0.144</u>	3.75	29.6	6.98

Knowledge of the source of the extrinsic value of  $\beta$  would change the material-improvement program from a cut-and-try experiment to one of removing the known imperfection. These three key questions actually apply to every material of current interest, not just to ZnSe.

It appears that we are now in a position to obtain answers to these questions by a joint theoretical and experimental program. In figure 3, the heavy curve and the heavy dot at  $10.6 \mu\text{m}$  are experimental values obtained at 300 K, and the remaining portion of the curve is a schematic illustration of the remainder of the absorption curve. There is a region of very small intrinsic absorption bounded by the fundamental lattice peak and the electronic absorption edge. At sufficiently small values of intrinsic absorption,  $\beta$  is expected to be dominated by extrinsic processes, as illustrated schematically on the figure.

To illustrate how the three questions above would be answered, assume that the schematic illustration in figure 3 is the experimental result. The different character of the curve to the right and left of  $\omega/\omega_f \approx 6$  suggests that the curve to the left is intrinsic and to the right is extrinsic. This can be verified by measuring the temperature dependence, which is well understood for the intrinsic multiphonon absorption. The temperature dependence illustrated in figure 3 suggests that identification of the transition from intrinsic to extrinsic behavior was correct. The temperature and frequency dependence of the extrinsic processes is needed in order to identify the physical sources of the absorption coefficient in the extrinsic region.

Sufficient power to perform calorimetric measurements is not available at all frequencies of interest. Transmission measurements cannot yield values of  $\beta$  below approximately  $10^{-2} \text{ cm}^{-1}$  for 1 cm-thick samples. Thus, the light curve to the right of  $\omega/\omega_f \approx 6$  cannot be obtained by calorimetric or transmission measurements. However, preliminary calculations indicate that it should be possible to obtain these values of  $\beta$  by emissivity measurements. These calculations indicate that values of  $\beta = 10^{-5} \text{ cm}^{-1}$  and possibly even lower can be measured by the emissivity technique.

The recent shift of interest to very small values of the absorption coefficient and the possibility of measuring these small values by emissivity measurements suggest a greatly increased use of emissivity measurements over the next few years.

### References

[1] Sparks, M., J. Appl. Phys. 42, 5029 (1971).

[2] Winsor, H. V., AFWL, Kirtland Air Force Base, New Mexico, private communication.

[3] Sparks, M. and Cottis, M., "Pressure-Induced Optical Distortion in Laser Windows," unpublished.

[4] Stickley, C. M., Advanced Research Projects Agency, Washington, D. C., private communication.

[5] Donlan, V., Air Force Materials Laboratory, Dayton, Ohio, private communication.

Figures

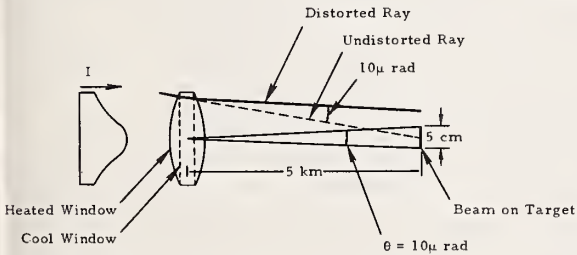


Figure 1. Thermally induced optical distortion

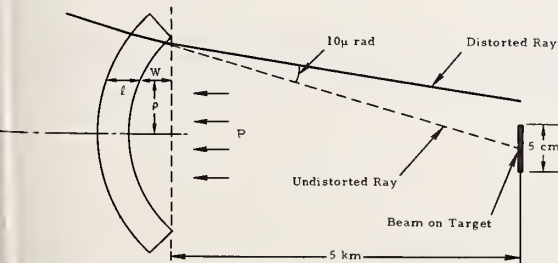


Figure 2. Pressure-induced optical distortion

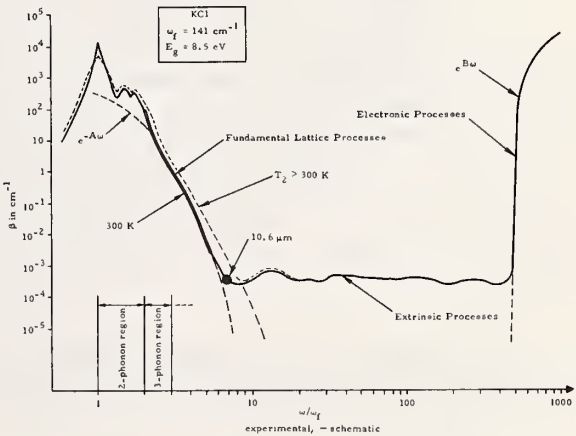


Figure 3. Study to determine intrinsic and extrinsic values of  $\beta$

Low Emittance and Absorptance Measurements  
of Windows and Mirrors

Geert Wijntjes  
Norman J.E. Johnson  
J. Morris Weinberg

Block Engineering, Inc.  
19 Blackstone Street  
Cambridge, Massachusetts 02139

A cryogenic interferometric spectrometer has been developed which can achieve a noise equivalent spectral radiance (NESR) of  $1.2 \times 10^{-11}$  watts/cm<sup>2</sup>-ster-cm<sup>-1</sup> at 10  $\mu$ m in 10 seconds of integration, with spectral resolution of 1 cm<sup>-1</sup>.

The application of this instrument to the measurement of low level emittance or absorptance in optical elements is described. In such measurements, the specimen is kept at 300°K and its surroundings at 77°K. The measurement is limited by the sensitivity of the instrument, the accuracy of the specimen temperature measurement, and the dynamic range of the measurement. The first limitation is expressed by the noise equivalent spectral emittance.

$$(NE\Delta\epsilon)_v = \frac{NESR}{R_v^0(T)}$$

where  $R_v^0(T)$  is the blackbody radiance at temperature  $T$ . With reasonable integration times the determination of emittance is feasible to a precision approaching a part in  $10^7$ , which represents the fundamental limitation to such measurement. The other limitations are proportional to the average emittance over the spectral range considered, and for average emittances below 0.01, permit absolute emittance measurements to a few parts in  $10^6$ . The high spectral resolution of this instrument permits examination of absorption band structure in substrate and coating materials, and the identification of contaminant organic materials. The measurement of bulk scattering in transmissive materials is also possible.

Key Words: Absorptance measurement, bulk scattering, coating measurement, emittance measurement, infrared absorptance, laser damage.

## 1. Introduction

The advent of high power infrared lasers with the requirement of high reflectivity mirrors and high transmission windows places crucial emphasis on precise measures



of the weak absorptance of such optical elements. Sparks<sup>[1]</sup> described how significant optical distortion is produced by distributed heating resulting from bulk absorption. Localized heating due to impurities can result in serious damage to optical elements and antireflection coatings. These phenomena may be difficult to evaluate at infrared wavelengths using contemporary techniques; e.g. an absorptive particle embedded in a visually opaque window may become the nucleus of a destructive hot spot, while its effect on the overall transmission may be less than one part in ten thousand. This paper describes an advanced technique for the determination of the spectral absorptance of such optical elements to a precision of one part per million in the 6 - 14 micron region, as well as means of evaluating the bulk scattering of transmissive elements.

A cryogenic interferometric spectrometer has been developed by Block Engineering, Inc. for the NASA Manned Spacecraft Center, which operates at liquid nitrogen temperature (77°K) with a detector cooled to liquid helium temperature (5°K). This instrument has a spectral range of 5 - 15 microns with a constant highest spectral resolution of 0.5  $\text{cm}^{-1}$  over the spectral range. A single scan produces an interferogram in approximately 0.5 seconds, providing information to produce the complete spectrum. Commonly, many scans are made and accumulated in computer storage or on tape to reduce noise in the interferogram and the resulting spectrum. The Fourier transformation of an interferogram to a spectrum is performed by a computer, which can also subtract the background radiation spectrum from that of the combined source and background radiation spectrum. Typically, a transformation utilizing 2K of core memory takes about 15 seconds, and the spectrum can be computer plotted linearly with wavelength or wave-number.

The instrument was calibrated in a cold chamber at Arnold Engineering Development Center (AFSC). On the basis of this calibration, an NESR of  $1.2 \times 10^{-11}$  watts/ $\text{cm}^2\text{-ster-cm}^{-1}$  can be realized in practice at 10 microns in a ten second integration time, with a spectral resolution of 1  $\text{cm}^{-1}$  (0.01 microns at 10 microns). The development of a cryogenic interferometer with this performance capability permits the evolution of techniques, such as those described here, to new levels of refinement.

## 2. Technique

As shown by Stierwalt and Potter<sup>[2]</sup>, the measurement of emission is an effective way to determine the absorptance of optical materials. In their method, the spectral radiance of a specimen at a known and controlled temperature is measured with a prism spectrometer relative to the radiance of a blackbody source at known temperature. The resulting difference between specimen and blackbody reference radiance is a direct measure of the specimen's emittance, and thus its absorptance. No indication of the precision of their measurements was given, but this is clearly a function of the precision with which the temperature and emittance of the blackbody reference and the temperature of the specimen are known, and of the sensitivity of the detector.

The great superiority of interferometric spectrometers to dispersive spectrometers lies in the multiplex ( Fellgett's) advantage. This gain can be realized by commercially available instruments at infrared wavelengths in the 10 micron region, together with the built-in computing capability provide immediate spectrum integration and transformation. The application of this type of instrument to emittance measurements provides a great increase in sensitivity without sacrifice of spectral resolution. Further gains in sensitivity are possible by cooling the interferometer to a temperature such that its own radiation for the particular wavelength region approaches zero. Cooling also increases detector sensitivity by as much as three orders of magnitude and, if one cools the specimen chamber as well, the sole remaining source of radiation is the specimen.

---

<sup>1</sup> Figures in brackets indicate the literature references at the end of this paper.

The sensitivity of a spectrometer can be expressed in terms of its noise equivalent spectral radiance

$$\text{NESR} = \frac{\text{NEP}}{\theta_i \eta_i \sqrt{T} \delta \nu} \text{ watts/cm}^2 \text{ ster cm}^{-1}.$$

Where the NEP is the effective noise equivalent power for the detector,  $\theta_i$  is the optical throughput (area x solid angle) and  $\eta_i$  the optical efficiency of the interferometer,  $T$  is the total time for  $N_s$  scans of the spectrum, and  $\delta \nu$  is the spectral resolution of the instrument in wavenumbers ( $\text{cm}^{-1}$ ). We may describe the NESR as the spectral radiance giving unity signal-to-noise ratio averaged over the time  $T$  of the measurement. (The use of wavenumber rather than wavelength here is common in interferometry and results in some simplification of expression.) The spectral radiance of the specimen is defined in terms of a blackbody as

$$R_\nu(T) = \epsilon_\nu R_\nu^0(T) \text{ watts/cm}^2 \text{ ster cm}^{-1}$$

where  $R_\nu^0(T)$  is the spectral radiance of a blackbody at temperature  $T$  and  $\epsilon_\nu$  is the spectral emittance of the specimen. The minimum detectable emittance difference is then

$$(\text{NE} \Delta \epsilon)_\nu = \frac{\text{NESR}}{R_\nu^0(T)}$$

The noise equivalent emittance is shown in figure 1 as a function of wavenumber for an interferometer equipped with a HgCdTe detector cooled to 77°K viewing a 300°K specimen. The interferometer is uncooled, and it is assumed that the detector views a 300°K background. (It would be necessary, of course, to provide a cooled background behind transmissive and in front of reflective specimens in order to distinguish the specimen emittance.)

In figure 2, the noise equivalent emittance is given for an interferometer equipped with a Ge:Hg detector cooled to 5°K. The interferometer and blackbody background are cooled to 77°K, while the specimen is maintained at 300°K. The dramatic improvement here can be achieved in practice because the 77°K background (shown by the dashed line) can be subtracted from the measured spectral emittance as indicated, permitting emittance differences smaller than a part in a million to be measured.

System sensitivity is fundamentally limited by detector noise, arising both from background radiation (photon noise) and from noise mechanisms within the detector itself. Modern cooled infrared detectors have internal noise equivalent powers ( $\text{NEP}_i$ ) of  $10^{-13}$  to  $10^{-14}$  watts, and are photon noise limited for backgrounds at elevated temperatures. The multiplex advantage of the interferometer is not fully realized until the detector is limited by internal noise and no further improvement is possible by reducing background radiation. The point at which the transition occurs, for a photoconductor, may be characterized by the product

$$\bar{\epsilon}_\nu (\nu_2 - \nu_1) \leq G_i = \frac{1.259 \times 10^{22} (\text{NEP}_i)^2 q_e}{\nu_0 \theta_i \eta_i R_\nu^0(T)} \text{ cm}^{-1}.$$

Here  $q_e$  is the detector quantum efficiency,  $\nu_1$  and  $\nu_2$  the limits of the spectral band,  $\nu_0$  the band center, and  $R_\nu^0(T)$ , assumed to vary slowly, is averaged over the band. Typically the factor  $G_i$  is about 0.1, and the compromise between average emissivity and spectral band is obvious. Figure 3 shows the optimization of a spectral band for emissivity measurement. As the spectral interval is increased beyond  $\nu_1$  and  $\nu_2$ , both  $\bar{\epsilon}_\nu$  and  $(\nu_2 - \nu_1)$  are increasing, and  $G_i$  is easily exceeded.

The absolute accuracy of an emittance measurement is related primarily to the error in the evaluation of the temperature of the specimen. From the Planck radiation law, one can obtain

$$\frac{\Delta \epsilon_T}{\epsilon_\nu} = \left[ \frac{x}{1 - e^{-x}} \right] \frac{\Delta T}{T} \text{ where } x = 1.438 \nu/T.$$



At 1000  $\text{cm}^{-1}$  (10 microns), with a 300°K specimen, the factor  $x/(1-e^{-x})$  is 4.83, showing the sensitivity of this factor. For a specimen with good thermal conductivity or very low overall emittance, however, it should be possible to reduce  $\Delta T/T$  to better than a part in ten thousand. The spectral emittances at different wavelengths are as precise as indicated in figure 2, relatively speaking.

For the curves, a spectral resolution of 1  $\text{cm}^{-1}$  was assumed, corresponding to 0.01 microns at 10 microns. This is in excess of the line spacing of a  $\text{CO}_2$  laser, which is about 1.6  $\text{cm}^{-1}$ , and is sufficient to allow identification of oil and aerosol contaminants. An integration time of 40 seconds was arbitrarily assumed as a reasonable period in which to obtain complete spectral information over the 6-14 micron region considered.

The values of NESR used to obtain these curves are based on calibrations of actual interferometers built at Block Engineering, Inc. The NESR and  $(NE\Delta\epsilon)_v$  can be improved linearly by decreasing the resolution, and as the square root by increasing the integration time. One can also heat the samples to a higher temperature, increasing their radiance and improving the emittance measurement at shorter wavelengths. Better detectors have recently become available for low background applications, offering improvement in sensitivity by more than a factor of five and providing a limiting value for  $(NE\Delta\epsilon)_v$  approaching  $10^{-7}$ .

For practical reasons, the total dynamic range of measurement is limited relative to the amplitude of the average radiance in the spectral band, giving the emittance uncertainty

$$\Delta\epsilon_R = \frac{\overline{\epsilon_v} R_v^0(T) (\nu_2 - \nu_1)}{R_v^0(T) \delta\nu 2^M \sqrt{N N_s}} = \frac{\overline{\epsilon_v}}{2^M} \sqrt{\frac{N}{N_s}}$$

where M is the number of bits in the digitization and N is the number of resolution elements  $\delta\nu$  in the spectral interval. (Other limitations in practice exist, but this probably gives a better feeling for the nature of the limitation.) The range of the emissivity measurement can be reduced to give full  $(NE\Delta\epsilon)_v$  sensitivity at emissivities of greatest interest. The spectral range can also be reduced, which can provide similar improvement to that discussed earlier in reference to figure 3.

We may compare these factors in the measurement of a  $300^\circ \pm 0.03^\circ\text{K}$  specimen in 40 scans with a 14 bit digitization and 1  $\text{cm}^{-1}$  resolution:

	$\lambda_2 - \lambda_1$	$\overline{\epsilon_v}$	$\epsilon_v (\nu_2 - \nu_1)$	$\Delta\epsilon_T$	$\Delta\epsilon_R$
Case A	6-14 $\mu\text{m}$	0.5	476.0 $\text{cm}^{-1}$	$2.4 \times 10^{-4}$	$1.5 \times 10^{-4}$
Case B	10-11 $\mu\text{m}$	0.01	0.91 $\text{cm}^{-1}$	$4.8 \times 10^{-6}$	$9.2 \times 10^{-7}$
Case C	10.55-10.65 $\mu\text{m}$	0.01	0.09 $\text{cm}^{-1}$	$4.8 \times 10^{-6}$	$1.4 \times 10^{-7}$
Case D	10.55-10.65 $\mu\text{m}$	0.002	0.02 $\text{cm}^{-1}$	$9.6 \times 10^{-7}$	$2.8 \times 10^{-8}$

The reduction of the spectral band is usually accomplished by placing a cooled narrow band filter between the detector and the interferometer. Clearly any spectral band within the limits of the detectors spectral response could have been chosen simply by changing the filter, however, the interferometer can be optimized for a given band.

### 3. Instrumentation

The generalized measurement technique is shown in figure 4, where a large vacuum chamber contains a cooled inner chamber in which the interferometer is mounted. The detector, mounted in its own dewar, views the specimen through the interferometer. An aperture, which defines the interferometer field of view, permits examination of the specimen while shielding the specimen support and heater from the interferometer. Behind the specimen is a blackbody calibration source, which is maintained at the 77°K background temperature during specimen measurement. This blackbody provides the transmitted radiation through the specimen, while the cold interferometer itself provides the reflected radiation. The system is calibrated by measuring this blackbody emission with the specimen removed. Generally, the calibration would be made with a cold grid in front of the blackbody to provide a precise attenuation of its radiation (probably 300°K). If it is desirable to examine small areas of the specimen, several scanning techniques are possible. A sliding cold mask with a small aperture could be used with some performance degradation, or the more complicated optical system suggested in the



figure, which would preserve optical throughput and system sensitivity could be incorporated.

The most critical aspect of these measurements is the support, heating, and temperature measurement of the specimen. As indicated earlier, the temperature of the specimen must be uniform over its clear aperture, stable during the measurement process, and measurable to a high degree of accuracy. The problem is simplified for mirrors which are opaque throughout the spectral region of interest, since support and heating can be accomplished from the back. Windows must be supported and heated at their edges by structure providing a minimum of extraneous radiation. One possible design utilizes a thin polished silver or aluminum tube, within which runs a heater wire and one or more temperature sensing elements. This tube nearly encircles the specimen, maintaining good thermal contact with it, and is attached to the wall at its ends. Another technique utilizes a number of blunt tipped, polished metal support and heater fingers which press radially against the specimen. If the specimen has poor thermal conductivity, induction, laser, or electron beam heating may be necessary in addition. The use of a laser of the type for which the specimen is intended may provide some useful information regarding the dynamic behavior of absorptance, with the laser turned on between scans of the interferometer.

Bulk scattering in windows may be evaluated by placing a highly emissive strip around the outer edge of the specimen, providing approximate blackbody radiation outside of the interferometer field of view. If external reflections have been carefully eliminated, the only significant contribution from this radiation source will be through scattering within the specimen. It should be noted that the representation in the figure is not intended as a working design, e.g., provision would be made for the removal of the specimen without re-evacuating and re-cooling the interferometer chamber.

#### 4. Measurement Error

The primary source of error arises in radiation from the heater support which may enter through multiple reflection, specimen surface scattering, and specimen bulk scattering. These effects may be minimized by keeping the heater area small relative to the sample aperture, and by providing the lowest possible surface emissivity for the structure. For an encircling ring heater, the ratio of areas effective is approximately  $4t/d$ , where  $t$  is the width of the heater element and  $d$  is the specimen diameter. The emissivity of the heater support can be reduced to 0.05 or less fairly easily.

The reduction of leakage radiation around the edges of the specimen and off the background blackbody (for a window) is essentially a problem in geometry. A reduction of  $\sum_n A_i r_i \Omega_i$  is achieved by  $n$  reflections of effective area  $A_i$  and effective solid angle  $\Omega_i$  for each surface of reflectance  $r_i$ . No difficulty should arise in reducing this leakage by a factor of a million, through low reflectance cold baffling.

Specimen surface and bulk scattering are not controllable, although minimizing heater radiance provides some improvement. This contribution may be precisely evaluated by measurement of specimen emissivity with the reflective heater support and again with a high emissivity heater support.

The radiation from the background at 77°K is less than a millionth of 300°K blackbody radiation at 10 microns, but is increasing very rapidly toward longer wavelengths. Its effect may be reduced by more than an order of magnitude by subtracting the spectrum of the background without the specimen from that with the specimen in the normal measurement mode.

Finally, the interferometer chamber and specimen housing are surrounded by a 300°K vacuum housing, and this radiation is large due to the large emitting area involved. No difficulty should arise if very effective baffling is used at the junction between the specimen housing and the interferometer chamber.

A graphic illustration of measurement errors is given in figure 5. Surface scattering is indicated as less than a part in a million, which assumes high quality optical surfaces are present in the specimen.

## 5. Conclusion

The application of a cooled interferometer system to the measurement of low emittance (absorptance) specimens provides remarkable improvement in sensitivity and spectral resolution. In addition, bulk scattering in specimens may be evaluated and scanning is possible to locate and evaluate inclusions and imperfections in substrates and coatings. These techniques may be applied easily to windows and mirrors, and are suitable for curved surfaces, since they do not depend on the focusing properties of the specimens. The only requirement is the capability of heating, supporting, and measuring the temperature of the specimens without introducing spurious radiation. Materials with low melting points may be evaluated without difficulty, since all specimens are maintained at room temperature.

The measurement of a mirror or window with an average emissivity of 0.01 measured in an 0.1 micron band at 10.6 microns with a spectral resolution of  $1 \text{ cm}^{-1}$  can be made with an uncertainty in emissivity less than  $5 \times 10^{-6}$  in absolute terms and  $6 \times 10^{-7}$  in relative terms over the spectral interval. The absolute error due to temperature stability is proportional to the emittance, and is less than  $1 \times 10^{-6}$  for an emissivity of 0.002. The spectral resolution considered is sufficient to permit analysis of organic impurities in transmissive substrates or on surfaces, as well as inorganic spectral band structure. The rapid spectral scan capability of this type of instrument, used in conjunction with a pulsed laser, allows controlled investigation of transient phenomena such as surface reactions and hot spot formation.

## 6. References

- [1] Sparks, M., J. Appl. Phys. 42, 5029 (1971). [2] Stierwalt, D. L. and Potter, R. F., Emittance Studies, Chapt. 3, Semiconductors and Semimetals, Vol. 3, Academic Press, New York, New York (1967).

## 7. Figures

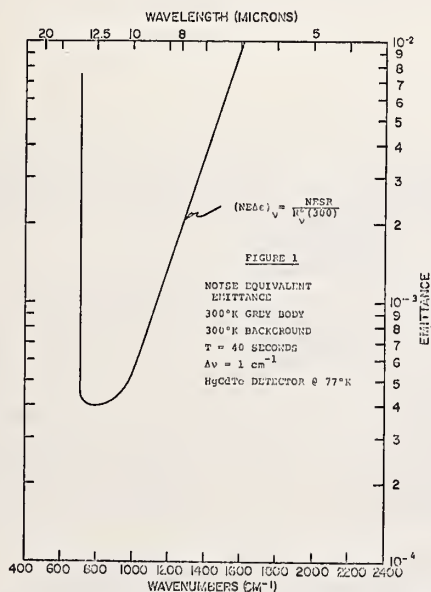


Figure 1. Noise equivalent emittance  $(NE\Delta\epsilon)_\lambda$ .

300°K Grey Body  
300°K Background  
T = 40 Seconds  
 $\Delta\nu = 1 \text{ cm}^{-1}$   
HgCdTe Detector @ 77°K

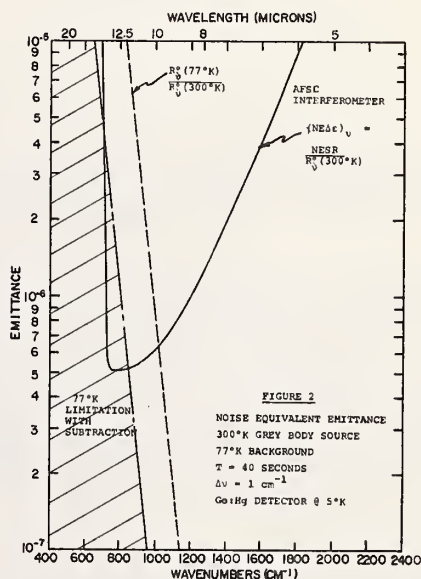


Figure 2. Noise equivalent emittance.

300°K Grey Body Source  
77°K Background  
T = 40 Seconds  
 $\Delta\nu = 1 \text{ cm}^{-1}$   
Ge:Hg Detector @ 5°K

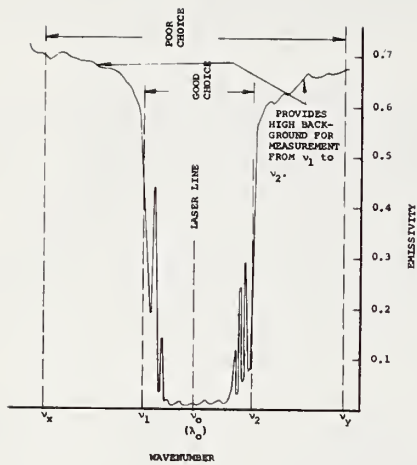


Figure 3. Optimization of spectral band.

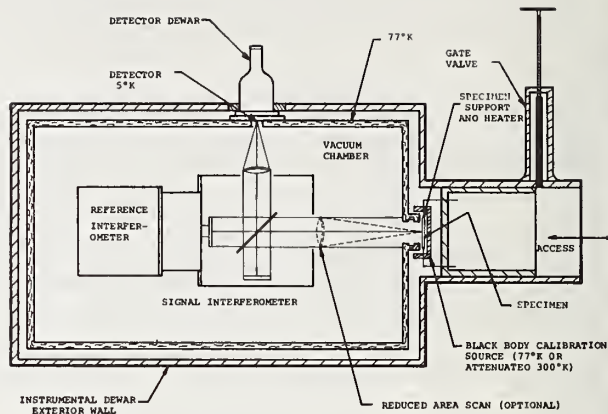


Figure 4. Sketch of measurement technique.

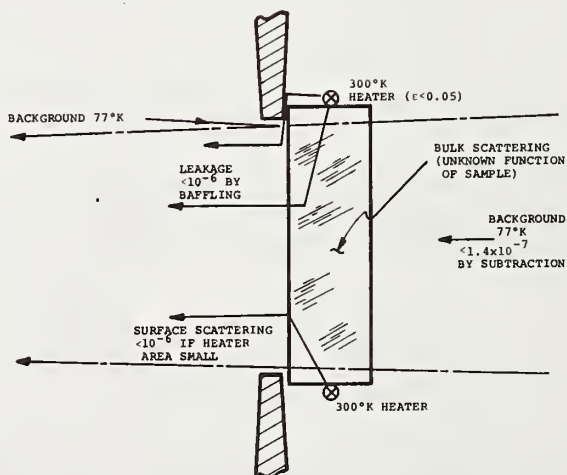


Figure 5. Measurement errors (10 microns).



# Investigation of Pulsed CO<sub>2</sub> Laser Damage of Metal and Dielectric-Coated Mirrors\*

V. Wang, A. I. Braunstein, M. Braunstein, and J. Y. Wada

Hughes Research Laboratories  
Malibu, California 90265

Recent progress made in pulsed high power CO<sub>2</sub> lasers has increased the power handling capabilities of mirrors and mirror coatings. Discussed in this paper are surface damage mechanisms based upon simple physical models (i.e., surface heating, thermally induced stress, absorption centers, etc.) and the experimental results obtained using a pulsed CO<sub>2</sub> laser. Various substrates (Mo, Cu, Ni, quartz, graphite, etc.), metal films (Au, Ag, and Cu), and dielectric coatings (Ge, ThF<sub>4</sub>, CdTe) were exposed to 10.6  $\mu$ m pulses of 1 to 10  $\mu$ sec duration with energy fluxes of up to 200 J/cm<sup>2</sup>. The measured threshold values (> 140 J/cm<sup>2</sup> for 10  $\mu$ sec pulses) of polished metal mirrors were generally in agreement with the predicted values based on the simple model. Thin film coated mirrors exhibited slightly lower threshold values ( $\approx$  75 to 140 J/cm<sup>2</sup> for 10  $\mu$ sec pulses) than that of simple metal metals. The thresholds for those limited numbers of dielectric mirrors tested were even lower ( $\approx$  10 J/cm<sup>2</sup> for pulses of 1 to 10  $\mu$ sec lengths); this low performance is attributed to inclusions which act as local absorption centers within the dielectric.

Key Words: Damage mechanisms, inclusions in dielectrics, multilayer dielectric mirrors, pulsed CO<sub>2</sub> laser damage, thin film coated metal, uncoated metal mirrors.

## 1. Introduction

Recent rapid progress made in pulsed high energy CO<sub>2</sub> lasers has substantially increased the power handling capabilities of mirrors and mirror coatings. Demands for low-loss mirrors capable of withstanding 10.6  $\mu$ m laser flux of tens to hundreds of joules per square centimeter are becoming more critical.

In this paper, we have examined damage mechanisms of the mirror surface based upon a simple physical model. The response characteristics of the surface of a mirror are discussed in Section 2 for a typical liquid cooled metal mirror subjected to an incident flux over a wide range of pulselengths extending from submicroseconds to essentially cw conditions (a few seconds). Particular attention is directed to the range of 1 to 50  $\mu$ sec in which high energy operation of atmospheric pressure electrical CO<sub>2</sub> lasers are most common. In this range of pulselength, flux loading is limited by thermally induced stresses which produce cracking and bond separation of coatings, by excessive temperature rise which may lead to increased surface absorption, or by beam scattering (caused by oxidation and melting effects). The figures of merit of pulse mirrors applicable in this range of operation are reviewed.

Measurements of damage threshold values of various substrates (Mo, Cu, Ni, quartz, etc.), metal films (Au, Ag, and Cu), and dielectric coatings (ThF<sub>4</sub>/CdTe) were performed using a pulsed CO<sub>2</sub> laser which is described in Section 2. The mirror samples were

---

\* Part of this work was conducted under the sponsorship of the Air Force Weapons Laboratory under Contract F29601-71-C-0101.

exposed to 10.6  $\mu\text{m}$  pulses of 1 to 10  $\mu\text{sec}$  duration with energy fluxes of up to 200 J/cm<sup>2</sup>. The measured threshold values of polished metal mirrors were generally in agreement with the predicted value based on the simple model. Thin film coated mirrors exhibited slightly lower threshold values than that of simple metal mirrors. A limited number of low loss multilayer dielectric coated mirrors were examined, and the threshold values were even lower than those of the thin metal film coated mirrors. In Section 4, the experimental data and interpretation of these results are presented.

## 2. Power Limitations of Pulsed Mirrors

A typical high power mirror designed to operate in a cw mode of operation is shown in fig. 1. This mirror consists of a thin faceplate which is supported off a rigid backup plate by columns. The faceplate structure is liquid cooled in order to prevent excessive heating and distortion of the mirror surface.

The calculated power and energy density limitations of this type of mirror over a wide range of pulselengths are shown in figs. 2(a) and 2(b), respectively. As shown in these figures, the pulse response characteristics can be divided into the following three regions:

- Quasi-cw limited ( $\tau > 10^{-2}$  sec)
- Faceplate distortion limited ( $10^{-4}$  sec  $< \tau < 10^{-2}$  sec)
- Surface thermal effect limited ( $\tau < 10^{-4}$  sec)

### 2.1 Quasi-Cw Limited Region

In this region, the pulsewidth of the incident flux is sufficiently long for the heat transfer rate between the faceplate and the liquid coolant and, consequently, the faceplate temperature, to reach a steady-state condition. The time constant which characterizes the minimum pulselength required to reach a near steady state is established by the film heat transfer coefficient of the faceplate coolant interface. The maximum incident flux in this quasi-cw region is limited by the thermal distortion of the faceplate, support column, and backup plates resulting from absorbed flux. A surface figure requirement of about 1/20 of wavelength (at 10.6  $\mu\text{m}$ ) will limit the allowable absorbed energy flux of available mirrors to a few hundred watts per cm<sup>2</sup>.

### 2.2. Faceplate Distortion Limited

In this intermediate pulse region, the pulsewidth is shorter than the time constant associated with the heat transfer between the faceplate and the coolant. The liquid cooling becomes ineffective in keeping the faceplate from heating excessively. The allowable incident flux in this region is limited by the out-of-plane distortion of the faceplate caused by the absorbed flux. Since the heat transferred to the coolant is small over the duration of the pulse, the absorbed energy will be stored, in the thin faceplate. The faceplate distortion is simply proportional to the absorbed energy density. This region, therefore, is characterized by an allowed energy density which remains at a constant value while the allowed incident power increases inversely proportional to the pulsewidth.

### 2.3. Surface Thermal Effect Limited

As the pulsewidth is made narrower, the depth of heat penetration over the duration of the applied pulse will be limited by the diffusibility of material to a depth only a small fraction of the faceplate thickness ( $\sim 1$  mm). The allowable flux in this region is no longer bounded by the out-of-plane distortion criterion; the surface temperature rise becomes a dominant factor. Although catastrophic damage may not occur over one pulse, it is possible that the repeated pulsing might lead to a gradual deterioration of the dielectric coatings and the surface finish. Accordingly, the 400°C surface temperature has been used as a guideline upper limit value for those data plotted in fig. 2. Stress yield conditions in many metals occur at temperatures below 400°C. It is particularly significant with copper, as shown in fig. 2(b).

Typically, the heat penetration (or thermal skin) depths of good mirror materials (in a 50  $\mu\text{sec}$  period) are approximately 0.1 mm or smaller. Because of this small heat

penetration depth, conventional cooling techniques are ineffective over the duration of the pulse. For repetitive pulsing, however, liquid cooling must be included.

#### 2.4. Figures of Merit for 1 to 50 $\mu$ sec Pulsewidths

In the range of 1 to 50  $\mu$ sec pulsewidths, thermal effects occur over a distance which is large compared to the electromagnetic skin depth for penetration of the incident radiation into a metallic reflector ( $\sim 600 \text{ \AA}$ ). Thus, the heat applied to the mirror can be reasonably approximated as being applied at the front surface of the mirror and diffused into the faceplate.

The thermal behavior of a simple mirror substrate can be described by the diffusion equation

$$\frac{\partial T}{\partial t} = \kappa \nabla^2 T \quad (1)$$

$T$  = temperature

$t$  = time

$\kappa$  = thermal diffusivity =  $\frac{K}{\rho C_p}$

$K$  = conductivity

$\rho$  = density

$C_p$  = specific heat

For most cases where the diffusion of the heat into the solid occurs over an area wide compared to the depth of penetration, the following one-dimensional equation will be valid:

$$\frac{\partial T}{\partial t} = \kappa \frac{d^2 T}{dx^2} \quad (2)$$

The solution to the diffusion equation for a uniform step input of laser radiation of pulselength  $\tau$  is given in table 1. The corresponding values of the expansion-induced stress are also summarized in the same table.

Table 1. Figures of Merit

<p>Surface Temperature (<math>k\rho C_p</math>):</p> $\Delta T \approx \frac{2}{\sqrt{\pi}} \left( \frac{\epsilon}{A} \right) (k\rho C_p \tau)^{-1/2}$ <p>Surface Expansion (<math>\rho C_p / \alpha</math>):</p> $S = \frac{2\alpha}{\sqrt{\pi}} \left( \frac{\epsilon}{A} \right) (\rho C_p)^{-1}$ <p>Thermal Stress Limit (<math>\frac{\sigma_y}{\alpha E}</math>):</p> $\sigma \approx \frac{\alpha E}{(1-\nu)} \frac{2}{\sqrt{\pi}} \left( \frac{\epsilon}{A} \right) (k\rho C_p \tau)^{-1/2}$	<p><math>\frac{\epsilon}{A}</math> = Energy per unit area</p> <p><math>\tau</math> = Pulse length</p> <p><math>k</math> = Thermal conductivity</p> <p><math>\rho</math> = Density</p> <p><math>C_p</math> = Specific heat</p> <p><math>\nu</math> = Poisson's ratio</p> <p><math>\sigma_y</math> = Yield stress</p> <p><math>\alpha</math> = Coefficient of thermal expansion</p> <p><math>E</math> = Young's modulus</p>
---	---

The surface temperature rise of a substrate material is seen to be a function of the product ( $k\rho C_p$ ). Among metals, the thermal conductivity is most widely varying of these three coefficients, so high conductivity materials generally give the lowest temperature rise. Also, for a given absorbed energy, the temperature rise is expected to be proportional to the square root of the pulse length. Surface expansion, on the other hand, is independent of both pulselength and thermal conductivity. Also presented in table 1 the thermally induced stress can be shown to be proportional to the coefficient of thermal expansion, the modulus of elasticity, and the temperature rise.



The limitations imposed upon various mirror materials by the temperature and stress yield limits are as shown in fig. 2 and discussed in the preceding section.

### 3. Test Apparatus

The test apparatus consists of a transverse discharge pulsed CO<sub>2</sub> laser operating at 10.6  $\mu$ m as shown in fig. 3. A stable resonator is used with a partially transmitting output mirror and a 6.4 cm germanium lens to focus the output beam upon the test samples. Typical temporal profiles of the output beam are shown in figs. 4(a) and 4(b), respectively, for pulses of 1 and 10  $\mu$ sec; these pulselengths are measured at the half-power points. Beam energy measurements were made using pyroelectric and calorimetric methods.

The test samples are placed at varying distances near or in front of the focal point. The test samples are mounted upon a rotary table in a common plane along with plexiglas targets which are used to determine the approximate beam diameter of the laser beam at a test sample surface. Beam patterns burned into these plexiglas samples are used to determine the area, and therefore the energy density of the incident beam. The threshold of mirror damage was determined by visual observation of the irradiated areas (for changes such as oxidation or enhanced diffused scattering) and microscopic inspection of the mirror sample after testing.

### 4. Test Results and Discussion

#### 4.1. Uncoated Metal Mirrors

Several metal substrate mirrors including copper, molybdenum and electroless nickel were tested. Copper was observed to fail through localized melting and oxidation which resulted in noticeable discolorations and enhanced diffused scattering. Figure 5 shows a sample of the affected area where a copper substrate was exposed to a 2  $\mu$ sec pulse of approximately 200 J/cm<sup>2</sup>. Visible in this sample are two damaged sites about 10<sup>-2</sup> cm in diameter. Spot size of the beam as defined earlier is about 0.8 mm in this test. In this case, power levels at the focus are high enough to consistently cause air breakdown when the sample pieces are positioned. It appears that the surface heating and its effect triggered air breakdown near the focus.

On the basis of the physical model discussed earlier, copper can be expected to have the lowest temperature rise but to undergo thermal stress yielding at relatively low temperatures ( $\sim$ 130°C). Since copper would yield by plastic deformation due to thermally induced compression at the surface, this stress effect appears not to cause any noticeable damage to the mirror in a single pulse operation. Repetitive pulse operation may, however, result in earlier failure due to fatigue. Brittle materials such as BeO would be more susceptible to failure at their thermal stress limit by fracture.

Two electroless nickel mirror samples on copper substrates were also tested. Cracking of electroless nickel plating occurs at a threshold of damage of roughly 30 J/cm<sup>2</sup> for 10  $\mu$ sec. Electroless nickel (Kanigen) is a relatively thick ( $8 \times 10^{-3}$  cm) catalytically deposited amorphous nickel-phosphorous alloy. After heat treating, its high degree of hardness and lack of crystal structure make a desirable substrate for polishing. However, with a thermal conductivity approximately one-one hundredth that of copper, temperature rise can be expected to be an order of magnitude higher, making it a poor choice for pulsed mirrors.

The results of the metal mirror tests are summarized in table 2. As expected, high thermal conductivity substrates exhibit better resistance to damage.

#### 4.2. Thin Film Coated Mirrors

Since the absorption coefficient of thin films of Cu or Ag is generally lower than that of simple refractory substrates, improvements in damage resistance might be expected by employing low loss metallic films over a substrate, thus lowering the absorbed energy. Figures 6, 7, and 8 illustrate some of the damage mechanisms seen in Au and Cu thin films over various substrate combinations which were exposed near their threshold of damage. Figure 6 is a molybdenum substrate coated with  $5 \times 10^{-3}$  cm of Au alloy and overcoated with  $7.5 \times 10^{-5}$  cm of pure gold as the reflecting surface. This thickness of Au alloy is approximately equal to the thermal penetration depth of the energy during a pulse. Damage occurs at 75 J/cm<sup>2</sup> for 10  $\mu$ sec pulses and the damage appears to be the result of melting the Au. The diameter of the damage area in this micrograph is

Table 2. Metal Mirrors

Substrate	Coating	Absorption	Tested Energy Density* at Threshold & Pulse Length
Copper	None	~ 2%	> 140 J/cm <sup>2</sup> (10 $\mu$ sec)
Mo	None	2%	> 140 J/cm <sup>2</sup> ( 2 $\mu$ sec)
Electroless Nickel	None	8.6%	10-30 J/cm <sup>3</sup> ( 1 $\mu$ sec)
* $\pm$ 30%			

approximately 1.2 mm. The underlying Mo substrate with its high melting temperature can be seen intact in the micrograph while the resultant gold droplets show indication of surface tension effects during melting.

In fig. 7, a composite mirror consisting of a Mo substrate with approximately  $10^{-2}$  cm of Cu plating and a vacuum deposited low-loss Cu reflecting surface about  $10^{-5}$  cm in thickness has been exposed to an average flux of 140 J/cm<sup>2</sup>. In this case, the Cu layer is sufficiently thick to essentially constitute an infinitely thick substrate from the standpoint of pulsed thermal effects. With this mirror, oxidation and loss of the vacuum deposited reflective layer after exposure to 140 J/cm<sup>2</sup> can be seen in fig. 7.

In contrast to this, a similar mirror employing a sputtered copper thin film showed no visual signs of damage at 140 J/cm<sup>2</sup>. It may be speculated that this sputtering process results in better thermal and mechanical bonding of the reflective film to the substrate, thus enhancing the heat transfer from the reflector into the substrate material.

A similar mirror using Ag and a thin ThF<sub>4</sub> protective overcoat was also tested. The ThF<sub>4</sub> overcoat is sufficiently thin ( $\sim 1000$  Å) that the electric field within the dielectric is low due to the standing wave effect of the metal reflector. Heating would be expected to originate in the metal reflector rather than from absorption in the dielectric. At  $\sim 70$  J/cm<sup>2</sup> initial signs of scattering were visible in the ThF<sub>4</sub> overcoating, presumably due to substrate heating.

A clear example of softening of a ThF<sub>4</sub> overcoat can be seen in a Quartz/Ag/ThF<sub>4</sub> mirror shown in fig. 8. Here, energies of 10 J/cm<sup>2</sup> and above cause extensive damage including the wrinkled pattern visible away from the central region of oxidized Ag. In the case of an electroless nickel substrate and an Ag reflector without an overcoat shown in fig. 9, the damage mechanism at 40 J/cm<sup>2</sup> is cracking and delamination of the Ag film. Another type of thin film damage, similar in nature to the Au/Mo mirror mentioned previously, can be seen in a vacuum deposited thin film of Cu on Mo (fig. 10). At 140 J/cm<sup>2</sup>, surface tension forces after melting caused by beading of the Cu upon the Mo substrate, as seen in fig. 10. Table 3 summarizes the thresholds measured for thin film metallic reflectors. Copper reflectors upon copper substrates exhibited the best resistance to damage. Gold and molybdenum substrates exhibited similar results. The presence of a dielectric overcoat, which allows easier handling and cleaning of metal mirrors, reduces the threshold only moderately. Electroless nickel and quartz fared the most poorly.

#### 4.3. Multilayer Dielectric Coated Mirrors

The third type of mirrors tested has the potential for the lowest absorption and thus the possibility for very high incident energy fluxes. These dielectric enhanced multilayer mirrors consist of a metallic reflector coated with quarter-wave layers of alternately high and low index dielectric materials. In addition to materials limitations stemming from melting and oxidation of the dielectric, and the possibility of delamination from either poor bonding, residual stresses, or thermal expansion induced stress, there also exists damage by localized pitting due to inhomogeneous thin films. This last mechanism presently limits performance of this type of mirror to well below the performance of simple metal mirrors.



Table 3. Thin Film Metallic Mirrors

Substrate	Coating	Absorption	Tested Energy Density* at Threshold & Pulse Length
Copper	Sputtered Cu	~ 2%	> 140 J/cm <sup>2</sup> (10 μsec)
Copper	Vacuum deposited Cu	~ 1%	~ 140 J/cm <sup>2</sup> (10 μsec)
Copper	Ag/ThF <sub>4</sub>	~ 1%	40-70 J/cm <sup>2</sup> (10 μsec)
Mo/braze	50 μin Au	~ 1.5%	~ 75 J/cm <sup>2</sup> (10 μsec)
Mo	Vacuum deposited Cu	1%	75-140 J/cm <sup>2</sup> (10 μsec)
Electroless nickel	Ag	0.7%	20-40 J/cm <sup>2</sup> (2 μsec)
Quartz	Ag/ThF <sub>4</sub>	~ 1%	~ 10 J/cm <sup>2</sup> (2 μsec)
* ±30%			

Some examples of the damage seen in a two-layer dielectric enhanced mirror consisting of CdTe, ThF<sub>4</sub>, and Cu are shown in figs. 11 through 15. Because of the more complex structure, the failure of this type of reflective coating is striking, as shown in figs. 11 and 12. The effects of melting of the dielectric, and surface tension forces at the threshold are shown in fig. 13. The phenomena of local pitting, which occurs on both high and low conductivity substrates, independent of the number of layers of dielectric and the pulselength over the range tested, occurs around 10 J/cm<sup>2</sup>. Figure 14 is a photograph of a two-layer CdTe/ThF<sub>4</sub>/Cu mirror on an Mo substrate with an absorption of 0.5%. After exposure to 10 J/cm<sup>2</sup> the copper reflector can be seen to be damaged in the bottom of the pit in the dielectric, but the damage does not extend to the Mo substrate. The size of the local damage sites are about 10<sup>-2</sup> cm, far smaller than the beam diameter of 3 mm. A six-layer CdTe/ThF<sub>4</sub> mirror upon an Ag reflector and electroless nickel substrate with an absorption below 0.2% also begins to pit at about 10 J/cm<sup>2</sup>. In this case, more structure is visible in the pitted region due to the larger number of layers of dielectric as shown in fig. 15. The nucleus of the damage appears to be scattered at various heights within the dielectric as a result of the varying depths of the craters, as evidenced by the number of rings visible within each site.

Results of these tests upon dielectric multilayer mirrors are summarized in table 4. In all cases, damage begins to occur at about 10 J/cm<sup>2</sup>. If a simple thermal model of heating is assumed for an electroless nickel substrate and a temperature limitation of 400°C is assumed, then the relationship between incident energy, pulselength, and absorption is illustrated in fig. 16. The experimental points are indicated by the dot symbols, for electroless nickel, and the square symbols for molybdenum substrates.

Table 4. Dielectric Mirrors

Substrate	Coating (No. of Dielectric Layers)	Absorption	Tested Energy Density* at Threshold & Pulse Length
Electroless nickel	Cu/ThF <sub>4</sub> /CdTe (2)	0.5%	10 J/cm <sup>2</sup> (2 μsec)
Electroless nickel	Ag/ThF <sub>4</sub> /CdTe (6)	0.2%	10 J/cm <sup>2</sup> (1 μsec)
Electroless nickel	Ag/ThF <sub>4</sub> /CdTe (6)	0.2%	10 J/cm <sup>2</sup> (8 μsec)
Molybdenum	Cu/ThF <sub>4</sub> /CdTe (2)	0.5%	10 J/cm <sup>2</sup> (10 μsec)
* ±30%			



A model which assumes localized absorption centers imbedded within or between the dielectric films which then cause local heating and damage to the dielectric would be consistent with these observed results. First, the measured average absorption of a dielectric mirror is decreased by the use of additional layers. While decreasing the flux incident upon the metallic reflector, the flux incident upon the first few layers, and thus incident upon absorption centers located within these first layers, remains independent of the number of layers. Second, the substrate would not be expected to have an appreciable effect upon small absorption centers located within the dielectric, due to a relative lack of thermal conduction between the absorption center and the substrate. Finally, as long as the thermal conductivity and the size of an absorption center are sufficiently small, thermal diffusion of absorbed energy does not significantly modify the local temperature rise, thus making the process independent of pulse length.

A similar problem of small inclusions within a dielectric has been encountered (and solved) in the development of high power 1.06  $\mu\text{m}$  laser glass as well as in the development of high reflectance mirrors in the visible. The solution is basically one of careful control of process and materials.

## 5. Summary

The status of the three types of mirrors tested thus far can be summarized in table 5. At present, simple metal mirrors have exhibited the highest resistance to damage with threshold values in excess of 140 J/cm<sup>2</sup> for 8 to 10  $\mu\text{sec}$  pulses. The range of incident flux which was predicted to cause damage agrees well with the measured threshold values. A simple extrapolation of these results indicates that an incident flux in excess of 500 J/cm<sup>2</sup> for pulses of 50  $\mu\text{sec}$  can be handled with simple metal mirrors.

Table 5. Summary of Measurements

CO<sub>2</sub> Laser Beam  
(8-10  $\mu\text{sec}$ )

	Metal	Thin Film Coated Metal	Multilayer Dielectric
Mirror Material	Cu	Cu on Cu	CdTe-ThF <sub>4</sub> -Cu on Mo
Absorption	~2%	~1%	~0.5%
Measured Threshold (Av)	>140 J/cm <sup>2</sup>	75-140 J/cm <sup>2</sup>	7-10 J/cm <sup>2</sup>

For thin metal mirrors, performance has been comparable to simple metal mirrors, with measured thresholds of 75 to 140 J/cm<sup>2</sup> for the best mirrors. As with the simple reflecting substrate mirrors, damage resistance is a function of thermal conductivity. In addition, however, the thermal and mechanical bond of the thin film to the substrate plays an important role in the performance of these mirrors.

At present, dielectric enhanced multilayer mirrors exhibit the lowest damage resistance with threshold values of approximately 10 J/cm<sup>2</sup>. This low performance is attributed to local absorption centers within the dielectric which nucleate damage sites in the dielectric. It is expected that removal of these centers will considerably improve their performance. With the provision that the expected low absorption of these mirrors can be maintained uniformly over the surface, the ultimate performance of these mirrors may be far superior to metal reflectors, especially at short pulse-lengths (~10<sup>-9</sup> sec).

## 6. Acknowledgment

We wish to acknowledge the many helpful discussions enjoyed with several colleagues, especially Drs. O. P. Judd, P. O. Clark, and F. J. McClung at the Hughes Aircraft Company. Thanks are extended to J. F. Moyer, J. E. Fitzgerald, J. L. Schmid and L. J. McNulty for their able assistance in preparation of mirror samples and experiments.

## 7. Figures

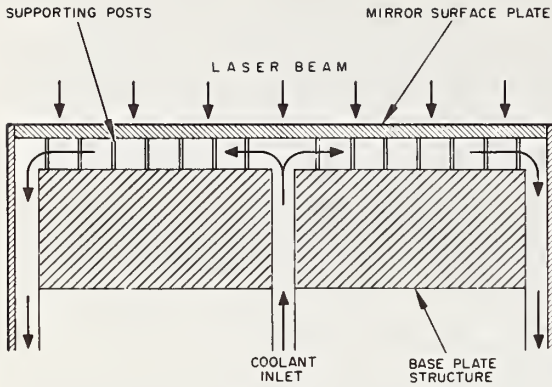


Figure 1. CW water-cooled metal mirror.

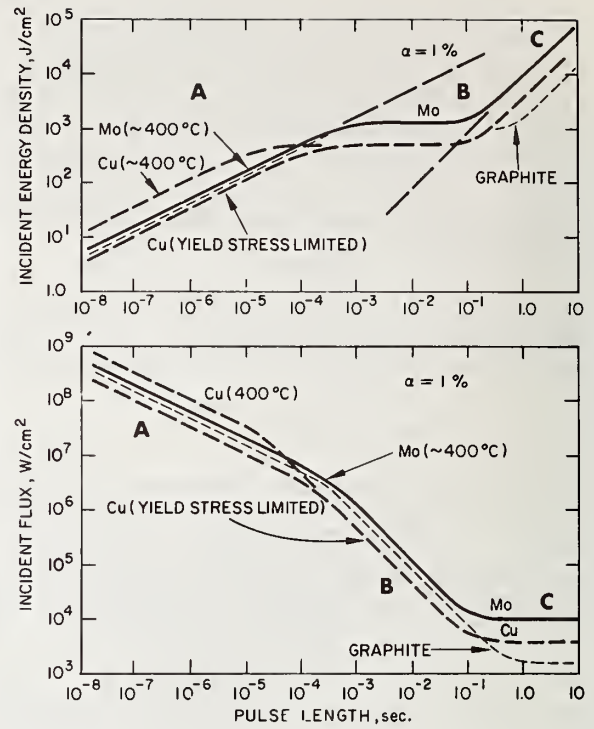


Figure 2. Calculated maximum mirror loading versus pulse length.

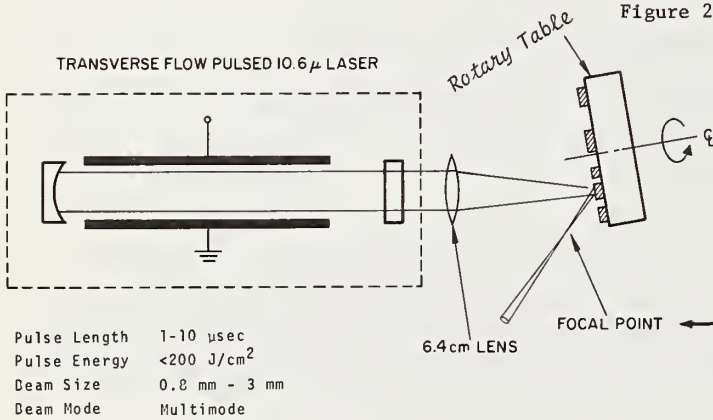


Figure 3. Schematic of test apparatus.

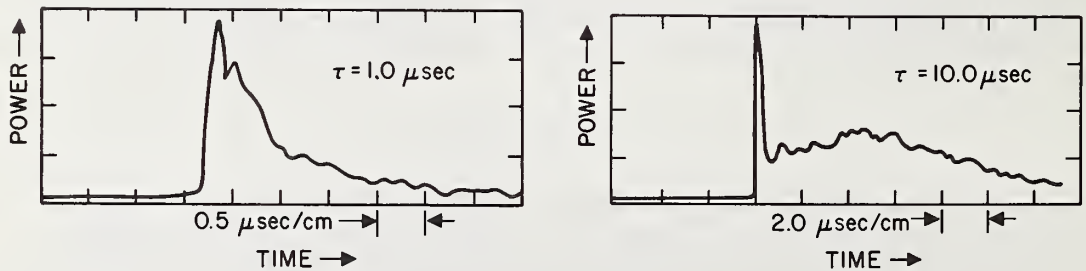


Figure 4. Typical laser output pulse shape.

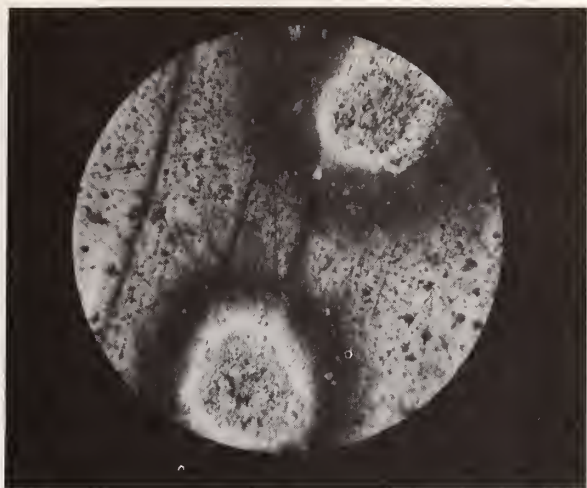


Figure 5. Two damage sites on a simple copper substrate  $200 \text{ J/cm}^2$  (375X).

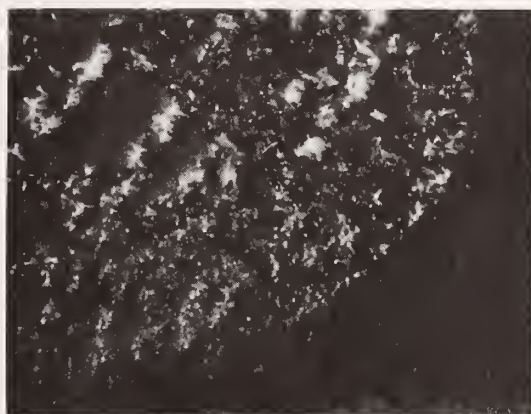


Figure 6. Gold on Mo substrate  $75 \text{ J/cm}^2$  (150X).

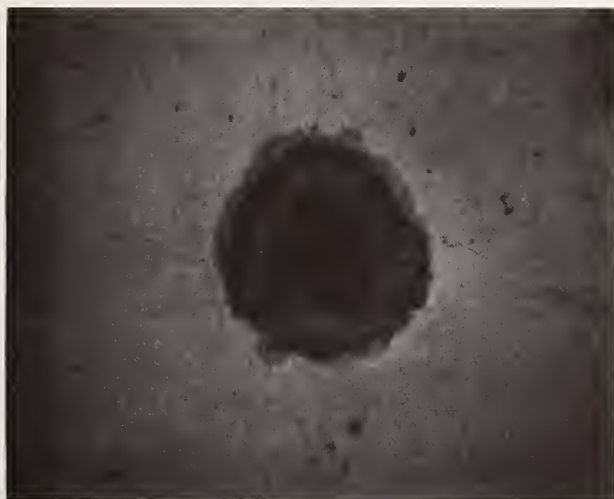


Figure 7. Vacuum deposited Cu on a Cu substrate  $140 \text{ J/cm}^2$ .



Figure 8. Ag/ThF<sub>4</sub> on Quartz  $10 \text{ J/cm}^2$  (75X).



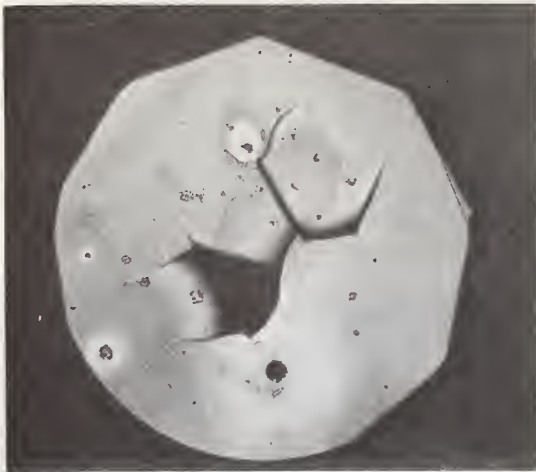


Figure 9. Ag thin film on an electroless nickel substrate  $40 \text{ J/cm}^2$  (150X).



Figure 10. Vacuum deposited Cu on a Mo substrate  $140 \text{ J/cm}^2$  (187X).

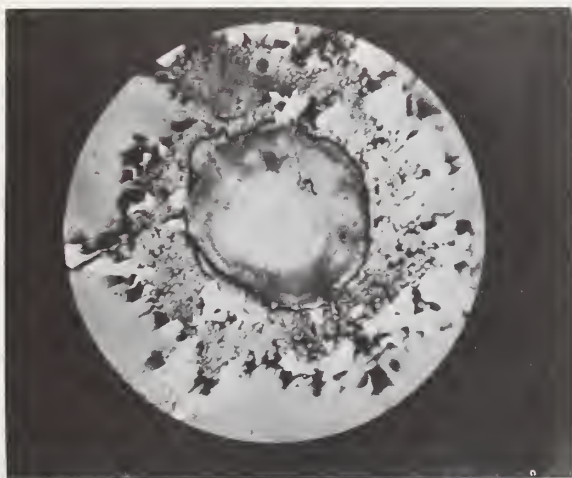


Figure 11. CdTe/ThF<sub>4</sub> two layer dielectric enhanced mirror  $30 \text{ J/cm}^2$  (37X).

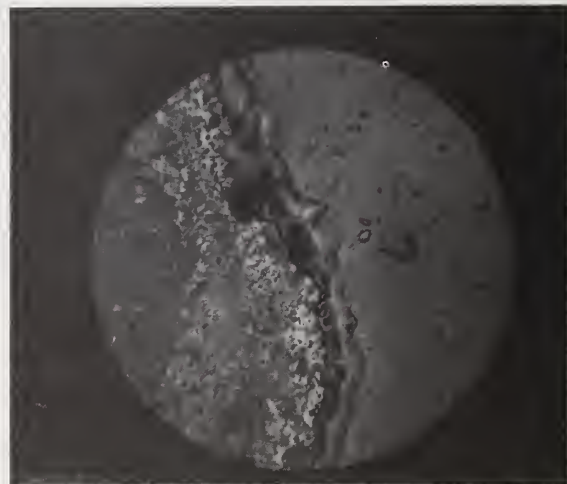


Figure 12. CdTe/ThF<sub>4</sub> two layer dielectric enhanced mirror  $30 \text{ J/cm}^2$  (750X).

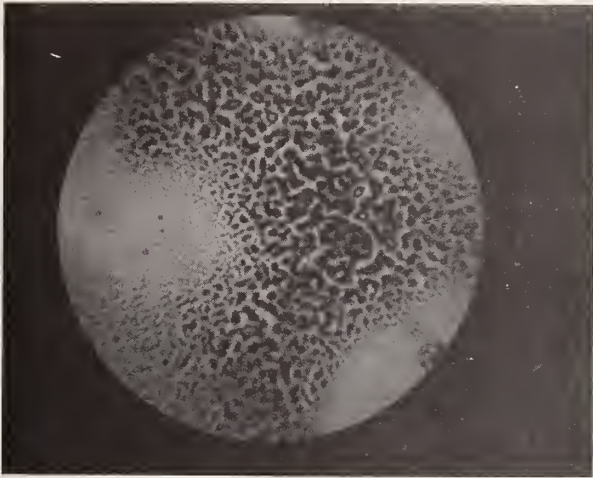


Figure 13. CdTe/ThF<sub>4</sub> two layer dielectric enhanced mirror, threshold 10 J/cm<sup>2</sup> (375X).

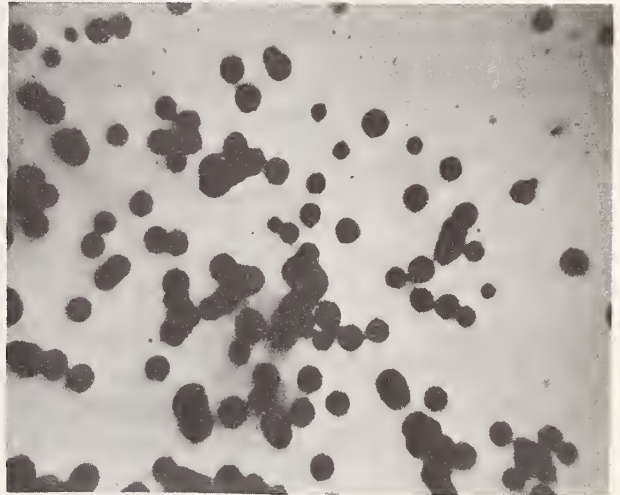


Figure 14. CdTe/ThF<sub>4</sub> two layer dielectric enhanced mirror, threshold 10 J/cm<sup>2</sup> (37X).

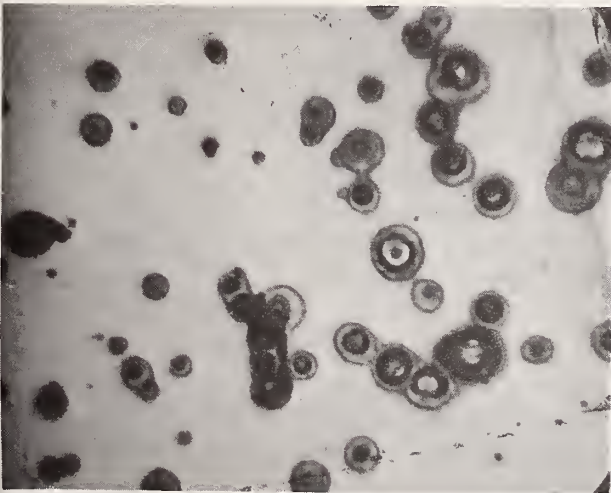


Figure 15. CdTe/ThF<sub>4</sub> six-layer dielectric enhanced mirror, threshold 10 J/cm<sup>2</sup> (37X).

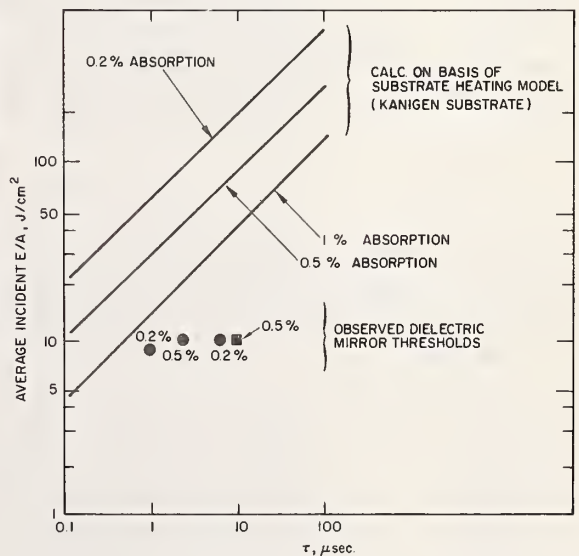


Figure 16. Damage threshold pulse energy versus pulsewidth for dielectric mirrors.

## Appendix

### Participants

N. C. Anderholm	Div 5214, Sandia Lab., Box 5800, Albuquerque NM 87115
L. J. Aplet	Hughes Aircraft, Culver City CA 90230
R. R. Austin	Perkin-Elmer, Norwalk CT 06897
E. D. Baird	Lawrence Livermore Lab., P O Box 808, Livermore CA 94550
M. Bass	Raytheon, 28 Seyon St., Waltham MA 02154
H. & J. Bennett	Michelson Lab., Code 6018, Naval Weapons Center, China Lake CA 93555
R. A. Berg	Lawrence Livermore Lab., P O Box 808, Livermore CA 94550
E. A. Blankenship	USAF Weapons Lab.(SYX), Kirtland AFB NM 87117
E. S. Bliss	AFMRL/USAF, Hanscomb Field, Bedford MA 01730
N. Boling	Owens-Illinois, 1700 N. Westwood, Toledo OH 43651
H. S. Boyne	Div 271, National Bureau of Standards, Boulder CO 80302
P. Braunlich	Bendix Research Lab., Bendix Center, Southfield MI 48076
C. J. Broomer	Broomer Research Corp., 23 Sheer Plaza, Plainview NY 11803
W. F. Brunner	Lawrence Livermore Lab., P O Box 808, Livermore CA 94550
P. Bryce	Alberta University, Edmonton, Canada
A. Y. Cabezas	2342 Selby Ave., Los Angeles CA 90064
V. Costich	Coherent Radiation, 3210 Porter Dr., Palo Alto CA 94304
T. G. Crow	ILS Inc., 3404 N. Orange Blossom Tr., Orlando FL 32805
J. Davisson	US Naval Research Lab., Washington DC 20390
G. DeBell	Spectra-Physics, 1250 W. Middlefield, Mt. View CA 94040
L. DeShazer	Dept. of Physics, USC, Los Angeles CA 90007
R. Doussain	Laboratoire National d'Essais Paris, 1 Rue Gaston Boissier, Paris, France
G. Dube	Owens-Illinois, 1700 N. Westwood, Toledo OH 43651
S. J. Ekstrom	Lawrence Livermore Lab., P O Box 808, Livermore CA 94550
A. Feldman	A259 Materials, National Bureau of Standards, Washington DC 20234
J. A. Fleck	Lawrence Livermore Lab., P O Box 808, Livermore CA 94550
D. Fradin	McKay Lab., Harvard University, 90 Oxford St., Cambridge MA 02138
D. L. Franzen	Div 271, National Bureau of Standards, Boulder CO 80302
T. Gallagher	Valpey, 36 Pope Rd., Holliston MA 01746
C. Giuliano	Hughes Research Labs., Malibu CA 90265
A. J. Glass	Wayne State University, 5050 Anthony Wayne Dr., Detroit MI 48202
A. M. Glass	Bell Labs., Mountain Ave., Murray Hill NJ 07976
A. Glassman	Lawrence Livermore Lab., P O Box 808, Livermore CA 94550
H. H. Grimes	NASA-Lewis, 21000 Brookpark Rd., Cleveland OH 44135
A. H. Guenther	USAF Weapons Lab./DYD, Kirtland AFB NM 87117



B. Guscott	KMSF, Research Park, Ann Arbor MI 48108
Y. H. Hahn	Laser Energy, Inc., 325 Mt. Read Blvd., Rochester NY 14611
N. F. Harmon	The MITRE Corp., P O Box 208, Bedford MA 01730
T. Harris	Spacerays, 4 Standish Circle, Andover MA 01810
N. L. Hecht	Univ. Dayton Research Institute, University of Dayton, Dayton OH 45409
R. W. Hellwarth	USC, University Park, Los Angeles CA 90007
L. M. Hobrock	Hughes Aircraft Co., Culver City CA 90230
S. J. Holmes	Northrop, 3401 W. Broadway, Hawthorne CA 01970
D. Horowitz	A259 Materials, National Bureau of Standards, Washington DC 20234
R. C. Hyer	Los Alamos Scientific Lab., Los Alamos NM 87544
T. Izumitani	Hoya Glass Works, 58-685 Hodokubo Hino, Tokyo, Japan
D. A. Jennings	Div 271, National Bureau of Standards, Boulder CO 80302
C. J. Johnson	II-VI, Inc., 207 Garden Lane, Glenshaw PA 15116
E. Jones	Div 5214, Sandia Corp., Box 5800, Albuquerque NM 87115
A. Kahan	AFCRL, Hanscomb Field, Bedford MA 01730
J. M. Khan	Lawrence Livermore Laboratory, P O Box 808, Livermore CA 94550
W. J. Lange	Westinghouse Research, Pittsburgh PA 15235
J. K. Larin	Laser Optics, Inc., P O Box 3, Danbury CT 06810
R. Lawson	Dept. of Elect. Engineering, University of Alberta, Edmonton, Alberta, Canada
C. Layne	Lawrence Livermore Laboratory, P O Box 808, Livermore CA 94550
H. Lee	Owens-Illinois, 1700 N. Westwood, Toledo OH 43651
H. R. Leider	Lawrence Livermore Laboratory, P O Box 808, Livermore CA 94550
R. A. Lindberg	NASA-Lewis Research Center, 21000 Brookpark Road, Cleveland OH 44135
G. M. Loiacono	Isomet Corp., 103 Bauer Drive, Oakland NJ 07436
P. Mace	Los Alamos Scientific Lab., Los Alamos NM 87544
R. W. MacPherson	DREV, P O Box 880, Courcellette, P. Q., Canada
A. Maimoni	Lawrence Livermore Laboratory, P O Box 808, Livermore CA 94550
J. Marburger	Dept. of Physics & Elect. Engineering, USC, Los Angeles CA 90007
B. Martin	Dept. P14, International Business Machines, Inc., Endicott NY 13760
J. McMahon	National Radiation Laboratory, Washington DC 20390
P. J. Mendoza	Union Carbide-Korad Dept., 2520 Colorado Ave., Santa Monica CA 90404
J. de Metz	CEA Li meil, PO 27 Villeneuve St. Georges, 91 France
D. Milam	ARCRL/USAF, Hanscomb Field, Bedford MA 01730
P. Miles	Raytheon Co.-Research Div., 28 Seyon St., Waltham MA 02154
S. A. Miller	NELC, 271 Catalina Blvd., San Diego CA 92106
J. Moffat	ILC, Inc., 164 Commercial St., Sunnyvale CA 94022
L. P. Mott	Optical Coating Lab., 5789 Giffen Ave., Santa Rosa CA 95403
J. Murachver	EG&G, 35 Congress St., Salem MA 01970

B. E. Newnam	3121 Veteran Ave., Los Angeles CA 90034
P. E. Nielsen	AFWL/SYT, Kirtland AFB NM 87117
R. O'Neil	MIT/Lincoln L-113, Wood St., Lexington MA 02173
D. Osborn	Sylvania, 100 Fergeson Dr., Mt. View CA 94040
A. Owyong	Div 5214, Sandia Lab., P O Box 5800, Albuquerque NM 87115
J. H. Parks	Physics Dept., USC, Los Angeles CA 90007
R. Pollack	LASL, Box 1663, Los Alamos NM 87544
R. Puttbach	Airtron Div.-Litton, 200 E. Hanover Ave., Morris Plains NY 10453
K. D. Pyatt, Jr.	Systems Science and Software, Box 1620, La Jolla CA 92037
W. Reichelt	LASL(L-1), Los Alamos NM 87544
R. L. Rewski	USAF Avionics Lab., AFAL/TEO Wright-Patterson AFB OH 45433
L. W. Riley	Apollo Lasers, 6365 Arizona Circle, Los Angeles CA 90045
O. Roth	Dept. 28Z, IBM, Box 1900, Boulder CO 80302
P. Rushworth	Martin Marietta, Box 5837, Orlando FL 32805
T. Saito	USAF Weapons Lab/SYX, Kirtland AFB NM 87117
J. R. Schneider	Physics Dept., University of Dayton, Dayton OH 45409
D. Segawa	Hoya Glass Works, P O Box 210, Menlo Park CA 94025
L. L. Shaw	Lawrence Livermore Lab., P O Box 808, Livermore CA 94550
C. Y. She	Dept. of Physics, Colorado State University, Fort Collins CO 80521
J. Sieman	USAF-Hughes Aircraft, Mail Sta. C-160, Culver City CA 90230
J. L. Smith	US Army Missile Command/AMSMI-RRD, Redstone Arsenal AL 35809
M. J. Soileau	USAF Weapons Lab/LMO, Kirtland AFB NM 87117
L. H. Solomon	Itek Corp., 10 Maguire Road, Lexington MA 02173
M. Sparks	Xonics, Inc., 6837 Havenhurst Ave., Van Nuys CA 91406
R. Speck	Lawrence Livermore Laboratory, P O Box 808, Livermore CA 94550
K. Steinbruegge	Westinghouse Resarch Labs., Pittsburgh PA 15235
D. F. Stevison	AFML/LP, Wright-Patterson AFB OH 45433
C. M. Stickley	ARPA, Materials Sciences, 1400 Wilson, Arlington VA 22209
D. L. Stierwalt	NELC, 271 Catalina Blvd., San Diego CA 92106
D. Sullivan	Hughes Aircraft, Meul Station B-156, Culver City CA 90230
B. R. Suydam	LASL, Box 1663, Los Alamos NM 87544
E. Teppo	Naval Weapons Center, Code 4051, China Lake CA 93555
J. Terrell	LASL, Box 1663, Los Alamos NM 87544
P. D. Thomas	Dept. 52-22, Lockheed Research, 3251 Hanover, Palo Alto CA 94304
H. M. Thompson	Cornell Aero Lab., Inc., 4455 Genesee, Buffalo NY 14221
J. H. Tillotson	KMS Fusion, Box 1567, Ann Arbor MI 48106

V. Wang	Hughes Research Lab., 3011 Malibu Canyon Road, Malibu CA 90265
S. W. Warren	ITT Components, Edinburgh Way, Harlow, Essex, England
B. Watt	LASL, Box 1663, Los Alamos NM 87544
R. Webb	Allied Chemical Corp., P O Box 1021-R, Morristown NJ 07960
E. D. West	Div 271, National Bureau of Standards, Boulder CO 80302
R. V. Wicks	USAF Weapons Lab/SYX, Kirtland AFB NM 87117
J. D. Wilcox	Lawrence Livermore Laboratory, P O Box 808, Livermore CA 94550
E. Woodbury	Hughes Aircraft, 18621 Tarzana Drive, Tarzana CA 91356
R. Woodcock	American Optical Corp., Southbridge MA 01550
G. Wyntjes	Block Eng., Inc., 19 Blackstone St., Cambridge MA 07138





U.S. DEPT. OF COMM. BIBLIOGRAPHIC DATA SHEET		1. PUBLICATION OR REPORT NO. NBS-SP -372	2. Gov't Accession No.	3. Recipient's Accession No.
4. TITLE AND SUBTITLE  Laser Induced Damage in Optical Materials : 1972			5. Publication Date October 1972	
			6. Performing Organization Code	
7. AUTHOR(S) Various: Edited by Alexander J. Glass, Wayne State University and Arther H. Guenther, Kirtland AFB, New Mexico			8. Performing Organization	
9. PERFORMING ORGANIZATION NAME AND ADDRESS  NATIONAL BUREAU OF STANDARDS, Boulder Labs. DEPARTMENT OF COMMERCE Boulder, Colorado 80302			10. Project/Task/Work Unit No. 2710585/2710900	
			11. Contract/Grant No.	
12. Sponsoring Organization Name and Address American Society for Testing and Materials and by the National Bureau of Standards (Div. 271) Boulder Laboratories, Boulder, Colorado 80302			13. Type of Report & Period Covered Final	
			14. Sponsoring Agency Code	
15. SUPPLEMENTARY NOTES				
16. ABSTRACT (A 200-word or less factual summary of most significant information. If document includes a significant bibliography or literature survey, mention it here.)  The fourth ASTM Symposium on Laser Induced Damage in Optical Materials was held at the National Bureau of Standards in Boulder, Colorado on June 14-15 of this year. This symposium is held as part of the activity of Subcommittee II on Lasers and Laser Materials, of the ASTM. Subcommittee II is charged with the responsibility of formulating standards for laser materials, components, and devices. The chairman of Subcommittee II is Haynes Lee, of Owen-Illinois, Inc. Co-chairmen for the damage symposia are Dr. Arthur H. Guenther, of the Air Force Weapons Laboratory, and Professor Alexander J. Glass, Chairman of the Department of Electrical Engineering at Wayne State University. Approximately 125 attendees at the symposium heard 21 papers on topics relating to laser-induced damage in glass, crystalline materials, nonlinear optical materials, thin film dielectric coatings, and infrared components. Particular attention was given to the process of plasma formation at dielectric surfaces, the role played by self-focusing in bulk damage in solids, damage morphology of thin film coatings, and the role of absorption in IR component failure. The proceedings of these Symposia represent the major source of information in the field of laser-induced damage in optical materials. The Symposia themselves, along with the periodic meetings of Subcommittee II, provide a unique forum for the exchange of information regarding laser materials specifications among the manufacturers and users of laser devices, components, and systems. The Symposium also serves as a mechanism of information gathering, to enable the Subcommittee to write informed and realistic specifications.				
17. KEY WORDS (Alphabetical order, separated by semicolons) IR windows and mirrors; laser damage; laser materials; self-focusing; thin films.				
18. AVAILABILITY STATEMENT  <input checked="" type="checkbox"/> UNLIMITED.  <input type="checkbox"/> FOR OFFICIAL DISTRIBUTION. DO NOT RELEASE TO NTIS.			19. SECURITY CLASS (THIS REPORT)  UNCLASSIFIED	21. NO. OF PAGES  215
			20. SECURITY CLASS (THIS PAGE)  UNCLASSIFIED	22. Price  \$1.75





## PERIODICALS

**JOURNAL OF RESEARCH** reports National Bureau of Standards research and development in physics, mathematics, and chemistry. Comprehensive scientific papers give complete details of the work, including laboratory data, experimental procedures, and theoretical and mathematical analyses. Illustrated with photographs, drawings, and charts. Includes listings of other NBS papers as issued.

*Published in two sections, available separately:*

### • Physics and Chemistry

Papers of interest primarily to scientists working in these fields. This section covers a broad range of physical and chemical research, with major emphasis on standards of physical measurement, fundamental constants, and properties of matter. Issued six times a year. Annual subscription: Domestic, \$9.50; \$2.25 additional for foreign mailing.

### • Mathematical Sciences

Studies and compilations designed mainly for the mathematician and theoretical physicist. Topics in mathematical statistics, theory of experiment design, numerical analysis, theoretical physics and chemistry, logical design and programming of computers and computer systems. Short numerical tables. Issued quarterly. Annual subscription: Domestic, \$5.00; \$1.25 additional for foreign mailing.

## TECHNICAL NEWS BULLETIN

The best single source of information concerning the Bureau's measurement, research, developmental, cooperative, and publication activities, this monthly publication is designed for the industry-oriented individual whose daily work involves intimate contact with science and technology—for engineers, chemists, physicists, research managers, product-development managers, and company executives. Includes listing of all NBS papers as issued. Annual subscription: Domestic, \$3.00; \$1.00 additional for foreign mailing.

### Bibliographic Subscription Services

The following current-awareness and literature-survey bibliographies are issued periodically by the Bureau: Cryogenic Data Center Current Awareness Service (weekly), Liquefied Natural Gas (quarterly), Superconducting Devices and Materials (quarterly), and Electromagnetic Metrology Current Awareness Service (monthly). Available only from NBS Boulder Laboratories. Ordering and cost information may be obtained from the Program Information Office, National Bureau of Standards, Boulder, Colorado 80302.

## NONPERIODICALS

**Applied Mathematics Series.** Mathematical tables, manuals, and studies.

**Building Science Series.** Research results, test methods, and performance criteria of building materials, components, systems, and structures.

**Handbooks.** Recommended codes of engineering and industrial practice (including safety codes) developed in cooperation with interested industries, professional organizations, and regulatory bodies.

**Special Publications.** Proceedings of NBS conferences, bibliographies, annual reports, wall charts, pamphlets, etc.

**Monographs.** Major contributions to the technical literature on various subjects related to the Bureau's scientific and technical activities.

**National Standard Reference Data Series.** NSRDS provides quantitative data on the physical and chemical properties of materials, compiled from the world's literature and critically evaluated.

**Product Standards.** Provide requirements for sizes, types, quality, and methods for testing various industrial products. These standards are developed cooperatively with interested Government and industry groups and provide the basis for common understanding of product characteristics for both buyers and sellers. Their use is voluntary.

**Technical Notes.** This series consists of communications and reports (covering both other-agency and NBS-sponsored work) of limited or transitory interest.

**Federal Information Processing Standards Publications.** This series is the official publication within the Federal Government for information on standards adopted and promulgated under the Public Law 89-306, and Bureau of the Budget Circular A-86 entitled, Standardization of Data Elements and Codes in Data Systems.

**Consumer Information Series.** Practical information, based on NBS research and experience, covering areas of interest to the consumer. Easily understandable language and illustrations provide useful background knowledge for shopping in today's technological marketplace.

## CATALOGS OF NBS PUBLICATIONS

**NBS Special Publication 305, Publications of the NBS, 1966-1967.** When ordering, include Catalog No. C13.10:305. Price \$2.00; 50 cents additional for foreign mailing.

**NBS Special Publication 305, Supplement 1, Publications of the NBS, 1968-1969.** When ordering, include Catalog No. C13.10:305/Suppl. 1. Price \$4.50; \$1.25 additional for foreign mailing.

**NBS Special Publication 305, Supplement 2, Publications of the NBS, 1970.** When ordering, include Catalog No. C13.10:305/Suppl. 2. Price \$3.25; 85 cents additional for foreign mailing.

Order NBS publications (except Bibliographic Subscription Services) from: Superintendent of Documents, Government Printing Office, Washington, D.C. 20402.

**U.S. DEPARTMENT OF COMMERCE**  
**National Bureau of Standards**  
Washington, D.C. 20234

OFFICIAL BUSINESS

Penalty for Private Use, \$300

POSTAGE AND FEES PAID  
U.S. DEPARTMENT OF COMMERCE  
215

